



Universidad Nacional Autónoma de México
Programa de Posgrado en Astrofísica
Instituto de Radioastronomía y Astrofísica

**X-ray reflection features and soft
excess in type-1 AGN and the
infrared emission of the dusty torus
in NGC 1068**

T E S I S

Para optar por el grado de

Doctor en Ciencias
(Astrofísica)

PRESENTA:

César Ivan Victoria Ceballos

Tutor:

Dr. Omaira González Martín, Instituto de Radioastronomía y Astrofísica

Morelia, Michoacán, Enero de 2024



Universidad Nacional
Autónoma de México

Dirección General de Bibliotecas de la UNAM

Biblioteca Central



UNAM – Dirección General de Bibliotecas
Tesis Digitales
Restricciones de uso

DERECHOS RESERVADOS ©
PROHIBIDA SU REPRODUCCIÓN TOTAL O PARCIAL

Todo el material contenido en esta tesis esta protegido por la Ley Federal del Derecho de Autor (LFDA) de los Estados Unidos Mexicanos (México).

El uso de imágenes, fragmentos de videos, y demás material que sea objeto de protección de los derechos de autor, será exclusivamente para fines educativos e informativos y deberá citar la fuente donde la obtuvo mencionando el autor o autores. Cualquier uso distinto como el lucro, reproducción, edición o modificación, será perseguido y sancionado por el respectivo titular de los Derechos de Autor.

Las galaxias activas contienen en su centro un agujero negro supermasivo (SMBH, por sus siglas en inglés) acretaando material, que en este proceso libera enormes cantidades de energía, lo que se traduce en luminosidades del orden de 10^{40-48} erg/s. Se dice entonces que, estas galaxias tienen un núcleo activo, y es comunmente llamado núcleo activo galáctico, (AGN, por sus siglas en inglés).

En este trabajo de tesis exploramos el espectro de los AGNs en dos diferentes longitudes de onda: infrarojo y rayos-X, ya que estas son las longitudes de onda que permiten aislar de mejor manera la emisión nuclear de la galaxia. A través del estudio en infrarojo hemos investigado el toro de polvo en la galaxia NGC 1068, mientras que a través del estudio en rayos-X exploramos las diferentes estructuras que contribuyen al espectro observado en una muestra de 22 AGNs. En ambos casos realizamos nuestro trabajo a través del ajuste espectral de diferentes modelos a los datos disponibles en cada longitud de onda estudiada. Los resultados presentados en esta tesis contribuyen a la resolución de tres grandes preguntas sobre los AGN, que aún permanecen bajo debate, ¿Cuál es la distribución geométrica y propiedades del polvo en los AGN?, ¿Cuáles son los medios de reflexión de los rayos-X en los AGN tipo 1? y ¿Cuál es el posible origen del exceso suave presente en los AGN tipo 1?.

En primer lugar presentamos los resultados obtenidos del estudio del toro de polvo en NGC 1068. Para este, usamos espectros infrarojos de banda N y banda Q de Michelle/Gemini, que cubren el rango de mediano infrarojo en las longitudes de onda de 7-13 μm y 18-23 μm , respectivamente. Nuestro principal resultado acerca de la geometría del toro de polvo en NGC 1068 es que el modelo más simple que ajusta a las observaciones consiste en dos

toros concéntricos con diferentes tamaños y propiedades: un toro interno más denso y más pequeño con radio externo de 1.8 pc, un segundo toro que alcanza una extensión de 28 pc y es menos denso. Otro de nuestros resultados principales es acerca del tamaño de los granos de polvo. Encontramos que se requieren granos sustancialmente más grandes que aquellos asumidos típicamente en los modelos actuales. Específicamente, de un tamaño usual de $0.25 \mu\text{m}$, nuestro modelo requiere granos de $1 \mu\text{m}$ para explicar el espectro infrarrojo observado para NGC 1068. Estos resultados pueden interpretarse como una evidencia convincente de un toro de polvo complejo en NGC 1068. Especulamos que esto puede entenderse como un disco/toro compacto interno más un toro/viento externo extendido, conformando un disco ensanchado o un modelo de fuente dinámica para el polvo.

En segundo lugar presentamos los resultados obtenidos de nuestro estudio en rayos-X para la muestra de 22 AGNs tipo 1. El primer objetivo de este trabajo fue determinar las estructuras físicas donde ocurre la reflexión de rayos-X: disco de acreción, BLR o toro. Nuestro principal resultado fue que el 67% de los objetos de la muestra requieren tanto de reflexión en el disco de acreción como de reflexión en el toro, para explicar sus espectros observados. Sólo un objeto es ajustado a través de reflexión en el toro y sólo dos objetos son ajustados considerando sólo reflexión en el disco de acreción. Finalmente, encontramos que tres objetos de la muestra ajustan igualmente tanto al modelo de reflexión en el toro como al modelo de reflexión en el disco de acreción.

Este trabajo lo hemos extendido hacia bajas energías para estudiar el origen de la emisión soft. Nuestros resultados principales muestran que para ninguno de los objetos en nuestra muestra el escenario de comptonización puede explicar el exceso suave. Por el contrario, este puede ser explicado para todos los objetos mediante la contribución por emisión de cuerpo negro. Aunado a esta componente de cuerpo negro, la mayoría de objetos requiere dos componentes de este tipo, más la contribución a bajas energías del disco de acreción y/o el efecto debido a la presencia de material parcialmente ionizado parcialmente cubierto sobre nuestra línea de visión.

Como resultado de este trabajo de tesis hemos ayudado al avance en la respuesta a tres de las preguntas que aún se encuentran abiertas en el área de los AGN: la caracterización del toro de polvo, los medios de reflexión de la emisión primaria de rayos-X y el posible origen

del exceso suave. Los resultados generales obtenidos en esta tesis, tanto para la emisión infraroja como para el espectro de rayos-X, demuestran que las componentes estudiadas son más complejas de lo que se asume comúnmente, y que esto debe ser considerado en trabajos futuros y en el desarrollo de modelos que intentan explicar la naturaleza de los AGN.

Esta tesis es una compilación de dos artículos donde soy el autor principal, ambos ya publicados en la revista “The Astrophysical Journal”, y un capítulo sobre el estudio del exceso suave, que pretendemos publicar próximamente.

ABSTRACT

Active galaxies contain a supermassive black hole (SMBH) at their center accreting material, which in this process releases enormous amounts of energy, which translates into luminosities of the order of up to 10^{44} erg /s. It is then said that these galaxies have an active nucleus, and it is commonly called the active galactic nucleus (AGN).

In this thesis we explore the spectrum of AGNs at two different wavelengths: infrared and X-rays, since they are the wavelengths where the nuclear emission of the galaxy can be best isolated. Through the infrared study we have investigated the dust torus in the galaxy NGC 1068, while through the X-ray study we explore the different structures that contribute to the spectrum observed in a sample of 22 AGNs. In both cases we carry out our work through the spectral fitting of different models to the data available at each wavelength studied. The results presented in this thesis contribute to the resolution of three major questions about AGN, which are still under debate: What is the geometric distribution and properties of the dust in AGN? Where does the reflection of X-rays occur in type 1 AGN? and what is the possible origin of the soft excess present in type 1 AGN?

First, we present the results obtained from the dust torus study in NGC 1068. For this, we use N-band and Q-band infrared spectra from Michelle/Gemini, which cover the mid-infrared range at the wavelengths of 7-13 μm and 18-23 μm , respectively. Our main result about the geometry of the dust torus in NGC 1068 is that it is actually two concentric tori with different sizes and properties: a denser and smaller internal torus with external radius of 1.8 pc, a second torus which reaches an extension of 28 pc and is less dense. Another of our main results is about the size of the dust grains. We find that substantially larger grains are required than those typically assumed in current models. Specifically, of a

usual size of $0.025 \mu m$, our model requires grains of $1 \mu m$ to explain the observed infrared spectrum for NGC 1068. These findings can be interpreted as a compelling evidence for a complex dusty torus for NGC 1068. We speculate that this can be understood as inner compact disk/torus plus an outer extended torus/wind, conforming either a flared disk or a dynamical fountain model for the dust.

Secondly, we present the results obtained from our X-ray study for the sample of 22 type 1 AGNs. The first objective of this work was to determine the physical structures where the X-ray reflection occurs (accretion disk, BLR or torus) since, while in type 2 AGN the reflection is dominated by the torus, in type 1 AGN a contribution is also expected from the accretion disk and/or the BLR. Our main result was that 67% of the objects in the sample require both reflection in the accretion disk and reflection in the torus, to explain their observed spectra. Only one object is fitted through reflection in the torus and only two objects are fitted considering only reflection in the accretion disk. Finally, we find that three objects in the sample fit equally well both the reflection model in the torus and the reflection model in the accretion disk.

We have extended this work towards low energies to study the origin of the soft emission. Our main results show that for none of the objects in our sample the comptonization scenario can explain the soft excess. On the contrary, this can be explained for all objects by the contribution of a black-body. In addition to this black-body component, most objects require another black-body, plus the contribution at low energies from the accretion disk and/or the effect due to the presence of partially ionized material partially covered over our line of sight.

As a result of this thesis work we have helped advance the answer to three of the questions that are still open in the area of AGN: the characterization of the dusty torus, the reflection media of the primary X-ray emission, and the possible origin of the soft excess. The general results obtained in this thesis, both for the infrared emission and for the X-ray spectrum, demonstrate that the components studied are more complex than is commonly assumed, and that this should be considered in future work and in the development of models that attempt to explain the nature of AGN.

This thesis is a compilation of two main articles where I am the main author, both

already published in “The Astrophysical Journal”, and a chapter on the study of soft excess, which we intend to publish soon.



*A mi esposa,
que me inspira y motiva todos los días...*

*En el fondo, los científicos somos gente con suerte:
podemos jugar a lo que queramos durante toda la vida.*

Lee Smolin (1955 -?) Físico teórico y cosmólogo.

Contents

Resumen	i
Abstract	iv
1 Introduction	1
§1.1 Active galactic nuclei	1
§1.1.1 AGN components	1
§1.1.2 AGN classification	4
§1.1.3 Unified model of the AGN	6
§1.2 AGN at X-ray wavelengths	7
§1.3 AGN at infrared wavelengths	9
§1.4 Motivation of this work	9
§1.4.1 X-ray reflection and soft excess of type-1 AGN	9
§1.4.2 Complexity of the AGN dusty torus: the case of NGC 1068	12
§1.5 Aims of this work	13
2 Dust emission in NGC 1068	15
3 X-ray reflection at hard energies	37
4 The soft excess in AGN	59
§4.1 Introduction	59
§4.2 Soft band spectral fitting procedure	61
§4.2.1 Initial setup for the spectral fitting	61
§4.2.2 Initial extrapolation	62
§4.2.3 Cold partial covering	63

§4.2.4	The soft excess as Comptonized material	64
§4.2.5	The soft excess as a blackbody	65
§4.2.6	Soft excess as host-galaxy circumnuclear contributors	65
§4.2.7	Soft excess as partially ionized partial covering	66
§4.2.8	Simultaneous fit of the soft and hard spectra	68
§4.3	Results	69
§4.3.1	Initial extrapolation	69
§4.3.2	Cold partial covering scenario	70
§4.3.3	The soft excess as Comptonized material	72
§4.3.4	The soft excess as Black-body	73
§4.3.5	Soft excess as host-galaxy circumnuclear contributors	73
§4.3.6	Soft excess as partially ionized partial covering	74
§4.3.7	Simultaneous fit of the soft and hard spectra	81
§4.4	Summary and conclusions	81
5	Summary and discussion	89
6	Future work	93
7	Appendix	95
§7.1	Testing a complex model to fit the soft excess.	95

1.1 Active galactic nuclei

Black holes (BHs) are regions in space whose gravitational field is so strong that nothing can escape its pull, not even light. There are two primary types of black holes classified according to their mass: stellar black holes and supermassive black holes (SMBHs). The stellar black holes are formed after the gravitational collapse of massive stars when they exhaust their nuclear fuel. These black holes present characteristic masses of around 3-30 M_{\odot} . The supermassive black holes are the largest known black holes, with masses of the order of $10^6 - 10^9 M_{\odot}$. It is known that these SMBHs are located in the center of the galaxies, although their origin remains unknown (Kormendy, & Ho, 2013).

When the SMBH at the center of galaxies is in a state of accretion it is known as active galactic nucleus (AGN). The accretion process in AGN release energies of the order of $10^{38} - 10^{48} \text{erg s}^{-1}$, emitting in the entire electromagnetic spectrum.

1.1.1 AGN components

AGN are composed by different physical structures around the SMBH. Currently, the main components of AGN are as follows:

- The **SMBH**: Is the central region where the gravitational force prevents any particles

or even light from escaping from it. According to the “No hair theorem” (Heusler, 1996), a black hole can be characterized by three parameters: its mass, its charge, and its angular momentum (called spin of the BH). In order to describe the basic properties of a SMBH of mass M_{BH} it is convenient use the gravitational radius r_g , which is defined as:

$$r_g = \frac{GM}{c^2} \simeq 1.5 \times 10^{23} \frac{M_{\text{BH}}}{10^8} \text{cm} \quad (1.1)$$

where G is the gravitational constant, M is the mass of the object, and c is the speed of light. The spin (a) of the BH can be defined in terms of its angular momentum as:

$$a = \frac{cJ}{GM_{\text{BH}}^2} \quad (1.2)$$

where c is the speed of light, J is the angular momentum defined as $J \simeq M_{\text{BH}} r_g c$, and G is the gravitational constant. The spin parameter can take values between -1 and 1, where the plus and minus signs refer to the direction of the rotation.

- The **accretion disk**: Is the infalling rotation-dominated accretion flow. Accretion disks are classified according to their shape into thin, slim, and thick disks. Also, the accretion disks can be optically thin or thick, depending on the column density and the level of ionization of the gas.

Two physical parameters governing the properties of the accretion disks: the accretion rate and the size. These parameters determine the geometry of the disk, the temperature of the gas, the luminosity and the emitted spectrum.

The size of the accretion disk is defined by its inner and outer radii. The inner radius is where the assumption of bound Keplerian motion breaks down, commonly named inner stable circular orbit (ISCO). The outer radius has a typical size of $\sim 10^{-3}$ pc (Guo et al., 2022).

The accretion state of the system can be quantified using two fundamental quantities: the Eddington luminosity (L_{edd}) and the Eddington accretion rate (\dot{m}_{edd}). The Eddington luminosity is defined as the maximum luminosity that an accreting body can have when

it is in hydrostatic equilibrium. This quantity is defined as:

$$L_{Edd} = \frac{4\pi GcM_{BH}m_p}{\sigma_T} \simeq 1.5 \times 10^{38} \left(\frac{M_{BH}}{M_\odot}\right) \text{erg s}^{-1} \quad (1.3)$$

where, σ_T is the Thompson cross-section, m_p is the proton mass, G is the gravitational constant, and c is the speed of light. On the other hand, the Eddington accretion rate is the accretion rate required to produce a luminosity of L_{edd} , which is defined as:

$$\dot{m}_{Edd} = \frac{L_{Edd}}{\epsilon c^2} \approx \frac{1}{\epsilon} 2 \times 10^{-9} M_\odot \text{yr}^{-1} \quad (1.4)$$

where ϵ is the efficiency defined as $\epsilon = \frac{L}{M_{BH}c^2}$.

- The **Corona**: Is defined as a plasma of relativistic electrons, where UV and optical photons from the accretion disk are Compton upscattered in the X-ray band (Haardt & Maraschi, 1993). The exactly size, shape, and location of the corona in the AGN remains unknown. (Fabian et al., 2009; Alston et al., 2020)

- The **Broad Line Region (BLR)**: Is a dust-free region conformed by large-column-density ($\sim 10^{23} \text{cm}^{-2}$), high-density ($\sim 10^{10} \text{cm}^{-3}$) clouds of ionized gas with high rotational velocities ($\sim 10^3 - 10^4 \text{ km/s}$), localized at about 0.1 - 1 pc from the SMBH.

- The **Torus**: Is an axisymmetric structure of dust which assumes the shape of a donut, with a small central opening and a much larger outer dimension. The typical inner and outer radius of the torus is assumed to be 0.1 and 10 pc, respectively.

- The **Narrow Line Region (NLR)**: Is a region of smaller column density ($\sim 10^{20-21} \text{cm}^{-2}$), lower density ($\sim 10^4 \text{cm}^{-3}$), and lower velocity ($\sim 100 - 500 \text{ km/s}$) ionized gas, compared to that in the BLR, localized outside of the torus at 100 -1000 pc from the SMBH.

- The **relativistic jet**: Is plasma ejected from the innermost parts of the AGN at relativistic velocities in perpendicular direction of the accretion disk. The relativistic jet can reach scales from tens to million pc.

We show in Figure 1.1 a sketch of the above mentioned components of the AGN.

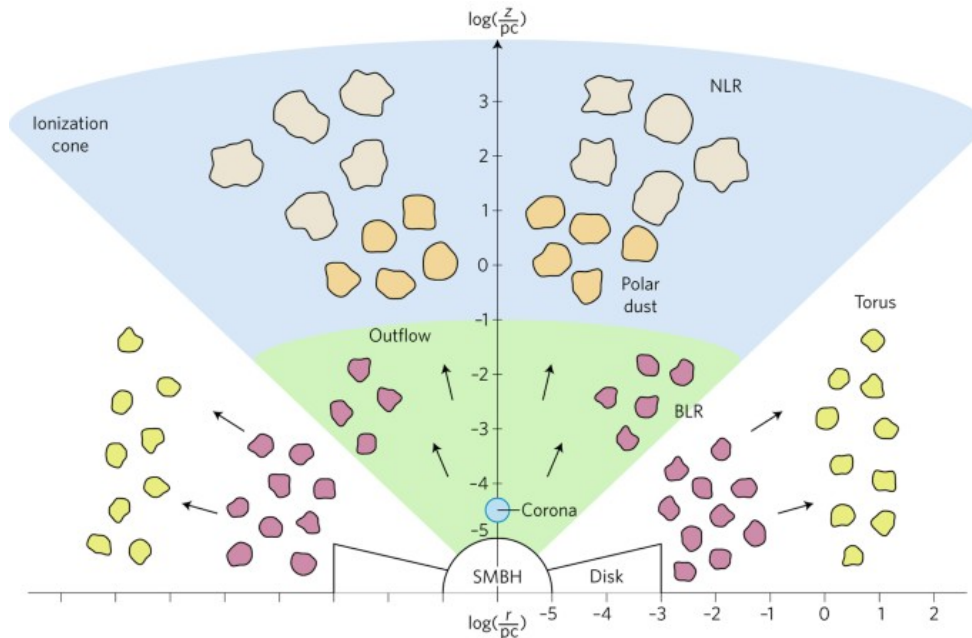


Figure 1.1: Scheme of a AGN and their physical components. Figure from Ramos Almeida & Ricci (2017)

1.1.2 AGN classification

There are a variety of subgroups of AGNs, which are classified based on their observed characteristics at different wavelengths. The most general classification includes five main classes of AGNs: Seyfert galaxies, quasars, radio galaxies, blazars, and LINERs.

- **Seyfert galaxies.** This type of AGN have bolometric luminosities of order of $10^{42} - 10^{45}$ erg/s. The Seyfert galaxies can be classified into two types according to the width and equivalent width of their permitted and forbidden emission lines: i) Type-1 Seyfert galaxies (Sy1), which show broad and narrow emission lines (H α , HeI, HeII, [OIII], and [NII]), and ii) Type-2 Seyfert galaxies (Sy2), which only show narrow emission lines ([OI], [SII], and [FeVII]). Figure 1.2 shows the typical optical spectrum of the type-1 and type-2 AGN. There are two subcategories of Sy1 galaxies: Narrow-line Seyfert 1 (NLSy1) and broad-line Seyfert 1 (BLSy1). NLSy1 show narrower broad Balmer line widths and stronger optical FeII emissions compared to the BLSy1 galaxies.

- **Quasars.** These AGN have high bolometric luminosities, of order of $10^{45} - 10^{48}$ erg/s. Their optical spectrum is similar to those of the Sy1, with prominent broad lines

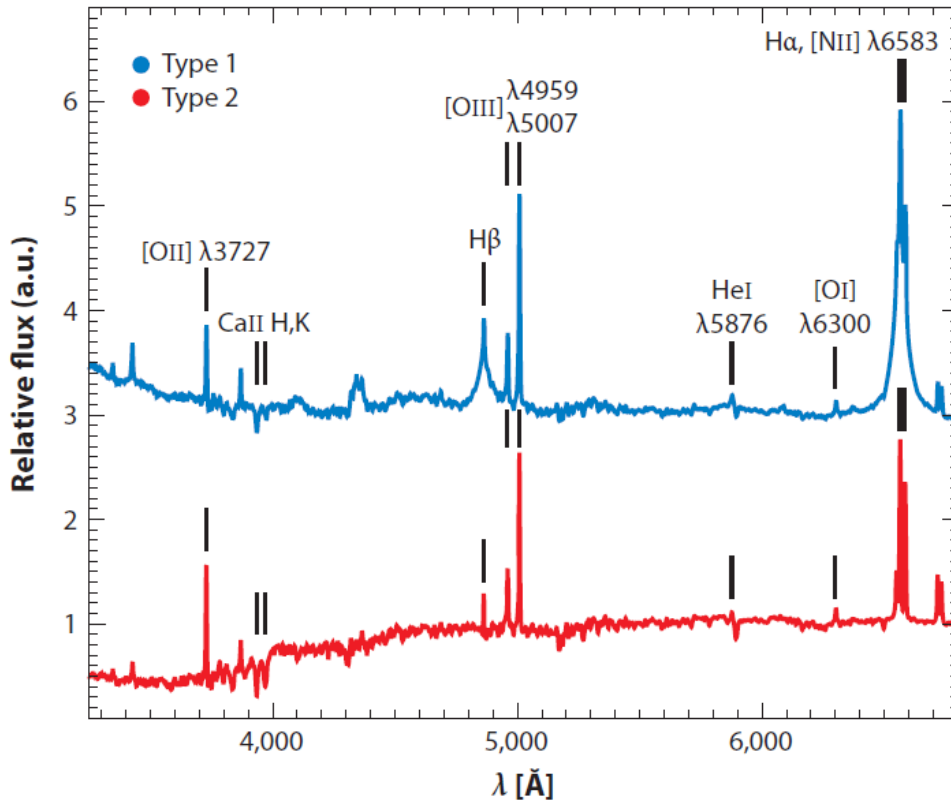


Figure 1.2: Optical spectrum of type-1 (blue) and type-2 (red) AGN. Figure from Hickox & Alexander (2018)

and weaker narrow lines. These objects are located at high redshift ($0.1 < z < 7.5$).

- **Radio galaxies.** These type of AGN are strong radio sources. Radio galaxies can be sub-divided into FRI and FRII, according to the ratio between nuclear and extended flux at radio frequencies (Fanaroff & Riley, 1974). The FRI are those whose emission lines come from the unresolved nuclear source, and they are located at low redshift. FRII are mostly extended, showing regions of radio emission at scales much larger than the host galaxy, called lobes. These objects are located at higher redshifts.

- **Blazars.** Are distinguished by the presence of parsec-scale relativistic radio jets pointing directly towards the line of sight to the observer. Their SED extends into the gamma-ray band due to particle acceleration processes. There are two subclasses of Blazars: the BL Lac objects and the optically violent variables (OVVs). BL Lac objects do not show emission lines, or they are extremely weak. OVVs have strong broad emission

lines.

- **LLAGN**. They are the dominant population of AGN in the local Universe (Ho et al., 1997). Their name is the acronym of Low-luminosity AGNs. They are less luminous than Seyferts or Quasars ($B=15.5$ mag). Their optical spectrum is dominated by strong emission lines of low ionization.

1.1.3 Unified model of the AGN

Due to the existence of the different types of AGN, some models have been proposed to explain their diverse observational properties. Currently, the most accepted model is the so called "unified model" proposed by Antonucci (1993) and Urry & Padovani (1995). The unified model of AGN suggests that the apparent differences between various AGN classes arise from the relative orientation of the torus to our line of sight.

According to the unified model, the different types of AGN can be explained as follows. The key to distinguish between the Sy1 and Sy2 galaxies is the existence of a dust structure surrounding the central engine, obscuring the inner parts of the AGN on the line of sight (LOS). Typically this structure has been called the dusty torus, due to its geometric shape, however different distributions have been proposed for the dust such as those proposed by Fritz et al. (2006); Nenkova et al. (2008b); Hönig & Kishimoto (2017). When the torus intercepts the LOS, the BLR is blocked up, hence, the optical spectrum only shows narrow lines from the NLR, ie. hosting a Sy2 nucleus. On the other hand, when the LOS do not intercept the torus, the optical spectrum shows narrow lines from the NLR and also broad lines of the BLR, ie. hosting a Sy1 nucleus. The main difference between the QSOs and Sy1 galaxies is their luminosity, where QSOs are high-luminosity versions of Sy1 galaxies. In both cases the BLR is not obscured by the torus, and their optical spectrum shows broad and narrow lines. Finally, the key between the radio loud and radio quiet galaxies is the radio power of the relativistic jet. According with Kellermann et al. (1994), the radio loudness parameter (R), defined as the ratio between the monochromatic luminosity at 5 GHz and the optical B band at 4400 Å, discriminates between both kinds of radio galaxies, where $R_{RL} > 10$ and $R_{RQ} < 10$. We show in Figure 1.3 a LOS scheme of the unified model.

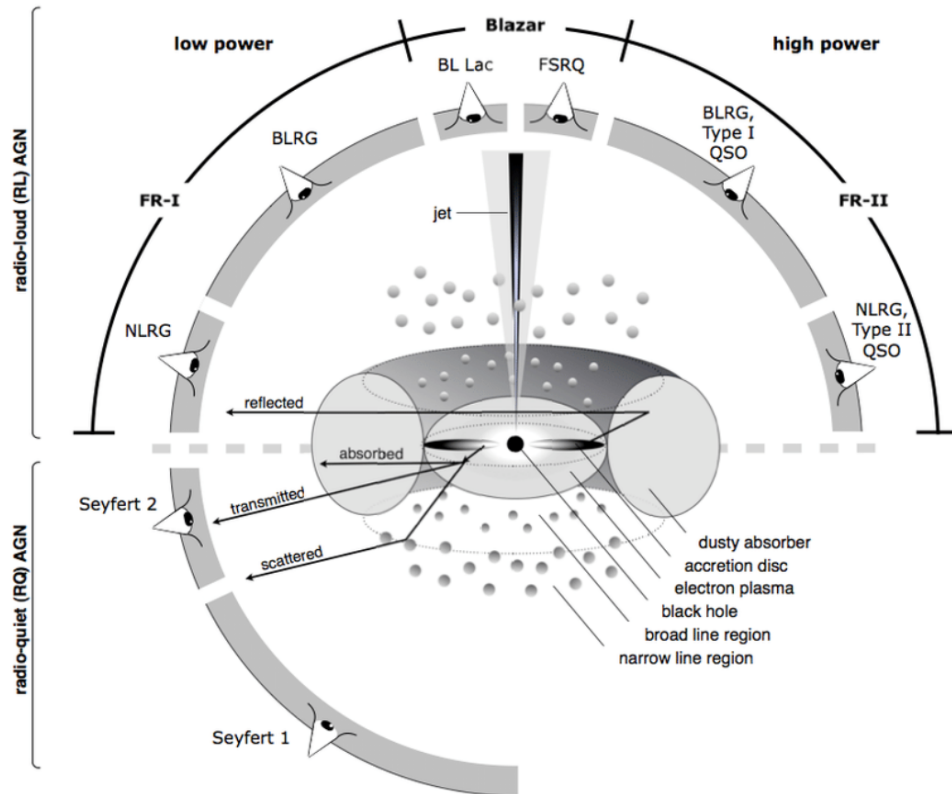


Figure 1.3: Scheme of the unified model proposed by Antonucci (1993) and Urry & Padovani (1995). Figure from Beckmann & Shrader (2012).

1.2 AGN at X-ray wavelengths

The X-ray spectrum of AGN covers the energy range from ~ 0.2 up to 100 keV, and it is composed by the primary emission, reflection features, and the soft excess. The primary emission is produced in the X-ray corona, and it is typically modelled with a power-law with an exponential cut-off of order of several hundred keV, as a function of the photon index, Γ of ~ 1.9 (Pounds et al., 1990; Zdziarski et al., 1995). The reflection features appear when the X-ray photons are reflected by the surrounding medium, such the accretion disc, the BLR, and/or the torus (Matsuoka et al., 1990). Reflection features are: a hump-like continuum at ~ 30 keV, product of the electron down scattering of high-energy photons and photoelectric absorption of low-energy photons, namely Compton hump; and several fluorescent emission lines, where the most notable is the $\text{FeK}\alpha$ emission line at 6.4 keV (George & Fabian, 1991). We show in Figure 1.4 a typical X-ray spectrum of type-1 AGN.

The reflection features depend on the dynamical, geometrical, and chemical properties of the medium where the X-ray photons are reflected. Currently, it is well accepted that the Compton hump is produced by the X-ray reflection on the inner parts of the torus as well as the $\text{FeK}\alpha$ emission line is narrow Liu (2016), and it depends on both the torus covering factor and column density (Ghisellini et al., 1994). When the $\text{FeK}\alpha$ line originates from neutral material, it is observed with a narrow profile. However, it can be broad and blurred by relativistic effects, when it is emitted close to the SMBH (Laor, 1991). The study of the reflection features in the AGN is one of the aims of this work.

The X-ray spectrum of the AGN below ~ 2 keV shows an excess of X-ray emission compared to the 2-10 keV continuum extrapolation, commonly named as soft excess. Currently, the origin of this feature remains a matter of debate, however, several scenarios have been proposed to explain it. Among them, there are three mainly scenarios: warm Comptonization, relativistically blurred reflection, and relativistically smeared absorption. A detailed description of these scenarios is given in Section 1.4.1. The study of the soft excess in the AGN is one of the objectives of this work. We dedicate the Chapter 4 of this thesis to investigate this phenomenon.

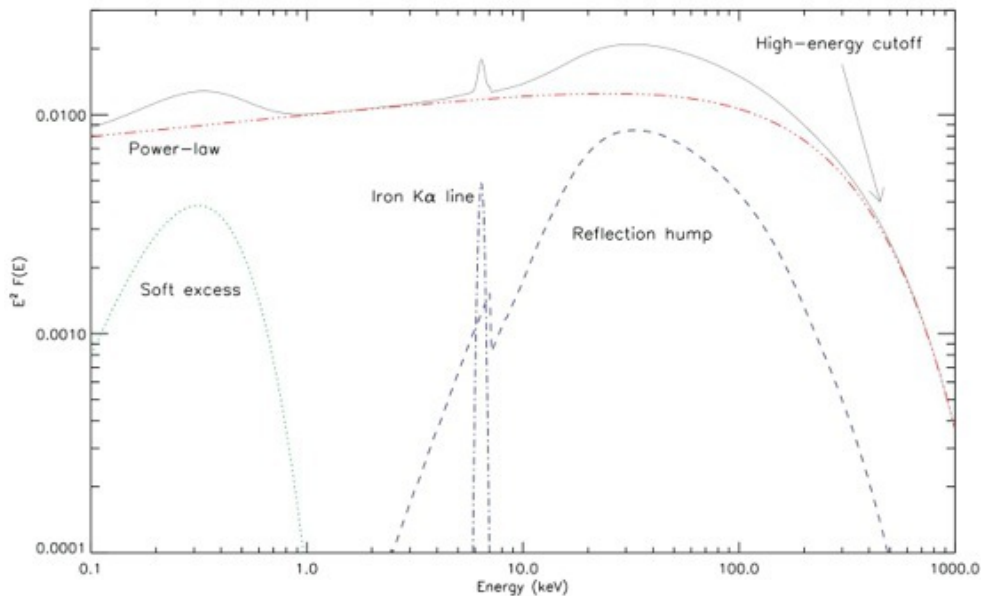


Figure 1.4: Typical X-ray spectrum and main components of type-1 AGN. Figure from Ricci (2011)

1.3 AGN at infrared wavelengths

The infrared emission in the AGN is due to the presence of dust, mainly from the torus surrounding the SMBH. Dust in the torus scatters and absorbs the UV and optical photons from the accretion disk, and re-emit them at the infrared band. The minimum distance from the central engine at which is located the dust in the AGN is determined by the sublimation temperature of the dust grains (Barvainis, 1987), typically around of 1500 K for silicates.

The infrared spectrum of the AGN goes from ~ 1 micron up to few 10s of micron, covering the near-infrared (NIR), mid-infrared (MIR) and far-infrared (FIR) bands. The FIR band covers the wavelengths over $25 \mu\text{m}$. The MIR band falls within the range between $5\text{-}25 \mu\text{m}$. NIR band cover the wavelength range of approximately 1 to $5 \mu\text{m}$. Each of these band give us information about the dust at different temperatures and locations.

The MIR emission is primarily associated with the thermal radiation originating from the dusty torus, however, this emission at MIR wavelengths also has contribution of the dust in the interstellar medium and the star formation in the host galaxy. There are two mainly features in the MIR spectrum of the AGN: i) several emission lines associated with the polycyclic aromatic hydrocarbon (PAH) molecules, and ii) the so called silicate features at 10 and 18 microns, which are observed as absorption/emission features. We show in Figure 1.5 the infrared spectrum of a typical type-II AGN.

1.4 Motivation of this work

1.4.1 X-ray reflection and soft excess of type-1 AGN

The X-ray emission in AGN arises from the hot corona located close to the SMBH, which consists of a population of high-energy electrons. The UV and optical photons from the accretion disk reach the corona and they are Compton upscattered and re-emitted in the X-ray energies (Haardt & Maraschi, 1993). This emission from the corona is named primary emission or intrinsic emission. X-ray photons are isotropically emitted by the corona, and they can reach the surrounding medium, such as the accretion disk, the BLR, and/or the

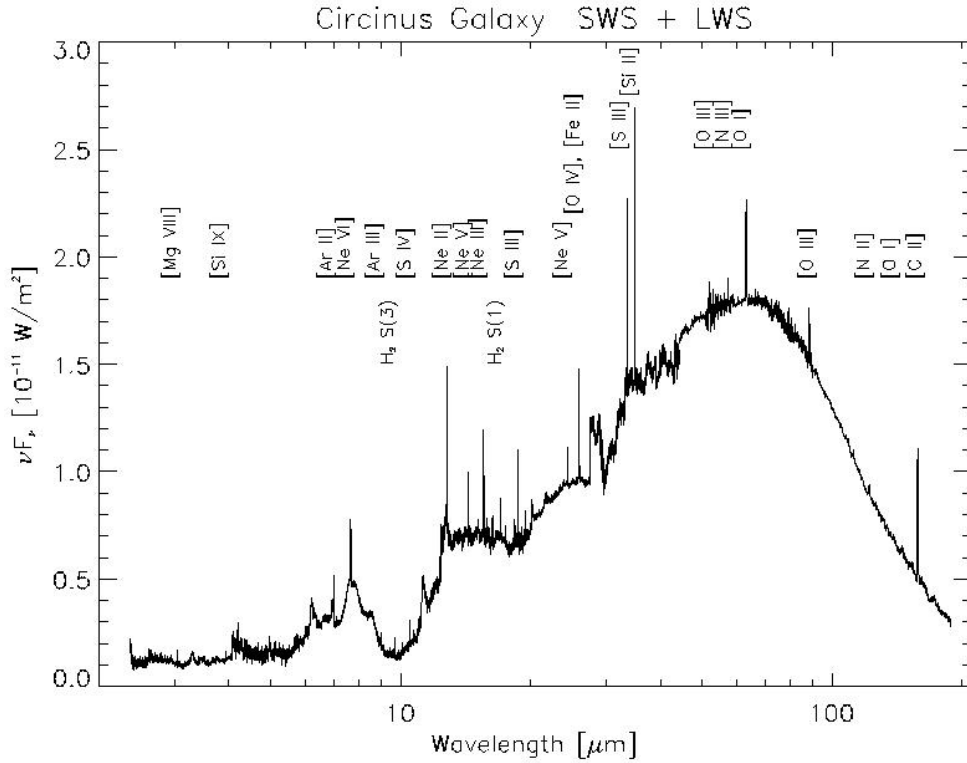


Figure 1.5: Infrared spectrum of typical AGN. Figure from Moorwood (1997)

torus (Matsuoka et al., 1990), where they are reprocessed and reflected, producing the reflected emission.

Different origins have been proposed to explain the observed reflection features in the hard X-ray spectrum of type-1 AGN, among which is relativistic reflection, and distant reflectors (Nardini et al., 2011; Patrick et al., 2011; Mehdipour et al., 2015). In the same way, there are different models, which are used to fit the X-ray spectrum of the AGN. For instance, PEXRAV (Magdziarz & Zdziarski, 1995) assumes optically thick cold material distributed in a slab, RELXILL (Dauser et al., 2010; García et al., 2014) models irradiation of accretion by a broken power law emissivity, REFLIONX (Ross et al., 1999; Ross & Fabian, 2005) assumes an optically-thick atmosphere, and it adds fluorescence lines.

Since the reflection features in the X-ray spectrum of the AGN are present in a wide range, the best way to study the nature of the reflection component is by using high-energy and -quality observations. The Nuclear Spectroscopic Telescope Array (*NuSTAR* Harrison et al., 2013) has an unprecedented sensitivity to hard X-ray photons, while, *XMM-Newton*

(Jansen et al., 2001) provides an excellent resolution below 10 keV and in particular around the FeK α emission line. Different authors have exploited the advantages offered by these two telescopes conducting studies with simultaneous observations to study the hard X-ray spectrum of various AGN (e.g. Porquet et al., 2018; Liu et al., 2020; Diaz et al., 2020; Traina et al., 2021; Marchesi et al., 2022). The nature of the Compton reflector is well established for type-2 AGN, mostly dominated by reflection in the distant and neutral torus (Brightman & Nandra, 2011; Ricci et al., 2015; Marchesi et al., 2018). While type-1 AGN are the ideal laboratories to explore the contribution of the disk and BLR to this reflection component (Falocco et al., 2014; Panagiotou & Walter, 2019).

The soft emission observed below ~ 1 -2 keV has a different origin for type-1 or type-2 AGN. In type-2 AGN it is attributed to star formation of the host galaxy or to the NLR (Bianchi et al., 2010; Gómez-Guijarro et al., 2017). The soft emission in type-1 AGN, commonly called soft excess, remains a matter of debate (Done, 2007; García et al., 2019; Gliozzi & Williams, 2020; Nandi et al., 2021). In order to explain the nature of the soft excess in type-1 AGN, various scenarios have been proposed. Since the emission from the accretion disk can be approximated as a combination of black-body spectra (Shakura & Sunyaev, 1973), the first attempts try to explain the soft excess as the hard tail of the black-body emission from the accretion disk, and was modelled using a black-body, with effective temperature of ~ 0.1 - 0.2 keV. This characteristic temperature of the soft excess can be explained with atomic processes through partially ionized material with strong velocity gradients (Done, 2007; Done & Nayakshin, 2007). From this, there are two possible physical scenarios: 1) relativistically-blurred reflection (Crummy et al., 2006; García et al., 2019; Waddell & Gallo, 2020), which explain that the soft excess is originated in the accretion disk, and 2) relativistically smeared absorption (Gierliński & Done, 2004; Middleton et al., 2007; Done & Nayakshin, 2007), in which the soft excess is actually the intrinsic emission at low energies absorbed by smeared, partially ionized material. An alternative scenario proposes that the soft excess can be explained by a warm Comptonized component (Magdziarz et al., 1998; Done et al., 2012; Gliozzi & Williams, 2020), where the UV photons from the accretion disk are Comptonized by a corona above the disk, which is optically thicker and cooler than the X-ray corona.

1.4.2 Complexity of the AGN dusty torus: the case of NGC 1068

According to the unified model of the AGN (Antonucci, 1993; Urry & Padovani, 1995), the dust structure surrounding the central engine is the angular-disk to explain the different types of AGN observed. However, the physical details of this structure, such as the dust characteristics (both in terms of chemical composition and of grain size distribution) and its geometrical distribution, are still quite poorly understood (see Ramos Almeida & Ricci, 2017, for a review).

The fitting of the spectral energy distribution (SED) to dust models using different distributions and/or chemical compositions is a way to study the torus in AGN. A variety of different models have been developed to explain the distribution of dust in these objects. The first models assume smooth dust distributions using radial and vertical density profiles (Pier, & Krolik, 1992; Granato, & Danese, 1994; Efstathiou, & Rowan-Robinson, 1995; van Bemmelen, & Dullemond, 2003; Schartmann et al., 2005). Other authors have developed radiative transfer models to reproduce geometries where the dust is distributed in clouds (Nenkova et al., 2008a,b; Hönig & Kishimoto, 2010). Models considering smooth plus clumpy distributions has also been proposed (Stalevski et al., 2012; Siebenmorgen et al., 2015). A more complex model includes a compact, geometrically thin disk in the equatorial region of the AGN, and an extended, elongated polar structure (Hönig & Kishimoto, 2017). Even with such detailed modelling, there are objects needing further complexity. Our work is focused in one of these particular cases: NGC 1068.

Early works in the infrared domain as those presented by Chelli et al. (1987) and Cameron et al. (1993) pointed out that complex structures must be present at small scales in NGC 1068 since the mid-infrared continuum is extended within 1.5 arcsec. Bock et al. (2000), Wittkowski et al. (2004) and Jaffe et al. (2004) presented spatially-resolved images at near- and mid-infrared wavelengths using interferometric techniques. They favor a multi-component model for the dust distribution in NGC 1068, where part of the flux originates from a hot and small ($\lesssim 1$ pc) component with also a large warm component (2.1×3.4 pc). Mason et al. (2006) found that the MIR emission originates in two distinct components. A compact bright source with radius < 15 pc, which they identified with the

obscuring torus, and a diffuse component with dust in the ionization cones. More recently, Pasetto et al. (2019) fit the SED of NGC 1068 using a smooth torus model, finding that the torus has a complex structure, since they are not able to fit both spectral bands with the same values for the parameters of the torus model.

1.5 Aims of this work

The overarching goal of this thesis work is to address some of the questions that currently remain open in the field of AGN: i) the geometry, chemical composition and distribution of the dusty torus; ii) the physical components in which X-ray reflection occurs; and iii) the origin of the soft excess. By achieving these objectives we intend to give new clues about the physics involved in the three phenomena studied, to achieve a better understanding of the general panorama in AGNs. With this in mind, this thesis work is focused on three main objectives:

- **The study of the dusty torus in the type-2 AGN NGC 1068.** (Chapter 2).

We aim to investigate the physical characteristics of the torus and the physical and chemical characteristics of the dust. For this purpose we perform the analysis into two steps: (i) we used XSPEC spectral fitting package to test already available models and (ii) we used the 3D Monte Carlo radiative spectral energy distribution transfer code SKIRT to build grids of synthetic SEDs, based on the result obtained from the first step.

- **The study of the reflection medium of the primary X-ray radiation in a sample of type-1 AGN.** (Chapter 3).

We aim to investigate what is the physical component where the X-ray reflection occurs. For this purpose we select and test a set of available reflection models on a sample of type-1 AGN with simultaneous observations of *XMM-Newton* and *NuSTAR*, using the XSPEC spectral fitting package.

- **The study of the soft excess in a sample of type-1 AGN.** (Chapter 4).

We aim to investigate what is the possible origin of the observed soft excess in type-1 AGN. For this purpose we select and test a set of available physical and phenomenological models on the same sample of type-1 AGN, performing a spectral fitting using the XSPEC spectral fitting package.

CHAPTER 2

DUST EMISSION IN NGC 1068

The physical and chemical properties of the dusty torus in the AGN are still quite poorly understood. Different authors have proposed different models trying to explain the distribution of the dust and its properties. The most simple models consider a smooth distribution of the dust in a toroidal geometry (Pier, & Krolik, 1992; Granato, & Danese, 1994; Efstathiou, & Rowan-Robinson, 1995; van Bemmell, & Dullemond, 2003; Schartmann et al., 2005). Other models reproduce geometries where the dust is distributed in clouds (Nenkova et al., 2008a,b; Hönic & Kishimoto, 2010). A kind of model use a mix of smooth plus clumpy distributions of the dust (Stalevski et al., 2012; Siebenmorgen et al., 2015). More recently, a more complex model includes a compact, geometrically thin disk in the equatorial region of the AGN, and an extended, elongated polar structure Hönic & Kishimoto (2017).

In this chapter we study the infrared emission in the type-2 AGN NGC 1068. For this, we use ground-based N- and Q-band *Michelle*/*Gemini* spectra, which covers the MIR wavelengths of 7-23 μm (7-13 μm for N-band and 18-23 μm for Q-band). Also, we developed new radiative transfer models. Note that, adding FIR data to our study would help to better determine some parameters of the torus, eg. the outer radius (since the dust is colder at a larger radius). Similarly, adding NIR data would help better determine the inner radius of the torus. However, at NIR wavelengths there is a contribution from star

formation, so it is more difficult to separate the torus emission. In future work this could be explored by adding these bands.

We perform our analysis in two steps: first, we use four different available dust models: the Smooth torus model by Fritz et al. (2006), the Clumpy torus model by Nenkova et al. (2008b), the Two phase torus model by Stalevski et al. (2016), and the Clumpy disk and outflow model by Hönic & Kishimoto (2017). We perform our spectral fitting using the XSPEC ¹ fitting package, which is a command-driven, interactive, spectral-fitting program within the HEASOFT ² software. We find that the Smooth torus model by Fritz et al. (2006) offers the best results. We show in Figure 2.1 an illustration of the four dust models tested.

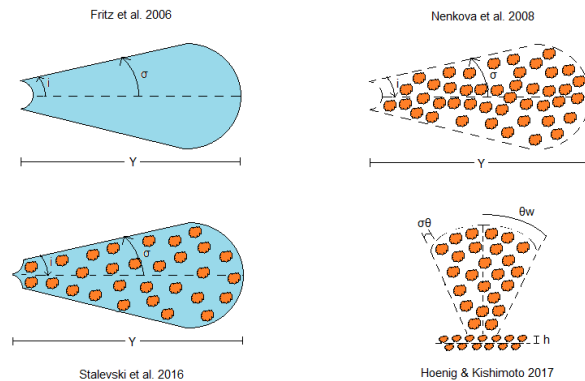


Figure 2.1: Illustration of the dust models tested: the smooth torus model by Fritz et al. (2006) (*top left*), the clumpy torus model by Nenkova et al. (2008b) (*top right*), the two phase torus model by Stalevski et al. (2016) (*bottom left*), and the clumpy disk and outflow model by Hönic & Kishimoto (2017) (*bottom right*).

In the second step, we create grids of synthetic SEDs using the 3D Monte Carlo radiative transfers code (SKIRT BAES ET AL., 2003, 2011). For these grids we use the same geometry of the Smooth torus model by Fritz et al. (2006), and also we consider two concentric tori, which allow us to test a more complex geometry. For the emission of the core we use a template from the SED of NGC 1068.

Our main result shows that the MIR N- and Q- band spectra of NGC 1068 is well fitted

¹<http://heasarc.gsfc.nasa.gov/docs/xanadu/xspec/>

²<https://heasarc.gsfc.nasa.gov>

by considering two concentric tori with the following common parameters for both tori: 1) a fractional contribution for graphite and silicate grains of 49% and 51%, respectively; 2) graphite from (Li & Draine, 2001) and silicate from (Min et al., 2007); 3) size of graphite and silicate particles of 0.1-1 μm ; 4) inner radius of both tori of 0.2 pc; 5) viewing angle $i=71^\circ$; and 6) foreground extinction $A_V = 2$ mag. The parameters changing from both tori are: i) the exponent of the power-law describing the radial distribution $p_1=0.2$ and $p_2=1$, ii) the exponent of the polar distribution $q_1=3.2$, and $q_2=5.8$, iii) the half opening angle $\sigma_1=42^\circ$ and $\sigma_2=58^\circ$, iv) the outer radius $R_{\text{max},1}=1.8$ pc and $R_{\text{max},2}=28$ pc, and v) the equatorial optical depth to $\tau_{9.7\mu\text{m},1}=12$ and $\tau_{9.7\mu\text{m},2}=0.3$.

Author disclosure:

The realization of this work was carried out mainly by my authorship. My advisor, Dr. Omaira González Martín, contributed to the interpretation of the results and revised the wording of the article. The other co-authors contributed by suggesting modifications and corrections to the final version of the article. This work was accepted on December 15, 2021 and published on February 24, 2022 in The Astrophysical Journal.

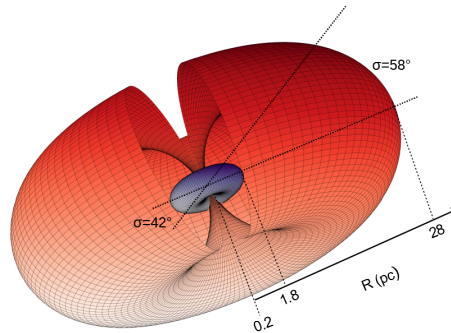


Figure 2.2: Sketch of the dusty distribution of NGC 1068 obtained through our best model: two concentric tori with inner radius of 0.2 pc and outer radius of 1.8 and 28 pc for the smallest (purple) and largest (red) torus respectively. The viewing angle of both tori is $i = 71^\circ$.



The Complex Infrared Dust Continuum Emission of NGC 1068: Ground-based N - and Q -band Spectroscopy and New Radiative Transfer Models

César Ivan Victoria-Ceballos¹ , Omaira González-Martín¹ , Jacopo Fritz¹ , Cristina Ramos Almeida^{2,3} , Enrique López-Rodríguez⁴ , Santiago García-Burillo⁵ , Almudena Alonso-Herrero⁶ , Mariela Martínez-Paredes⁷ , Donaji Esparza-Arredondo¹ , and Natalia Osorio-Clavijo¹

¹ Instituto de Radioastronomía y Astrofísica (IRYA-UNAM), 3-72 (Xangari), 8701, Morelia, México; c.victoria@iry.unam.mx

² Instituto de Astrofísica de Canarias, Calle Vía Láctea, s/n, E-38205 La Laguna, Tenerife, Spain

³ Departamento de Astrofísica, Universidad de La Laguna, E-38206 La Laguna, Tenerife, Spain

⁴ Kavli Institute for Particle Astrophysics & Cosmology (KIPAC), Stanford University, Stanford, CA 94305, USA

⁵ Observatorio Astronómico Nacional (OAN-IGN)-Observatorio de Madrid, Alfonso XII, 3, E-28014, Madrid, Spain

⁶ Centro de Astrobiología (CSIC-INTA), ESAC Campus, E-28692 Villanueva de la Cañada, Madrid, Spain

⁷ Korea Astronomy and Space Science Institute 776, Daedeokdae-ro, Yuseong-gu, Daejeon, (34055), Republic of Korea

Received 2021 October 7; revised 2021 December 3; accepted 2021 December 15; published 2022 February 24

Abstract

Thanks to ground-based infrared and submillimeter observations the study of the dusty torus of nearby active galactic nuclei has greatly advanced in the last years. With the aim of further investigating the nuclear mid-infrared emission of the archetypal Seyfert 2 galaxy NGC 1068, here we present a fitting to the N - and Q -band Michelle/Gemini spectra. We initially test several available spectral energy distribution (SED) libraries, including smooth, clumpy and two-phase torus models, and a clumpy disk+wind model. We find that the spectra of NGC 1068 cannot be reproduced with any of these models. Although, the smooth torus models describe the spectra of NGC 1068 if we allow variation of some model parameters among the two spectral bands. Motivated by this result, we produced new SEDs using the radiative transfer code SKIRT. We use two concentric tori that allow us to test a more complex geometry. We test different values for the inner and outer radii, half-opening angle, radial, and polar exponent of the power-law density profile, opacity, and viewing angle. Furthermore, we also test the dust grains' size and different optical and calorimetric properties of silicate grains. The best-fitting model consists of two concentric components with outer radii of 1.8 and 28 pc, respectively. We find that the size and the optical and calorimetric properties of graphite and silicate grains in the dust structure are key to reproducing the spectra of NGC 1068. A maximum grain size of $1 \mu\text{m}$ leads to a significant improvement in the fit. We conclude that the dust in NGC 1068 reaches different scales, where the highest contribution to the mid-infrared is given by a central and compact component. A less dense and extended component is present, which can be either part of the same torus (conforming a flared disk) or can represent the emission of a polar dust component, as already suggested from interferometric observations.

Unified Astronomy Thesaurus concepts: Active galactic nuclei (16); Dust continuum emission (412); Infrared astronomy (786); Seyfert galaxies (1447)

1. Introduction

According to the unified model of active galactic nuclei (AGN; Antonucci 1993; Urry & Padovani 1995), a dust structure surrounding the central engine and causing obscuration is the angular stone to explain the different types of AGN observed. This structure, commonly called the dusty torus, is located a few parsecs from the supermassive black hole (SMBH). However, the physical details of this structure, such as the dust characteristics (both in terms of chemical composition and grain size distribution) and its geometrical distribution, are still quite poorly understood (see Ramos Almeida & Ricci 2017, for a review).

One way to study the dusty torus in AGN is throughout the fitting of the spectral energy distribution (SED) to dust models using different distributions and/or chemical compositions. Initially, for the sake of simplicity, most authors have used smooth dust distributions using radial and vertical density profiles (Pier & Krolik 1992; Granato & Danese 1994; Efstathiou &

Rowan-Robinson 1995; van Bemmel & Dullemond 2003; Schartmann et al. 2005). Other authors have developed radiative transfer models to reproduce geometries where the dust is distributed in clouds (Nenkova et al. 2008a, 2008b; Hönic & Kishimoto 2010). This is the so-called clumpy distribution. A mix of smooth and clumpy distributions has also been proposed (Stalevski et al. 2012; Siebenmorgen et al. 2015). More recently, a more complex scenario has been proposed to explain the infrared nuclear emission of Seyfert galaxies. Hönic & Kishimoto (2017) produced a model that includes a compact, geometrically thin disk in the equatorial region of the AGN, and an extended, elongated polar structure (see also Stalevski et al. 2019). The interpretation of high spatial resolution spectra, achieved by means of SED fitting techniques exploiting theoretical emission models, is the key to an unbiased study of the dust properties in AGN, limiting the effect of the host galaxy emission (Ramos Almeida et al. 2009, 2011; Alonso-Herrero et al. 2011; González-Martín et al. 2019a).

NGC 1068 ($D = 10.58$ Mpc; we used the average distance independent of redshift reported in NED⁸) is considered to be the

Original content from this work may be used under the terms of the [Creative Commons Attribution 4.0 licence](https://creativecommons.org/licenses/by/4.0/). Any further distribution of this work must maintain attribution to the author(s) and the title of the work, journal citation and DOI.

⁸ The NASA/IPAC Extragalactic Database (NED) is operated by the Jet Propulsion Laboratory, California Institute of Technology, under contract with the National Aeronautics and Space Administration.

prototype Seyfert 2 galaxy (Bland-Hawthorn et al. 1997) showing broad lines using polarized light (Miller & Antonucci 1983; Antonucci & Miller 1985), where the central source is obscured by dust. Although NGC 1068 is probably one of the best explored AGN at all wavelengths, there is still controversy on the geometry of the obscurer (e.g., Gravity Collaboration et al. 2020, and references therein). This torus has been studied in a large number of works.

Works at submillimeter wavelengths are particularly relevant because they have observed the nuclear molecular gas and dust with unprecedented spatial resolution. García-Burillo et al. (2016) used the Atacama Large Millimeter Array (ALMA) to map the molecular and continuum emission from the circumnuclear disk of NGC 1068 and resolve its dusty torus with a size of ~ 4 pc. Imanishi et al. (2018) found sizes of 13×4 pc and 12×5 pc for the molecular torus as seen by HCN $J=3-2$ and HCO⁺ $J=3-2$, respectively. Lopez-Rodriguez et al. (2020) detected the polarization signature of the torus by means of magnetically aligned dust grain emission. They find that the torus is inhomogeneous and turbulent. Through the HCN ($J=3-2$) transition, Impellizzeri et al. (2019) identified two disk counter-rotating, an inner disk spanning $0.5 \lesssim r \lesssim 1.2$ pc, and an outer disk extending up to ~ 7 pc. Indeed, the inner disk seems to be linked to the kinematics of the maser spots, which are located in a rotating disk with inner radius of ~ 0.65 pc and outer radius of ~ 1.1 pc (Greenhill & Gwinn 1997), which traces the outer, colder part of the accretion disk. García-Burillo et al. (2019) also found that the molecular torus has a radial stratification extending over a range of 10–30 pc, since different tracers show different sizes: the HCO⁺(4–3), CO(2–1), and CO(3–2) with a full size of 11, 26, and 28 pc, respectively.

At mid-infrared (MIR) wavelengths several studies have also tried to infer the properties of the dust in NGC 1068. Early works already showed a complex and extended morphology at MIR (Cameron et al. 1993; Bock et al. 2000), which were later confirmed by interferometry (Wittkowski et al. 2004; Jaffe et al. 2004; López-Gonzaga et al. 2014) and spectroscopy (Mason et al. 2006; Raban et al. 2009). SED fitting including MIR emission has also been very useful. For instance, Lopez-Rodriguez et al. (2018) used Stratospheric Observatory for Infrared Astronomy (SOFIA), infrared and submillimeter observations in order to characterize the emission and distribution of the dust in NGC 1068, which was first studied by Alonso-Herrero et al. (2011). They found that a clumpy torus is able to reproduce the observed emission, although with some discrepancies mainly at short wavelengths. More recently Pasetto et al. (2019) fitted the SED of NGC 1068 to MIR spectra (N and Q bands) using a smooth torus model finding that the torus has a more complex structure, since they are not able to fit both spectral bands with the same values for the parameters of the torus model. Note that in these works only one or two torus models were used for the SED fitting.

The aim of this work is to reproduce the 7–23 μm MIR spectra of NGC 1068 (divided into N - and Q -band spectra at 7–13 and 18–23 μm , respectively). This kind of work can only be done for NGC 1068 because it is the only AGN with both N - and Q -band ground-based observations, and therefore, with enough spatial resolution to isolate the nuclear dust continuum emission from other dust contributors. Future James Web Space Telescope (JWST) observations will allow these types of studies for dozen of nearby AGN. Thus, this work also aims to

refine the SED fitting technique in preparation for oncoming JWST observations. For that purpose, we explore here available models and create new SEDs. In particular, we test four different torus models to reproduce the SED of NGC 1068: the smooth torus model by Fritz et al. (2006), the clumpy torus model by Nenkova et al. (2008b), the two-phase torus model by Stalevski et al. (2016), and the clumpy disk+wind model by Hönl & Kishimoto (2017). We confirm the complex dust distribution needed to reproduce the MIR spectra by producing new synthetic SEDs using the 3D Monte Carlo radiative transfer code SKIRT.⁹

The paper is organized as follows. Section 2 gives a brief summary of the available dusty models used in this paper. Section 3 describes the spectral fitting of the data to existing models. We explore the dust properties using the radiative transfer code SKIRT in Section 4 and a discussion of these results is in Section 5. Finally, in Section 6 we summarize our main results.

2. Torus Models

Here, we give a brief summary of the four AGN dust models tested in this paper. The parameters and a sketch of the dust distribution for each model are included in Table 1 and in Figure 9, respectively (see also González-Martín et al. (2019a), and references therein):

1. Smooth torus model by Fritz et al. (2006): They use a toroidal geometry, consisting of a flared disk that can be represented as two concentric spheres, delimiting, respectively, the inner and the outer torus radius, having the polar cones removed (see the top-left panel in Figure 9). For the composition of dust, they consider a typical silicate and graphite grain size with radius 0.025–0.25 and 0.005–0.25 μm , respectively, in almost equal percentages (52.9% silicate and 47.1% graphite).
2. Clumpy torus model by Nenkova et al. (2008b): They use a formalism that accounts for the concentration of dust in clouds, forming a torus-like structure (see the top-right panel in Figure 9). They assume spherical dust grains and a standard Galactic mix of 53% silicate and 47% graphite grains.
3. Two-phase torus model by Stalevski et al. (2016): They model the dust in a toroidal geometry with a two-phase medium, consisting of high-density clumps embedded in a smooth dusty component of low density (see the bottom-left panel in Figure 9). The dust chemical composition is set to a mixture of silicate and graphite grains. The fraction of total dust mass in clumps compared to the total dust mass is set to 0.97.
4. Clumpy disk and outflow model by Hönl & Kishimoto (2017): They model the dust in a clumpy disk-like geometry and a polar hollow cone (see the bottom-right panel in Figure 9). The dust chemical composition is set to only large graphites (0.1–1 μm) in the outflow. For the disk, the dust composition consists of graphites of 0.1–1 μm in the inner part, and a mixture of graphites and silicates of 0.025–0.25 μm in the rest of the disk.

⁹ <https://www.skirt.ugent.be>

Table 1
Summary of Used Dusty Models Described in Section 2

Model	Parameter	Dust Distribution	Dust Composition	Grain Size (μm)
Fritz et al. (2006)	Viewing angle toward the torus, i Half-opening angle of the torus, σ Index of the logarithmic azimuthal density distribution, Γ Index of the logarithmic radial density distribution, β Ratio between the external and internal radius, Y Edge-on optical depth at $9.7 \mu\text{m}$, $\tau_{9.7 \mu\text{m}}$	Smooth torus	Silicate and graphite	Silicate: 0.025–0.25 Graphite: 0.005–0.25
Nenkova et al. (2008b)	Viewing angle toward the torus, i Number of clouds in the equatorial plane, N Half-opening angle of the torus, σ Ratio between the external and internal radius, Y Slope of the radial density distribution of clouds, q Optical depth of the individual clouds, τ_{ν}	Clumpy torus	Standard ISM	Silicate: 0.025–0.25 Graphite: 0.005–0.25
Stalevski et al. (2016)	Viewing angle toward the torus, i Half-opening angle of the torus, σ Index of the logarithmic azimuthal density distribution, p Index of the logarithmic radial density distribution, q Ratio between the external and internal radius, Y Edge-on optical depth at $9.7 \mu\text{m}$, $\tau_{9.7 \mu\text{m}}$	Smooth and clumpy torus	Silicate and graphite	Silicate: 0.025–0.25 Graphite: 0.005–0.25
Hönig & Kishimoto (2017)	Viewing angle toward the torus, i Number of clouds in the equatorial plane, N_0 Index of the radial distribution of clouds, a Half-opening angle of the wind, θ Angular width of the walls of the cone, σ Power-law index for dust cloud distribution along the wind, a_w Wind-to-disk ratio, f_{wd} Optical depth of individual clouds, τ_{cl} (fixed)	Clumpy disk and outflow	Standard ISM ISM large	Standard: 0.025–0.25 Large: 0.1–1

Note. We show the parameters in Column 2, dusty distribution in Column 3, dust chemical composition in Column 4, and grain size in Column 5.

3. Data and Spectral Fitting

We use the N -band (7–13 μm) and Q -band (17–23 μm) spectra obtained with Michelle spectrometer located in the 8.1 m Gemini-North Telescope. This data set was processed for a previous analysis by Alonso-Herrero et al. (2011). They scale the spectra to the corresponding $0''.4$ photometric points in order to match the angular resolutions of the imaging and spectroscopic data. The spectra were extracted as point-like sources, following the center and the trace of the standard star. Point-spread function (PSF) and slit-loss corrections were applied to the spectrum. Further details are included in Alonso-Herrero et al. (2011). In Figure 1, we show the N - and Q -band spectra of NGC 1068. We include the photometric points reported by Tomono et al. (2001) using a circular aperture of $0''.4$ diameter (similar to the spatial resolution achieved by the ground-based spectra), and the photometric point used in Lopez-Rodriguez et al. (2018) estimated by using their PSF-scaling method. Note that all but two photometric points (at 9.69 and 10.38 μm) agree with the spectra. A similar figure is shown in Alonso-Herrero et al. (2011). This comparison ensures proper flux calibration of the N - and Q -band spectra.

We used the four dust models presented in Section 2 in order to fit the N - and Q -band spectra. Spectral fitting is performed using the XSPEC¹⁰ fitting package, which is a command-driven,

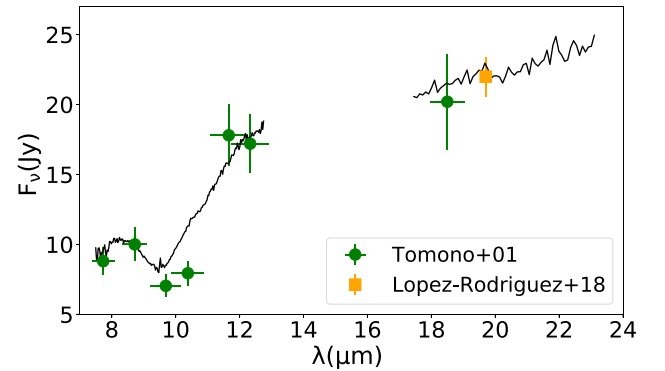


Figure 1. N - and Q -band spectra of NGC 1068 (black lines). The green circles and orange square symbols are the photometry of Tomono et al. (2001) and Lopez-Rodriguez et al. (2018), respectively.

interactive, spectral-fitting program within the HEASOFT¹¹ software. XSPEC (Arnaud 1996) already includes a large number of incorporated models but new models can be uploaded using the additive table, using the ATABLE task. We converted the spectra to XSPEC format in order to upload and fit them to the dust models within XSPEC. In order to assess

¹⁰ <http://heasarc.gsfc.nasa.gov/docs/xanadu/xspec/>

¹¹ <https://heasarc.gsfc.nasa.gov>

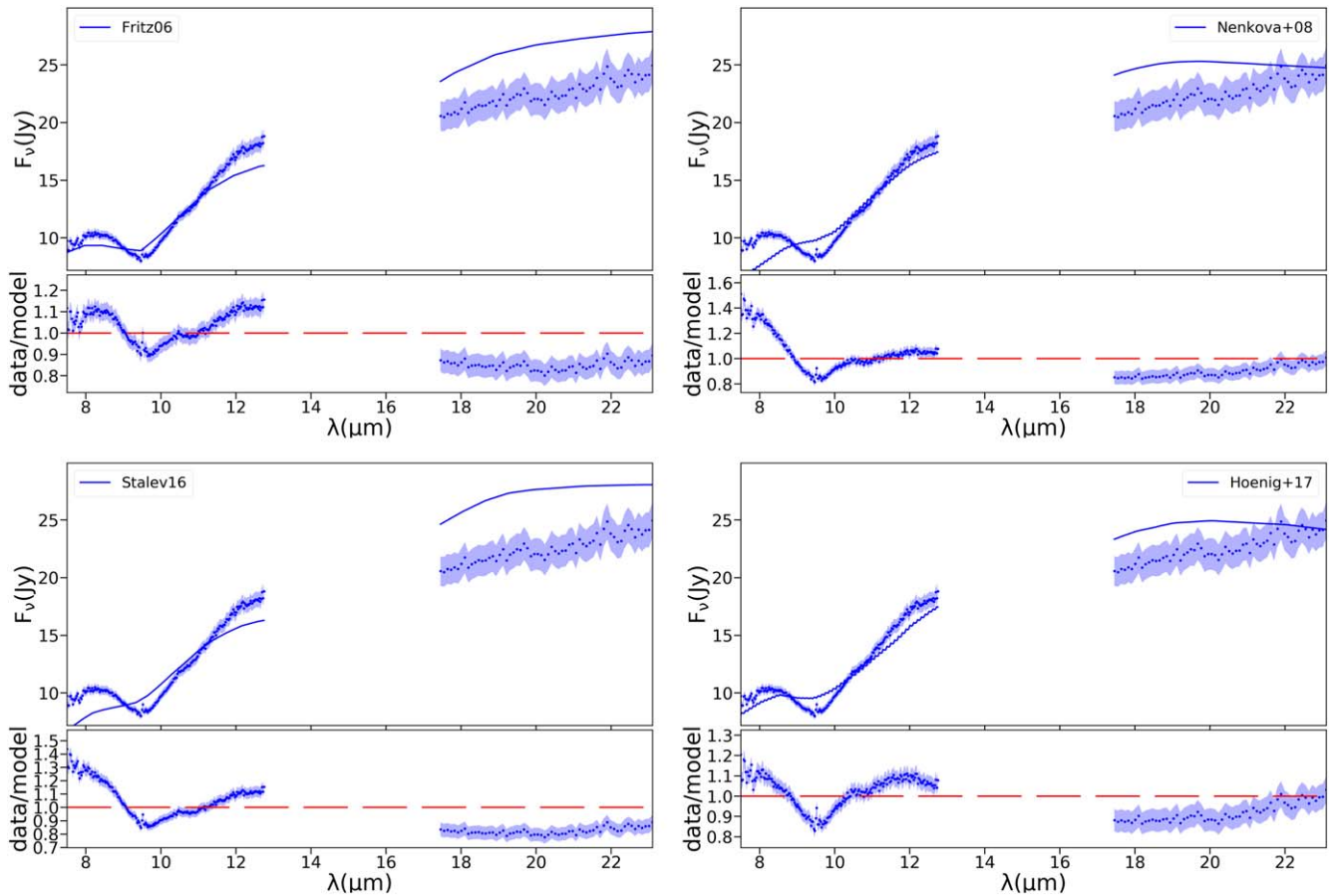


Figure 2. MIR spectral fit to NGC 1068 with the four models fitted: the smooth torus model by Fritz et al. (2006) (top left), the clumpy torus model by Nenkova et al. (2008b) (top right), the two-phase torus model by Stalevski et al. (2016) (bottom left), and the clumpy disk+wind model by Hönic & Kishimoto (2017) (bottom right). We show the best fit (blue solid line) to the data in the top panel and the ratio between model and data in the bottom panel. The dark blue dots show the data and the blue shaded area shows the error on the measurement.

the goodness of fit for each model, we used the reduced χ^2 statistics value.

We first test whether both N - and Q -spectra could be fitted with a single SED dust model (Section 3.1), then we tested more complex SEDs by allowing some parameters to vary among the two bands (Section 3.2.)

3.1. Single SED Dust Model

This initial attempt assumes that a single SED is able to simultaneously fit the N and Q bands. This is the same approximation done in previous works (e.g., Alonso-Herrero et al. 2011; García-Bernete et al. 2019). Figure 2 shows the best fit for the four dust models tested. All the models provide unacceptable fits with reduced χ^2 , $\chi_r^2 = \chi^2/\text{dof} > 4$. Among them, the best fit is obtained with the disk+wind clumpy model by Hönic & Kishimoto (2017) ($\chi_r^2 = 4.41$), followed by the smooth torus model by Fritz et al. (2006) ($\chi_r^2 = 4.98$). The other two models provide $\chi_r^2 > 10$. Tables 5–8 (Column 2) in Appendix B show the values obtained for each parameter and the goodness of the fit throughout the χ^2/dof . In general, all models overestimate the Q -band flux and they struggle to reproduce the $10 \mu\text{m}$ silicate absorption feature. A clear flux deficit at short wavelengths (below $9 \mu\text{m}$) is also visible irrespective of the model used.

3.2. Two SED Dust Model

Due to the poor fits obtained with the one-SED models, which tend to overpredict the Q -band flux compared with observed spectrum, and show poor agreement in the $10 \mu\text{m}$ silicate absorption profiles, we propose that a combination of models might provide a better fit, allowing complex dust geometries. Note that this is not an attempt to obtain a physically motivated fit but to explore the complexity that can achieve a better match to the data. In Section 4, we then use these results to explore new SEDs using the radiative transfer code SKIRT, which produces physically motivated SEDs. Therefore, this exploration of complex models is needed to obtain the initial guess for the parameters in the radiative transfer modeling. This was already explored by Pasetto et al. (2019) by unlinking the slope of the azimuthal distribution of dust, γ , and the edge-on optical depth at $9.7 \mu\text{m}$, $\tau_{9.7 \mu\text{m}}$, for the smooth model presented by Fritz et al. (2006). This provided a much better fit in Pasetto et al. (2019). Here, we perform a systematic analysis using the four AGN dust models described in Section 2.

Using the best fit from each model (Section 3.1), we separately fit the N - and Q -band spectra, allowing just one parameter to vary between the two fits. In other words, we kept all the parameters fixed during the fit, except for one of them. We found that changing the parameters does not always result in an improvement of the fit. Tables 5–8 (Column 3 onward) in

Appendix B show the values obtained and the best statistics (i.e., χ^2/dof) when each parameter of the model is untied between bands. In order to study if the fit improved by allowing to vary one of the parameters, we used the f-statistic test (f-test). For the smooth torus model by Fritz et al. (2006), the fit improves by untying any parameter. For the clumpy torus by Nenkova et al. (2008b), the two-phase torus by Stalevski et al. (2016), and the clumpy disk+wind by Hönic & Kishimoto (2017), we obtain improved spectral fits by untying any parameter except for Y , p , and i , respectively. However, the improvement is not enough to obtain $\chi_r^2 \leq 2$ for the clumpy torus by Nenkova et al. (2008b) and clumpy disk+wind by Hönic & Kishimoto (2017). For two-phase torus by Stalevski et al. (2016), the fit improves with $\chi_r^2 \leq 2$ only by untying the half-opening angle of the torus σ ; and for the smooth torus model by Fritz et al. (2006), the fit improves significantly by untying any parameter except for the viewing angle, i ($\chi_r^2 = 2.17$). Thus, unlinking almost any parameter improves the final fit, pointing to the complex nature of the source.

We then test if untying two parameters significantly improves the resulting fit. We discard the subsequent analysis of clumpy torus by Nenkova et al. (2008b) and clumpy disk+wind by Hönic & Kishimoto (2017) due to the poor spectral fit obtained so far. In general, we consider those parameters that produce a statistical improvement (see above). For the smooth torus model by Fritz et al. (2006), we discard the model obtained by untying viewing angle, i , because we do not expect two different values for the viewing angle of the torus. In the case of the two-phase torus by Stalevski et al. (2016), we only consider the model obtained by untying the half-opening angle, σ , because untying the other parameters does not produce a significant improvement.

We show in Table 2 the results for the smooth torus model by Fritz et al. (2006) obtained by untying two parameters between the N and Q bands. We have 10 possible combinations of the parameters. We discard six of them because they do not provide physically plausible scenarios (e.g., due to the better resolution of the N band compared to the Q band, values for Y in the N band larger than the Q band are not expected). We have four scenarios that significantly improved the fits by untying: (1) σ and γ ; (2) σ and β ; (3) γ and τ ; and (4) β and τ . Figure 3 shows the best fit obtained for these four scenarios. For the two-phase torus model by Stalevski et al. (2016), we discard the combination untying σ with any other parameter because any of them results in a physically plausible scenario, since the half-opening angle of the torus related to the N band (with better resolution) is bigger than that related to the Q band (with worse resolution). Table 9 in Appendix B shows the results of combining the half-opening angle, σ , with the other parameters for the two-phase torus model by Stalevski et al. (2016).

4. SED Simulations with SKIRT

In order to better explore the complex torus structure of NGC 1068, we produced synthetic SEDs based on the results from the previous section. For this, we used the 3D Monte Carlo radiative SED transfer code SKIRT (Baes et al. 2003, 2011). SKIRT offers state-of-the-art software for simulating radiative transfer in dusty astrophysical systems. We created grids of the parameters based on the smooth torus geometry used by Fritz et al. (2006), which provides the best-fit statistics. We remark that clumpy distributions were not tested

to be consistent with the results obtained using the available SED models (see Section 3).

We fitted the NGC 1068 N - and Q -band spectra including the foreground extinction using the extinction law described by Calzetti et al. (2000). We assumed a ratio of total to selective extinction $R_V = 3.1$ and an optical extinction in the range of $A_V = [0-10]$ magnitudes. This extinction is applied to each SED to test if additional foreground extinction improves the final fit.

In order to determine the best synthetic SED, we used the χ^2 statistics through the standard $\chi_r^2 = \chi^2/\text{dof}$, where dof is the total number of data bins in the spectrum. We also use the Bayes factor (see Appendix C for details) to evaluate to what extent a model is better than another one. When the Bayes factor is ≤ 0.01 , the first model is preferred. The second model is preferred when the Bayes factor is ≥ 100 .

We initially used a mix of graphite and silicate grains from Li & Draine (2001) (already available within SKIRT), hereafter identified as Graph_L and Sil_L, respectively. We also selected a smooth distribution of the dust particles covering a minimum grain size of $\text{size}(\text{min}) = 0.005$ and a maximum grain size of $\text{size}(\text{max}) = 0.25 \mu\text{m}$. Moreover, we assume a percentage within the dust mix of 49% and 51% for the graphite and silicate grains, respectively, close to the dust mix used by Fritz et al. (2006). Geometry, grain size, composition, and optical depth are further explored in Sections 4.1–4.3.

4.1. Grids A and B: Geometry and Optical Depth

Following the results found in Section 3.2, we constructed a dust geometry conformed by two tori coexisting in the same plane and we explore the parameters of each of the two tori. We varied the radial power-law exponent, p , the polar index, q , the half-opening angle, σ , the maximum/outer radius, R_{max} , the edge-on optical depth and τ between the two tori for this first grid. Note that the symbols of the parameters are according to the SKIRT notation. In order to cover a large range of values and to optimize the computational time (roughly 2–3 days per simulation using up to 30 GB of RAM and 12 cores) we impose the following physical restrictions. First, the outer radius should be smaller in one of the tori. Moreover, the radial power-law exponent, q , the polar index, γ , and the equatorial optical depth, $\tau_{9.7 \mu\text{m}}$, must be different for each torus. Finally, the viewing angle of the system, i , is the same for both tori. These restrictions allowed reducing the number of SEDs produced by focusing in meaningful scenarios. All together we produce a total of 2376 synthetic SEDs. We call this set of models Grid A. The set of parameters tested are included in Column 2 of Table 3.

The best-fit parameters are given in Column 3 of Table 3. Note that suffixes 1 and 2 are used to discriminate between the two tori. Although the best fit shows a poor statistic ($\chi_r^2 = 5.27$), it is as good as a single SED from the smooth torus by Fritz et al. (2006) and the clumpy disk-wind model by Hönic & Kishimoto (2017), and already better than the two-phase torus by Stalevski et al. (2016) and the clumpy torus model by Nenkova et al. (2008b). Figure 4 (top panel) shows the best fit for Grid A. The center of the silicate absorption feature appears at shorter wavelengths compared to the data and the slope between the N and Q bands also fails to be reproduced by this SED.

We then create a new grid with the best values obtained previously and a larger range of values for the outer radius of

Table 2
 Values of the Parameters and Statistics Obtained with the Smooth Torus model by Fritz et al. (2006) When Two Parameters are Unlinked at the Q band Compared to the N band

Param	Band	Unlinking										
		σ/γ	σ/β	σ/Y	σ/τ	γ/β	γ/Y	γ/τ	β/Y	β/τ	Y/τ	
i	N	40 ± 0.5	>0.01	>0.01	>0.01	>0.01	>0.01	>0.01	>0.01	>0.01	$40.35^{+0.18}_{-0.91}$	$40.0^{+0.27}_{-2.2}$
	Q
σ	N	$25.49^{+0.69}_{-0.51}$	>20	$33.89^{+2.17}_{-0.87}$	>20	>20	>20	>20	>20	>20	$30.42^{+2.41}_{-1.2}$	$36.19^{+1.93}_{-1.83}$
	Q	>20	$39.98^{+0.6}_{-0.5}$	$40.08^{+1.64}_{-0.54}$	>20
γ	N	0.02	0.08 ± 0.01	0.17 ± 0.6	$0.05^{+0.03}_{-0.02}$	$2.0^{+0.3}_{-0.5}$	$0.05^{+0.05}_{-0.01}$	>0.01	$0.18^{+0.11}_{-0.7}$	$2.0^{+0.01}_{-0.08}$	$1.99^{+0.02}_{-0.27}$	
	Q	< 6	>0.01	$5.06^{+1.78}_{-2.91}$	$3.56^{+1.78}_{-0.47}$	
β	N	>-1	>-1	>-1	>-1	>-1	>-1	>-1	$-0.25^{+0.02}_{-0.11}$	>-1	>-1	
	Q	...	>-1	-0.94 ± 0.01	>-1	$-0.82^{+0.04}_{-0.05}$...	
Y	N	>10	>10	>10	>10	$13.26^{+0.75}_{-0.81}$	>10	>10	$113.45^{+30.39}_{-71.94}$	$134.89^{+4.76}_{-4.08}$	$137.0^{+5.15}_{-4.35}$	
	Q	>10	$22.31^{+3.46}_{-3.31}$...	>10	...	>10	
$79.7 \mu\text{m}$	N	$2.0^{+0.02}_{-0.07}$	$2.0^{+0.02}_{-0.05}$	$1.87^{+1}_{-0.03}$	$1.84^{+0.12}_{-0.1}$	$2.0^{+0.02}_{-0.01}$	$1.84^{+0.6}_{-0.11}$	1.8 ± 0.1	1.93 ± 0.02	$5.98^{+0.03}_{-0.22}$	$5.73^{+0.28}_{-0.18}$	
	Q	$0.15^{+0.04}_{-0.03}$	$0.28^{+0.05}_{-0.14}$...	$0.14^{+0.05}_{-0.02}$	$1.6^{+0.9}_{-1.0}$	
χ^2/dof		94.04/258	151.45/258	77.76/258	67.37/258	89.16/258	67.75/258	68.88/258	101.66/258	83.82/258	68.54/258	

Note. Note that the viewing angle is measured with respect to the equatorial plane.

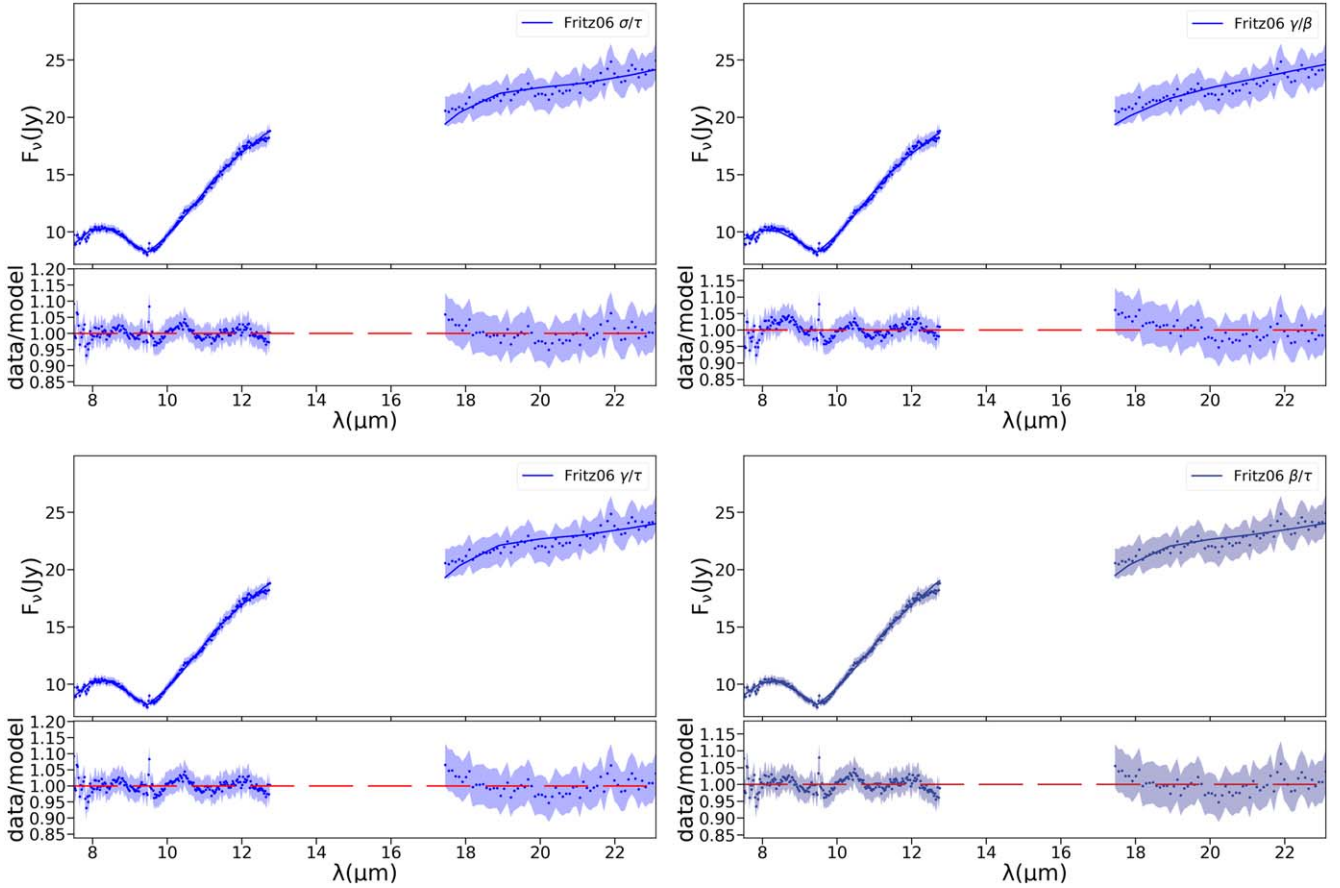


Figure 3. Spectral fit to the smooth torus model by Fritz et al. (2006) with two parameters unlinked: σ/τ (top left), γ/β (top right), γ/τ (bottom left), and β/τ (bottom right). The description is the same as that given in Figure 2.

Table 3
Parameters Tested in the Grids Described in Sections 4.1 and 4.2

Param	Geometry and Optical Depth (Section 4.1)				Grain Size and Composition (Section 4.2)					
	Grid A		Grid B		Grid C		Grid D		Grid E	
	Grid	Best Fit	Grid	Best Fit	Grid	Best Fit	Grid	Best Fit	Grid	Best Fit
i	[60, 75, 90] $^\circ$	60	[60 $^\circ$, 75 $^\circ$, 90 $^\circ$]	60	[50 $^\circ$ –75 $^\circ$]	55	[50 $^\circ$ –75 $^\circ$]	60	[50 $^\circ$ –75 $^\circ$]	60
σ_1	[20, 40, 60] $^\circ$	40 $^\circ$	40 $^\circ$...	40 $^\circ$...	40 $^\circ$...	40 $^\circ$...
σ_2	[20, 40, 60] $^\circ$	60 $^\circ$	60 $^\circ$...	60 $^\circ$...	60 $^\circ$...	60 $^\circ$...
p_1	[0, 1]	0	0	...	0	...	0	...	0	...
p_2	[0, 1]	1	1	...	1	...	1	...	1	...
q_1	[0, 3, 6]	3	3	...	3	...	3	...	3	...
q_2	[0, 3, 6]	6	6	...	6	...	6	...	6	...
$R_{\max,1}$	[2, 20]	2	[1–4]	2	2	...	2	...	2	...
$R_{\max,2}$	[2, 20]	20	[1–5, 10, 20, 30]	30	30	...	30	...	30	...
τ_1	[2, 20]	20	20	...	20	...	20	...	20	...
τ_2	[2, 20]	2	2	...	2	...	2	...	2	...
A_V	[0–10]	0	[0–10]	1	[0–10]	6	[0–10]	3	[0–10]	3
Silicate	Sil _L	...	Sil _L	...	Sil _M	Sil _M	Sil _M	...	Sil _M	...
Graphite	Graph _L	...	Graph _L	...	Graph _L	...	Graph _L	...	Graph _L	...
log(size(min))	–2.3	...	–2.3	...	–2.3	...	–2.3	...	[–3, –2, –1, 0]	–2
size(max / min)	5	...	5	...	5	...	[20, 200]	200	[10,100,1000]	100
N_{SED}	2376		726		330		660		2970	
χ^2/dof		5.27		3.74		4.09		1.33		1.32

Note. Suffixes 1 and 2 are used to discriminate between the two tori. In the second grid, for those untested parameters, we use the values obtained with the best previous model. Sil_L and Graph_L: Optical and calorimetric properties of the dust silicate and graphite grains reported by Li & Draine (2001). Graph_M: Optical and calorimetric properties of the dust graphite grains reported by Min et al. (2007) (see the text).

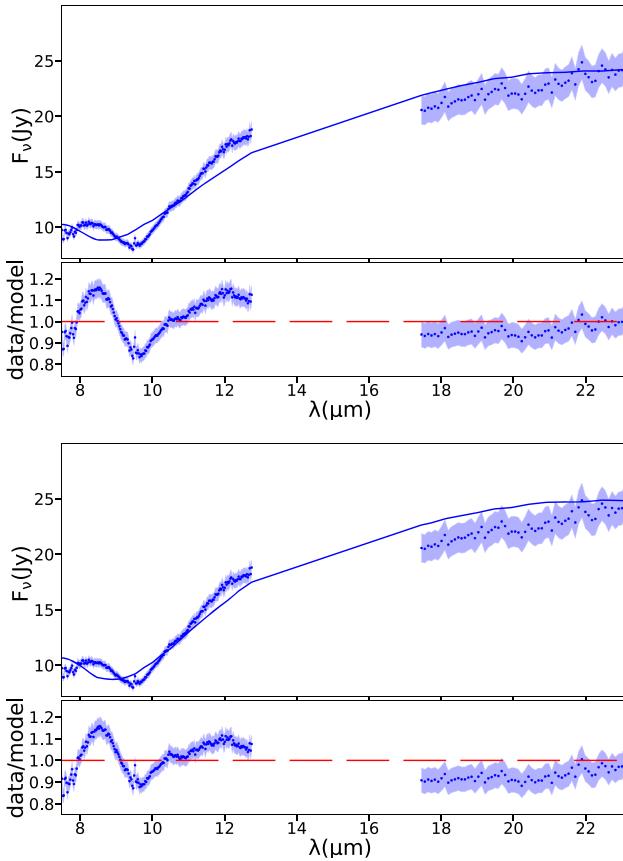


Figure 4. (Top) best fit of the N - and Q -band spectra using all the models in Grid A. (Bottom) same as Grid A but with a larger range of values for R_{\max} (Grid B). In each figure, we show the model with the blue solid line in the top panel and the ratio between the model and data in the bottom panel. The blue shaded area shows the error on the measurement.

the structure, R_{\max} , referred to as Grid B in Table 3. We impose again that the outer radius of the structure is at least equal or larger in one of the torus. Notice that we do not explore outer radius greater than 30 pc since they would be spatially resolved with the current data, which is not the case. The total number of SEDs produced was 726, including three viewing angles. The best fit ($\chi_r^2 = 3.74$, Figure 4, bottom panel) is already better than any single SED fit reported in Section 3. The best fit from the second grid has a Bayes factor of 10^{89} compared to the previous one. However, the issues found for the first grid remain, i.e., the center of the silicate feature is displaced compared to the spectrum and slope between the N and the Q bands is not well recovered. We also explored a broad range for the viewing angle, although this did not yield better results. Thus, hereinafter we focus our analysis on viewing angles in the range of $i = [50-75]^\circ$, which is also consistent with the type 2 nature of NGC 1068.

4.2. Grids C, D, and E: Dust Grain Size and Composition

As explained above, one of the main problems of our SED simulations is the spectral shape of the silicate absorption feature at $\sim 9.7 \mu\text{m}$. This silicate feature is strongly dependent on the dust composition and size. In particular, grain size is expected to be different from that of the interstellar medium (ISM). The inner torus radius versus luminosity relation derived by dust reverberation in AGN requires an emission

region more compact than expected. Having a smaller inner radius implies higher temperature than the silicate sublimation temperature, pointing to the existence of large graphite dust grain near AGN (Kishimoto et al. 2007). Indeed, large grains can survive close to the accretion disk, whereas small grains are more easily destroyed. Moreover, the dense environment of AGN promote dust aggregation, possibly making it more efficient for larger than average dust aggregates to form large dust particles.

Although silicate grains with various compositions display a spectral feature in the $10 \mu\text{m}$ region due to the Si–O stretching mode, there are differences in the spectral appearance (both the peak and shape) depending on the composition of the silicates (see Figure 4 by Min et al. 2007). Furthermore, the shape and position of the $10 \mu\text{m}$ silicate feature also has a strong dependence on grain shape. Indeed, the absorption spectrum caused by homogeneous spherical particles is very different from that caused by other particle shapes, being much larger than the differences due to various nonspherical particle shapes (Min et al. 2003). In general, the spectral extinction features caused by irregularly shaped particles are much broader and shifted toward the red with respect to those caused by homogeneous spherical particles (see Figure 3 by Min et al. 2007). In practice, both composition and particle shape affect the scattering and absorption efficiencies, increasing the impact on the resulting spectrum.

In the previous simulations, we used graphite and silicate grains reported by Li & Draine (2001) (referred to here as Graph_L and Sil_L) and we assumed dust grains with sizes in the range of $0.005-0.25 \mu\text{m}$, consistent with most of the AGN dust SED libraries reported in the literature (e.g., Fritz et al. 2006). In order to explore the effect of the optical and calorimetric properties of the dust, we changed the silicate grains from Li & Draine (2001) to those reported by Min et al. (2007) and available in SKIRT (hereinafter Sil_M).

We initially explored only the effect on the new silicate by Min et al. (2007) keeping the size of the particles and the values of the parameters obtained with the best fit in Section 4.1 (Grid C in Table 3). The resulting fit shows a statistic of $\chi_r^2 = 4.09$, which is worse than the best fit obtained with silicates from Li & Draine (2001). However, the effect of the inclusion of these particles together with a change in grain size results in a significant improvement of the results. We therefore explored different dust grain sizes for both tori, fixing the minimum grain size and allowing to vary the maximum grain size (Grid D in Table 3). We obtain a best fit with $\chi_r^2 = 1.33$. This fit has a Bayes factor of 1.8×10^{140} compared to the previous one. Note that we also investigate if keeping the canonical grain size of $0.005-0.25 \mu\text{m}$ for the largest torus and allowing larger particles of $0.005-1.0 \mu\text{m}$ only for the small torus improves the result. However, this SED produces a slightly worse fit than that of $size_1 = size_2 = 0.005-1.0 \mu\text{m}$.

We also explored whether covering size ranges (i.e., from minimum to maximum grain size distributions) of one, two, and three orders of magnitude for the particles size have an impact on the final fit (Grid E in Table 3). The best statistical fit is found using dust grain sizes of $size_1 = size_2 = 0.001-1 \mu\text{m}$, $size_1 = size_2 = 0.01-1 \mu\text{m}$, and $size_1 = size_2 = 0.1-1 \mu\text{m}$ with $\chi_r^2 = 1.52$, $\chi_r^2 = 1.32$, and $\chi_r^2 = 2.07$, respectively. Thus, in all the cases the best fit is found when the maximum particle grain size is $\sim 1 \mu\text{m}$. Moreover, the preferred minimum grain size is in the range of $0.005-0.01 \mu\text{m}$. These minimum grain

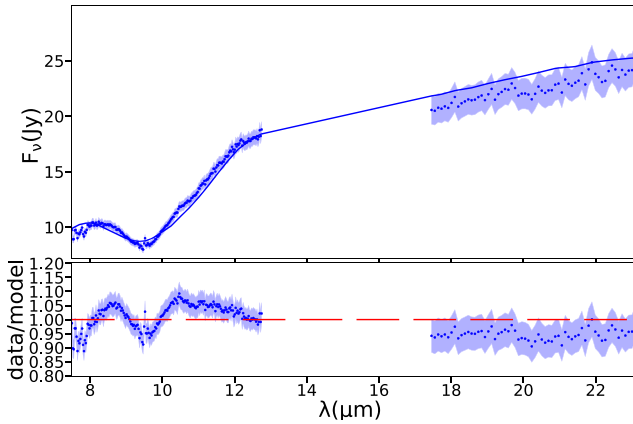


Figure 5. Best model for using graphite by Li & Draine (2001), silicate by Min et al. (2007), and $\text{size}_1 = \text{size}_2 = 0.005\text{--}1\ \mu\text{m}$ (Grid E). The description in this figure is the same as that reported in Figure 4.

sizes have a Bayes factor of 8.8×10^{-12} and 8.6×10^{-44} compared to the fit obtained with 0.001 and $0.1\ \mu\text{m}$, respectively. Figure 5 shows the best resulting fit for Grid E.¹² It is clear how this fit better describes the silicate absorption feature and the slope between the N and Q bands at the same time.

4.3. Grids F, G, and H: Optical Depth and Dust Grain Size

In order to test the effect of the optical depth, which is sensitive to the other physical parameters, we created a new grid with 19,008 SEDs (Grid F in Table 4) exploring a range of values according to the latest best model. The test resulted in a best fit ($\chi_r^2 = 1.04$). This model has a Bayes factor of 8.7×10^{59} compared to that obtained previously. Notice that we made these grids with grain sizes of $0.005\text{--}1\ \mu\text{m}$ (one of the three combinations producing the best fit from the previous tests).

We then create a new grid of SEDs (Grid G in Table 4) exploring the optical extinction $\tau_{9,7}$ around the best values from the previous test. Moreover, we tested the best grain sizes obtained in the previous section. In total, 14,256 SEDs are created. We obtained the best fit with $\chi_r^2 = 0.48$ using grain sizes of $0.1\text{--}1.0\ \mu\text{m}$, which is significantly larger than those used in the currently available models. The best fit has a Bayes factor of 3.92×10^{32} compared to that obtained in the previous test. Figure 6 shows the resulting best fit.

Finally, the best fit is expected to depend on the fine-tuning of the parameters. For that purpose we explore again a range of parameters around the best fit obtained so far (Grid H in Table 4).

The statistic for this fit is $\chi_r^2 = 0.4$. This fit has a Bayes factor 4.5×10^4 compared to that obtained previously. Figure 7 shows the final best fit obtained.

Figure 8 shows a sketch of the dusty distribution that we obtain through our best model. The smallest (purple) and largest (red) component are two concentric torus with inner radius of $0.2\ \text{pc}$ (according with the dust sublimation radius) and line of sight $i = 71^\circ$. The ionization cone in NGC 1068 as seen in Hubble Space Telescope (HST) images is centered around $\text{PA} = 10^\circ$, while modeling of HST spectra based on the

kinematics of the gas indicates the ionization cone with an opening angle of 80° centered around $\text{PA} = 30^\circ$ (Das et al. 2006), roughly perpendicular to the maser spots. Using SED fitting, Lopez-Rodriguez et al. (2018) derived a viewing angle of $i = 75_{-4}^{+8^\circ}$ while García-Burillo et al. (2016) found $i = 66_{-4}^{+9^\circ}$. Gravity Collaboration et al. (2020) found an inclination angle of $70 \pm 5^\circ$ through image reconstruction of their interferometric observations of the near-infrared (NIR) emitting-dust. All of them are consistent with an almost edge-on orientation of the torus, as expected for the type 2 classification of NGC 1068, which agrees with the value reported in our work.

Some authors have found that the inclination parameter is very difficult to restrict. Ramos Almeida et al. (2014) concluded that the inclination of the torus is better restricted by using the combination of sub-arcsecond resolution NIR and MIR. However, at least for NGC 1068, the inclination angle can be restricted using only MIR spectra. This is due to the availability of spectroscopic data. Indeed, González-Martín et al. (2019a) found that the viewing angle can be well restricted using only MIR spectroscopy as long as the wavelength range covers at least between 5 and $25\ \mu\text{m}$. Alternatively, the use of combined X-ray and MIR spectra simultaneously has been demonstrated to allow to recover the viewing angle, at least for another type 2 AGN IC 5063 (Esparza-Arredondo et al. 2019).

5. Discussion

5.1. Geometry of the Dust Component

Early works in the infrared domain such as the one presented by Cameron et al. (1993) pointed out that complex structures must be present at small scales in NGC 1068 since the MIR continuum is extended within $1''$. Using higher resolution data, Bock et al. (2000) showed there was a central core component ($<0.2''$), which they associated with the AGN dust torus. However, this core was still not resolved within scales of tens of parsecs. Wittkowski et al. (2004) and Jaffe et al. (2004) presented spatially resolved images at NIR and MIR wavelengths using interferometric techniques. They favor a multi-component model for the dust distribution in NGC 1068, where part of the flux originates from a hot and small ($\lesssim 1\ \text{pc}$) component with also a large warm component ($2.1 \times 3.4\ \text{pc}$). Consistent with this result, Mason et al. (2006) found that the MIR emission originates in two distinct components. A compact bright source with radius $<15\ \text{pc}$, which they identified with the obscuring torus, and a diffuse component with dust in the ionization cones. Mid-infrared interferometric instrument (MIDI) observations by Raban et al. (2009) found that the N -band MIR emission can be represented by two components. They identified the first component as the inner funnel of the torus, with $0.45 \times 1.35\ \text{pc}$. The second component was identified with the cooler body of the torus, with a size of $3 \times 4\ \text{pc}$.

From the analysis presented here we conclude that to obtain a good spectral fit using the available AGN dust models it is necessary to consider a two-phase composite geometry for the dusty torus. Indeed, none of the proposed models are able to explain the N - and Q -band spectral range simultaneously (see Section 3). Alonso-Herrero et al. (2011) attempted to simultaneously fit the N and Q spectra in addition to the NIR and MIR photometric points. They manage to produce a

¹² Note that minimal differences are found between $0.005\text{--}1\ \mu\text{m}$ and $0.01\text{--}1\ \mu\text{m}$.

Table 4
Parameter Grids Tested in Section 4.3

Param	Optical Depth and Dust Grain Size (Section 4.3)				Final Grid (Section 4.3)	
	Grid F		Grid G		Grid H	
	Grid	Best Fit	grid	Best Fit	Grid	Best Fit
i	[55–90] $^\circ$	63	[55–90] $^\circ$	67	[55–90] $^\circ$	71
σ_1	40 $^\circ$...	40 $^\circ$...	[38, 40, 42] $^\circ$	42
σ_2	60 $^\circ$...	60 $^\circ$...	[58, 60, 62] $^\circ$	58
p_1	0	...	0	...	[0, 0.1, 0.2]	0.2
p_2	1	...	1	...	[0.8, 1, 1.2]	1
q_1	3	...	3	...	[2.8, 3, 3.2]	3.2
q_2	6	...	6	...	[5.8, 6, 6.2]	5.8
$R_{\max,1}$	2	...	2	...	[1.8, 2, 2.2]	1.8
$R_{\max,2}$	30	...	30	...	[28, 30, 32]	28
τ_1	[8–22]	12	[11, 12, 13]	13	[9–14]	12
τ_2	[0.4–2.4]	0.4	[0.3, 0.4, 0.5]	0.3	[0.1–0.5]	0.3
A_V	[0–10]	4	[0–10]	0	[0–10]	2
Silicate	Sil _M	...	Sil _M	...	Sil _M	...
Graphite	Graph _L	...	Graph _L	...	Graph _L	...
log(size(min))	–2.3	...	[–3, –2.3, –2, –1]	–1	–1	...
size(max / min)	200	...	[10, 100, 200, 1000]	10	10	...
N_{SED}	19,008		14,256		288,684	
χ^2/dof		1.04		0.48		0.40

Note. Suffixes 1 and 2 is used to discriminate between the two tori. For Grid F we vary the optical depth in steps of $\Delta(\tau_1) = 2$ and $\Delta(\tau_2) = 0.2$.

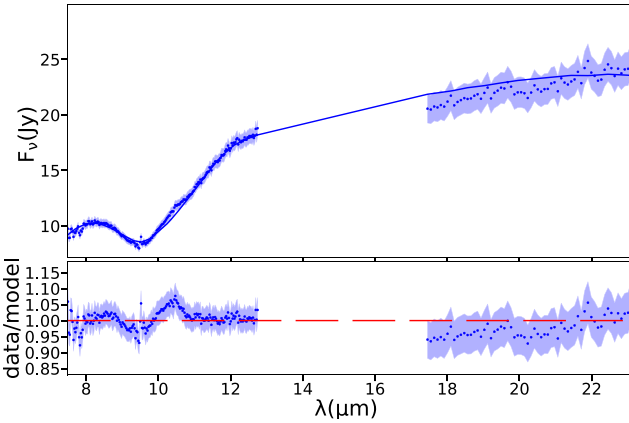


Figure 6. Best model exploring the effect on the optical depth, using $\text{size}_1 = \text{size}_2 = 0.1\text{--}1\ \mu\text{m}$ (Grid G, see Section 4.3). The description in this figure is the same as that reported in Figure 4.

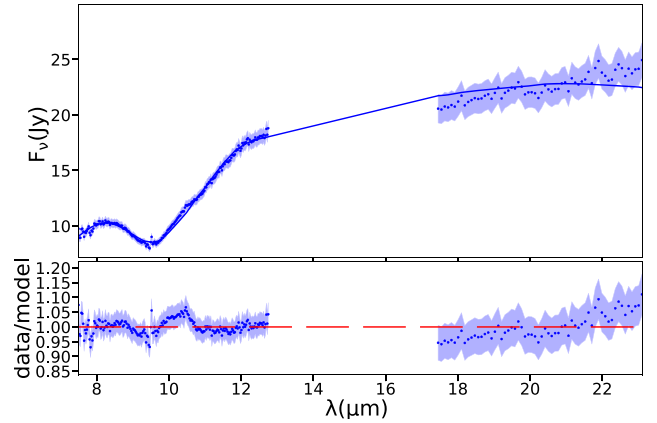


Figure 7. Best model obtained after fine-tuning the parameters (Grid H, see Section 4.3). The description in this figure is the same as that reported in Figure 4.

reasonable fit, using an early version of the clumpy torus model by Nenkova et al. (2008b). The current version of this clumpy torus model did not produce good fits ($\chi_r^2 > 4$). Using the available models, we explored the possibility of adding complexity to them by untying one or two parameters between the fits of the two spectra. We found that the fit improves significantly from the statistical point of view. We interpret this as a signal of the complexity of the AGN dust torus in NGC 1068, consistent with early works.

Through MIR interferometry as well, López-Gonzaga et al. (2014) found that the emission of the core of NGC 1068 can be divided into two distinct regions. However, these two components are not concentric, with one consistent with a hot emission surrounded by warm dust and a large warm diffuse region approximately 7 pc away from the other. These two components could be associated with two different AGN,

conforming a dual or binary AGN. Indeed, Wang et al. (2020) suggested that a binary SMBH could support the counter-rotating structures reported by Imanishi et al. (2018) and Impellizzeri et al. (2019) to explain the molecular gas observations of the torus of NGC 1068.

If the two AGN are far enough to not significantly influence the heating of dust associated to the other AGN, then the total SED should be reproduced with a combination of two AGN dust models. We tested this hypothesis using XSPEC spectral-fitting software as we did for the single models (i.e., dust+dust models). However, this test did not yield a good spectral fit ($\chi^2/\text{dof} \geq 5$). Instead, allowing the parameters of the models to vary independently for the N and Q bands produced a good fit, as already mentioned above.

Another possibility is that the two AGN are close enough to heat both AGN dust components. This scenario better matches the results by Wang et al. (2020) because they assume two

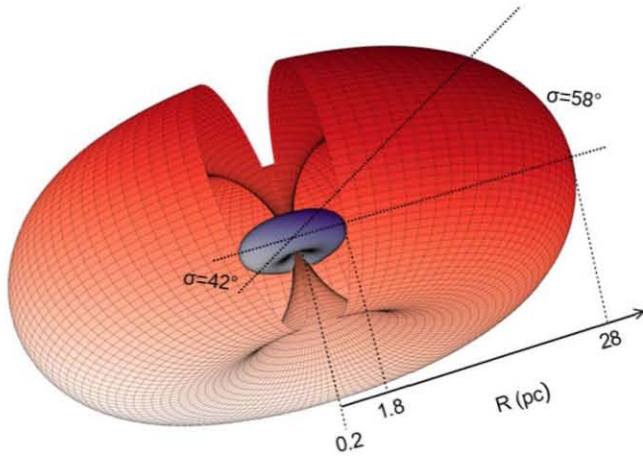


Figure 8. Sketch of the dusty distribution of NGC 1068 obtained through our best model: two concentric tori with inner radius of 0.2 pc and outer radius of 1.8 and 28 pc for the smallest (purple) and largest (red) torus, respectively. The viewing angle of both tori is $i = 71^\circ$ (shown here perpendicular to the page). We also chose the position angle as $PA = 113^\circ$ and the bottom view of the torus to be consistent with the results presented by García-Burillo et al. (2019). Note that we can only distinguish whether the torus is face-on or edge-on with our modeling.

AGN with a separation of ~ 0.1 pc, which is a separation below the expected inner radius of the torus. However, note that this separation is not consistent with the 7 pc distance between the two dust components found by López-Gonzaga et al. (2014). In the SMBH binary case, the sum of two AGN dust models is not an accurate way to test this scenario and new radiative transfer models are needed including this complexity. We also tested this scenario by producing synthetic SEDs for two nonconcentric tori. Details on these new SEDs are reported in Appendix F. However, the best model obtained is $\sim 1 \times 10^{12}$ times worse than the model with two concentric tori reported in our results. Note that the inner radius of the torus is larger than the binary AGN separation given by Wang et al. (2020) so this two concentric tori could virtually mimic the dual AGN claimed in their work. Thus, we do not rule out two nonconcentric tori associated with a binary SMBH with separations below the inner radius of the torus.

Studies at other wavelengths can also provide information about the complexity of torus. For example, through X-ray data, the reflection component can be used to probe the matter distribution of the gaseous (neutral and distant) torus (see Liu et al. 2016). Bauer et al. (2015) concluded that a complex reflector structure consisting of multiple components (two nuclear and one extended) is needed to fit the combined Nuclear Spectroscopic Telescope Array (NuSTAR), Chandra, X-ray Multi-Mirror Mission Newton (XMM-Newton), and Swift Burst Alert Telescope (Swift-BAT) spectra of NGC 1068. This is consistent with the two nuclear components shown in our work, although it is worth noting that the comparison between the X-ray gaseous torus and the MIR dusty torus might be very complex (Esparza-Arredondo et al. 2021).

Through radio-interferometry, molecular line and continuum observations are used for investigating the morphological structure of the torus (Imanishi et al. 2018). Although dust continuum from ALMA might have some issues due to jet contamination (Pasetto et al. 2019; García-Burillo et al. 2021). García-Burillo et al. (2019) inferred a size of 28 pc using the

CO(3-2) line, which is in agreement with the large torus found in our work. This might be explained due to the fact that ALMA could be imaging the cooler (and therefore extended) dust, being the outer layer of the small torus found in our work. In support on the large torus, Lopez-Rodriguez et al. (2020) reproduced $860 \mu\text{m}$ polarimetric observations of NGC 1068, using synthetic polarimetric observations generated with the CLUMPY torus model by Nenkova et al. (2008b) with an outer radius higher than 9 pc. Furthermore, Gratadour et al. (2015) observed the core of NGC 1068 with the Spectro-Polarimetric High-contrast Exoplanet REsearch (SPHERE) instrument on the Very Large Telescope, using adaptive optics-assisted polarimetric observations in the NIR, finding evidence of an extended torus with 15×27 pc. Very recently, using Very Large Telescope Interferometer/Multi AperTure mid-Infrared SpectroScopic Experiment (VLTI/MATISSE) observations, Gamez-Rosas et al. (2021) found that the torus of NGC1068 contains an optically thick ring on parsec scales and an optically less thick disk that extends to at least 10 pc, which is in agreement with our model where the smallest component is denser than the larger component.

The smallest torus with 1.8 pc (see Figure 8) has a high optical depth $\tau_{9.7 \mu\text{m}} = 12$; in the radial direction, the dust distribution is almost constant ($\rho \sim r^{-0.2}$), while in the polar direction it decays quickly ($\rho \sim e^{-3.2|\cos\Theta|}$). The largest component has a smaller optical depth $\tau = 0.3$ compared with that of the smallest torus and the dust density decreases with r^{-1} and $e^{-5.8|\cos\Theta|}$ in the radial and polar directions, respectively. Our result might be interpreted as a complex distribution of dust rather than two distinctive components. Our components might be a simplification of a structure where the dust in the outskirts is geometrically thicker than the inner side and the opacity also abruptly falls toward the outskirts.

Alternatively, we could also think that the large torus is just the inner dust from the host galaxy or a polar contribution to the dust, as suggested for other nearby AGN (Hönig et al. 2013; López-Gonzaga et al. 2014; Asmus 2019) and also for NGC 1068 (Mason et al. 2006; Liu et al. 2019). This polar dust could produce mostly silicate emission features (Hönig & Kishimoto 2017). Although not included here, we also produce the SEDs of the two components alone. This polar dust resembles that of the large torus component modeled in this work due to its low opacity if the inner torus is not presented (although the inner torus gives the highest fraction contribution). Under this latter scenario, the complexity found for NGC 1068 might be the result of a more dynamic model, as is the case of the fountain model by Wada (2012). Under this model the radiation from the central source drives the onset of biconical outflows that start forming at the inner region and subsequently propagate outward. Most of this material becomes a truncated wind that backflows toward the disk plane forming a geometrically thick disk. The small torus found in this work could be related to the thick inner disk, which is the origin of the launching wind, while the large torus could be related to the failed wind producing the geometrically thick disk. García-Burillo et al. (2019) also found a kinematic model for the molecular torus, where the gas presents circular motions and a fraction of it, inside the torus, is launched as an outflow. In our two component model, the small torus could be related to the torus component in the model by García-Burillo et al. (2019), and the large torus could be related to the outflow component. As a final remark, in an attempt to find similarities

among other astronomical objects, our resulting geometry is not far from that proposed for protoplanetary disks; a warm zone emitting at around $10\ \mu\text{m}$ and a much colder region emitting longward to $20\ \mu\text{m}$. Olofsson et al. (2009) show in their Figure 14 a schematic view of the disk in one of these systems, which might imply a grand unification between the dust in protoplanetary disks and that found in AGN.

Note that, if a distance of 14 Mpc is adopted (commonly used in other studies, e.g., Mason et al. 2006) instead of the 10.6 Mpc used in this paper, the luminosity would be higher by a factor of ~ 1.7 and the physical lengths (such as the inner and outer torus radius) would be higher by a factor of ~ 1.3 .

5.2. Dust Composition and Dust Grain Size

Besides the geometry, an important aspect explored in this work is that SED fitting allows studying the composition of the dust, which cannot be done with other techniques. Unfortunately, available SED libraries that explore grain size, size particle distribution or composition have not been produced to so far, although some works have made an effort to explore it (e.g., Hönl & Kishimoto 2010). Thus, new radiative transfer simulations, such as those produced in this work, are mandatory to study if dust composition or dust grain size are important to accurately reproduce the shape of the AGN dust continuum.

In this work, we demonstrate that an important ingredient to explain the MIR N - and Q -band spectra of NGC 1068 is the size of the particles. Since significantly better spectral fits are found if both graphite and silicate grains have grain sizes in the range of $0.1\text{--}1\ \mu\text{m}$ using the silicates used in Min et al. (2007). We also find an important improvement in the best-fit model from setting the maximum dust grain size to $1\ \mu\text{m}$, while varying the minimum particle size results in marginally changing the final SED. This particle size is much larger than that assumed for publicly available AGN dust models since they rely on the results for the ISM (usually $0.005\text{--}0.25\ \mu\text{m}$; Fritz et al. 2006; Nenkova et al. 2008b; Stalevski et al. 2016).

Some authors (e.g., Nikutta et al. 2009) have argued that the $10\ \mu\text{m}$ silicate feature can be explained through a clumpy dust distribution with a standard ISM dust. In Section 3, we tested a clumpy torus model for NGC 1068, however the silicate absorption profile showed poor agreement. Feltre et al. (2012) performed a comparison between the smooth and clumpy models by Fritz et al. (2006) and Nenkova et al. (2008b), respectively. They found that the behavior of the silicate feature at $9.7\ \mu\text{m}$ is quite distinct between the two models. However, they concluded that such difference arises from the dust chemical composition assumed by the models and not from the smooth or clumpy morphology, in agreement with our findings.

Some works have already explored the effect on the size of the particles in the context of AGN. Schartmann et al. (2005) explored models of dusty tori in AGNs. They tested effects of a broadening of the grain size distribution, spreading the grain size range with grains of $0.005\text{--}10$ and $0.001\text{--}10\ \mu\text{m}$. They found that the differences are nearly negligible for a face-on view angle, but for inclination angles, close to edge-on, a reduced relative depth of the silicate feature toward smaller wavelengths is visible. NGC 1068 has an almost edge-on view of the torus ($\sim 71^\circ$) so the importance of the dust grain sizes is justified. Other authors have also found evidence supporting large dust sizes. Through the ratio of the optical extinction in the visual band to the optical depth of the $9.7\ \mu\text{m}$ silicate

absorption feature, $A_V/\Delta\tau_{9.7}$, Lyu et al. (2014) obtained a mean ratio of $A_V/\Delta\tau_{9.7} \approx 5.5$ from a sample of 110 type 2 AGNs, which is considerably lower than that of the local ISM of the Milky Way ($A_V/\Delta\tau_{9.7} \approx 18.5$), implying that AGN dust grain size could exceed $\sim 0.4\ \mu\text{m}$ (Shao et al. 2017).

Although the dependence of the dust sublimation radius on grain size might be complex (see Figure 1 in Absil et al. 2013), Kishimoto et al. (2007) suggested that the dust sublimation radius vary with the square root of the dust size. In the context of debris disks, Kobayashi et al. (2011) developed the equation that links the sublimation radius (we express it in units of parsecs), the grain size (μm), luminosity (erg s^{-1}), and sublimation temperature (K) as follows:

$$R_{\text{sub}} = 0.11 \left(1 + \frac{1}{x}\right)^{1/2} \left(\frac{L_{\text{bol}}}{10^{45}}\right)^{1/2} \left(\frac{T_{\text{sub}}}{1300}\right)^{-2}, \quad (1)$$

where $x = 2\pi s_{\text{grain}}(T_{\text{sub}}/2898\ \text{K})$ and s_{grain} is the grain size. Therefore, the resulting larger grain sizes naturally imply dust located closer to the torus. Considering that the AGN dust models use $s_{\text{grain}} = 0.25\ \mu\text{m}$, while we have found $s_{\text{grain}} = 1\ \mu\text{m}$, the largest grains might be located up to a factor of 2 closer to the accretion disk. However, we tested the inner radius without a significant improvement in the final fit. Conversely, also in the context of protoplanetary disks, the analysis of the shape and strength of both the amorphous $10\ \mu\text{m}$ feature and the crystalline feature around $23\ \mu\text{m}$ provides evidence for the prevalence of micron-sized (amorphous and crystalline) grains in the upper layers of disks (Olofsson et al. 2009). Observations of dust in disks from submillimeter to centimeter wavelengths have provided strong evidence for grain growth in disks (Testi et al. 2001; Calvet et al. 2002). Pérez et al. (2012) found that the maximum size of the particle-size distribution increases from submillimeter sizes in the outer disks to millimeter and centimeter sizes in the inner disks. Indeed, dust grains in the planet-forming regions around young stars are expected to be heavily processed due to coagulation, fragmentation, and crystallization (Olofsson et al. 2009), and similar mechanisms might also explain the large grains found in NGC 1068.

6. Summary

We have studied the dusty torus in NGC 1068 using N - and Q -band Michelle/Gemini spectra. For this purpose we perform the analysis into two steps: (1) we used the XSPEC spectral-fitting package to test already available models and (2) we used the 3D Monte Carlo radiative SED transfer code SKIRT to build grids of synthetic SEDs, based on the result obtained from the first step. The main results are as follows:

1. Available SED models: Among the available models, the resulting best fit was obtained using the clumpy disk +wind model by Hönl & Kishimoto (2017). However, the best fit was statistically unsatisfactory. We then explored the possibility of adding complexity to the models by untying one and then two parameters when doing the fits of the N and Q spectra separately. We found that the fit significantly improves using the smooth torus model by Fritz et al. (2006) and four combinations of untied parameters. In this scenario, the emission in the two spectral ranges here considered is dominated by dust with different geometrical locations and distributions.

These components are characterized by different values of the equatorial optical depth, the opening angle, and the parameters regulating the dust density gradients. We interpret these results as a signal of the complexity of the dust in NGC 1068.

2. **New SEDs with SKIRT:** For the 3D Monte Carlo radiative simulations, we used two concentric tori that allow us to test more complex dusty geometries. The final best fit has the following common parameters for both tori: (1) a fractional contribution for graphite and silicate grains of 49% and 51%, respectively; (2) graphite from (Li & Draine 2001) and silicate from (Min et al. 2007); (3) size of graphite and silicate particles of 0.1–1 μm ; (4) inner radius of both tori of 0.2 pc; (5) viewing angle $i = 71^\circ$; and (6) foreground extinction $A_V = 2$ mag. The parameters changing from both tori are (1) the exponent of the power law describing the radial distribution $p_1 = 0.2$ and $p_2 = 1$, (2) the exponent of the polar distribution $q_1 = 3.2$, and $q_2 = 5.8$, (3) the half-opening angle $\sigma_1 = 42$ and $\sigma_2 = 58$, (4) the outer radius $R_{\text{max},1} = 1.8$ pc and $R_{\text{max},2} = 28$ pc, and (5) the equatorial optical depth to $\tau_{9.7 \mu\text{m},1} = 12$ and $\tau_{9.7 \mu\text{m},2} = 0.3$.

These findings can be interpreted as a compelling evidence for a complex dusty torus for NGC 1068. We speculate that this can be understood as inner compact disk/torus plus an outer extended torus/wind, conforming either a flared disk or a dynamical fountain model for the dust. Furthermore, some mechanism for grain growth needs to be claimed to explain the large grains to fit the MIR ground-based spectra of NGC 1068. Note that these results were obtained considering a smooth distribution of dust. Therefore, some parameters of the torus likely depend on the assumption of this distribution. In order to consider a similar geometry with other distributions, like clumpy, future efforts should test these scenarios. As a final remark, it has been largely discussed by the community that the complexity of the models, model parameter degeneration, and spatial resolution might be an issue when inferring the properties of the dust using SED fitting techniques (Ramos Almeida et al. 2014; González-Martín et al. 2019a). However, this detailed work demonstrates that useful information can be achieved from SED fitting when the full MIR spectral coverage is available and specific synthetic SEDs are produced to explain the observations.

We thank to the anonymous referee for his/her useful comments. C.V.-C. acknowledges support from a CONACyT scholarship. We thank the UNAM PAPIIT project IN105720 (PI OG-M). S.G.B. acknowledges support from the research projects PID2019-106027GA-C44, and S.G.B. and A.A.H. from research project PGC2018-094671-B-I00 funded by MCIN/AEI/ 10.13039/501100011033 and by ERDF A way of making Europe. C.R.A. acknowledges financial support from the European Union’s Horizon 2020 research and innovation program under Marie Skłodowska-Curie grant agreement No 860744 (BiD4BEST), from the State Research Agency (AEI-MCINN) and from the Spanish MCIU under grants “Feeding and feedback in active galaxies” with reference PID2019-106027GB-C42, “Quantifying the impact of quasar feedback on galaxy evolution (QSOFEED),” with reference EUR2020-112266, and from the Consejería de Economía, Conocimiento y Empleo del Gobierno de Canarias and the European Regional Development Fund (ERDF) under grant with reference ProID2020010105.

Software: XSPEC (Arnaud 1996), HEASoft (NASA High Energy Astrophysics Science Archive Research Center (HEASARC), 2014), SKIRT (Baes et al. 2003, 2011), Python/C language (Oliphant 2007), NumPy (Harris et al. 2020), SciPy (Virtanen et al. 2020), and Matplotlib (Hunter 2007).

Appendix A Dust Models

In order to show the geometry and dust distribution of the models tested in Section 2, a sketch of the models is shown in Figure 9. The smooth torus model by Fritz et al. (2006), the clumpy torus model by Nenkova et al. (2008b), and two-phase torus model by Stalevski et al. (2016) assume the dust distribution in a toroidal geometry. The clumpy disk and outflow model by Hönig & Kishimoto (2017) consider the dust distributed in a disk-like geometry plus a polar hollow cone. The smooth torus model by Fritz et al. (2006) considers a continuous distribution of dust toward the torus. The clumpy torus model by Nenkova et al. (2008b) considers a toroidal distribution of dusty clumps. The two-phase torus model by Stalevski et al. (2016) considers a dust distribution of clumps embedded in a smooth component. The clumpy disk and outflow model by Hönig & Kishimoto (2017) considers a dust distribution in a clumpy disk plus a polar hollow cone.

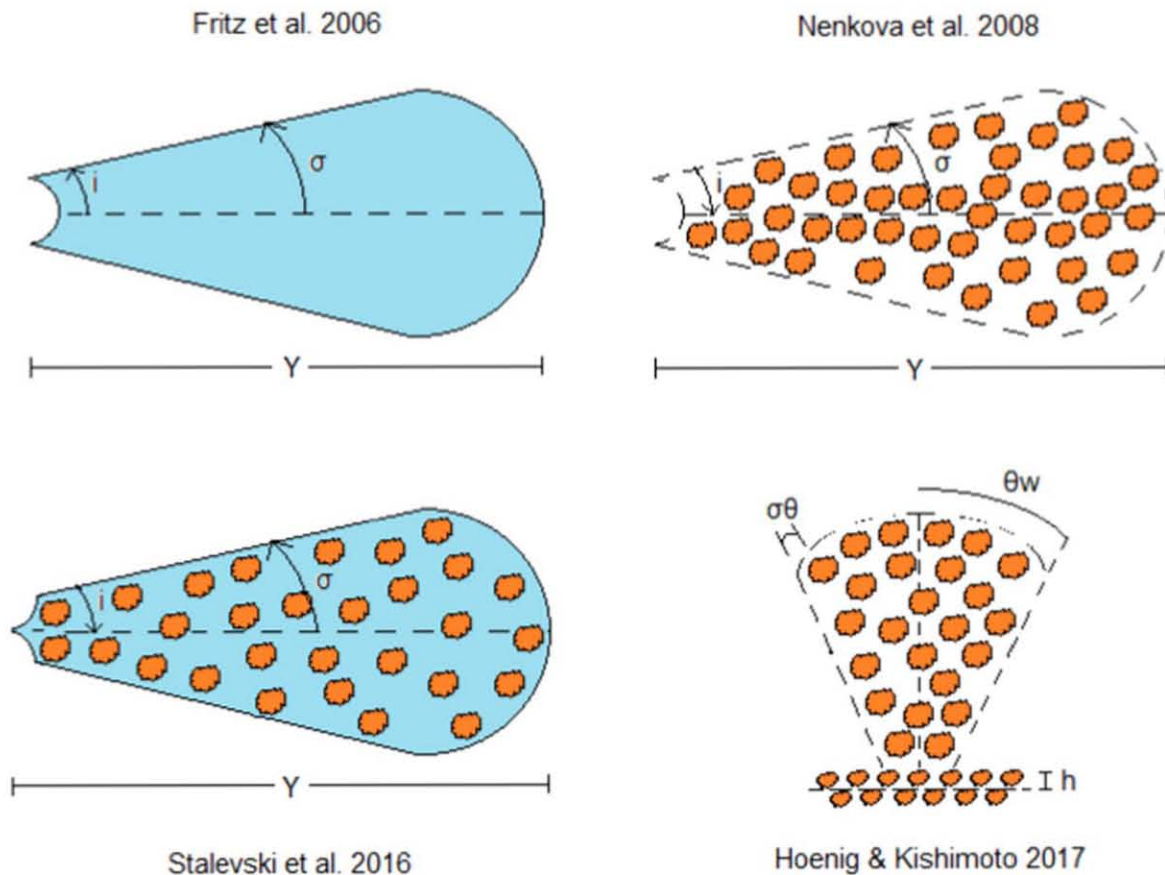


Figure 9. Illustration of the dust models described in Section 2: the smooth torus model by Fritz et al. (2006) (top left), the clumpy torus model by Nenkova et al. (2008b) (top right), the two-phase torus model by Stalevski et al. (2016) (bottom left), and the clumpy disk and outflow model by Hönig & Kishimoto (2017) (bottom right).

Appendix B Models' Parameters

In order to reproduce the SED of NGC 1068, we test the four dust models described in Section 2. Our best fit assuming that a single SED of the models is able to reproduce the N and Q bands at the same time is shown in Tables 5–8 (Column 2). In all cases, many of the parameters are not well restricted. We also show the goodness of the fit throughout the χ^2/dof . Tables 5–8 (Column 3 onward) show the best fits obtained by unlinking one parameter in the Q band. The smooth torus

model by Fritz et al. (2006) restricts all parameters by untying the optical depth at $9.7 \mu\text{m}$, $\tau_{9.7 \mu\text{m}}$. The clumpy torus model by Nenkova et al. (2008b), the two-phase model by Stalevski et al. (2016), and the clumpy disk and outflow model by Hönig & Kishimoto (2017) do not restrict all the parameters well in any case. Finally, Table 9, shows the best fits for the two-phase model by Stalevski et al. (2016) untying the half-opening angle with the other parameters. The table with the results for the smooth torus model by Fritz et al. (2006) untying two parameters is shown in Section 3.2.

Table 5
Fitting Results of the N - and Q -band Spectra to the Smooth Torus Model by Fritz et al. (2006)

Param	Linking Parameters	Band	Unlinking					
			i	σ	γ	β	Y	τ
i	>0.01	N	22.5 ± 0.2	$60.16 \pm_{1.32}^{1.07}$	$49.15 \pm_{10.1}^3$	>0.01	$34.76 \pm_{1.5}^{0.6}$	$1.13 \pm_{0.48}^{0.58}$
		Q	>0.01
σ	>20	N	>20	>20	>20	>20	$23.94 \pm_{2.23}^{2.33}$	$57.63 \pm_{2.23}^{0.8}$
		Q	...	$58.5 \pm_{0.42}^{0.7}$
γ	$1.998 \pm_{0.006}^{0.004}$	N	3.99 ± 0.004	>0.01	>0.01	$1.99 \pm_{0.16}^{0.04}$	$2.0 \pm_{0.06}^{0.01}$	$2.0 \pm_{0.09}^{0.02}$
		Q	$5.42 \pm_{0.12}^{0.04}$
β	-1.0	N	-1.0	-1.0	-1.0	-0.01	-1.0	-0.78 ± 0.01
		Q	-0.9 ± 0.02
Y	>10	N	>10	>10	$59.93 \pm_{1.28}^{1.53}$	>10	>10	$12.64 \pm_{0.31}^{0.27}$
		Q	>10	...
$\tau_{9.7 \mu\text{m}}$	$2.82 \pm_{0.01}^{0.03}$	N	<10	$1.99 \pm_{0.05}^{0.03}$	$1.73 \pm_{0.02}^{0.04}$	2.0	$5.28 \pm_{1.85}^{0.1}$	$2.0 \pm_{0.01}^{0.02}$
		Q	0.3 ± 0.01
χ^2/dof	1293.66/260		560.78/259	95.7/259	106.7/259	138.26/259	96.67/259	207.13/259

Note. Column 1: symbol of the parameter (see Table 1). Column 2: using a single SED by linking for the parameters in the N and Q bands. Columns 3–9: unlinking one of the parameters in the Q band with respect to those of the N band. The χ^2/dof value for each fit is shown in the bottom row.

Table 6
Same as in Table 5 for the Clumpy Torus Model by Nenkova et al. (2008b)

Param	Linking Parameters	Band	Unlinking					
			i	N_0	σ	Y	q	τ
i	>0.01	N	>0.01	>0.01	>0.01	>0.01	>0.01	>0.01
		Q	>0.01
N_0	<15	N	<15	<15	<15	<15	<15	<15
		Q	...	$5.87 \pm_{0.03}^{0.08}$
σ	<70	N	$56.44 \pm_{0.78}^{0.25}$	$65.07 \pm_{0.54}^{0.11}$	$64.86 \pm_{0.67}^{0.23}$	<70	<70	$64.92 \pm_{0.22}^{0.2}$
		Q	$32.5 \pm_{0.4}^{0.2}$
Y	<100	N	<100	<100	<100	<100	<100	<100
		Q	<100
q	$1.84 \pm_{0.03}^{0.04}$	N	$0.52 \pm_{0.03}^{0.07}$	$0.57 \pm_{0.04}^{0.11}$	$0.58 \pm_{0.06}^{0.05}$	$1.83 \pm_{0.03}^{0.04}$	$0.5 \pm_{0.04}^{0.01}$	1.32 ± 0.04
		Q	< 2.5	...
τ_V	>10	N	20.0 ± 0.02	$20.0 \pm_{0.05}^{0.01}$	19.99 ± 0.3	>10	$13.48 \pm_{0.18}^{0.19}$	20.0 ± 0.02
		Q	>10
χ^2/dof	2682.42/260		1655.51/259	1496.7/259	1476.82/259	2682.42/259	1913.35/259	1722.95/259

Table 7
Same as in Table 5 for the Two-phase Torus Model by Stalevski et al. (2016)

Param	Linking Parameters	Band	Unlinking					
			i	σ	p	q	Y	τ
i	>0.01	N	$40.0 \pm_{0.08}^{0.05}$	$88.66 \pm_{0.9}^{0.23}$	>0.01	>0.01	88.84 ± 0.02	89.15 ± 0.02
		Q	> 0.0190
σ	$69.9 \pm_{0.44}^{0.04}$	N	69.99 ± 0.05	$11.69 \pm_{0.04}^{0.07}$	$69.99 \pm_{0.73}^{0.04}$	$53.59 \pm_{0.63}^{0.44}$	< 80	< 80
		Q	...	< 80
p	<1.5	N	<1.5	<1.5	<1.5	<1.5	<1.5	<1.5
		Q	<1.5
q	<1.5	N	<1.5	$0.54 \pm_{0.28}^{0.46}$	<1.5	<1.5	<1.5	<1.5
		Q	<1.5
Y	<30	N	<30	<30	<30	<30	<30	<30
		Q	<30	...
$\tau_{9.7 \mu\text{m}}$	5.0	N	<11	<11	5.0	<11	<11	<11
		Q	7.46 ± 0.07
χ^2/dof	3021.44/260		2390.52/259	205.26/259	3021.32/259	1256.69/259	1042.39/259	677.04/259

Table 8
Same as in Table 5 for the Clumpy Disk Plus Outflow Model by Hönic & Kishimoto (2017)

Param	Linking Parameters	Band	Unlinking							
			i	N_0	a	θ	σ	a_w	h	f_{wd}
i	>0.01	N	>0.01	>0.01	>0.01	>0.01	>0.01	>0.01	>0.01	>0.01
		Q	>0.01
N_0	<10	N	<10	7.0 ± 0.01	5.99 ± 0.1	$7.0 \pm_{0.03}^{0.01}$	7.0	<10	$5.44 \pm_{0.05}^{0.04}$	7.0
		Q	...	<10
a	-2.15 ± 0.01	N	-2.15 ± 0.01	-2.07	-2.0	-2.04	-2.0	-2.0	-2.0	-2.0
		Q	$-2.45 \pm_{0.01}^{0.02}$
θ	<15	N	<15	<15	<15	<15	<15	$10.0 \pm_{0.01}^{0.03}$	$10.0 \pm_{0.01}^{0.04}$	<15
		Q	<15
σ	<45	N	<45	<45	<45	<45	<45	<45	<45	<45
		Q	<45
a_w	>-2.5	N	>-2.5	>-2.5	>-2.5	>-2.5	>-2.5	-2.38 ± 0.01	>-2.5	>-2.5
		Q	>-2.5
h	<0.5	N	<0.5	<0.5	<0.5	<0.5	<0.5	<0.5	0.14	<0.5
		Q	<0.5	...
f_{wd}	0.6	N	0.6	0.6	0.6	<0.75	0.71	0.6	0.6	0.69 ± 0.01
		Q	<0.75
χ^2/dof	1138.56/258		1138.51/257	651.11/257	618.99/257	736.4/257	540.26/257	1057.5/257	769.98/257	538.73/257

Table 9
Same as in Table 2 for the Two Phase Torus Model by Stalevski et al. (2016)
When We Unlink Two Parameters between the N and Q bands

Param	Band	Unlinking			
		σ/p	σ/q	σ/Y	σ/τ
i	N	$80.0 \pm_{0.03}^{0.1}$	$80.0 \pm_{0.05}^{0.13}$	$89.17 \pm_{0.07}^{0.03}$	$80.0 \pm_{0.08}^{0.11}$
	Q
σ	N	$19.0 \pm_{0.85}^{1.35}$	$19.25 \pm_{0.16}^{0.28}$	$10.67 \pm_{0.03}^{0.08}$	$18.53 \pm_{0.13}^{0.45}$
	Q	11.8	$11.99 \pm_{0.09}^{0.16}$	10.0	11.59 ± 0.1
p	N	<1.5	<1.5	<1.5	<1.5
	Q	<1.5
q	N	<1.5	<1.5	<1.2	<1.5
	Q	...	<1.5
Y	N	<30	<30	<30	<30
	Q	<30	...
τ	N	$3.93 \pm_{0.04}^{0.11}$	$3.9 \pm_{0.04}^{0.13}$	<11	$4.04 \pm_{0.04}^{0.14}$
	Q	<11
χ^2/dof		207.14/258	184.63/258	145.01/258	174.9/258

Appendix C The Bayes Factor

In order to evaluate to what extent a model is better than another one we calculate the Bayes factor through the Akaike information criterion, AIC_c . To this end, we use Equation (5) in Emmanoulopoulos et al. (2016) to calculate the AIC_c

$$AIC_c = 2k - 2C_L + \chi^2 + \frac{2k(k+1)}{N-k-1}, \quad (2)$$

where C_L is the constant likelihood of the true hypothetical model, k is the number of free model parameters, and N is the number of data points.

We then calculate the difference between two different models, $\Delta[AIC_c]$

$$\Delta[AIC_c] = AIC_{c,2} - AIC_{c,1}. \quad (3)$$

Finally, we estimate the evidence ratio, ϵ

$$\epsilon = e^{-\frac{\Delta[AIC_c]}{2}}. \quad (4)$$

The evidence ratio or Bayes factor, is a measure of the relative likelihood of one versus other model. When the Bayes factor is ≤ 0.01 , the first model is more likely to be the *correct* model. When the Bayes factor is ≥ 100 the second model is more likely to be the correct model.

Appendix D Graphite/Silicate Fraction

Several of the AGN dust models (e.g., Hönic & Kishimoto 2010) rely on composition constants derived by Mathis et al. (1977) for the ISM. In particular, the normalization with respect to hydrogen abundance is $\log(A) = -15.24$ and -15.21 for graphite and silicate grains, respectively (i.e., 51.7% of silicate). However, Draine & Lee (1984) updated these numbers to $\log(A) = -25.11$ and -25.16 for silicate and graphite, respectively (i.e., 52.9% of silicate). This is the composition assumed by the smooth torus model by Fritz et al. (2006). Weingartner & Draine (2001) also gave the same abundance for the silicate but a different number for graphite with $\log(A) = -25.13$ (i.e., 52.4% of silicate). This is the assumed normalization factors in the two-phase torus model presented by Stalevski et al. (2016). This fraction might have an impact on the results. In Section 3 we used ratios of 49% and 51% for graphite and silicate grains, respectively. However, this is further explored in this section. We create a grid covering a range percentages of silicates, $f_{\text{sil}} = [30, 40,$

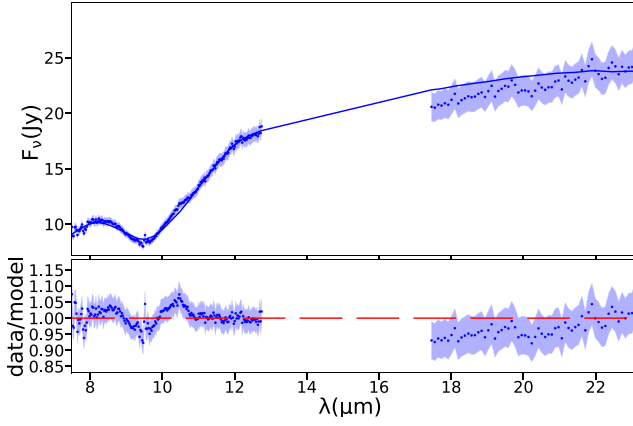


Figure 10. Best model exploring for different graphite/silicate ratios (see Appendix D). The description in this figure is the same as that reported in Figure 4.

45%–55%, 60%, and 70%]. Note that in this grid, we do not include the previously used ratios of particles (49% and 51% for graphite and silicate grains, respectively). We obtained the best fit with $\chi_r^2 = 0.51$ for 51% of graphite and 49% of silicates. This fit has a Bayes factor of 4×10^{-7} compared to the best fit obtained in Section 4.3. Figure 10 shows the best fit obtained with 51% graphite and 49% silicate.

Appendix E Inner Radius of the Torus

We explored the scenario when the inner radius of the largest torus is different from that of the smallest torus. We initially kept the inner radius of the smallest torus fixed to 0.2 pc and we tested a range of values of the largest torus: $R_{\text{in},2} = [0.1, 0.2, 0.3, 0.4, 0.5, 0.6]$ pc. The other parameters are fixed to the best values obtained in Section 4.3. The grid has 2376 SEDs and the best fit was obtained with $\chi_r^2 = 1.06$ for $R_{\text{in},2} = 0.1$ pc, with an inclination angle of $i = 61^\circ$ and $A_v = 5$ magnitudes. This fit has a Bayes factor of 3.9×10^{-39} compared to the best fit in Section 4.3. Figure 11 (top-left panel) shows this result.

Graphite grains can sustain higher temperatures than silicate grains, with the former being able to heat up to ~ 1900 – 2000 K and the latter sublimating at ~ 800 – 1200 K, depending on density (García-González et al. 2017, and references therein). This implies a different sublimation radius for the graphite compared to silicate grains. In order to explore this, we create a complex system of tori, composed by two tori for graphite and two tori for silicate grains. All the parameters are the same, changing the sublimation radius for each kind of particle. For this, we made two grids of SEDs; first, we assume sublimation temperatures of 1500 and 1000 K for graphite and silicate, respectively (i.e., the sublimation radii for graphite and silicate grains at 0.4 and 1.2 pc, respectively). However, this fit is not

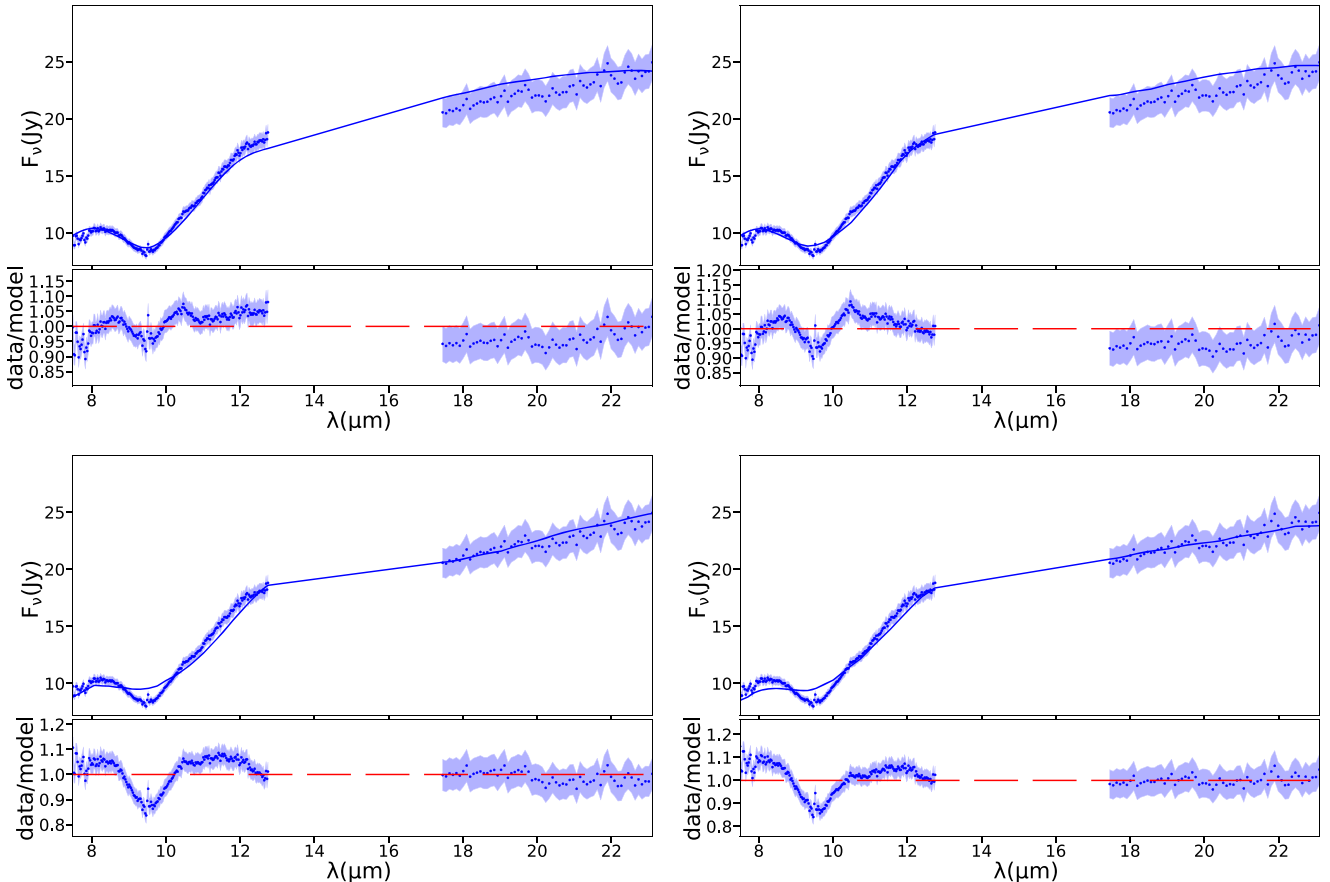


Figure 11. (Top left) Best model obtained when we test for different inner radius for the largest torus. (Top right) Best fit obtained from the model with a reshaped inner wall of the torus. (Bottom) Best fit when we consider different sublimation temperature for graphite and silicate using $T(\text{graphite}) = 1500$ K and $T(\text{silicate}) = 1000$ K (left) and $T(\text{graphite}) = 2000$ K and $T(\text{silicate}) = 1500$ K (right). The description in this figure is the same as that reported in Figure 4.

satisfactory ($\chi_r^2 = 2.38$), with $i = 64^\circ$ and $A_V = 0$ mag. Then, we assume sublimation temperatures of 2000 and 1500 K for graphite and silicate, respectively (i.e., the sublimation radius for graphite and silicate was set to 0.17 and 0.4 pc, respectively). However, this fit is not statistically acceptable with $\chi_r^2 = 2.48$, with $i = 62^\circ$ and $A_V = 0$ mag. These SEDs have Bayes factors of 5.9×10^{-116} and 9×10^{-122} compared to the best fit in Section 4.3, respectively. Figure 11 (bottom panels) shows these two fits. While they are quite good at reproducing the slope between the N and Q bands, they fail to reproduce the $10 \mu\text{m}$ silicate feature.

Finally, the inner region of the torus might be reshaped to account for this anisotropic irradiation by the accretion disk, with the strongest emission perpendicular to the disk and none in the equatorial plane (Stalevski et al. 2016). In this case, the incident flux is a function of the distance and the polar angle. In order to explore this, we used the anisotropic disk emission by Netzer (1987), where the flux as a function of the polar angle Θ is (see also Netzer 2013):

$$F_{\text{AGN}} = (1/3)\cos\theta(1 + 2\cos\theta). \quad (5)$$

In this case, the sublimation radius is

$$R_d(\theta) = (0.4)L_{45}(\theta)^{1/2}T_{\text{sub}1500\text{pc}}^{-2.6}\text{pc}, \quad (6)$$

where $L_{45}(\theta) = [s + (1 - s)(1/3)\cos\theta(1 + 2\cos\theta)]L_{\text{bol}45}$, where $L_{\text{bol}45}$ is the AGN luminosity in units of 10^{45}erg/s^{-1} and s is the softening factor introduced to prevent the inner dust radius from reaching zero at the equatorial plane ($s = 1$ recovers the isotropic scenario).

We created a new grid including 48 SEDs with a range of inner radii of $R_{\text{in}} = [0.2, 0.3, 0.4, 0.5, 0.6, 0.7, 1.0]$ pc, and a cutoff radius at half of the R_{in} (i.e., $R_{\text{cutoff}} = [0.1, 0.15, 0.2, 0.25, 0.3, 0.35, 0.5]$ pc). We have obtained that the best fit shows $\chi_r^2 = 1.14$ for $R_{\text{in}} = 0.5$ pc and $R_{\text{cutoff}} = 0.25$ pc, with an inclination angle of 68° and extinction of 0 magnitudes (see Figure 11, top-right panel). The reshaping of the inner radius of the torus is not an improvement compared to those SEDs obtained without taking this effect into account. Indeed, the model shown in Section 4.3 without reshaping has a Bayes factor of 1.1×10^{43} compared to this fit.

Appendix F Nonconcentric Tori

In order to test the scenario in which the two components found through our analysis are associated with two different AGN (according to recent literature, see the Discussion section), we produced new synthetic SEDs for two nonconcentric tori, with the same parameters obtained in our final best model but considering each torus hosts an AGN. For simplicity, we assume that the luminosity of each AGN is half of the total luminosity of NGC 1068. We explored several distances between the two AGN, from 0.1–25 pc (11 steps), where the radiation from both AGNs reaches both tori, and from 30–40 pc (six steps), where each AGN affects only one of the tori. We also explore the resulting SED when the separation occurs along the height or along the width of the torus. Our best model shows a statistic of $\chi_r^2 = 0.63$ with an offset of 10 pc between each AGN, a viewing angle of 90° and a foreground extinction of $A_V = 3$ mag. This fit has a Bayes factor of 4.1×10^{-14} compared to the best fit in Section 4.3. Figure 12

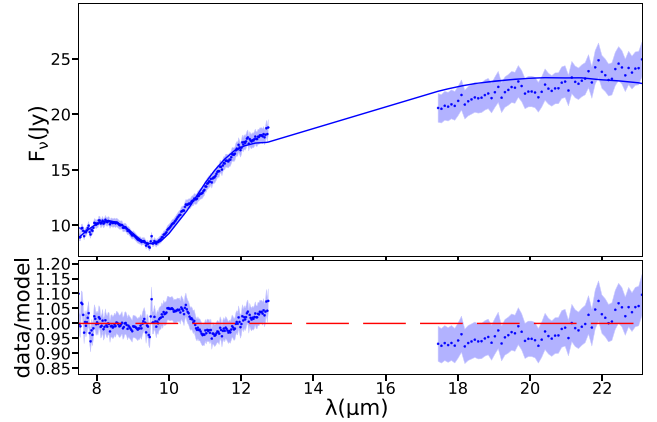


Figure 12. Best model obtained when we test for two nonconcentric tori (see Appendix F). The description in this figure is the same as that reported in Figure 4.

shows the resulting SED with these two nonconcentric tori. Although the fit is quite good, in particular around the silicate absorption feature at $10 \mu\text{m}$, it is not better than that provided by the two concentric torus, discussed in the main body of this paper.

ORCID iDs

César Ivan Victoria-Ceballos  <https://orcid.org/0000-0001-5625-7815>
 Omaira González-Martín  <https://orcid.org/0000-0002-2356-8358>
 Jacopo Fritz  <https://orcid.org/0000-0002-7042-1965>
 Cristina Ramos Almeida  <https://orcid.org/0000-0001-8353-649X>
 Enrique López-Rodríguez  <https://orcid.org/0000-0001-5357-6538>
 Santiago García-Burillo  <https://orcid.org/0000-0003-0444-6897>
 Almudena Alonso-Herrero  <https://orcid.org/0000-0001-6794-2519>
 Mariela Martínez-Paredes  <https://orcid.org/0000-0002-0088-0103>
 Donaji Esparza-Arredondo  <https://orcid.org/0000-0001-8042-9867>
 Natalia Osorio-Clavijo  <https://orcid.org/0000-0002-3467-8077>

References

- Absil, O., Defrère, D., Coudé du Foresto, V., et al. 2013, *A&A*, **555**, A104
 Alonso-Herrero, A., Ramos Almeida, C., Mason, R., et al. 2011, *ApJ*, **736**, 82
 Antonucci, R. 1993, *ARA&A*, **31**, 473
 Antonucci, R. R. J., & Miller, J. S. 1985, *ApJ*, **297**, 621
 Arnaud, K. A. 1996, in ASP Conf Ser. 101, *Astronomical Data Analysis Software and Systems V*, ed. G. H. Jacoby & J. Barnes (San Francisco, CA: ASP), 17
 Asmus, D. 2019, *MNRAS*, **489**, 2177
 Baes, M., Davies, J. I., Dejonghe, H., et al. 2003, *MNRAS*, **343**, 1081
 Baes, M., Verstappen, J., De Looze, I., et al. 2011, *ApJS*, **196**, 22
 Bauer, F. E., Arévalo, P., Walton, D. J., et al. 2015, *ApJ*, **812**, 116
 Bland-Hawthorn, J., Gallimore, J. F., Tacconi, L. J., et al. 1997, *Ap&SS*, **248**, 9
 Bock, J. J., Neugebauer, G., Matthews, K., et al. 2000, *AJ*, **120**, 2904
 Calvet, N., D’Alessio, P., Hartmann, L., et al. 2002, *ApJ*, **568**, 1008
 Calzetti, D., Armus, L., Bohlin, R. C., et al. 2000, *ApJ*, **533**, 682
 Cameron, M., Storey, J. W. V., Rotaciuc, V., et al. 1993, *ApJ*, **419**, 136
 Das, V., Crenshaw, D. M., Kraemer, S. B., et al. 2006, *AJ*, **132**, 620

- Draine, B. T., & Lee, H. M. 1984, *ApJ*, **285**, 89
- Efstathiou, A., & Rowan-Robinson, M. 1995, *MNRAS*, **273**, 649
- Emmanoulopoulos, D., Papadakis, I. E., Eftipopoulos, A., et al. 2016, *MNRAS*, **461**, 1642
- Esparza-Arredondo, D., González-Martín, O., Dultzin, D., et al. 2019, *ApJ*, **886**, 125
- Esparza Arredondo, D., González Martín, O., Dultzin, D., et al. 2021, *A&A*, **651**, A91
- Feltre, A., Hatziminaoglou, E., Fritz, J., et al. 2012, *MNRAS*, **426**, L20
- Fritz, J., Franceschini, A., & Hatziminaoglou, E. 2006, *MNRAS*, **366**, 767
- Gamez Rosas, V., Isbell, J. W., Jaffe, W., et al. 2021, arXiv:2112.13694
- García-Bernete, I., Ramos Almeida, C., Alonso-Herrero, A., et al. 2019, *MNRAS*, **486**, 4917
- García-Burillo, S., Alonso-Herrero, A., Ramos Almeida, C., et al. 2021, *A&A*, **652**, A98
- García-Burillo, S., Combes, F., Ramos Almeida, C., et al. 2016, *ApJL*, **823**, L12
- García-Burillo, S., Combes, F., Ramos Almeida, C., et al. 2019, *A&A*, **632**, A61
- García-González, J., Alonso-Herrero, A., Hönig, S. F., et al. 2017, *MNRAS*, **470**, 2578
- González-Martín, O., Masegosa, J., García-Bernete, I., et al. 2019a, *ApJ*, **884**, 10
- González-Martín, O., Masegosa, J., García-Bernete, I., et al. 2019b, *ApJ*, **884**, 11
- González-Martín, O., Rodríguez-Espinosa, J. M., Díaz-Santos, T., et al. 2013, *A&A*, **553**, A35
- Granato, G. L., & Danese, L. 1994, *MNRAS*, **268**, 235
- Gratadour, D., Rouan, D., Grosset, L., et al. 2015, *A&A*, **581**, L8
- Gravity Collaboration, Pfuhl, O., Davies, R., et al. 2020, *A&A*, **634**, A1
- Greenhill, L. J., & Gwinn, C. R. 1997, *Ap&SS*, **248**, 261
- Harris, C. R., Millman, K. J., van der Walt, S. J., et al. 2020, *Natur*, **585**, 357
- Hönig, S. F., & Kishimoto, M. 2010, *A&A*, **523**, A27
- Hönig, S. F., Kishimoto, M., Tristram, K. R. W., et al. 2013, *ApJ*, **771**, 87
- Hönig, S. F., & Kishimoto, M. 2017, *ApJL*, **838**, L20
- Hunter, J. D. 2007, *CSE*, **9**, 90
- Imanishi, M., Nakanishi, K., Izumi, T., et al. 2018, *ApJL*, **853**, L25
- Impellizzeri, C. M. V., Gallimore, J. F., Baum, S. A., et al. 2019, *ApJL*, **884**, L28
- Jaffe, W., Meisenheimer, K., Röttgering, H. J. A., et al. 2004, *Natur*, **429**, 47
- Kishimoto, M., Hönig, S. F., Beckert, T., et al. 2007, *A&A*, **476**, 713
- Kobayashi, H., Kimura, H., Watanabe, S.-I., et al. 2011, *EP&S*, **63**, 1067
- Li, A., & Draine, B. T. 2001, *ApJ*, **554**, 778
- Liu, J., Hönig, S. F., Ricci, C., et al. 2019, *MNRAS*, **490**, 4344
- Liu, J., Liu, Y., Li, X., et al. 2016, *MNRAS*, **459**, L100
- López-Gonzaga, N., Jaffe, W., Burtscher, L., et al. 2014, *A&A*, **565**, A71
- Lopez-Rodriguez, E., Alonso-Herrero, A., García-Burillo, S., et al. 2020, *ApJ*, **893**, 33
- Lopez-Rodriguez, E., Fuller, L., Alonso-Herrero, A., et al. 2018, *ApJ*, **859**, 99
- Lyu, J., Hao, L., & Li, A. 2014, *ApJL*, **792**, L9
- Martínez-Paredes, M., González-Martín, O., Esparza-Arredondo, D., et al. 2020, *ApJ*, **890**, 152
- Mason, R. E., Geballe, T. R., Packham, C., et al. 2006, *ApJ*, **640**, 612
- Mathis, J. S., Rimpl, W., & Nordsieck, K. H. 1977, *ApJ*, **217**, 425
- Miller, J. S., & Antonucci, R. R. J. 1983, *ApJL*, **271**, L7
- Min, M., Hovenier, J. W., & de Koter, A. 2003, *A&A*, **404**, 35
- Min, M., Waters, L. B. F. M., de Koter, A., et al. 2007, *A&A*, **462**, 667
- NASA High Energy Astrophysics Science Archive Research Center (HEASARC) 2014, HEASoft: Unified Release of FTOOLS and XANADU, Astrophysics Source Code Library, ascl:1408.004
- Nenkova, M., Sirocky, M. M., Ivezić, Ž., & Elitzur, M. 2008a, *ApJ*, **685**, 147
- Nenkova, M., Sirocky, M. M., Nikutta, R., Ivezić, Ž., & Elitzur, M. 2008b, *ApJ*, **685**, 160
- Netzer, H. 1987, *MNRAS*, **225**, 55
- Netzer, H. 2013, in *The Physics and Evolution of Active Galactic Nuclei*, 2013, ed. H. Netzer (Cambridge: Cambridge Univ. Press)
- Nikutta, R., Elitzur, M., & Lacy, M. 2009, *ApJ*, **707**, 1550
- Oliphant, T. E. 2007, *CSE*, **9**, 10
- Olofsson, J., Augereau, J.-C., van Dishoeck, E. F., et al. 2009, *A&A*, **507**, 327
- Pasetto, A., González-Martín, O., Esparza-Arredondo, D., et al. 2019, *ApJ*, **872**, 69
- Pérez, L. M., Carpenter, J. M., Chandler, C. J., et al. 2012, *ApJL*, **760**, L17
- Pier, E. A., & Krolik, J. H. 1992, *ApJ*, **401**, 99
- Raban, D., Jaffe, W., Röttgering, H., et al. 2009, *MNRAS*, **394**, 1325
- Ramos Almeida, C., Alonso-Herrero, A., Levenson, N. A., et al. 2014, *MNRAS*, **439**, 3847
- Ramos Almeida, C., Levenson, N. A., Alonso-Herrero, A., et al. 2011, *ApJ*, **731**, 92
- Ramos Almeida, C., Levenson, N. A., Rodríguez Espinosa, J. M., et al. 2009, *ApJ*, **702**, 1127
- Ramos Almeida, C., & Ricci, C. 2017, *NatAs*, **1**, 679
- Schartmann, M., Meisenheimer, K., Camenzind, M., et al. 2005, *A&A*, **437**, 861
- Shao, Z., Jiang, B. W., & Li, A. 2017, *ApJ*, **840**, 27
- Siebenmorgen, R., Heymann, F., & Efstathiou, A. 2015, *A&A*, **583**, A120
- Stalevski, M., Fritz, J., Baes, M., et al. 2012, *MNRAS*, **420**, 2756
- Stalevski, M., Ricci, C., Ueda, Y., et al. 2016, *MNRAS*, **458**, 2288
- Stalevski, M., Tristram, K. R. W., & Asmus, D. 2019, *MNRAS*, **484**, 3334
- Testi, L., Natta, A., Shepherd, D. S., et al. 2001, *ApJ*, **554**, 1087
- Tomono, D., Doi, Y., Usuda, T., et al. 2001, *ApJ*, **557**, 637
- Urry, C. M., & Padovani, P. 1995, *PASP*, **107**, 803
- van Bemmell, I. M., & Dullemond, C. P. 2003, *A&A*, **404**, 1
- Virtanen, P., Gommers, R., Oliphant, T. E., et al. 2020, *NatMe*, **17**, 261
- Wada, K. 2012, *ApJ*, **758**, 66
- Wang, J.-M., Songsheng, Y.-Y., Li, Y.-R., et al. 2020, *MNRAS*, **497**, 1020
- Weingartner, J. C., & Draine, B. T. 2001, *ApJ*, **548**, 296
- Wittkowski, M., Kervella, P., Arsenault, R., et al. 2004, *A&A*, **418**, L39

CHAPTER 3

X-RAY REFLECTION AT HARD ENERGIES

In this chapter we investigate the reflection medium of the primary radiation in the type-1 AGN. For this study, we select a sample of 22 type-1 AGN with available simultaneous observations of *XMM-Newton* and *NuSTAR* telescopes. The combination of both satellites allow us to perform a study covering a broad spectral range, from 3 to 70 keV, where it is expected to detect the reflection features. We select the sample according to two criteria. First, we consider simultaneous observations in order to **for** account the high X-ray variability of the sources. Second, we select those sources with the longest exposure time, in order to have the best quality data.

For our study, we consider three different reflection scenarios: i) neutral/distant material, associated with the torus, ii) ionized gas, associated with the BLR, iii) relativistic/ionized plasma, associated with the accretion disk. We test these scenarios in the sample through using different available models. In a first step we consider a total of nine different models, and test it a sub-sample of five objects. For reflection in an ionized medium such as the accretion disk or the BLR we contemplate four models: (1) *pexriv* (Magdziarz & Zdziarski, 1995), (2) *reflionx* (Ross et al., 1999; Ross & Fabian, 2005), (3) *relxill* (Dauser et al., 2010; García et al., 2014), and (4) *refsch* (Fabian et al., 1989; Magdziarz & Zdziarski, 1995). We also use the convolution model *kdblur* in order to account for the relativistic effects when it is needed. For the reflection in an neutral/distant

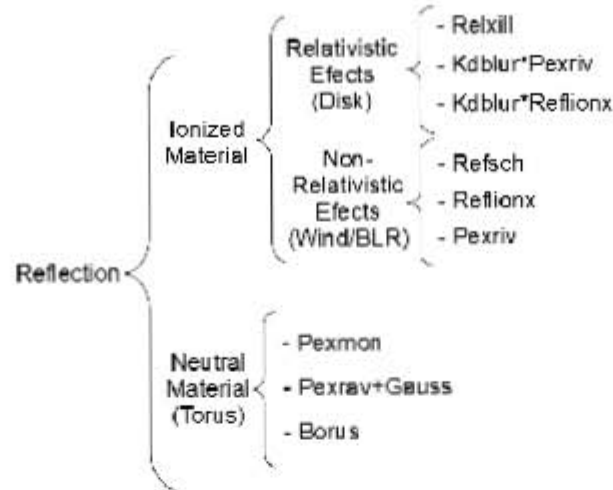


Figure 3.1: Scheme of reflection models used in this work. Each group of three models corresponds to a different physical scenario (neutral or ionized material, which corresponds to the torus, the accretion disk or the BLR), and each model in the same group represents the same scenario. A detailed description of each model can be seen in the article presented in this chapter.

medium such as the torus we use three models: (1) *pexmon* (Nandra et al., 2007), (2) *pexrav* (Magdziarz & Zdziarski, 1995), and (3) *borus02* (Baloković et al., 2018). For the *pexrav* model, we also add a Gaussian line component in order to account for the FeK α emission line feature. We named this model *pexrav + gauss*. We show in Figure 3.1 a scheme of the nine reflection models mentioned above. We find that two of the nine models give the best results: a model of relativistic/ionized reflection (*relxill* DAUSER ET AL., 2010; GARCÍA ET AL., 2014) and a model of neutral/distant reflection (*pexrav + gauss* MAGDZIARZ & ZDZIARSKI, 1995).

In a second step, we test these two models in the full sample, and also, we consider a third model, which is a combination of both scenarios, i.e., relativistic/ionized plus neutral/distant reflection, called *hybrid* model.

The main results of our study are: 1) We find that 18 sources shows evidence of the reflection. Among them, 12 objects prefer a hybrid reflection model, which incorporates neutral and relativistic ionized medium; one object is best modelled by a neutral reflection model; two objects prefer a relativistic ionized reflection model; and three objects equally prefer the neutral and relativistic ionized reflection models. 2) We find that four objects

do not present the reflection component. We propose the variability of activity of sources as a possible explanation. 3) For most objects, the intrinsic luminosity represents between 80% and 100% of the total luminosity. The neutral reflection component has the smallest contribution to the total luminosity, representing this with less than 10%. The ionized reflection component contributes over 10% for almost all objects.

Author disclosure:

The completion of this work was carried out mainly by my authorship with the main supervision of Dr. Omaira González Martín along the data analysis and interpretation of results. The other co-authors contributed by suggesting modifications and corrections to the written manuscript. This work was accepted on July 12, 2023 and published on August 25, 2023 in The Astrophysical Journal.

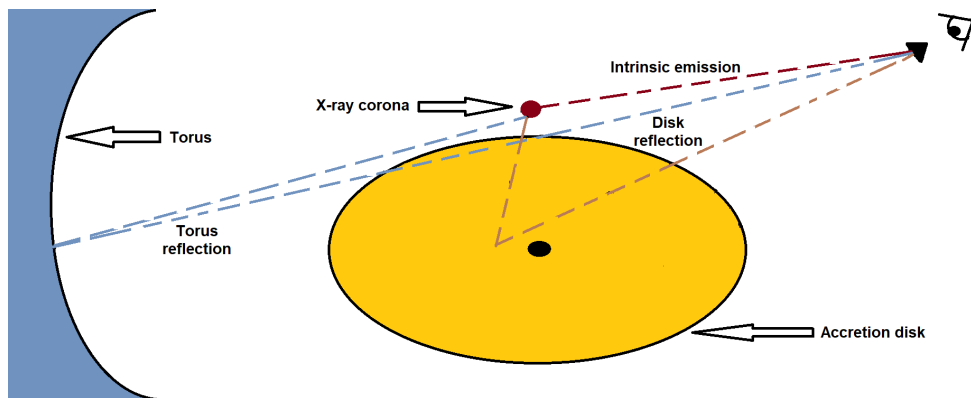






Figure 3.2: Sketch of the reflection scenario preferred by the sample, which considers the intrinsic emission from the corona and reflection due to the accretion disk and the torus. Note that the inclination of the accretion disk with respect to the line of sight may not completely correspond to a type-1 AGN, however it is oriented this way for illustrative purposes.



Testing Physical Scenarios for the Reflection Features of Type-1 AGNs using XMM-Newton and NuSTAR Simultaneous Observations

César Ivan Victoria-Ceballos¹ , Omaira González-Martín¹ , Josefa Masegosa², Anna Lia Longinotti³ ,
Donaji Esparza-Arredondo^{4,5}, and Natalia Osorio-Clavijo¹ 

¹ Instituto de Radioastronomía y Astrofísica (IRyA-UNAM), 3-72 (Xangari), 8701, Morelia, Mexico; c.victoria@irya.unam.mx

² Instituto de Astrofísica de Andalucía (IAA-CSIC), Glorieta de la Astronomía s/n E-18008, Granada, Spain

³ Instituto de Astronomía, (IA-UNAM), Circuito Exterior, Ciudad Universitaria, Ciudad de México 04510, Mexico

⁴ Instituto de Astrofísica de Canarias, Calle Vía Láctea, s/n, E-38205 La Laguna, Tenerife, Spain

⁵ Departamento de Astrofísica, Universidad de La Laguna, E-38206 La Laguna, Tenerife, Spain

Received 2023 February 17; revised 2023 July 3; accepted 2023 July 12; published 2023 August 25

Abstract

Above ~ 3 keV, the X-ray spectrum of active galactic nuclei (AGNs) is characterized by the intrinsic continuum and Compton reflection features. For type-1 AGNs, several regions may contribute to the reflection. To investigate the nature of the reflecting medium, we perform a systematic analysis of the reflector using XMM-Newton and Nuclear Spectroscopic Telescope Array observations of a sample of 22 type-1 AGNs. We create a baseline model that includes Galactic absorption and an intrinsically absorbed power law, plus a reflection model. We test a set of nine reflection models in a subsample of five objects. Based on these results, we select three models to be tested on the entire sample, accounting for distinct physical scenarios: neutral/distant reflection, ionized/relativistic reflection, and neutral/distant+ionized/relativistic reflection, namely, a hybrid model. We find that 18 sources require the reflection component to fit their spectra. Among them, 67% prefer the hybrid model. Neutral and ionized models are equally preferred by three sources. We conclude that both the neutral/distant reflector most probably associated with the inner edges of the torus and the ionized/relativistic reflector associated with the accretion disk are required to describe the reflection in type-1 AGNs.

Unified Astronomy Thesaurus concepts: X-ray active galactic nuclei (2035)

1. Introduction

The typical X-ray spectrum above ~ 3 keV of active galactic nuclei (AGNs) is composed by the intrinsic continuum and reflection features. The primary X-ray emission originates in the corona of relativistic electrons close to a supermassive black hole (SMBH), where UV and optical photons from the accretion disk are Compton upscattered (Haardt & Maraschi 1993). Pounds et al. (1990) find that the intrinsic continuum can be modeled with a power law as a function of the photon energy of photon index $\Gamma \sim 1.9$. Zdziarski et al. (1995) find that this power-law continuum has an exponential cutoff of the order of several hundred keV.

X-ray photons in the corona are emitted in all directions, and they can reach and be reflected by the surrounding medium, such the accretion disk, the broad-line region (BLR), and/or the torus (Matsuoka et al. 1990). Some distinctive features can be observed in the X-ray spectra when the X-ray photons are reflected by one or more of these components. Such features are a hump-like continuum peaking at ~ 30 keV, which is a product of the electron down scattering of high-energy photons and photoelectric absorption of low-energy photons, and several fluorescent emission lines, most notably the FeK α emission line at 6.4 keV (George & Fabian 1991).

The reflecting medium may arise from several AGN components around the SMBH. The resulting reflection features depend on the dynamical, geometrical, and chemical properties. For instance, the accretion disk and the BLR are the

closest regions to the SMBH and are composed of ionized gas, while the obscuring torus, which is much more distant from the SMBH, is composed of neutral gas. When the FeK α line originates from neutral material, it is observed with a narrow profile. However, it can be broad and blurred by relativistic effects when it is emitted close to the SMBH (Laor 1991).

Different origins have been proposed to explain the hard X-ray spectrum of AGNs, among which are relativistic reflection and distant reflectors (Nardini et al. 2011; Patrick et al. 2011; Mehdipour et al. 2015). Similarly, several models have been used throughout the fitting of the spectral energy distribution of AGNs. For instance, PEXRAV (Magdziarz & Zdziarski 1995) assumes optically thick cold material distributed in a slab, RELXILL (Dauser et al. 2010; García et al. 2014) models irradiation of accretion by a broken power-law emissivity, and REFLIONX (Ross et al. 1999; Ross & Fabian 2005) assumes an optically thick atmosphere and adds fluorescence lines.

Given that the reflection features in the X-ray spectrum of AGNs are present in a wide range, the best way to study the nature of the reflection component is by using high-energy and high-quality observations. The Nuclear Spectroscopic Telescope Array (NuSTAR; Harrison et al. 2013) has an unprecedented sensitivity to hard X-ray photons, while XMM-Newton (Jansen et al. 2001) provides an excellent resolution below 10 keV, and in particular around FeK α emission line. Several authors have exploited the advantages offered by these two telescopes to conduct studies with simultaneous observations to examine the hard X-ray spectrum of various AGNs (e.g., Porquet et al. 2018; Diaz et al. 2020; Liu et al. 2020; Traina et al. 2021; Marchesi et al. 2022).



Original content from this work may be used under the terms of the [Creative Commons Attribution 4.0 licence](https://creativecommons.org/licenses/by/4.0/). Any further distribution of this work must maintain attribution to the author(s) and the title of the work, journal citation and DOI.

While the nature of the Compton reflector is well established for type-2 AGNs, which are mostly dominated by reflection in the distant and cold torus (Brightman & Nandra 2011; Ricci et al. 2015; Marchesi et al. 2018), type-1 AGNs are ideal laboratories to explore the contribution of the disk and BLR to this reflection (Falocco et al. 2014; Panagiotou & Walter 2019).

The aim of this work is to investigate the reflection medium of the primary X-ray radiation in a sample of type-1 AGNs. We used simultaneous observations from XMM-Newton and NuSTAR satellites, covering a spectral range from 3 keV up to ~ 70 keV, in which it is expected to detect the reflection features. This paper is organized as follows. Section 2 describes the sample selection and the data reduction. Section 3 describes the X-ray models that we tested and the fitting procedure. We present our main results and discuss them in Sections 4 and 5, respectively.

2. Sample and Data Reduction

2.1. Sample Selection

We select our sample according two criteria. First, to account for the variability of the sources, we select a sample of AGNs with simultaneous observations of XMM-Newton and NuSTAR. We consider observations that, given the exposure time, overlap even though they started on different days as simultaneous. Our second criterion is that for those sources with two or more simultaneous observations, we select those with the longest exposure time, which allows us to have the best quality data. According to these two criteria, we obtain a sample of 63 AGNs: 26 Sy1–Sy1.8, 20 Sy2, five NLSy1, nine QSOs, two blazars, and one unclassified AGN. Among these sources, the type-1 AGNs are the main target of our investigation, and therefore we discard the Sy2 sources, the blazar objects, the QSOs (because of their high redshift), the radio sources (because of their flat spectra), and the unclassified AGNs. We also discard four NLSy1 and five Seyfert galaxies due to their noisy NuSTAR spectrum. Our final sample contains 22 sources: one NLSy1, 19 Sy1–Sy1.5, and two Sy1.8. Table 1 shows the final list of objects with the observation details of the two observatories.

2.2. Data Reduction

XMM-Newton and NuSTAR data reduction was performed with the XMM-Newton Science Analysis System (SAS)⁶ and the NuSTAR Data Analysis Software (NuSTARDAS)⁷ package, respectively. For XMM-Newton, we use data from the EPIC pn camera (Strüder et al. 2001) because of the higher count rate and lower distortion due to pile-up. We use circular regions with 40'' radii to extract the spectra. The background events were selected from a source-free circular region with 40'' radii on the same CCD as the source. For NuSTAR data, we use 65'' radius circular extraction regions for both source and background spectra. The background region was selected from a region on the same chip that was uncontaminated with source photons.

3. X-Ray Spectral Models and Fitting

3.1. Baseline Model

In general terms, the X-ray spectra of AGNs above ~ 3 keV shows two main components: the intrinsic continuum modeled by a cutoff power law, and the reflection component that can be

associated to an ionized or neutral medium. We create a baseline model considering these features:

$$M = \text{Cte} * \text{Abs}_{\text{Gal}} * (\text{absorber} * \text{intrinsic} + \text{reflection}), \quad (1)$$

where Cte is a multiplicative constant to account for NuSTAR and XMM-Newton cross-calibration issues. Abs_{Gal} accounts for the Galactic absorption (using the NH tool within FTOOLS, which is fixed to the HI maps of Kalberla et al. 2005). Meanwhile, absorber * intrinsic represents the intrinsic continuum absorbed by the material along the LOS to the observer, which we model with a cutoff power law affected by a neutral absorber. The last component in the baseline model accounts for the reflection. Several models are used (see below) depending on the material producing this reflection (geometry and composition). Free and fixed parameters for the reflection component depend on the model used.

Note that if we consider the emission from ionized/relativistic reflection by the accretion disk, then it should be affected by the same column density that affects the intrinsic emission; however, this effect is observed at low energies (below 3 keV). The absorber affecting the ionized reflection will be considered when an analysis of the data below 3 keV is performed.

3.2. Reflection Models

To explore the different reflection possibilities, we consider the physical scenarios shown in Figure 1:

1. *Reflection in an ionized medium.* We contemplate four ionized reflection models to account for the reflection in a medium, such as the accretion disk, wind, or the BLR: (1) PEXRIV (Magdziarz & Zdziarski 1995), (2) REFLIONX (Ross et al. 1999; Ross & Fabian 2005), (3) RELXILL (Dauser et al. 2010; García et al. 2014), and (4) REFSCHE (Fabian et al. 1989; Magdziarz & Zdziarski 1995). We also use the convolution model KDBLUR to account for the relativistic effects when it is needed.
2. *Reflection in a neutral medium.* For the reflection in a neutral/distant medium, such as the molecular torus, we use three models: (1) PEXMON (Nandra et al. 2007), (2) PEXRAV (Magdziarz & Zdziarski 1995), and (3) BORUS02 (Baloković et al. 2018). For the PEXRAV model, we also add a Gaussian line component to account for the FeK α emission line feature. We named this model PEXRAV + GAUSS. Note that PEXRAV and PEXMON models are made by using physical approximations on the geometry, assuming the reflecting medium as a semi-infinite plane-parallel surface. Note also that these models consider the reflection medium to be neutral. It is possible to attribute these characteristics to the torus because it is composed of neutral material and, due to the distance between the X-ray corona and the torus, it is reasonable to think of the torus as a semi-infinite plane-parallel surface, seen from the corona. Several authors have previously used these models to represent the putative torus, among them are Ricci et al. (2011), Brightman & Ueda (2012), Reis et al. (2012), Bauer et al. (2015), Brightman et al. (2015), Laha & Ghosh (2021), Osorio-Clavijo et al. (2022), and Inaba et al. (2022).

Figure 2 shows an example of the spectra produced for each of these nine X-ray reflection models. For all of them, we link

⁶ <https://www.cosmos.esa.int/web/xmm-newton/sas>

⁷ <https://heasarc.gsfc.nasa.gov/docs/nustar/analysis/>

Table 1
Observational Parameters for the Sample

	R.A. J2000.0	Decl. J2000.0	z	Type	XMM-Newton					NuSTAR				
					Obs ID	Obs. date	Exp. (ks)	Counts	Bins	Obs ID	Obs. date	Exp. (ks)	Counts	Bins
(1)	(2)	(3)	(4)	(5)	(6)	(7)	(8)	(9)	(10)	(11)	(12)	(13)	(14)	(15)
Mrk 335	00 06 25.7	+20 13 31	0.035	Sy1.2	0780500301	18-07-11	114.5	6892.7	55	80201001002	18-07-10	82.26	3359.5	138
Fairall 9	01 23 45.3	-58 46 46	0.047	Sy1.2	0741330101	14-05-09	141.4	116551	155	60001130002	14-05-09	49.21	24661.9	352
Mrk 1040	02 28 17.1	+31 20 07	0.011	Sy1.5	0760530301	15-08-15	84.6	106701	466	60101002004	15-08-15	64.24	43260.9	499
Mrk 1044	02 30 07.8	-08 58 13	0.016	Sy1	0824080301	18-08-03	140.7	103577	155	60401005002	18-08-03	267.08	92680.2	560
NGC 1365	03 33 32.5	-36 09 34	0.004	Sy1.8	0692840401	13-01-23	133.62	141235	466	60002046007	13-01-23	73.65	54529	542
Ark 120	05 16 07.0	-00 10 16	0.032	Sy1	0721600401	14-03-22	133.3	211387	466	60001044004	14-03-22	65.45	62593.4	511
Mrk 382	07 55 30.2	+39 12 37	0.027	Sy1	0843020801	19-10-30	34.5	3586.6	69	60501008002	19-10-29	52.36	1934.1	80
NGC 3227	10 23 37.2	19 52 38	0.004	Sy1.5	0782520201	16-11-09	92	71597	466	60202002002	16-11-09	49.8	49452.5	515
NGC 3783	11 39 08.1	-37 43 39	0.011	Sy1	0780860901	16-12-11	115	93018	174	80202006002	16-12-11	25.66	24209	406
NGC 4051	12 03 04.7	+44 33 30	0.003	Sy1.2	0830430201	18-11-07	83.2	48490	699	60401009002	18-11-04	311.14	130991	758
NGC 4151	12 10 43.7	+39 24 06	0.002	Sy1.5	0679780301	12-11-14	12.21	37955	699	60001111005	12-11-14	61.53	393011	1024
Mrk 766	12 18 18.6	+29 48 01	0.013	Sy1.5	0763790401	15-07-05	29.3	20186	199	60101022002	15-07-05	23.57	10318.9	238
NGC 4593	12 39 45.0	-05 20 06	0.008	Sy1	0740920201	14-12-29	26	21054	279	60001149002	14-12-29	23.32	14279.4	296
IRAS 13197-1627	13 22 30.6	-16 43 14	0.020	Sy1.8	0763220201	16-01-17	142.5	12003	233	60101020002	16-01-17	78.5	9925.79	284
IRAS 13224-3809	13 25 13.2	-38 25 20	0.066	NLSy1	0792180301	16-08-01	140.5	2704	22	60202001012	16-08-01	171.65	2328.62	50
MCG -06-30-15	13 36 02.0	-34 17 10	0.008	Sy1.2	0693781401	13-02-02	48.92	50651	155	60001047005	13-02-02	29.65	23126.7	360
NGC 5548	14 17 52.3	+25 05 17	0.025	Sy1.5	0720111001	13-07-23	57	71133	466	60002044005	13-07-23	49.52	46097.7	510
Mrk 841	15 03 54.3	+10 25 17	0.036	Sy1.5	0763790501	15-07-14	29.5	14721	155	60101023002	15-07-14	23.42	10118.8	249
IGRJ 19378-0617	19 37 30.9	-06 14 15	0.010	Sy1	0761870201	15-10-01	141.4	131342	349	60101003002	15-10-01	65.52	32697.6	364
Mrk 915	22 36 43.4	-12 34 11	0.024	Sy1	0744490401	14-12-02	135	38862	279	60002060002	14-12-02	52.98	12994.4	298
MR 2251-178	22 54 09.9	-17 33 03	0.064	Sy1	0763920601	15-06-17	38.9	52739	349	60102025004	15-06-17	23.19	32048.2	399
NGC 7469	23 03 12.4	+08 50 48	0.014	Sy1.2	0760350501	15-12-23	90.9	92397	266	60101001008	15-12-22	23.48	17163.1	315

Note. (1) Name of the source; (2) R.A. (in hours, minutes, and seconds); (3) decl. (in degrees, minutes of arc, and seconds of arc); (4) redshift; (5) AGN classification; (6)–(10) observation ID, date of the observation, exposure time of the observation in ks, number of counts in the 3–10 keV band background-subtracted, and number of bins in the 3–10 keV band in XMM-Newton; (11)–(15) observation ID, date of the observation, exposure time of the observation in ks, number of counts in the 3–60 keV band background-subtracted, and number of bins in the 3–60 keV band in NuSTAR.

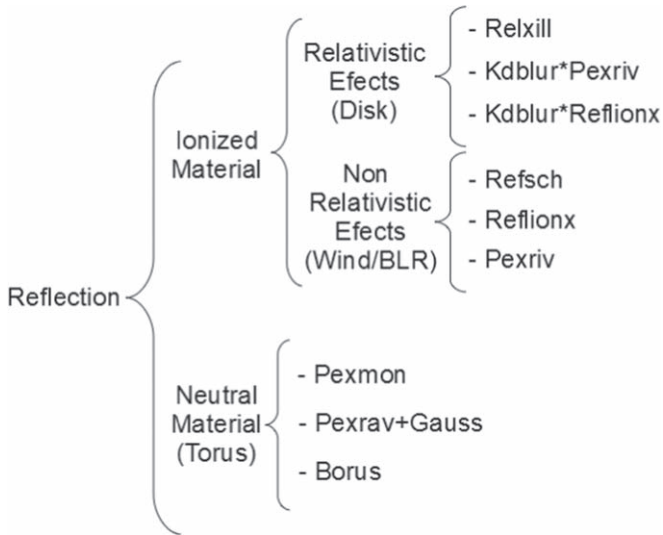


Figure 1. Scheme of reflection models used, accounting the scenarios described in Section 3.2.

parameters to the same value when they are common in several models. The main difference between neutral, ionized, and relativistic/ionized models is that the last two constantly grow from high to low energies, except PEXRIV and REFSCH; while the neutral models show a decrease below ~ 6 keV. Meanwhile, neutral models show a narrow FeK α emission line compared to the ionized or ionized/relativistic models. Finally, note that despite the fact that the PEXMON and PEXRAV models do not assume a toroidal geometry, they naturally reproduce the reflection by the torus because the physical approximation by which they are built is valid for the torus. This is highlighted in Figure 2, where the spectral shape produced by BORUS⁸ model is consistent with that of PEXMON and PEXRAV models.

We will fit these nine models on a subsample of five test objects to obtain the models that give the best fits, and we then use them to fit the full sample of 22 sources (see Section 3.5). Table 2 shows the parameters of each tested reflection model. Note that, for the power law, we fixed the energy cutoff to a high value of 1000 keV. In all of the reflection models, we linked the energy cutoff and the photon index to such of the power law when these parameters are required.

3.3. Considerations for the Simultaneous Fitting of XMM-Newton and NuSTAR Spectra

XMM-Newton spectra have, in general, a larger number of counts compared to the NuSTAR spectra (see Table 1). This could yield to an over-weight of the XMM-Newton compared to the NuSTAR spectra because the former have systematically the largest number of bins in the composed NuSTAR+XMM-Newton spectra. To validate the use of χ^2 techniques allowing both spectra to account similarly in the resulting spectral fit, we re-binned the XMM-Newton spectra according with NuSTAR spectra, so that we have the same spectral bins in each spectral file in the common spectral band (3–10 keV). For this, we use the GRPPHA task within FTOOLS, which group the spectrum from a lower to an upper channel with grouping a certain

⁸ The sharp decrease of flux shown for BORUS model at 1 keV (Figure 2, right-hand panel) is probably associated with the energy range where this model is evaluated. Note that this does not affect our analysis because we use data above 3 keV.

amount of channels per bin. To estimate the amount of channels per bin, we computed the number of channels in NuSTAR that correspond to an spectral bin in XMM-Newton in the 3–10 keV energy band using the lower and upper channel of XMM-Newton equivalent to that of NuSTAR for this energy range. To determine the confidence intervals of the parameters in the models, we estimate the 1σ errors, which corresponds to a probability of 68%. The 1σ error is calculated through the ERROR command within XSPEC. For this, we set $\Delta\chi^2 = 1$, while the parameter and all of the other nonfrozen parameters are varied.

3.4. Statistical Techniques

To determine the best model, we use the χ^2 statistics through the standard $\chi_r^2 = \chi^2/\text{dof}$, where dof are the degrees of freedom. We use F-statistics to compare between two models where one of them comes from adding an extra model component to the previous one. When the F-test probability is low ($\leq 10^{-4}$), the model significantly improves the fit. We also use the Akaike information criterion (AIC) to evaluate to what extent a model is better than another. To this end, we use the Equation (5) in Emmanoulopoulos et al. (2016) to calculate the AIC_c :

$$AIC_c = 2k - 2C_L + \chi^2 + \frac{2k(k+1)}{N-k-1}, \quad (2)$$

where C_L is the constant likelihood of the true hypothetical model, k is the number of free model parameters, and N is the number of data points. We then calculate the difference between two different models, $\Delta[AIC_c]$:

$$\Delta[AIC_c] = AIC_{c,2} - AIC_{c,1}. \quad (3)$$

Finally, we estimate the evidence ratio, ϵ :

$$\epsilon = e^{-\frac{\Delta[AIC_c]}{2}}, \quad (4)$$

which is a measure of the relative likelihood of one versus another model. When the evidence ratio is almost 300, the model is the best among the alternatives.

3.5. Spectral Fitting Procedure

We start our analysis by fitting the spectra to our baseline model to check the presence of the reflection component. To do this, we compare the power-law fit with a model which accounts for the reflection component (RELXILL). To determine the best model, we use the χ^2 statistics through the standard $\chi_r^2 = \chi^2/\text{dof}$, where dof are the degrees of freedom. We use the F-statistics to compare between two models where one of them comes from adding an extra model component to the previous one. When the F-test probability is low ($\leq 10^{-4}$), the model significantly improves the fit. We also use the AIC to evaluate to what extent a model is better than another. Note that we use AIC when comparing models not related to each other and F-test when comparing nested models. Objects for which the reflection component is not statistically needed will be discarded in the following analysis.

Our aim is to test as many models that can be used as baseline model as possible. However, this is time consuming when considering the nine baseline models, which makes the analysis unpractical for a large sample of objects, such as the one analyzed here.

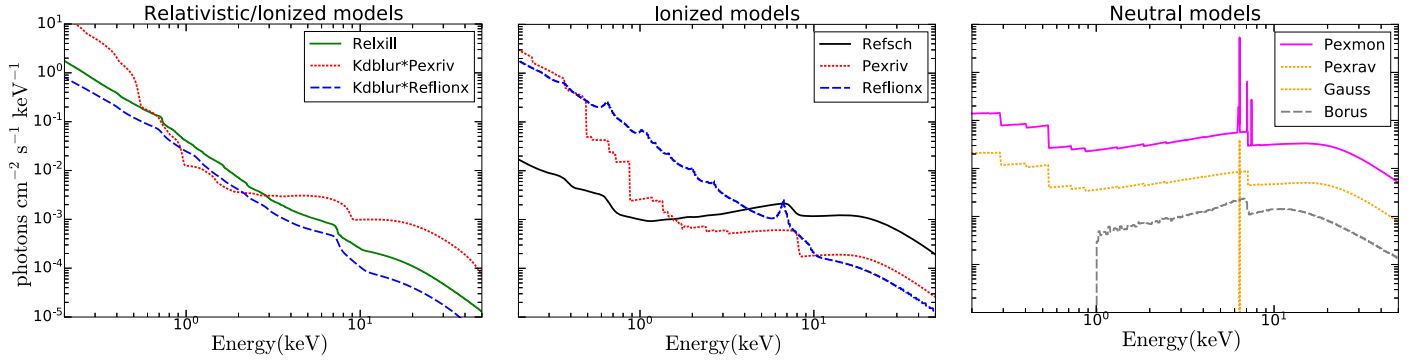


Figure 2. Example of the resulting X-ray spectra of the reflection models used in this analysis (see Section 3.2). Ionized and relativistic, ionized, and neutral models are shown in the left-hand, middle, and right-hand panels, respectively. For all models, the photon index $\Gamma = 2$, the high-energy cutoff $E_{\text{cut}} = 300$, the abundance $Z = Z_{\odot}$, the iron abundance $Z_{\text{Fe}} = Z_{\odot}$, the viewing angle toward the system $i = 45^{\circ}$, the inner radius of the disk $R_{\text{in}} = 2r_g$, the outer radius of the disk $R_{\text{out}} = 100r_g$, the disk temperature $T_{\text{disk}} = 30,000$ K, the index emissivity $\text{Index} = 3$, and the ionization parameter $\xi = 1000$, when the parameter is inside the model. In addition, for BORUS, the column density $\text{NHTor} = 10^{24}$ cm^{-2} , the angular size $\text{thTor} = 45^{\circ}$; for GAUSS, the center and the width of the emission line are $E_{\text{line}} = 6.4$ keV and $\sigma = 0.01$ keV, respectively; and for RELXILL, the spin of the black hole is set to $a = 0.998$.

Table 2
Parameters of the Reflection Models Tested in Section 3.2

	PEXMON	PEXRAV+GAUSS	BORUS	PEXRIV	REFLIONX	REFSCH	RELXILL	KDBLUR
Γ	Γ_{PL}	Γ_{PL}	Γ_{PL}	Γ_{PL}	Γ_{PL}	Γ_{PL}	Γ_{PL}	...
E_{cut}	$E_{\text{cut,PL}}$	$E_{\text{cut,PL}}$	$E_{\text{cut,PL}}$	$E_{\text{cut,PL}}$
rel_{refl}	-1^*	-1^*	...	-1^*	...	-1^*	-1^*	...
Z	0.5–5	0.5–5	...	0.5–5	...	0.5–5
Z_{Fe}	0.5–5	0.5–5	0.5–5	0.5–5	0.5–5	0.5–5	0.5–5	...
Incl	5–85	18–87	20–85	18–87	...	20–85	5–80	20–85
E_{line}	...	6.3–6.6
σ	...	0.002–0.1
NHTor	10^{22} – 10^{25}
thTor	5–80
T_{disk}	10^4 – 10^6	...	10^4 – 10^6
ξ	10^{-3} – 10^3	10 – 10^4	0.1 – 10^3	0.01–4.7	...
R_{in}	10^*	1^*	10^*
R_{out}	400^*	100^*	400^*
Index1	= Index2	...
Index2	–9.8–9.8	...
R_{br}	$((R_{\text{out}} - R_{\text{in}})/2) + R_{\text{in}}^*$...
a	0.01–0.998	...

Notes. Values represent the range in which the parameter is evaluated. Γ : photon index; E_{cut} : cutoff energy (in keV); rel_{refl} : strength of the reflection characterized by the reflection scaling factor; Z and Z_{Fe} : abundance of elements heavier than He, and iron abundance, respectively (relative to solar); E_{line} : Gaussian line energy (in keV); σ : Gaussian line width (in keV); Incl: inclination angle (in degrees); NHTor and thTor: column density (in square centimeters), and angular size (in degrees) of the torus, respectively; T_{disk} : disk temperature (in kelvins); ξ : ionization parameter (in erg cm s^{-1} and log for RELXILL); R_{in} and R_{out} : inner and outer radius of the disk, respectively (ISCO for RELXILL and R_g for all other models); Index1, Index2 and R_{br} : index emissivity between R_{in} and R_{br} , and index emissivity between R_{br} and R_{out} , respectively; a : spin of the black hole. Asterisks indicate when the values were fixed. Note that Γ and E_{cut} were linked to the corresponding value of the power-law.

Thus, we select a subsample of five objects to which we fit our set of the nine reflection models described in Section 3.2. Our criteria for the selection of this subsample was to choose sources that have previously been fitted with different models, with the intention of not biasing the subsample toward objects that clearly prefer some model. Note that the test objects were not selected using the number of counts or signal-to-noise ratio (S/N) to avoid bias in the selection of the models preferred by the objects because the model preferred by sources with a high number of counts may not be the best model for sources with smaller number of counts. The five test objects are NGC 3783, MCG -06-30-15, Fairall 9, Mrk 1044, and Mrk 335. X-ray spectrum of NGC 3783 and Fairall 9 are well fitted by using absorption components (Blustin et al. 2002; Krongold et al. 2003, 2005) and through reflection of the accretion disk (Gondoin et al. 2001; Emmanoulopoulos et al. 2011),

respectively. MCG -06-30-15 and Mrk 335 have been well fitted through relativistic reflection (Longinotti et al. 2007; Chiang & Fabian 2011) and absorption models (O’Neill et al. 2007; Miller et al. 2009). The X-ray spectrum of Mrk 1044 has been fitted using relativistic and distant reflection (Mallick et al. 2018), and also by adding wind components (Dewangan et al. 2007; Krongold et al. 2021). In this way, we cover the different reflection scenarios: two objects extensively fitted through disk reflection or only absorption scenario, and three objects fitted with equal success using one or the other model. The results from these objects determine a subset of models that we apply to the overall sample of type-1 AGNs.

Note that to confirm that the choice of the subsample does not affect the result on the best models, we choose three other objects (in addition to the first five), namely Mrk 1040, Mrk 915, and Ark 120, to which we also fit the nine initial

Table 3

F-statistics Applied to the Sample Comparing a Simplest Power-law (Absorption*Power Law) and a Reflection (Absorption*Power Law+RELXILL) Model

Source	POWER LAW $\chi^2/\text{dof} = \chi_r^2$	RELXILL	F-test
Mrk 335	443.8/188 = 2.36	255/183 = 1.4	✓
Fairall 9	766.4/502 = 1.53	561/497 = 1.13	✓
Mrk 1040	1237.8/960 = 1.29	998.3/955 = 1.05	✓
Mrk 1044	1111/710 = 1.56	768.2/705 = 1.09	✓
NGC 1365	3719.3/1003 = 3.71	1739/998 = 1.74	✓
Ark 120	1344.1/972 = 1.38	1060.4/967 = 1.1	✓
Mrk 382	161.7/143 = 1.13	151.1/138 = 1.1	0.09
NGC 3227	1425.4/976 = 1.46	1146.3/971 = 1.18	✓
NGC 3783	1755/575 = 3.05	1121.3/570 = 1.97	✓
NGC 4051	1857.1/1452 = 1.28	1457.9/1447 = 1.01	✓
NGC 4151	3036.9/1718 = 1.77	3291.8/1713 = 1.92	✓
Mrk 766	470.1/432 = 1.09	443.7/427 = 1.04	✓
NGC 4593	676.6/570 = 1.19	569.8/565 = 1.01	✓
IRAS 13197-1627	1697.2/512 = 3.31	665.7/507 = 1.31	✓
IRAS 13224-3809	314.2/245 = 1.28	301.5/240 = 1.26	0.07
MCG -06-30-15	691.2/510 = 1.36	497.5/505 = 0.99	✓
NGC 5548	1203.2/971 = 1.24	1079.1/966 = 1.12	✓
Mrk 841	413.8/398 = 1.04	402.7/393 = 1.02	0.05
IGRJ 19378-0617	973.4/708 = 1.37	742.7/703 = 1.06	✓
Mrk 915	694.2/572 = 1.21	595.5/567 = 1.05	✓
MR 2251-178	720/742 = 0.97	717.6/737 = 0.97	0.78
NGC 7469	707.9/465 = 1.52	489.8/460 = 1.06	✓

Notes. Column 1 shows the name of the source. Columns 2 and 3 shows the χ^2 statistic for the power-law and reflection models, respectively. Column 4 shows the F-test obtained. Sources in bold face indicate those sources that do not require a reflection component according to the F-test.

models. For these three new objects, we find that the preferred models are PEXRAV+GAUSS and RELXILL. These results strongly suggest that the selection of objects for the subsample does not alter the results on the models selected for testing on the full sample.

3.6. Intrinsic Parameters

We also study the relation between the final preferred models and the SMBH mass, luminosity, and the Eddington ratio of the sources (see Table 7). For this purpose, we compute the 2–10 keV luminosity for each component of the spectral fit using the CLUMINOSITY command within XSPEC. From the luminosity of the intrinsic continuum, we calculate the bolometric luminosity, L_{bol} , from X-rays following the relation from Marconi et al. (2004):

$$\log[L_{\text{bol}}/L_{2-10\text{keV}}] = 1.54 + 0.24\mathcal{L} + 0.012\mathcal{L}^2 - 0.0015\mathcal{L}^3, \quad (5)$$

where $\mathcal{L} = \log(L_{\text{bol}} - 12)$, and L_{bol} is in units of L_{\odot} . We then calculated the Eddington ratio, λ , which is defined as $\lambda = L_{\text{bol}}/L_{\text{edd}}$, where L_{edd} is the Eddington luminosity.

4. Results

4.1. The Existence of the Reflection Component

Table 3 shows the χ^2 results of the reflection component test. We corroborate the presence of the reflection component in 18 sources (marked with a check symbol in Table 3). These

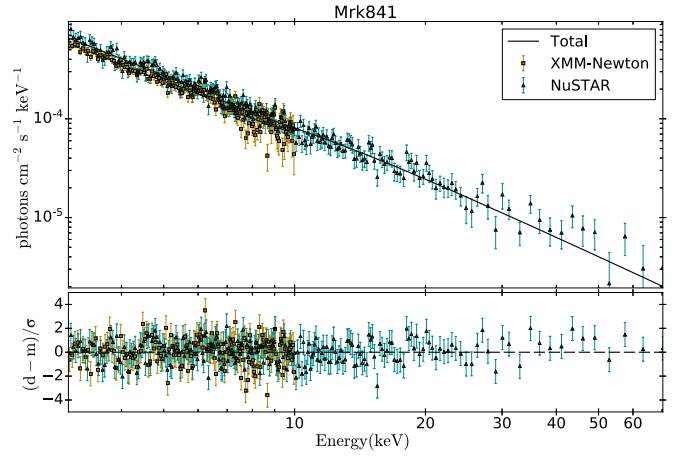


Figure 3. Power-law fit to Mrk 841. We show the best fit (black solid line) to the data in the top panel and the ratio between model and data in the bottom panel. The gold dots and dark cyan diamonds show the data from XMM-Newton and NuSTAR, respectively. The top panel shows the result of plotting UFSPEC in the XSPEC language. The data points plotted are calculated by D^*UM/FM , where D is the observed data, UM is the theoretical model integrated over the plot bin, and FM is the model times the response.

objects show an F-test probability $< 10^{-4}$, which confirms the improvement among these two models. Four sources, namely Mrk 382, IRAS 13224-3809, Mrk 841, and MR 2251-178 show an F-test probability of 0.09, 0.07, 0.05, and 0.78, respectively. Therefore, according to the F-statistics, these four objects do not need a reflection component to satisfactorily fit the spectrum. As an example of objects where the reflection component is not needed, we show in Figure 3 the absorbed power-law fit for Mrk 841. Note that the spectrum is well fitted with a power law with a photon index of 1.86, which is in good agreement with the photon index of ~ 1.9 that is expected for the AGNs (Zdziarski et al. 1995). In addition, note that the $\text{FeK}\alpha$ line and the Compton hump are absent, which are the main signatures of the reflection component. A similar behavior is observed in the other three nonreflection objects. The power-law fit of these sources is shown in the Appendix.

4.2. Test Objects

As described earlier, we selected five objects (all of them with clear signs of reflection in the NuSTAR observations) to perform an analysis on nine reflection models: three neutral, three ionized, and three ionized and relativistic models (see Section 3.2 and Table 1). In Table 4, we show the statistics obtained with each model tested on the five test objects. We also show the AIC to compare the goodness of fit between the models. We find that the PEXRAV+GAUSS and RELXILL models are the preferred models by the test objects. The PEXRAV+GAUSS model gives the best fit for three objects: NGC 3783, Fairall 9, and Mrk 335; and RELXILL model gives the best fit for two objects: MCG -06-30-15 and Mrk 1044. The best fits of MCG -06-30-15 and Fairall 9 are obtained through three models (RELXILL, KDBLUR*REFLIONX and PEXRAV+GAUSS, and PEXRAV+GAUSS, BORUS and RELXILL, respectively). For Mrk 1044, the best fits are obtained with two models (RELXILL and KDBLUR*REFLIONX). According to these results, we decided to choose the PEXRAV+GAUSS and RELXILL models, discarding from the subsequent analysis for the rest of the models. Note that the BORUS model provides a good fit to Fairall 9, and the KDBLUR*REFLIONX model

Table 4
Models Applied to the Test Objects Described in Section 3.5

Model	NGC 3783	MCG -6-30-15	Fairall 9 $\chi^2/\text{dof} = \chi_r^2/\text{AIC}$	Mrk 1044	Mrk 335
RELXILL	1121.3/570 = 1.97 5.3×10^{35}	497.5/505 = 0.99 1	561/497 = 1.13 70	768.2/705 = 1.09 1	255/183 = 1.4 3.1×10^7
KDBLUR*PEXRIV	1462.9/569 = 2.57 1.4×10^{110}	571.1/504 = 1.13 1.7×10^{16}	796/496 = 1.6 1.3×10^{53}	851.4/704 = 1.21 1.9×10^{18}	379.3/182 = 2.08 5.5×10^{34}
KDBLUR*REFLIONX	1236.4/571 = 2.17 3.1×10^{60}	507.6/506 = 1.0 91	603.1/498 = 1.21 5.7×10^{10}	775.1/706 = 1.1 19	302.5/184 = 1.64 3.5×10^{17}
REFSCH	1366.4/569 = 2.4 1.5×10^{89}	538.4/504 = 1.07 1.3×10^9	701.8/496 = 1.41 4.6×10^{32}	825/704 = 1.17 3.7×10^{12}	391.9/182 = 2.15 3.1×10^{37}
REFLIONX	1325.8/573 = 2.31 2.8×10^{79}	538.3/508 = 1.06 1.5×10^8	614.7/500 = 1.23 6.5×10^{12}	807/708 = 1.14 5.5×10^7	296.1/186 = 1.59 4.3×10^{15}
PEXRIV	1648.4/570 = 2.89 1.5×10^{150}	575.9/505 = 1.14 1.1×10^{17}	795.8/497 = 1.6 6.8×10^{52}	905.2/705 = 1.28 5.6×10^{29}	382/183 = 2.09 1.2×10^{35}
PEXMON	1120.8/572 = 1.96 1.4×10^{35}	541.9/507 = 1.07 1.5×10^9	598/499 = 1.2 2.6×10^9	1028.7/707 = 1.46 1.3×10^{56}	248.3/185 = 1.34 3.2×10^5
PEXRAV+GAUSS	955.7/569 = 1.68 1	507.6/504 = 1.01 268	551.4/496 = 1.11 1	960/704 = 1.36 7.6×10^{41}	219.3/182 = 1.2 1
BORUS	1057.4/571 = 1.85 4.2×10^{21}	542.6/506 = 1.07 3.6×10^9	556.8/498 = 1.12 5	1019.2/706 = 1.44 1.9×10^{54}	270.9/184 = 1.47 4.7×10^{10}

Notes. The first and second rows correspond to χ^2/dof and AIC statistics, respectively. We show in bold face the best model according to AIC. A number one in AIC rows indicates the best model, and other numbers indicate how many times the model is worse than the best model. Note that the model name represents the reflection component in our baseline model: absorber*intrinsic + reflection.

provides good fits to MCG -06-30-15 and Mrk 1044. However, we discard them because the physical scenario is properly described by PEXRAV+GAUSS and RELXILL models, respectively, and they are only good fits in one and two of the five test objects.

4.3. Spectral Fits for the Sample

We then used PEXRAV+GAUSS and RELXILL models for the 18 objects with evidence of the reflection component. Note that both PEXRAV+GAUSS and RELXILL models have six free parameters, in addition to the normalization (see Table 2). Furthermore, we also try a combined model that uses both neutral (PEXRAV+GAUSS) and ionized relativistic reflectors (RELXILL), namely the HYBRID model (HYBRID = POWERLAW + PEXRAV+GAUSS + RELXILL). We test these three models in our sample. To determine the best model, we first compare between the two simplest models (PEXRAV+GAUSS and RELXILL) using the AIC. We then compare the best model given by AIC and the more complex model (HYBRID) using the F-test. If the F-test of the HYBRID model is $\leq 10^{-4}$, then his model is preferred by the source. If not, then the preferred model is the one indicated by AIC among PEXRAV+GAUSS and RELXILL models (i.e., marked with the number one). Finally, if the AICs of both models give ≤ 300 , then both models are equally preferred by the analysis. Table 5 shows the statistics that were obtained.

We find that 12 out of the 18 objects (i.e., Mrk 335, Fairall 9, Mrk 1040, NGC 1365, Ark 120, NGC 3227, NGC 3783, NGC 4051, NGC 4151, IRAS 13197-1627, NGC 5548, and NGC 7469) prefer the hybrid model (i.e., 67%), one object (i.e., Mrk 915) prefers the neutral reflector (5%), two objects (i.e., Mrk 1044, and IGRJ 19378-0617) prefer the ionized model (11%), and three objects (i.e., Mrk 766, NGC 4593, and MCG -06-30-15) equally prefer both the neutral and ionized reflection models (17%).

Figure 4 shows the best fit of the 12 objects that prefer the hybrid model and also the residuals of the three models in order to compare them. The residuals of Mrk 335, Fairall 9, and NGC 7469 show that the main improvement using the hybrid model is between 6 and 7 keV through adding the ionized component. The residuals of the hybrid model of NGC 4151 and Ark 120 show a better fit above ~ 10 keV, and between 6 and 7 keV when compared to the neutral and ionized models. Note that the residuals of NGC 4151 around 6–7 keV are bigger in NuSTAR data, possibly due to the cross-calibration between the satellites. The residuals of the hybrid model of IRAS 13197-1627 show a better fit below ~ 6 keV when compared to the neutral and ionized models. NGC 1365 and NGC 3783 have the worst fits in the sample. The residuals of the three models of these two objects show clear deficiencies of the fit between ~ 6 and 8 keV. These two objects show possible emission lines below ~ 8 –9 keV, which were not considered in the baseline model. To obtain a better fit, the emission lines are requested to be added to the baseline model. Interestingly, the FeK α line is always fitted by the neutral component. Meanwhile, the ionized component is important to fit the edge around 7–9 keV and the range below ~ 6 keV. The Compton hump is fitted by the neutral component, except for three sources, i.e., NGC 1365, NGC 3783, and NGC 4151.

Figure 5 shows the two objects that prefer the ionized model, namely Mrk 1044 and IGRJ 19378-0617. In both objects, the neutral model fails to reproduce the data between 6 and 8 keV. In addition, the ionized component reproduces the FeK α line well. We show in Figure 6 the spectrum and residuals of Mrk 915, which is best fitted to the neutral model. The residuals of the three models in this object show minimal differences throughout the spectral range.

The fits of Mrk 766, NGC 4593, and MCG -06-30-15 are shown in Figure 7. According to the F-statistics, these objects equally prefer the neutral and ionized models. In both cases, the Compton hump is well fitted by the PEXRAV+GAUSS and

Table 5
Models Tested to the Full Sample

Source	PEXRAV+GAUSS	RELXILL	HYBRID	Source	PEXRAV+GAUSS	RELXILL	HYBRID
Mrk 335*	219.3/182 = 1.2	255/183 = 1.4	166.3/176 = 0.94	NGC 4151	2543.9/ 1712 = 1.49	3291.8/ 1713 = 1.92	2117.3/ 1706 = 1.24
AIC/F-test _{mod}	1	3×10^7	6.7×10^{-9}	AIC/F-test _{mod}	1	1.5×10^{162}	8.2×10^{-64}
Fairall 9	556.8/ 496 = 1.12	561/497 = 1.13	499.6/490 = 1.02	Mrk 766	447/426 = 1.05	443.7/427 = 1.04	436.2/ 420 = 1.04
AIC/F-test _{mod}	1	5	1×10^{-9}	AIC/F-test _{mod}	9	1	0.41
Mrk 1040	997.4/ 954 = 1.05	998.3/ 955 = 1.05	958.2/948 = 1.01	NGC 4593	559.4/564 = 0.99	569.8/565 = 1.01	550.1/ 558 = 0.99
AIC/F-test _{mod}	1	1	1.1×10^{-6}	AIC/F-test _{mod}	1	105	0.15
Mrk 1044	960/704 = 1.36	768.2/705 = 1.09	763.5/ 698 = 1.09	IRAS 13197- 1627	643.7/ 506 = 1.27	665.7/ 507 = 1.31	533.2/500 = 1.07
AIC/F-test _{mod}	7.5×10^{41}	1	0.74	AIC/F-test _{mod}	1	3.5×10^4	3.5×10^{-18}
NGC 1365*	2409.3/ 997 = 2.42	1739/998 = 1.74	1566.4/ 991 = 1.58	MCG -06-30-15	507.6/504 = 1.01	497.5/505 = 0.99	495.3/ 498 = 0.99
AIC/F-test _{mod}	6×10^{145}	1	1.7×10^{-19}	AIC/F-test _{mod}	268	1	0.946786
Ark 120	1057.1/ 966 = 1.09	1060.4/ 967 = 1.1	999.3/960 = 1.04	NGC 5548	1044/965 = 1.08	1079.1/ 966 = 1.12	1010.8/ 959 = 1.05
AIC/F-test _{mod}	1	3	7.1×10^{-10}	AIC/F-test _{mod}	1	2.4×10^7	2.5×10^{-5}
NGC 3227	1143/ 970 = 1.18	1146.3/ 971 = 1.18	1105.3/ 964 = 1.15	IGRJ 19378- 0617	946.2/ 702 = 1.35	742.7/703 = 1.06	730.9/ 696 = 1.05
AIC/F-test _{mod}	1	3	1.4×10^{-5}	AIC/F-test _{mod}	2.6×10^{44}	1	0.130678
NGC 3783*	955.7/ 569 = 1.68	1121.3/ 570 = 1.97	857.7/563 = 1.52	Mrk 915	583/566 = 1.03	595.5/ 567 = 1.05	580.4/ 560 = 1.04
AIC/F-test _{mod}	1	5.3×10^{35}	2.6×10^{-11}	AIC/F-test _{mod}	1	302	0.867129
NGC 4051	1469/ 1446 = 1.02	1457.9/ 1447 = 1.01	1418.1/ 1440 = 0.98	NGC 7469	493.2/ 459 = 1.07	489.8/ 460 = 1.06	439.5/453 = 0.97
AIC/F-test _{mod}	430	1	1.3×10^{-6}	AIC/F-test _{mod}	9	1	1.9×10^{-8}

Notes. Note that the model name represents the reflection component in our baseline model: absorber*intrinsic + reflection. The first and second row of each object shows the χ^2/dof statistics, and the AIC and F-test results, respectively. The preferred model by each object is given in bold face. The sources marked with an asterisk are those discarded in the analysis of the intrinsic properties of the sample due to poor spectral fitting (see Section 3.6).

RELXILL models. For Mrk 766, the main difference is in the FeK α line, which is fitted by a narrow Gaussian line in the neutral model, and with a broad line in the ionized model. For MCG -06-30-15, the FeK α line is well fitted by a broad line in both models.

We show in Table 6 the parameters obtained with the preferred model. The column density and photon index are constrained for almost all objects. For the neutral component, the central energy of the FeK α emission line is restricted in all but one object. The inclination angle is restricted for only one source. For the ionized component, the ionization parameter is restricted for almost all sources. Iron abundance is the least constrained parameter for this component. Note that we found high Iron abundance for NGC 3227 ($2.76 \pm_{0.46}^{0.46}$), NGC 3783 ($1.84 \pm_{0.09}^{0.12}$), and NGC 4593 ($2.75 \pm_{1.06}^{1.51}$). Similar results have been found previously for the last two sources. Brenneman et al. (2011) and Ursini et al. (2016) found Iron abundance of $3.7 \pm_{0.9}^{0.9}$ and $2.6 \pm_{0.4}^{0.2}$ for NGC 3783 and NGC 4593, respectively. Note also that we do not restrict the iron abundance and inclination of PEXRAV+GAUSS and RELXILL in the HYBRID model to the same value—because they are different media (torus and accretion disk, respectively), they are not expected to have the same value.

4.4. AGN Intrinsic Properties

To study the AGN intrinsic properties, we calculated the 2–10 keV band luminosity for each source in our sample and the contribution of each component to the total luminosity. In addition, we compile the SMBH mass from the literature and we calculate the Eddington ratio for each source. We show these parameters in Table 7. Figure 8 shows the histograms of the distribution of SMBH mass, intrinsic 2–10 keV luminosity, and Eddington ratio obtained for the sample. Note that we include those objects that do not require the reflection component (namely nonrefl.). In addition, we excluded NGC 1365, and NGC 3783 (marked with an asterisk in Table 5) from the following analysis because the fits obtained with the baseline models used in this work show the worst statistic of the sample ($\chi_r^2 > 1.5$), which is possibly due to the need to incorporate absorption/emission lines to the baseline model (Rivers et al. 2015; Mehdipour et al. 2017). Considering that the contribution of the emission/absorption lines in the baseline model may modify the model parameters, including the estimate of the intrinsic luminosity of the source will consequently affect the calculation of the Eddington ratio. In addition, we exclude Mrk 335 because the intrinsic continuum shows a smaller contribution than the reflection components

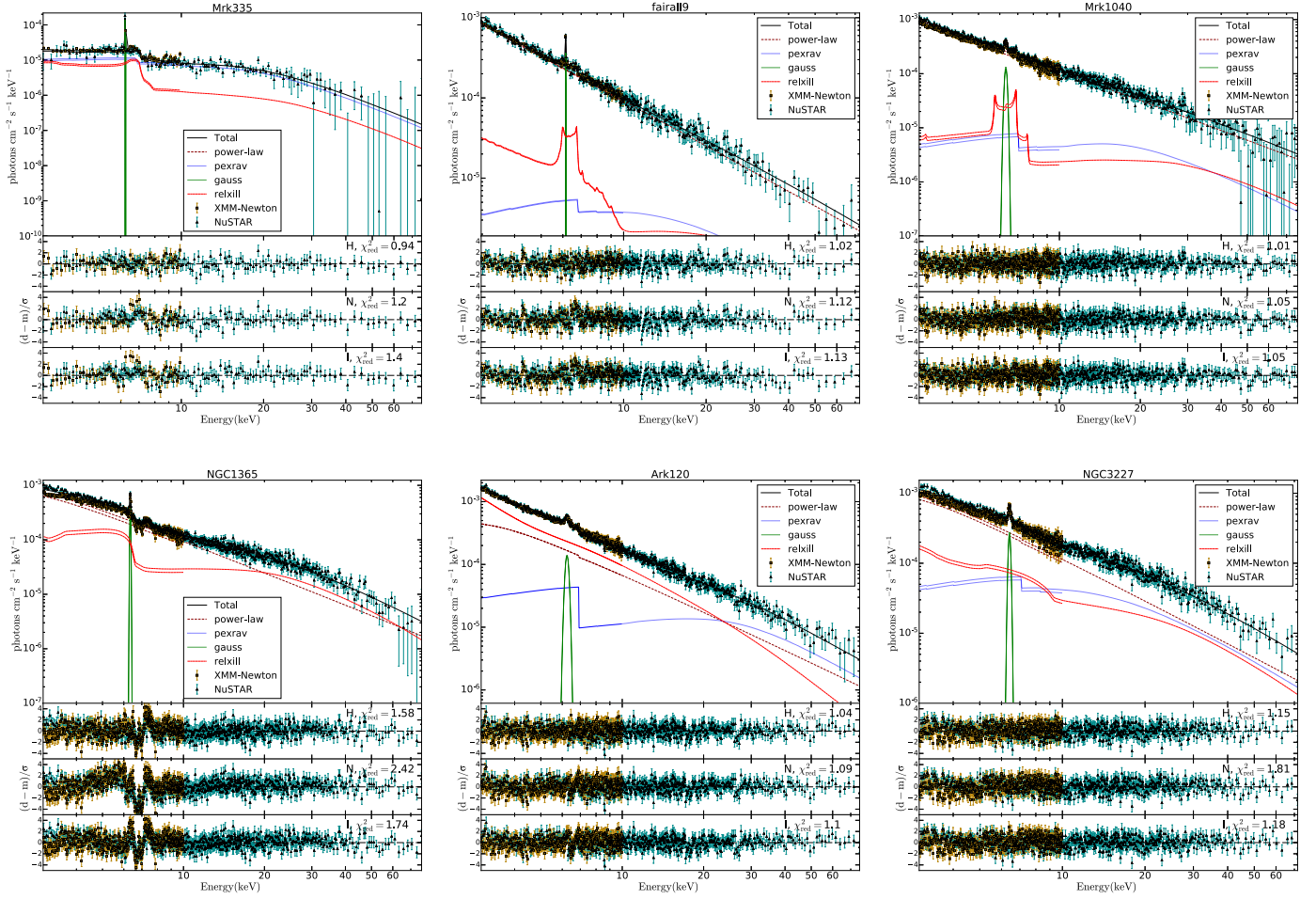


Figure 4. Best fit to the 12 objects that prefer the hybrid model. We show the best fit (black solid line) to the data in the top panel and the ratio between model and data of the hybrid, neutral, and ionized models (marked with letters H, N, and I, respectively) in the bottom panels. We also show the reduced χ^2 of the corresponding fit.

(see Figure 4), while the reflection is expected to represent a fraction of the intrinsic continuum.

We find that sources which prefer the neutral, hybrid, and nonrefl. models are in a wide SMBH mass range. Sources showing preferences for ionized reflection are characterized by lower SMBH masses, from $\log(M_{\text{BH}})$ of $6.23 \pm_{0.5}^{0.5}$ to $6.91 \pm_{0.07}^{0.07}$. Note that the uncertainties in the luminosities are quite small, so we can well differentiate the most luminous sources from the less luminous sources. The sources that prefer the ionized model show a narrow range of intrinsic luminosity, around $\log(L_{2-10 \text{ keV}}) = 42.6$. The other sources are between $\log(L_{2-10 \text{ keV}}) = 41.43 \pm_{0.02}^{0.02}$ and $\log(L_{2-10 \text{ keV}}) = 44.68 \pm_{0.01}^{0.01}$. The sources that do not require the reflection component show low ($\log(L_{2-10 \text{ keV}}) = 42.21 \pm_{0.01}^{0.01}$, $\log(L_{2-10 \text{ keV}}) = 42.57 \pm_{0.01}^{0.01}$) and high ($\log(L_{2-10 \text{ keV}}) = 43.85 \pm_{0.01}^{0.01}$, $\log(L_{2-10 \text{ keV}}) = 44.68 \pm_{0.01}^{0.01}$) luminosities, i.e., these objects do not show any preference for a particular range of luminosities. Finally, the highest Eddington ratios are found for sources that prefer the ionized or nonrefl. models. However, if we consider the lower limits of the Eddington ratio of these sources, then they move to lower values. The lower Eddington ratios are observed for the sources that prefer the hybrid model, i.e., Mrk 140, NGC 3227, NGC 4151 and IRAS 13197-1627 are the sources with the lowest Eddington ratios, even considering their uncertainties.

We also study the correlation between the photon index and the Eddington ratio. We find that the two sources preferring the ionized model have a higher photon index than those preferring the hybrid or nonrefl. models (see Figure 9). Two sources (i.e., Mrk 766 and MCG -06-30-15) of the three sources that equally prefer the neutral and ionized models show the highest photon index in two of the four sources that fit to neutral model and two of the five sources that fit to ionized model. In addition, for these sources, the ionized model produces steeper spectra. This could suggest that these two sources have intrinsically steep spectra; however, even when excluding these sources, the two objects that prefer only the ionized model show the highest photon index. According to our results, it is difficult to determine if there is any tendency for objects to have a higher photon index or Eddington rate. However, note that previous works have studied the correlation between these parameters. For instance, Fanali et al. (2013) study a sample of 71 type-1 AGNs. They found that the photon index depends significantly on the Eddington rate, where both parameters have a directly proportional relationship (see their Figure 5). Note that we also explored the dependence between the photon index, the SMBH mass, and 2–10 keV luminosity but did not find any correlation between these parameters.

Finally, we studied the luminosity contribution of each component to the baseline model. Figure 10 shows correlation

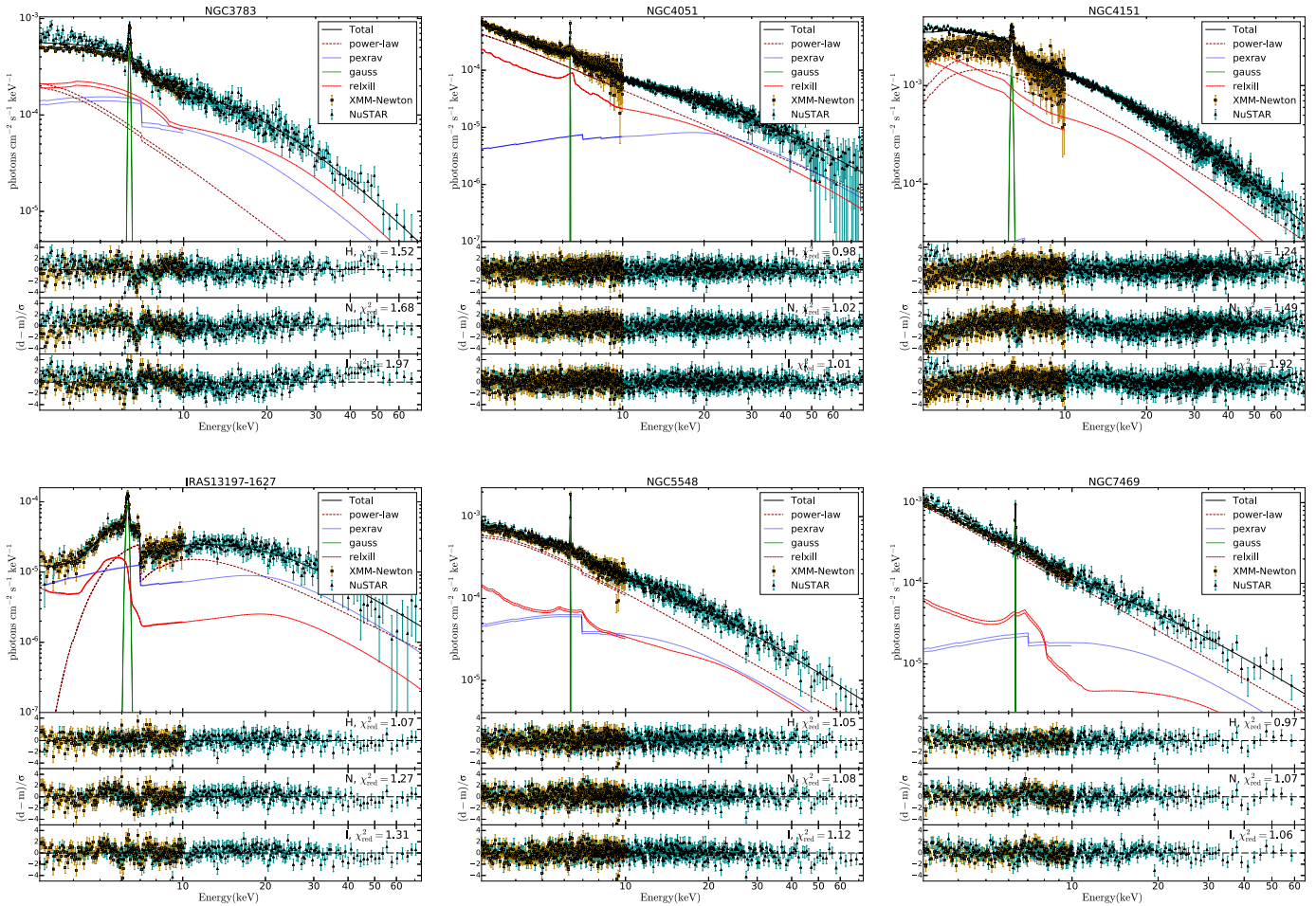


Figure 4. (Continued.)

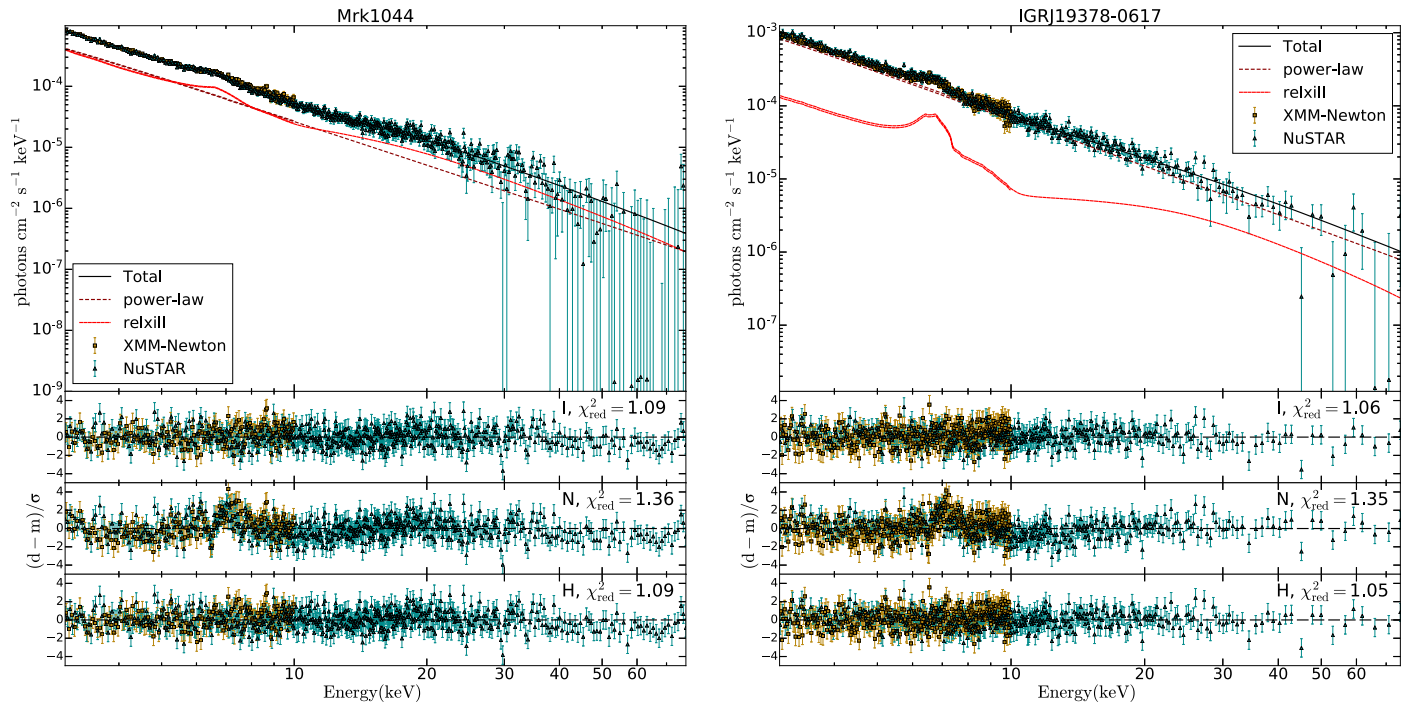


Figure 5. Best fit to the two objects that prefer the ionized model. The description is the same as that given in Figure 4.

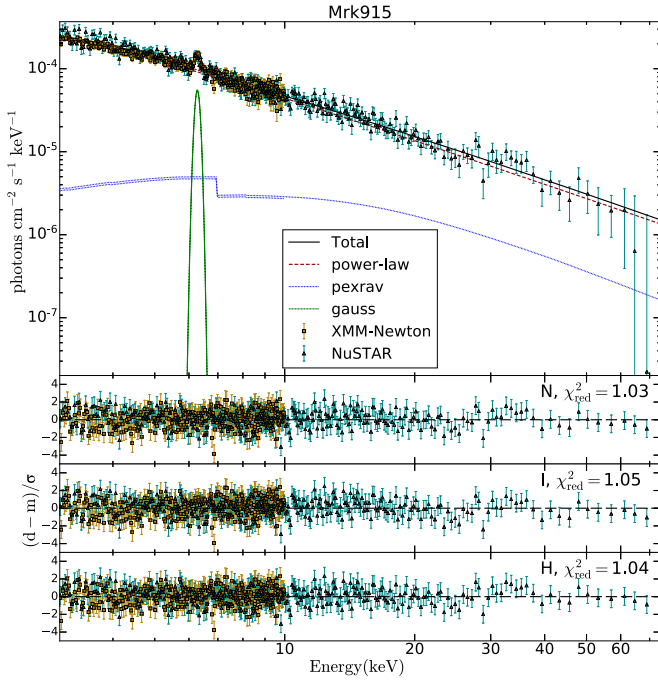


Figure 6. Best fit to the object preferring the neutral model. The description is the same as that given in Figure 4.

between the total luminosity versus the intrinsic continuum, and neutral, and ionized luminosities according to each model. We find that almost all sources have a contribution of the intrinsic continuum between 80% and 100%. This component ranges from $\log(L_{\text{Int}})$ of $41.43 \pm_{0.02}^{0.01}$ to $44.68 \pm_{0.01}^{0.01}$, with a mean value of $\log(L_{\text{Int}}) = 42.85 \pm_{0.01}^{0.01}$. The contribution of the neutral reflector is below 10% for all sources, ranging from $\log(L_{\text{pexrav}})$ of $40.03 \pm_{0.02}^{0.02}$ to $42.69 \pm_{0.04}^{0.04}$, with a mean value of $\log(L_{\text{pexrav}}) = 41.31 \pm_{0.04}^{0.04}$. Furthermore, the contribution of the FeK α to the total luminosity is only around 1%. This component ranges from $\log(L_{\text{Gauss}})$ of $39.20 \pm_{0.09}^{0.09}$ to $41.91 \pm_{0.02}^{0.02}$, with a mean value of $\log(L_{\text{Gauss}}) = 40.83 \pm_{0.05}^{0.04}$. For those sources that prefer the ionized model, the reflection component has a contribution close to 10% except to Mrk 1044, which has a contribution of the ionized reflector around 50%. Those sources that prefer the hybrid model have a contribution of the ionized component that is distributed in a wide range. Four sources are below 10%, four sources are between 10% and 50%, and one source is above 50%. The ionized component ranges from $\log(L_{\text{relxill}})$ of $41.43 \pm_{0.03}^{0.03}$ to $43.31 \pm_{0.01}^{0.01}$, with a mean value of $\log(L_{\text{relxill}}) = 41.43 \pm_{0.03}^{0.03}$.

5. Discussion

5.1. Nonreflection Component Objects

According to our analysis, four objects (Mrk 382, IRAS 13224-3809, Mrk.841, and MR 2251-178) in our sample do not require a reflection component to obtain a good fit. Interestingly, according to previous works, this result is in agreement for only two objects. The absence of reflection features have been observed previously in Mrk 382 by Singh et al. (1992) using EXOSAT observations. They conclude that the observation shows only the unprocessed X-ray emission of the source. They do not find evidence of intrinsic absorption, soft excess, or any line feature. Nardini et al. (2014) study the

spectrum of MR 2251-178 using XMM-Newton observations. They test several physical models to fit the spectrum; however, they conclude that the spectrum features can be ascribed to partial covering of the X-ray source. In the other two objects, reflection features have been observed previously. Gofford et al. (2011) also study the spectrum of MR 2251-178 using Suzaku and Swift/BAT data. They conclude that the spectrum can be equally well modeled with an absorption-dominated and partially covered continuum or as a fully covered intrinsic continuum component. Jiang et al. (2018) use simultaneous XMM-Newton and NuSTAR observations to study the spectra of IRAS 13224-3809. They find that the reflected spectrum is well fitted with two relativistic blurred reflection components from the inner accretion disk. Note that they use several observations, 12 of XMM-Newton and seven of NuSTAR, among which are the two observations used in this work. Bianchi et al. (2004) use simultaneous observations of XMM-Newton and BeppoSAX to study the spectrum of Mrk 841. They obtain a good fit using an isotropic-illuminated cold slab reflection component.

A plausible explanation for this discrepancy between our results and those found previously for IRAS 13224-3809 and Mrk 841 might be due to the variability of these AGNs, i.e., these systems might be in a state of a very high continuum level. Gallo et al. (2004) find that high-energy photons in IRAS 13224-3809 are produced by a combination of the intrinsic continuum associated with the corona and a reflection component associated with the disk. They conclude that although both processes occur simultaneously, only one dominates at a given time. Mrk841 is known for having a complex and variable iron line (Petrucci et al. 2002; Longinotti et al. 2004), which probably indicates emission from the accretion disk but is difficult to constrain in our analysis.

Note that to explore if our four sources have been observed in a lower intrinsic continuum states, we look for other simultaneous observations; however, we only find data of IRAS 13224-3809 and MR 2251-17. Again, we find that the simple power-law fit is enough to fit the spectra of IRAS 13224-3809. Tested observations of this source are separated by ~ 9 days. Furthermore, under the interpretation that these four sources are in a high state, we might also expect these sources to occupy the highest values of luminosities and/or Eddington rates. However, although two of them show among the highest luminosities in our sample, the other two show lower values (see Figure 8).

5.2. Reflection Scenarios

Among the sources for which we detect the presence of the reflection component, most objects require the hybrid scenario where both reflection from neutral and the relativistic/ionized media are required. In support of these results, Nardini et al. (2011) conclude that the presence of blurred disk reflection is a fundamental component of the X-ray spectra of type 1 AGNs. In addition, some authors have concluded that it is necessary to consider both neutral/distant and ionized/relativistic reflection components to satisfactorily fit the X-ray spectra above 3 keV of some AGNs. Parker et al. (2019) use XMM-Newton, NuSTAR, Swift, and Hubble Space Telescope observations of Mrk 335. They conclude that its spectrum is dominated at low energies (< 3 keV) by the photoionized emission and at high energies (> 5 keV) by distant reflection. They also find that relativistic reflection or partial covering gives a similar fit to the

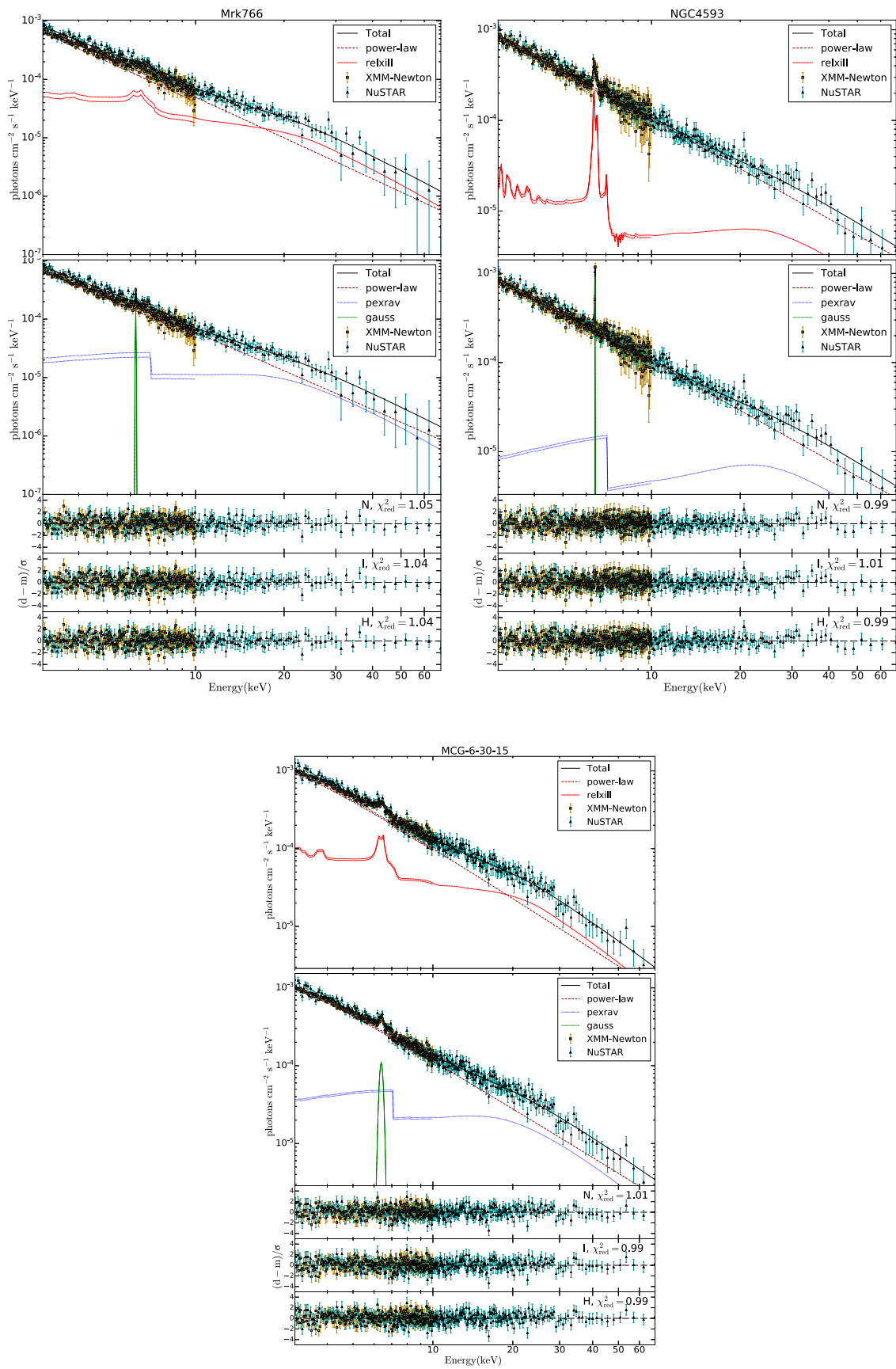


Figure 7. Best fit to the three objects that equally prefer the neutral and ionized models. The description is the same as that given in Figure 4.

Table 6
Spectral Fit Parameters Obtained with the Preferred Model for Each Source

	POWER LAW		PEXRAV+GAUSS					RELXILL				
	N_{H}	Γ	Z (Z_{\odot})	Z_{Fe} (Z_{\odot})	incl (cos)	E_{line} (keV)	σ (keV)	Index	a	incl (deg)	$\log(\zeta)$	Z_{Fe} (Z_{\odot})
Mrk 335 ^H	$1.74^{+0.19}_{-0.5}$...	$0.74^{+0.11}_{-0.55}$	$6.45^{+0.01}_{-0.01}$...	$4.0^{+1.6}_{-0.6}$	$0.57^{+0.13}_{-0.16}$	49^{+1}_{-2}	$2.11^{+0.53}_{-0.10}$...
Fairall 9 ^H	...	$1.85^{+0.01}_{-0.01}$	$1.09^{+0.49}_{-0.92}$	$6.44^{+0.01}_{-0.01}$	$0.82^{+0.07}_{-0.29}$...	$3.0^{+0.02}_{-0.06}$...
Mrk 1040 ^H	...	$1.81^{+0.03}_{-0.01}$	$6.39^{+0.01}_{-0.01}$	$0.07^{+0.02}_{-0.02}$
NGC 1365 ^H	$1.91^{+0.13}_{-0.07}$	$1.94^{+0.01}_{-0.01}$	$6.37^{+0.01}_{-0.01}$...	$3.50^{+0.03}_{-0.04}$	$2.70^{+0.01}_{-0.02}$...
Ark 120 ^H	$4.04^{+0.18}_{-0.98}$	$2.0^{+0.04}_{-0.01}$	$0.19^{+0.01}_{-0.12}$	$6.45^{+0.01}_{-0.01}$	$0.1^{+0.01}_{-0.02}$	7^{+7}_{-3}	$3.70^{+0.14}_{-0.01}$...
NGC 3227 ^H	$2.63^{+0.10}_{-0.40}$	$2.0^{+0.02}_{-0.13}$	$1.20^{+0.28}_{-0.37}$	$6.44^{+0.01}_{-0.01}$	$0.06^{+0.02}_{-0.01}$	$2.51^{+0.19}_{-0.79}$	$2.76^{+0.46}_{-0.41}$
NGC 3783 ^H	...	$2.17^{+0.09}_{-0.03}$	$6.44^{+0.01}_{-0.01}$	$0.05^{+0.01}_{-0.01}$...	$0.98^{+0.01}_{-0.01}$	75^{+1}_{-1}	...	$1.84^{+0.12}_{-0.09}$
NGC 4051 ^H	$1.25^{+0.10}_{-0.11}$	$2.01^{+0.01}_{-0.01}$	$3.01^{+0.27}_{-0.23}$	$6.42^{+0.01}_{-0.01}$...	$1.28^{+0.18}_{-0.36}$	$3.01^{+0.01}_{-0.01}$...
NGC 4151 ^H	$13.94^{+0.11}_{-0.96}$	$1.75^{+0.02}_{-0.04}$	$6.38^{+0.01}_{-0.01}$	$0.06^{+0.03}_{-0.03}$...	$0.42^{+0.10}_{-0.09}$	33^{+3}_{-2}	$3.02^{+0.04}_{-0.05}$...
IRAS 13197-1627 ^H	79^{+4}_{-4}	$1.88^{+0.09}_{-0.06}$	$1.1^{+0.3}_{-0.5}$	$1.0^{+0.2}_{-0.2}$...	$6.42^{+0.01}_{-0.01}$	$0.07^{+0.01}_{-0.01}$	$3.3^{+0.3}_{-0.3}$	$0.26^{+0.16}_{-0.17}$	12^{+3}_{-3}	$2.3^{+0.1}_{-0.2}$...
NGC 5548 ^H	...	$1.88^{+0.01}_{-0.01}$	$6.48^{+0.01}_{-0.01}$...	$0.95^{+0.18}_{-0.46}$	$2.36^{+0.02}_{-0.06}$...
NGC 7469 ^H	$0.32^{+0.26}_{-0.24}$	$1.95^{+0.08}_{-0.08}$	$1.64^{+1.0}_{-0.65}$	$6.43^{+0.02}_{-0.01}$...	$2.29^{+0.31}_{-0.31}$...	61^{+7}_{-7}	$2.99^{+0.10}_{-0.55}$...
Mrk 915 ^N	$2.97^{+0.42}_{-0.21}$	$1.72^{+0.01}_{-0.05}$	$6.43^{+0.01}_{-0.02}$	$0.08^{+0.02}_{-0.02}$
Mrk 766 ^N	$0.39^{+0.62}_{-0.33}$	$2.18^{+0.09}_{-0.06}$...	$1.03^{+0.55}_{-0.16}$
NGC 4593 ^N	$0.53^{+0.14}_{-0.22}$	$1.82^{+0.01}_{-0.04}$...	$2.75^{+1.51}_{-1.06}$...	$6.49^{+0.01}_{-0.02}$
MCG -06-30-15 ^N	$2.08^{+0.10}_{-0.26}$	$2.06^{+0.10}_{-0.05}$...	$0.81^{+0.15}_{-0.27}$...	$6.44^{+0.02}_{-0.03}$
Mrk 1044 ^I	$0.79^{+0.37}_{-0.35}$	$2.37^{+0.03}_{-0.03}$	$0.93^{+0.01}_{-0.04}$...	$3.18^{+0.06}_{-0.06}$	$0.81^{+0.14}_{-0.12}$
IGRJ 19378-0617 ^I	$0.53^{+0.22}_{-0.17}$	$2.18^{+0.03}_{-0.03}$	$2.19^{+0.17}_{-0.37}$...	44^{+7}_{-3}	$3.13^{+0.06}_{-0.06}$...
Mrk 766 ^I	...	$2.30^{+0.07}_{-0.10}$	$1.93^{+0.38}_{-0.83}$...	50^{+6}_{-12}	$1.70^{+0.16}_{-0.39}$	$0.68^{+0.17}_{-0.18}$
NGC 4593 ^I	$0.39^{+0.33}_{-0.30}$	$1.80^{+0.05}_{-0.03}$	$2.47^{+0.12}_{-0.11}$...
MCG -06-30-15 ^I	$2.37^{+0.22}_{-0.30}$	$2.15^{+0.08}_{-0.08}$	$1.45^{+0.37}_{-0.81}$...	31^{+10}_{-5}	$1.86^{+0.11}_{-0.17}$	$0.71^{+0.23}_{-0.14}$
Mrk 382 ^{NR}	...	$1.81^{+0.16}_{-0.14}$
IRAS 13224-3809 ^{NR}
Mrk 841 ^{NR}	...	$1.99^{+0.07}_{-0.07}$
MR 2251-178 ^{NR}	$1.61^{+0.19}_{-0.19}$

Notes. Superscript in the object name indicates the model corresponding to the parameters (“H” for hybrid, “N” for neutral, “I” for ionized, and “NR” for nonrel.). Dots indicate when the parameter could not be constrained. Dashes indicate when the model does not contain that parameter. Column density is in units of 10^{22} cm^{-2} , ionization parameter in $\log \text{ erg cm s}^{-1}$.

Table 7
Parameters of the Sample

Source	Type	z	$\log(M_{\text{BH}})$	$\log(\lambda)$	FeK α_{rev}	$L_{2-10 \text{ keV}}$				
						$\log(L_{\text{int}})$	$\log(L_{\text{Pexrav}})$	$\log(L_{\text{Gauss}})$	$\log(L_{\text{Relxill}})$	$\log(L_{\text{total}})$
(1)	(2)	(3)	(4)	(5)	(6)	(7)	(8)	(9)	(10)	(11)
Fairall 9	Sy1.2	0.047	$8.299^{+0.078}_{-0.116}$ (a)	$-1.36^{+0.09}_{-0.13}$...	$44.01^{+0.01}_{-0.01}$	$42.16^{+0.09}_{-0.10}$	$41.91^{+0.03}_{-0.04}$	$42.77^{+0.04}_{-0.05}$	$44.04^{+0.01}_{-0.01}$
Mrk 1040	Sy1.5	0.011	$7.77^{+0.14}_{-0.14}$ (c)	$-2.18^{+0.15}_{-0.15}$	Yes (2)	$42.80^{+0.01}_{-0.01}$	$41.02^{+0.06}_{-0.02}$	$40.80^{+0.03}_{-0.04}$	$41.24^{+0.04}_{-0.05}$	$42.82^{+0.01}_{-0.01}$
Ark 120	Sy1	0.032	$8.068^{+0.048}_{-0.063}$ (a)	$-1.20^{+0.07}_{-0.07}$	Yes (3)	$43.95^{+0.02}_{-0.01}$	$41.71^{+0.02}_{-0.02}$	$41.76^{+0.03}_{-0.03}$	$43.31^{+0.01}_{-0.01}$	$44.04^{+0.02}_{-0.01}$
NGC 3227	Sy1.5	0.004	$6.684^{+0.081}_{-0.102}$ (a)	$-2.17^{+0.09}_{-0.11}$	No (1)	$41.78^{+0.01}_{-0.01}$	$40.20^{+0.03}_{-0.04}$	$40.26^{+0.03}_{-0.03}$	$42.10^{+0.05}_{-0.07}$	$42.28^{+0.03}_{-0.05}$
NGC 4051	Sy1.2	0.003	$5.891^{+0.084}_{-0.145}$ (a)	$-1.73^{+0.10}_{-0.17}$	Yes (1)	$41.43^{+0.02}_{-0.02}$	$40.03^{+0.02}_{-0.02}$	$39.20^{+0.09}_{-0.09}$	$41.12^{+0.03}_{-0.03}$	$41.62^{+0.02}_{-0.02}$
NGC 4151	Sy1.5	0.002	$7.374^{+0.027}_{-0.032}$ (a)	$-2.39^{+0.04}_{-0.04}$	Yes (1)	$42.24^{+0.01}_{-0.01}$	$40.10^{+0.01}_{-0.01}$	$40.38^{+0.02}_{-0.01}$	$41.96^{+0.02}_{-0.01}$	$42.43^{+0.01}_{-0.01}$
IRAS 13197-1627	Sy1.8	0.020	$7.81^{+0.10}_{-0.10}$ (d)	$-2.14^{+0.11}_{-0.12}$...	$42.89^{+0.01}_{-0.02}$	$41.76^{+0.01}_{-0.02}$	$41.18^{+0.01}_{-0.03}$	$41.57^{+0.02}_{-0.02}$	$42.95^{+0.01}_{-0.02}$
NGC 5548	Sy1.5	0.025	$7.692^{+0.016}_{-0.016}$ (a)	$-1.24^{+0.03}_{-0.03}$	Yes (1)	$43.59^{+0.01}_{-0.01}$	$42.69^{+0.04}_{-0.04}$	$41.56^{+0.04}_{-0.03}$	$42.85^{+0.06}_{-0.07}$	$43.71^{+0.01}_{-0.01}$
NGC 7469	Sy1.2	0.014	$6.956^{+0.048}_{-0.050}$ (a)	$-1.17^{+0.06}_{-0.06}$	Yes (1)	$43.00^{+0.01}_{-0.01}$	$41.76^{+0.03}_{-0.03}$	$41.02^{+0.03}_{-0.04}$	$41.99^{+0.04}_{-0.05}$	$43.07^{+0.01}_{-0.01}$
Mrk 915	Sy1	0.024	$7.76^{+0.37}_{-0.37}$ (e)	$-1.89^{+0.38}_{-0.38}$...	$43.07^{+0.01}_{-0.01}$	$41.53^{+0.08}_{-0.11}$	$41.18^{+0.03}_{-0.04}$...	$43.09^{+0.01}_{-0.01}$
Mrk 766	Sy1.5	0.013	$6.822^{+0.050}_{-0.057}$ (a)	$-1.30^{+0.06}_{-0.07}$	No (1)	$42.75^{+0.01}_{-0.01}$	$41.62^{+0.03}_{-0.03}$	$40.34^{+0.13}_{-0.17}$...	$42.78^{+0.01}_{-0.01}$
NGC 4593	Sy1	0.008	$6.912^{+0.069}_{-0.068}$ (a)	$-1.66^{+0.08}_{-0.08}$	No (1)	$42.50^{+0.01}_{-0.01}$	$40.93^{+0.05}_{-0.06}$	$40.63^{+0.04}_{-0.04}$...	$42.52^{+0.01}_{-0.01}$
MCG -06-30-15	Sy1.2	0.008	$6.295^{+0.157}_{-0.237}$ (a)	$-0.98^{+0.17}_{-0.25}$	No (1)	$42.56^{+0.01}_{-0.01}$	$41.53^{+0.01}_{-0.01}$	$40.52^{+0.04}_{-0.04}$...	$42.60^{+0.01}_{-0.01}$
Mrk 1044	Sy1	0.016	$6.23^{+0.50}_{-0.50}$ (b)	$-0.74^{+0.52}_{-0.51}$	Yes (4)	$42.72^{+0.02}_{-0.01}$	$42.71^{+0.01}_{-0.02}$	$43.02^{+0.01}_{-0.01}$
IGRJ 19378-0617	Sy1	0.010	$6.8^{+0.40}_{-0.40}$ (g)	$-1.44^{+0.41}_{-0.41}$...	$42.60^{+0.01}_{-0.01}$	$41.90^{+0.02}_{-0.02}$	$42.68^{+0.01}_{-0.01}$
Mrk 766	Sy1.5	0.013	$6.822^{+0.050}_{-0.057}$ (a)	$-1.34^{+0.06}_{-0.07}$	No (1)	$42.71^{+0.01}_{-0.01}$	$41.99^{+0.01}_{-0.02}$	$42.79^{+0.01}_{-0.01}$
NGC 4593	Sy1	0.008	$6.912^{+0.069}_{-0.068}$ (a)	$-1.67^{+0.08}_{-0.08}$	No (1)	$42.49^{+0.01}_{-0.01}$	$41.21^{+0.03}_{-0.03}$	$42.51^{+0.01}_{-0.01}$
MCG -06-30-15	Sy1.2	0.008	$6.295^{+0.157}_{-0.237}$ (a)	$-1.05^{+0.17}_{-0.25}$	No (1)	$42.50^{+0.01}_{-0.01}$	$41.76^{+0.01}_{-0.01}$	$42.57^{+0.01}_{-0.01}$
Mrk 382	Sy1	0.027	$6.61^{+0.50}_{-0.50}$ (b)	$-1.28^{+0.51}_{-0.51}$...	$42.57^{+0.01}_{-0.01}$	$42.57^{+0.01}_{-0.01}$
IRAS 13224-3809	NLSy1	0.066	$6.8^{+0.50}_{-0.50}$ (f)	$-1.85^{+0.51}_{-0.51}$	Yes (1)	$42.21^{+0.01}_{-0.01}$	$42.21^{+0.01}_{-0.01}$
Mrk 841	Sy1.5	0.036	$8.17^{+0.10}_{-0.10}$ (d)	$-1.42^{+0.11}_{-0.11}$	No (1)	$43.85^{+0.01}_{-0.01}$	$43.85^{+0.01}_{-0.01}$
MR 2251-178	Sy1	0.064	$8.71^{+0.11}_{-0.11}$ (c)	$-0.97^{+0.12}_{-0.12}$...	$44.68^{+0.01}_{-0.01}$	$44.68^{+0.01}_{-0.01}$

Note. (1) Name of the source; (2) AGN classification; (3) redshift; (4) $\log(M_{\text{BH}}/M_{\odot})$; (5) Eddington ratio; (6) FeK α reverberation signatures; (7)–(11) 2–10 keV band, intrinsic, PEXRAV, GAUSS, and RELXILL luminosities (in erg s^{-1}).

References. (a) Bentz & Katz (2015), (b) Wang & Lu (2001), (c) Khoruzhev et al. (2012), (d) Vasudevan et al. (2010), (e) Hinkle & Mushotzky (2021), (f) Waddell & Gallo (2020), (g) Chang et al. (2021), (1) Kara et al. (2016), (2) Tripathi et al. (2011), (3) Lobban et al. (2018), (4) Mallick et al. (2018).

data. (Note that one of their XMM-Newton and NuSTAR observations is the same that we use for this source.) Lohfink et al. (2016) fit the X-ray spectrum of Fairall 9 using a model that includes a distant reflector and a relativistically blurred ionized reflection to account for the reflection component. Analyzing Suzaku data of Ark 120, Nardini et al. (2011) conclude that to obtain a self-consistent interpretation of the broad-band X-ray emission of Ark 120, a reflection model allowing for both warm/blurred and cold/distant reprocessing is necessary. Walton et al. (2018) find that the X-ray spectrum of IRAS 13197-1627 has contributions from relativistic reflection, absorption and further reprocessing by more distant material, and absorption from an ionized outflow. NGC 5548 exhibits contributions from cold/distant reflection according to Brenneman et al. (2012). However, Dehghanian et al. (2020) find that a translucent wind can contribute a part of the FeK α emission line, arguing for a disk wind model to explain the emission lines in the source.

Note that among the objects that prefer the hybrid model, NGC 1365 and NGC 3783 show indications of additional complex spectrum. In particular, emission/absorption lines between 7 and 10 keV are clearly visible (see Figure 4). In agreement with this result, Rivers et al. (2015) find multilayer variable absorbers in NGC 1365. They find the need for three and two distinct zones of neutral and ionized absorption, respectively. Their spectral fit includes four absorption lines at 6.7, 6.97, 7.88, and 8.27 keV. In addition, Risaliti et al. (2005)

find that the spectrum of NGC 1365 switched from reflection-dominated to transmission-dominated and back in the timescale of a few weeks, which is due the variation in the absorber along the line-of-sight. In addition, emission and absorption features in the X-ray spectra of NGC 3783 have been found by Mehdipour et al. (2017) and Mao et al. (2019) to be associated with an obscuring outflow.

We find that one reflection component is a good representation of the spectra for only three objects in our sample, i.e., Mrk 915, Mrk 1044, and IGRJ 19378-0617. Supporting these results, Ballo et al. (2017) find that the reflection component of Mrk 915 can be explained with a cold reflection from distant matter, and Mallick et al. (2018) find that the broad-band spectrum of Mrk 1044 can be explained through a relativistic reflection from a high-density accretion disk with a broken power-law emissivity profile.

Thanks to the combination of NuSTAR and XMM-Newton, we could disentangle among the distant/neutral, relativistic/ionized, and hybrid baseline models for the vast majority of sources. However, three sources, i.e., Mrk 766, NGC 4593, and MCG -06-30-15, equally prefer the neutral and the relativistic/ionized scenarios. Buisson et al. (2018) test the PEXRAV +GAUSS and RELXILL models for the combination of XMM-Newton, Swift, and NuSTAR data for Mrk 766, finding no statistical differences among them. Note that we use the same data of XMM-Newton and NuSTAR, and we obtain the same conclusion about the preferred model for this source. Among

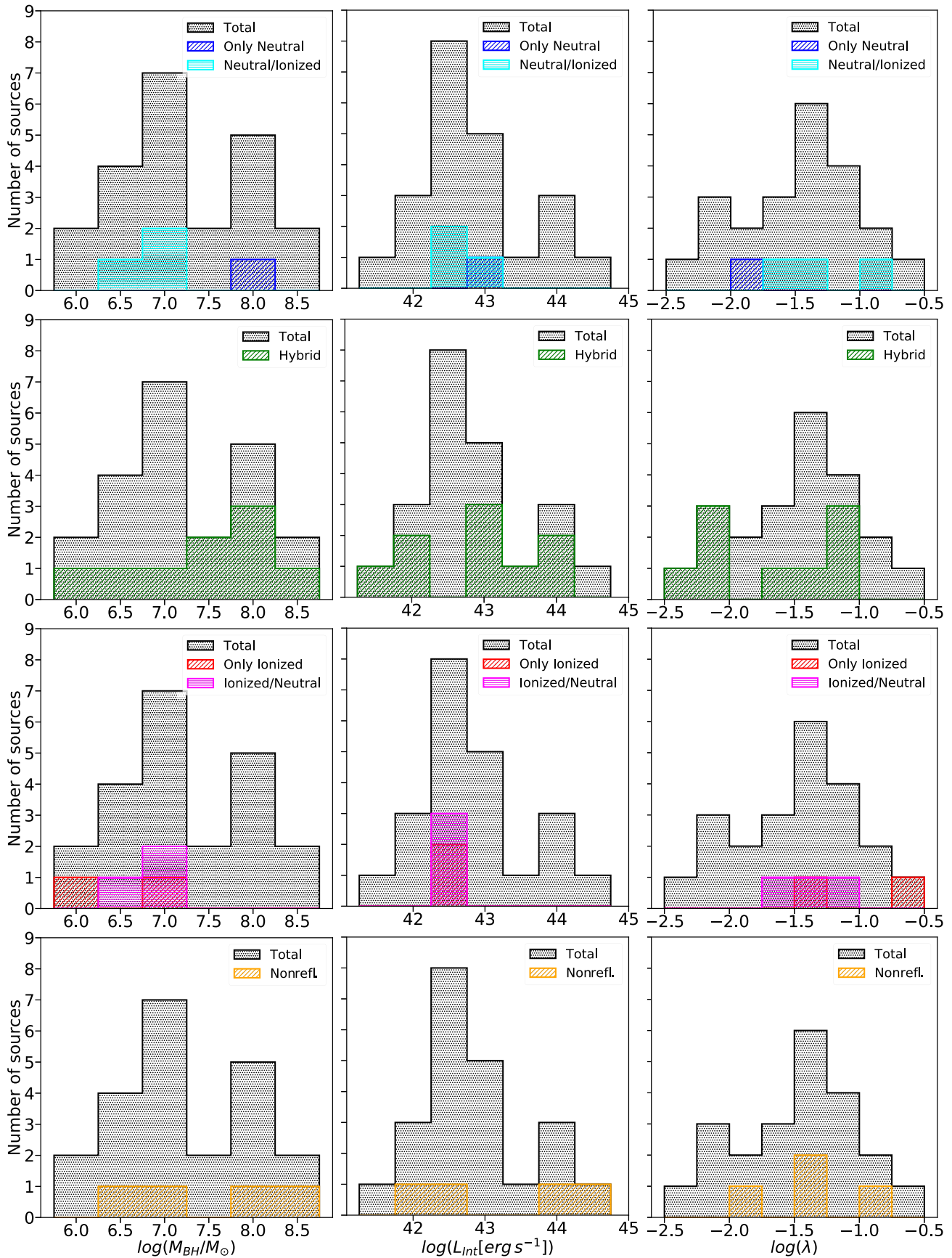


Figure 8. Histograms of the distribution of SMBH mass (top), intrinsic 2–10 keV luminosity (middle), and Eddington ratio (bottom) for the full sample (dotted) vs. the preferred model (dashed). Bars corresponding to the objects that prefer only the neutral or ionized models are given in blue and red colors. The bars of the objects that equally prefer both models are given in cyan and magenta. Note that we do not include the three sources discarded for the analysis in the intrinsic properties of the sample.

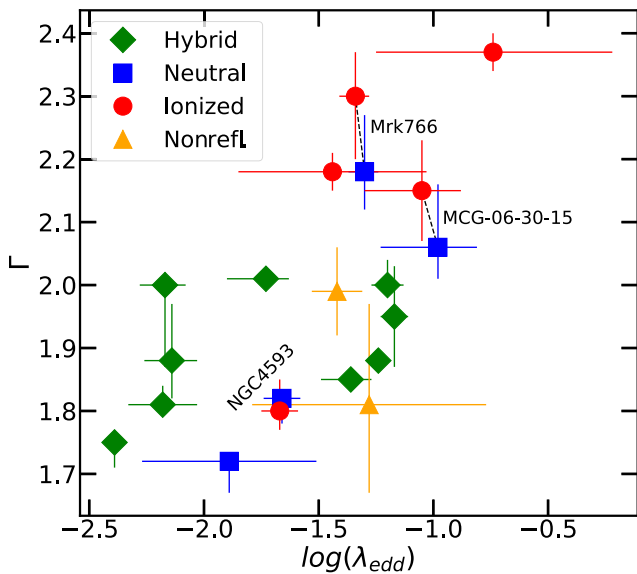


Figure 9. Photon index, Γ , vs. Eddington ratio. Green diamonds, blue squares, red circles, and yellow triangles correspond to the hybrid, neutral, ionized, and nonreflection models, respectively. Symbols of the three sources that equally prefer neutral or ionized models are joined with a dashed-black line. In addition, the name of these sources is written on the side. Note that we do not include the three sources discarded for the analysis on the intrinsic properties of the sample and do not include two nonrefl. sources because we could not get a value for the photon index of these objects.

them, a strongly debated case is MCG -06-30-15, where there is a long discussion of whether pure partial covering or disk reflection could explain the broadening of the emission line (Fabian & Vaughan 2003; Miller et al. 2008; Reynolds et al. 2009; Chiang & Fabian 2011). Among these works, Marinucci et al. (2014) test reflection and absorption models using XMM-Newton and NuSTAR data to study the variability of the source. They statistically disfavor the last model. Their reflection model includes both, cold distant, and relativistically blurred reflection. One of the three XMM-Newton observations of Marinucci et al. (2014) is also used in this work. Interestingly, the results of Marinucci et al. (2014) favors a hybrid model, while we found that our hybrid model is not required. However, we also found that MCG-06-30-15 equally prefers the neutral and the ionized model.

Under the unified model, where the different types of AGNs are explained through the viewing angle toward the observer, all objects in our sample should show the contribution of both, neutral/distant, and relativistic/ionized reflectors because our sample contains only type 1 AGNs. Supporting this, the hybrid baseline model is the best explanation for most objects in our sample. Furthermore, the role of each component to the spectral signatures is quite different—while the relativistic/ionized reflector mostly contributes to the broadening of the $\text{FeK}\alpha$ emission line and the continuum at lower energies, the distant/neutral reflector mainly contributes to the narrow component of the $\text{FeK}\alpha$ emission line and to the shape of the Compton hump above 10 keV (see Figure 4). However, even though most of the sources require these two components to fit their spectra, six objects only require one component, one of them is well fitted with only a neutral/distant reflector, and two objects are well fitted with only a relativistic/ionized reflector. For the other three objects, only neutral/distant or ionized/relativistic are equally preferred. Additionally, it is also worth noting that the relativistic/ionized reflector is, on average, contributing

more than the distant/neutral reflector to the 2–10 keV X-ray luminosity for our sample (see Figure 10). Contrary to the unified model, these results suggest that the difference between AGN types is due to their intrinsic properties rather than their orientation.

It is possible to test if the reflection occurs in the accretion disk through X-ray reverberation mapping around the $\text{FeK}\alpha$, which measures the time delays between the photons from the corona and the photons from the accretion disk (Uttley et al. 2014). $\text{FeK}\alpha$ reverberation signatures has been searched in 16 out of the 22 objects in our sample (compiled in Table 7, including Mrk 335, NGC 1365, and NGC 3783; Tripathi et al. 2011; Kara et al. 2016; Lobban et al. 2018; Mallick et al. 2018). Among them, 11 show $\text{FeK}\alpha$ time delays, and all but IRAS 13224-3809 are fitted in this work to the hybrid or the ionized model. Meanwhile, five sources do not show signatures of $\text{FeK}\alpha$ time delays—one does not show a reflection component, one is fitted to the neutral model, one is fitted to the hybrid model, and the other two are equally best fitted to both ionized and neutral models. These results are compatible with our best fitted models.

The two modes of accretion onto black holes (for stellar mass and supermassive black holes) are either via a geometrically thin and optically thick disk or via a truncated outer disk and a hot optically thin and geometrically extended advection-dominated flow, which are present in low-mass X-ray binaries (LMXBs) and AGNs (Meyer-Hofmeister et al. 2009). Studying the LMXBs, the authors claim that for high Eddington ratios, the disk reaches inward to the last stable orbit; however, a gap in the disk appears if the Eddington ratio begins to slow (see their Figure 1). In a study carried out on a sample of unobscured broad-line, narrow-line, and lineless AGNs, Trump et al. (2011) shows that the Eddington ratio governs their physical properties, arguing that the disappearance of the broad emission lines in their sample can be explained by an expanding radiatively inefficient accretion flow at the inner radius of the accretion disk. Assuming that the distant and neutral reflection component always shows the same contribution, which seems to be the case for type-2 and/or low-luminosity AGNs (Osorio-Clavijo et al. 2022), the preponderance of these two components might be related to this accretion state. In AGNs at a high state, the disk is well constructed until the innermost stable orbit, which is responsible for most of the reflection component. If that is the case, then the signatures of distant and neutral reflectors are simply diluted by this prominent disk-reflection component. Meanwhile, the objects that are fitted only with the neutral/distant reflection component might have an inner inefficient flow, which makes the accretion disk reflection negligible because the disk starts further out from the emitting X-ray corona. Objects that prefer the hybrid model are in an intermediate state. However, note that these objects shows a wide range of Eddington ratios, from $\log(\lambda) = -1.17 \pm_{0.06}^{0.06}$ up to $\log(\lambda) = -2.39 \pm_{0.04}^{0.04}$.

6. Summary

We have studied the scattered medium of a sample of 22 Seyfert galaxies using simultaneous observations of XMM-Newton and NuSTAR. For this purpose, we selected and tested a set of available reflection models using the XSPEC spectral fitting package. The main results are as follows:

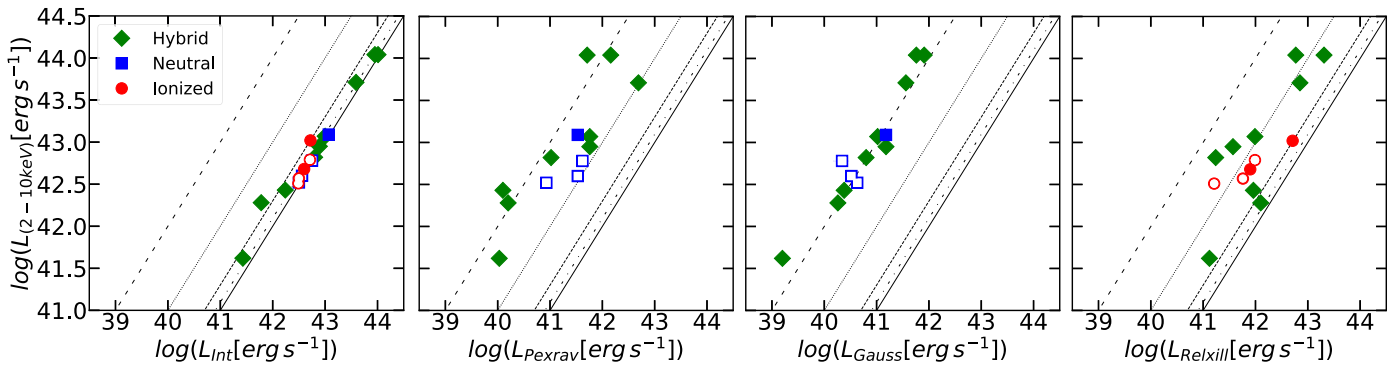


Figure 10. 2–10 keV band luminosity vs. that of intrinsic continuum (left hand), and neutral (middle) and ionized (right hand) according to each model. Lines represent the percentage of the quantity in the X-axis with respect to the Y-axis. From bottom to top 100%, 80%, 50%, 10%, and 1% of the intrinsic (left-hand panel) and reflection (right-hand panels) luminosities. Green diamonds, blue squares, and red circles correspond to the hybrid, neutral, and ionized models, respectively. Empty symbols correspond to the sources that equally prefer neutral or ionized model.

1. We find that 18 sources show evidence of the reflection. Among them, 12 objects prefer a hybrid reflection model, which incorporates neutral and relativistic ionized medium; one object prefers a neutral reflection model; two objects prefer a relativistic ionized reflection model; and three objects equally prefer the neutral and relativistic ionized reflection models.
2. We find that four objects do not present the reflection component. We propose the variability of activity of sources as a possible explanation.
3. For most objects, the intrinsic luminosity represents between 80% and 100% of the total luminosity. The neutral reflection component has the smallest contribution to the total luminosity, representing this with less than 10%. The ionized reflection component contributes over 10% for almost all objects.

These results suggest that a hybrid scenario, in which the reflection from type-1 AGNs has a contribution from at least two different media, can satisfactorily explain the observed spectra of most of these objects.

Acknowledgments

We thank the anonymous referee for his/her useful comments. C.V.-C. and N.O.-C. acknowledge support from a CONACyT scholarship. O.G.-M. acknowledges financial support by the UNAM PAPIIT projects IN105720 and IN109123, and support from the project CF-2023-G-100 CONACyT Frontera de la ciencia. J.-M. acknowledges financial support from the State Agency for Research of the Spanish MCIU through the “Center of Excellence Severo Ochoa” award to the Instituto de Astrofísica de Andalucía

(grant No. SEV-2017-0709) and the Spanish Ministry of Economy and Competitiveness under grant Nos. AYA2016-76682-C3 and PID2019-106027GB-C41. A.L.-L. acknowledges support from CONACyT grant No. CB-2016-01-286316 and from DGAPA PAPIIT IA-101623. D.E.-A. acknowledges financial support from MICINN (Spain) through the program Juan de la Cierva, and support from the Spanish Ministry of Science, Innovation, and Universities (MCIU), Agencia Estatal de Investigación (AEI), and the Fondo Europeo de Desarrollo Regional (EU-FEDER) under projects with references AYA2015-68217-P and PID2019-107010GB-100. This research has made use of dedicated servers (IRyAGN2, Galaxias and Arambolas servers and Calzonzin and Mouruka clusters) maintained by Daniel Díaz-González, Miguel Espejel, Alfonso Ginori González, and Gilberto Zavala at IRyA-UNAM. All of them are gratefully acknowledged.

Appendix Nonreflection Objects

Figure 11 shows the power-law fit to Mrk 382, IRAS 13224-3809, and MR 2251-178, which do not require the reflection component according to the F-test statistic (in addition to Mrk 841, which is described in Section 4.1. See also Figure 3). The spectrum of MR 2251-178 is well fitted with a power law. The FeK line or Compton hump features are absent in the spectrum. The case of IRAS 13224-3809 is more complex, where the spectrum shows poor S/N above ~ 10 keV. In this object, the S/N is likely to be the reason why we cannot find the presence of the reflection component in our analysis.

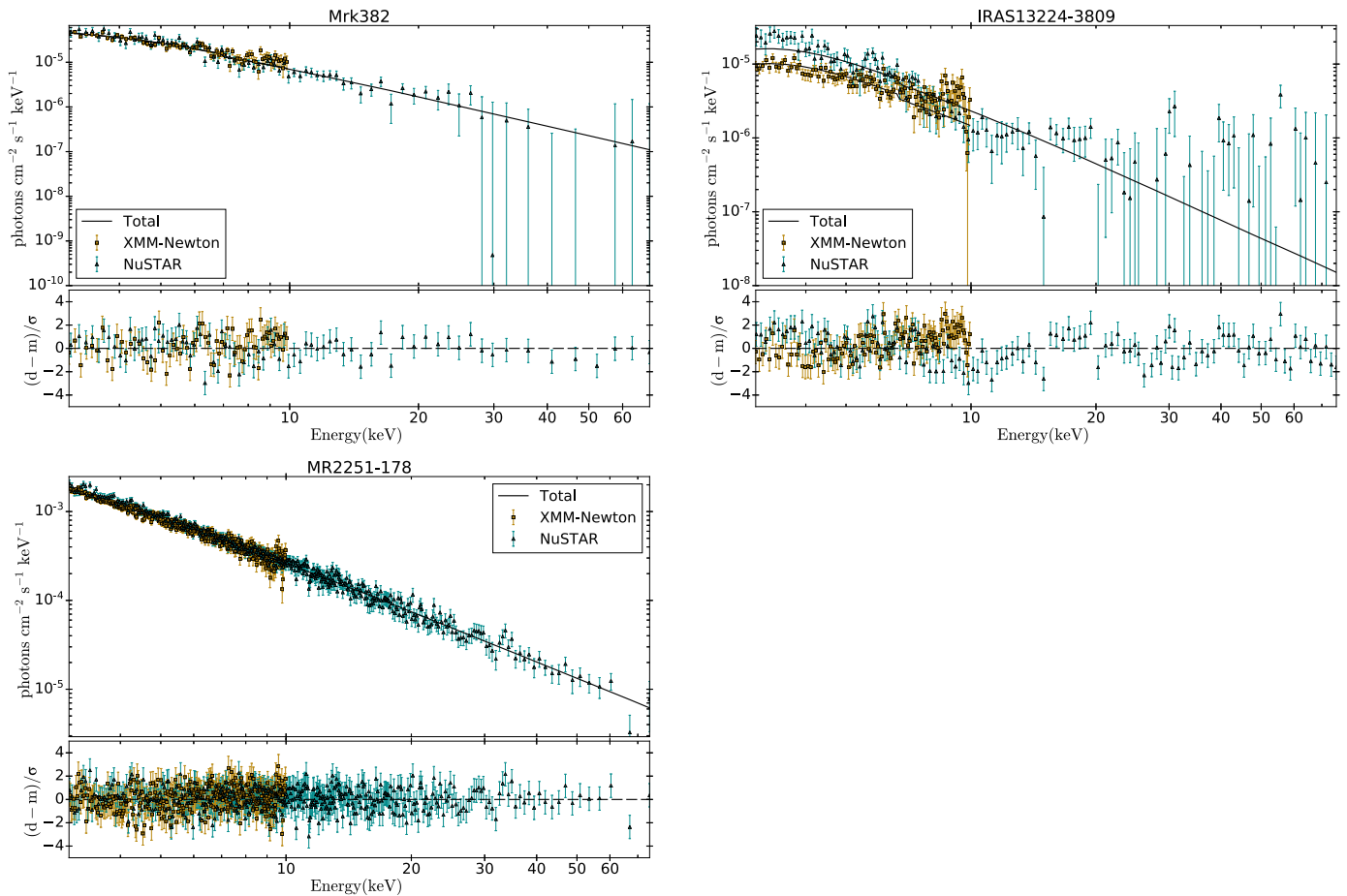



Figure 11. Power-law fit to Mrk 382 (top left-hand panel), IRAS 13224-3809 (top right-hand panel), and MR 2251-178 (bottom panel). We show the best fit (black and red solid lines) to the data in the top panel and the ratio between model and data in the bottom panel. The gold and dark cyan dots show the data from XMM-Newton and NuSTAR, respectively.

ORCID iDs

César Ivan Victoria-Ceballos  <https://orcid.org/0000-0001-5625-7815>

Omaira González-Martín  <https://orcid.org/0000-0002-2356-8358>

Anna Lia Longinotti  <https://orcid.org/0000-0001-8825-3624>

Natalia Osorio-Clavijo  <https://orcid.org/0000-0002-3467-8077>

References

Ballo, L., Severgnini, P., Della Ceca, R., et al. 2017, *MNRAS*, 470, 3924
 Baloković, M., Brightman, M., Harrison, F. A., et al. 2018, *ApJ*, 854, 42
 Bauer, F. E., Arévalo, P., Walton, D. J., et al. 2015, *ApJ*, 812, 116
 Bentz, M. C., & Katz, S. 2015, *PASP*, 127, 67
 Bianchi, S., Matt, G., Balestra, I., et al. 2004, *A&A*, 422, 65
 Blustin, A. J., Branduardi-Raymont, G., Behar, E., et al. 2002, *A&A*, 392, 453
 Brenneman, L. W., Elvis, M., Krongold, Y., et al. 2012, *ApJ*, 744, 13
 Brenneman, L. W., Reynolds, C. S., Nowak, M. A., et al. 2011, *ApJ*, 736, 103
 Brightman, M., Baloković, M., Stern, D., et al. 2015, *ApJ*, 805, 41
 Brightman, M., & Nandra, K. 2011, *MNRAS*, 413, 1206
 Brightman, M., & Ueda, Y. 2012, *MNRAS*, 423, 702
 Buisson, D. J. K., Parker, M. L., Kara, E., et al. 2018, *MNRAS*, 480, 3689
 Chang, N., Xie, F. G., Liu, X., et al. 2021, *MNRAS*, 503, 1987
 Chiang, C.-Y., & Fabian, A. C. 2011, *MNRAS*, 414, 2345
 Dauser, T., Wilms, J., Reynolds, C. S., et al. 2010, *MNRAS*, 409, 1534
 Dehghanian, M., Ferland, G. J., Kriss, G. A., et al. 2020, *ApJ*, 898, 141
 Dewangan, G. C., Griffiths, R. E., Dasgupta, S., et al. 2007, *ApJ*, 671, 1284

Diaz, Y., Arévalo, P., Hernández-García, L., et al. 2020, *MNRAS*, 496, 5399
 Emmanoulopoulos, D., Papadakis, I. E., Epitropakis, A., et al. 2016, *MNRAS*, 461, 1642
 Emmanoulopoulos, D., Papadakis, I. E., McHardy, I. M., et al. 2011, *MNRAS*, 415, 1895
 Fabian, A. C., Rees, M. J., Stella, L., et al. 1989, *MNRAS*, 238, 729
 Fabian, A. C., & Vaughan, S. 2003, *MNRAS*, 340, L28
 Falocco, S., Carrera, F. J., Barcons, X., et al. 2014, *A&A*, 568, A15
 Fanali, R., Caccianiga, A., Severgnini, P., et al. 2013, *MNRAS*, 433, 648
 Gallo, L. C., Boller, T., Tanaka, Y., et al. 2004, *MNRAS*, 347, 269
 García, J., Dauser, T., Lohfink, A., et al. 2014, *ApJ*, 782, 76
 George, I. M., & Fabian, A. C. 1991, *MNRAS*, 249, 352
 Gofford, J., Reeves, J. N., Turner, T. J., et al. 2011, *MNRAS*, 414, 3307
 Gondoin, P., Lumb, D., Siddiqui, H., et al. 2001, *A&A*, 373, 805
 Haardt, F., & Maraschi, L. 1993, *ApJ*, 413, 507
 Harrison, F. A., Craig, W. W., Christensen, F. E., et al. 2013, *ApJ*, 770, 103
 Hinkle, J. T., & Mushotzky, R. 2021, *MNRAS*, 506, 4960
 Inaba, K., Ueda, Y., Yamada, S., et al. 2022, *ApJ*, 939, 88
 Jansen, F., Lumb, D., Altieri, B., et al. 2001, *A&A*, 365, L1
 Jiang, J., Parker, M. L., Fabian, A. C., et al. 2018, *MNRAS*, 477, 3711
 Kalberla, P. M. W., Burton, W. B., Hartmann, D., et al. 2005, *A&A*, 440, 775
 Kara, E., Alston, W. N., Fabian, A. C., et al. 2016, *MNRAS*, 462, 511
 Khorunzhev, G. A., Sazonov, S. Y., Burenin, R. A., et al. 2012, *AstL*, 38, 475
 Krongold, Y., Longinotti, A. L., Santos-Lleó, M., et al. 2021, *ApJ*, 917, 39
 Krongold, Y., Nicastro, F., Brickhouse, N. S., et al. 2003, *ApJ*, 597, 832
 Krongold, Y., Nicastro, F., Brickhouse, N. S., et al. 2005, *ApJ*, 622, 842
 Laha, S., & Ghosh, R. 2021, *ApJ*, 915, 93
 Laor, A. 1991, *ApJ*, 376, 90
 Liu, H., Wang, H., Abdikamalov, A. B., et al. 2020, *ApJ*, 896, 160
 Lobban, A. P., Porquet, D., Reeves, J. N., et al. 2018, *MNRAS*, 474, 3237
 Lohfink, A. M., Reynolds, C. S., Pinto, C., et al. 2016, *ApJ*, 821, 11
 Longinotti, A. L., Nandra, K., Petrucci, P. O., et al. 2004, *MNRAS*, 355, 929

- Longinotti, A. L., Sim, S. A., Nandra, K., et al. 2007, *MNRAS*, **374**, 237
- Magdziarz, P., & Zdziarski, A. A. 1995, *MNRAS*, **273**, 837
- Mallick, L., Alston, W. N., Parker, M. L., et al. 2018, *MNRAS*, **479**, 615
- Mao, J., Mehdipour, M., Kaastra, J. S., et al. 2019, *A&A*, **621**, A99
- Marchesi, S., Ajello, M., Marcotulli, L., et al. 2018, *ApJ*, **854**, 49
- Marchesi, S., Zhao, X., Torres-Albà, N., et al. 2022, *ApJ*, **935**, 114
- Marconi, A., Risaliti, G., Gilli, R., et al. 2004, *MNRAS*, **351**, 169
- Marinucci, A., Matt, G., Miniutti, G., et al. 2014, *ApJ*, **787**, 83
- Matsuoka, M., Piro, L., Yamauchi, M., et al. 1990, *ApJ*, **361**, 440
- Mehdipour, M., Kaastra, J. S., Kriss, G. A., et al. 2015, *A&A*, **575**, A22
- Mehdipour, M., Kaastra, J. S., Kriss, G. A., et al. 2017, *A&A*, **607**, A28
- Meyer-Hofmeister, E., Liu, B. F., & Meyer, F. 2009, *A&A*, **508**, 329
- Miller, L., Turner, T. J., & Reeves, J. N. 2008, *A&A*, **483**, 437
- Miller, L., Turner, T. J., & Reeves, J. N. 2009, *MNRAS Lett.*, **399**, L69
- Nandra, K., O'Neill, P. M., George, I. M., et al. 2007, *MNRAS*, **382**, 194
- Nardini, E., Fabian, A. C., Reis, R. C., et al. 2011, *MNRAS*, **410**, 1251
- Nardini, E., Reeves, J. N., Porquet, D., et al. 2014, *MNRAS*, **440**, 1200
- O'Neill, P. M., Nandra, K., Cappi, M., et al. 2007, *MNRAS Lett.*, **381**, L94
- Osorio-Clavijo, N., González-Martín, O., Sánchez, S. F., et al. 2022, *MNRAS*, **510**, 5102
- Panagiotou, C., & Walter, R. 2019, *A&A*, **626**, A40
- Parker, M. L., Longinotti, A. L., Scharfel, N., et al. 2019, *MNRAS*, **490**, 683
- Patrick, A. R., Reeves, J. N., Porquet, D., et al. 2011, *MNRAS*, **411**, 2353
- Petrucci, P. O., Henri, G., Maraschi, L., et al. 2002, *A&A*, **388**, L5
- Porquet, D., Reeves, J. N., Matt, G., et al. 2018, *A&A*, **609**, A42
- Pounds, K. A., Nandra, K., Stewart, G. C., et al. 1990, *Natur*, **344**, 132
- Reis, R. C., Fabian, A. C., Reynolds, C. S., et al. 2012, *ApJ*, **745**, 93
- Reynolds, C. S., Fabian, A. C., Brenneman, L. W., et al. 2009, *MNRAS Lett.*, **397**, L21
- Ricci, C., Ueda, Y., Koss, M. J., et al. 2015, *ApJL*, **815**, L13
- Ricci, C., Walter, R., Courvoisier, T. J.-L., et al. 2011, *A&A*, **532**, A102
- Risaliti, G., Elvis, M., Fabbiano, G., et al. 2005, *ApJL*, **623**, L93
- Rivers, E., Risaliti, G., Walton, D. J., et al. 2015, *ApJ*, **804**, 107
- Ross, R. R., & Fabian, A. C. 2005, *MNRAS*, **358**, 211
- Ross, R. R., Fabian, A. C., & Young, A. J. 1999, *MNRAS*, **306**, 461
- Singh, K. P., Rao, A. R., & Vahia, M. N. 1992, *A&A*, **262**, 49
- Strüder, L., Briel, U., Dennerl, K., et al. 2001, *A&A*, **365**, L18
- Traina, A., Marchesi, S., Vignali, C., et al. 2021, *ApJ*, **922**, 159
- Tripathi, S., Misra, R., Dewangan, G., et al. 2011, *ApJL*, **736**, L37
- Trump, J. R., Impey, C. D., Kelly, B. C., et al. 2011, *ApJ*, **733**, 60
- Ursini, F., Petrucci, P.-O., Matt, G., et al. 2016, *MNRAS*, **463**, 382
- Uttley, P., Cackett, E. M., Fabian, A. C., et al. 2014, *A&ARv*, **22**, 72
- Vasudevan, R. V., Fabian, A. C., Gandhi, P., et al. 2010, *MNRAS*, **402**, 1081
- Waddell, S. G. H., & Gallo, L. C. 2020, *MNRAS*, **498**, 5207
- Walton, D. J., Brightman, M., Risaliti, G., et al. 2018, *MNRAS*, **473**, 4377
- Wang, T., & Lu, Y. 2001, *A&A*, **377**, 52
- Zdziarski, A. A., Johnson, W. N., Done, C., et al. 1995, *ApJL*, **438**, L63

4.1 Introduction

Different authors have studied the soft excess in individual objects and samples of several objects in order to clarify its origin. However, the understanding of this soft excess remains a matter of debate, mainly because it has been difficult to discern between the various proposed models. For instance, Sobolewska & Done (2007) test the comptonized emission, reflection, and absorption models to explain the soft excess in PG 1211+143. They found that their statistics criteria are not sufficient to discriminate among them, they favour the absorption model because it requires less extreme parameters. García et al. (2019) study the soft excess in Mrk 509. They find that the soft spectrum of this source can be statistically equally described by two different models, a warm corona or relativistically-blurred reflection of the accretion disk. However, they favour the relativistic reflection model because the parameters required by the warm corona are physically incompatible with the conditions of standard corona. Gliozzi & Williams (2020) study the soft excess a sample of 30 narrow-line Seyfert 1 (NLSy1) and 59 broad-line Seyfert 1 (BLSy1) galaxies, by performing their spectral analysis in the 0.5-10 keV band. They find that the soft excess is detected in both NLSy1 and BLSy1, however, the strength of the soft excess is larger in the NLSy1 compared to the BLSy1. Also, their results suggest that the origin of the

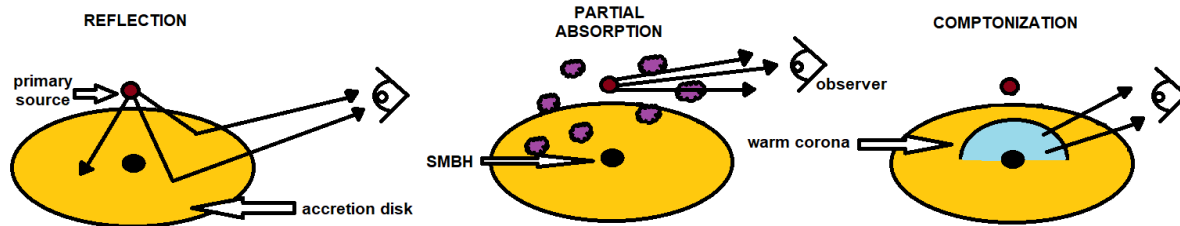


Figure 4.1: Sketch of the relativistically blurred reflection (left), relativistically smeared absorption (middle), and Comptonization (right) models. Purple clouds in partial absorption scenario represent the partially ionized material absorbing the intrinsic emission (wind close to the SMBH or clouds of the BLR). Note that the inclination of the accretion disk respect to the LOS may not completely correspond to a type-1 AGN, however it is oriented this way for illustrative purposes.

soft excess is a warm Comptonization component. On the other hand, Ding et al. (2022), study the soft excess in a sample of 15 NLSy1, by performing their spectral analysis below 10 keV. Their results suggest that the origin of the soft excess is different for NLSy1 and BLSy1, where the relativistic reflection model explains the soft excess in NLSy1, whereas, in BLSy1, the warm corona model is favoured. We show in Figure 4.1 a sketch of the relativistically blurred reflection, relativistically smeared absorption, and comptonization scenarios.

Note that, the works mentioned above are done using data below 10 keV. However, in order to investigate the origin of the soft excess, a broad band spectral analysis is necessary to discriminate between the different scenarios proposed, because different scenarios of the origin of the soft excess imply different behaviors in the soft ($\lesssim 2$ keV) and hard (~ 2 -70 keV) X-ray bands, e.g. the relativistically-blurred reflection scenario covers a broad energy range (soft and hard bands), while the Comptonization scenario drops very quickly in the soft band (Boissay et al., 2016). The goal of our work is to test different models proposed to explain the soft excess in type-1 AGN, by performing a broad band spectral analysis, from 0.5 to 70 keV, on the same sample we performed the hard band analysis in Chapter 3 which contains 22 type-1 AGN.

4.2 Soft band spectral fitting procedure

4.2.1 Initial setup for the spectral fitting

In order to investigate the soft excess in type-1 AGN, we use the same sample studied in Victoria-Ceballos et al. (2023). Note that in that analysis (Chapter 3) we modelled the hard X-ray band in the range of 3-70 keV. This sample contains 22 sources with simultaneous *XMM-Newton* and *NuSTAR* data, among which there are 1 NLSy1, 19 Sy1-Sy1.5, and 2 Sy1.8. We use this sample to take advantage of the detailed modeling performed on the hard band, through which we obtained the preferred reflection model through testing several models. This will facilitate the study on the soft band and allows a more robust analysis of the soft excess.

In Victoria-Ceballos et al. (2023), for the reflection component, which is present in 18 out of the 22 AGN, we systematically fit the spectra to three reflection scenarios: neutral/distant, ionized/relativistic, and the hybrid scenario, neutral/distant plus ionized/relativistic. We found that 12 sources prefer the hybrid scenario, two sources prefer the ionized/relativistic scenario, one source prefer the neutral/distant scenario, and three sources equally prefer the neutral/distant and ionized/relativistic scenario. The baseline model for these objects has the form:

$$M = Cte * Abs_{Gal}(absorber * intrinsic + reflection) \quad (4.1)$$

where reflection component is RELXILL, PEXRAV+GAUSS, or PEXRAV+GAUSS+RELXILL for the IONIZED, NEUTRAL and HYBRID scenarios, respectively. Note that there is no reflection component detected in sources preferring the NON-REFL scenario. Cte is a multiplicative constant to account the *NuSTAR* and *XMM-Newton* cross-calibration issues (the value of this constant was calculated in Victoria-Ceballos et al. (2023), and its value is close to unity). Abs_{Gal} accounts for the Galactic absorption (which we model with PHABS), and absorber * intrinsic represents the intrinsic continuum absorbed by the material along the LOS to the observer, which we model with a cutoff power-law affected by a neutral absorber (ZPCFABS*ZCUTOFFPL.)

Following these results, we use the preferred model by each source to study the soft excess in our sample. Note that, three objects (namely NGC 4593, Mrk 766, and MCG-06-30-15) are equally well fitted with two different models (IONIZED and NEUTRAL), so we performed spectral fits starting from both baseline models for these three objects. Keep in mind that in order to differentiate both models in the same object, we indicate throughout the text with a superscript I or N when the model is IONIZED or NEUTRAL, respectively. With this distinction we have a total of 25 spectra for our study of soft excess. We add the data between 0.5 and 3 keV provided by *XMM*-Newton for our study of the soft band. Therefore, we cover the full range of energies between 0.5 and 70 keV.

For our study of the soft excess we tested different scenarios and models: The scenario of the soft excess as the accretion disk tail, modeled by a black-body; the soft excess as comptonized material by a warm corona; the soft excess as absorption of the intrinsic emission by partially ionized material, and the scenario of the soft excess as relativistically-blurred reflection due to the accretion disk. Also, we tested the effect of the cold partial covering material absorbing the intrinsic emission (similar to the absorption by partially ionized material scenario), and we investigate the contribution to the soft band of the star formation activity, which could be seen as soft excess. We show in Figure 4.2 a scheme of the scenarios and models used in this chapter.

4.2.2 Initial extrapolation

We begin the study of the soft excess by extrapolating to the soft band (0.5-3 keV) the preferred model/s by each source obtained through our study of the X-ray reflection scenarios in the hard band (3-70 keV). For this first test, we add the soft spectrum and we keep all model parameters fixed. The objective of this first test is to investigate if the sources shows the soft excess or not, and if the model as it is (without any addition) is able to explain the soft excess when it exists.

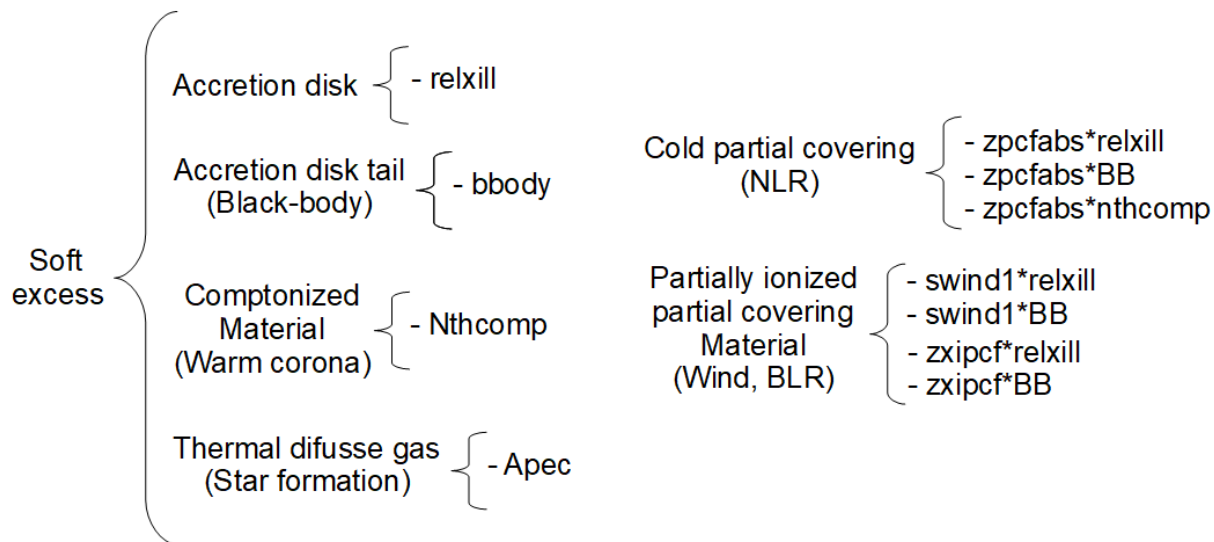


Figure 4.2: Scheme of the scenarios and models tested to explain the soft excess. Middle spanner shows the physical scenario associated to the physical structure (in parentheses). Last spanner shows the name of the model in XSPEC.

4.2.3 Cold partial covering

Then, due to the fact that the accretion disk and the hot corona are located at the inner part of the AGN, we assume that both components must be affected by the same absorption. Therefore, for our study of the soft band, we apply the same neutral absorption of the power-law to the ionized/relativistic reflection in those objects that have this component, i.e., for sources preferring the HYBRID and the IONIZED/RELATIVISTIC models. For this, we allow to vary the column density and covering fraction parameters of the neutral absorption component (ZPCFABS). The baseline model for this test has the form:

$$M = Cte * Abs_{Gal}[partial\ covering(intrinsic + reflection)] \quad (4.2)$$

We show in Figure 4.3 the effect of this component for different values of covering fraction and column density.

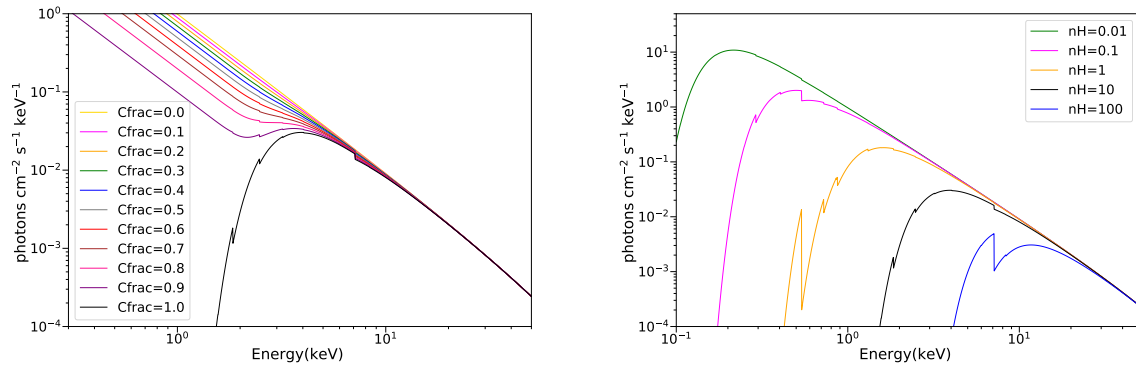


Figure 4.3: Example of the resulting X-ray spectra of an absorbed power-law with photon index $\Gamma = 2$. Left: for different values of the covering fraction, where $Cfrac=0$ implies no absorption, while $Cfrac=1$ implies full absorption of the source. All spectra correspond to a column density of 10^{23}cm^{-2} . Right: for different values of the column density (in units of 10^{22}cm^{-2}). All spectra correspond to a covering $Cfrac=1$.

4.2.4 The soft excess as Comptonized material

Motivated by the fact that the intrinsic emission is related to the comptonization of optical/UV photons from the accretion disk (Magdziarz et al., 1998; Gliozzi & Williams, 2020), we add a thermally comptonized continuum component, by using the NTHCOMP model available in XSPEC. The parameters of NTHCOMP are the power-law photon index, the electron temperature, the seed photon temperature, the type (0 or 1 for black body or disk-blackbody seed photons, respectively), the redshift, and its normalization. We link the photon index of NTHCOMP to the photon index of the power-law component, the redshift to that of the sources, and we allow to vary the electron and photon temperatures during the spectral fit. The baseline model for this test is:

$$M = Cte * Abs_{Gal}[comptonized + partial\ covering(intrinsic + reflection)] \quad (4.3)$$

Although, physically motivated, we obtain quite poor spectral fits with this model (see Section 4.3.3), so we ruled out continuing to add this model in subsequent tests.

4.2.5 The soft excess as a blackbody

In order to fit the soft excess, other authors have obtained satisfactory results by using a single black-body component (Vasudevan et al., 2014). So we decided to add this component to our baseline model. Note that the physical interpretation of this black-body component is not clear. We use this phenomenological model and then we will discuss the plausible origin for this component if needed. For this test, we use the ZBBODY model in XSPEC. The ZBBODY model contains three parameters: the temperature of the black-body, the redshift, and the normalization. To add further complexity required for some of the objects in our sample (see Section 4.3), we also include two black-bodies to the baseline models. We allow to vary the black-body temperature and normalization in the spectral fitting, and we do not link the parameters when we test this two black-bodies scenarios. The baseline models including one and two ZBBODY have the form:

$$M = Cte * Abs_{Gal}[blackbody + partial\ covering(intrinsic + reflection)](4.4)$$

$$M = Cte * Abs_{Gal}[blackbody + blackbody + partial\ covering(intrinsic + reflection)](4.5)$$

4.2.6 Soft excess as host-galaxy circumnuclear contributors

In order to test the possible contribution of the star formation activity in the host galaxy (González-Martín et al., 2006, 2009) in our spectra, we add the APEC model (Smith et al., 2001) in our baseline model. APEC reproduces the spectrum from optically thin thermal plasma, associated with heating by stellar processes (thermal diffuse gas). Their parameters are the plasma temperature, the metal abundances, the redshift, and its normalization. We fixed the redshift to that of the source and we allowed to vary all the other parameters during the spectral fit. Our baseline model for this test is:

$$M = Cte * Abs_{Gal}[apec + partial\ covering(intrinsic + reflection)] \quad (4.6)$$

Then, we test our baseline models considering both components, APEC and ZBBODY, ie.

considering the contribution of the star formation and the contribution of the black-body:

$$M = Cte * Abs_{Gal}[apec + blackbody + partial\ covering(intrinsic + reflection)] \quad (4.7)$$

4.2.7 Soft excess as partially ionized partial covering

In order to test the partially ionized absorption scenario to explain the soft excess (Gierliński & Done, 2004; Middleton et al., 2007), we decided to add an ionized absorption component on the intrinsic emission in our baseline model. For this, we test two models: 1) SWIND1, which considers absorption by partially ionized material with large velocity shear. The column density, ionization parameter, velocity smearing of the material, and the redshift, are the four parameters for this model. 2) ZXIPCF, which considers partial covering absorption by partially ionized material, and it contains four parameters: the column density, ionization parameter, covering fraction of the material, and the redshift. The main difference between both models are that ZXIPCF considers partial covering, while SWIND1 considers full covering. Note that, while BBODY, APEC, and NTHCOMP are additive model components, SWIND1 and ZXIPCF are multiplicative model components, which have an effect only on the component in which they are placed.

Since we got better fits with ZXIPCF, we opted to use this model for the rest of the work. We test their effect on the power-law in our baseline model, and we allow to vary all parameters, except the redshift, which we fixed to that of each source. The corresponding baseline model to this test has the following form:

$$M = Cte * Abs_{Gal}[(cold\ partial\ covering * warm\ partial\ covering * intrinsic) + reflection] \quad (4.8)$$

Note that, this baseline model includes both, neutral and ionized partial covering absorption. In Figure 4.4, we show an example of the resulting X-ray spectrum for an absorbed power-law by only ionized, and neutral/ionized material. As can be seen, the effect of ionized absorption is to add absorption lines to the spectrum, mainly below 3 keV, although it also has several absorption lines in the 6-8 keV range.

We also test the scenario in which the warm absorber also affects the ionized/relativistic

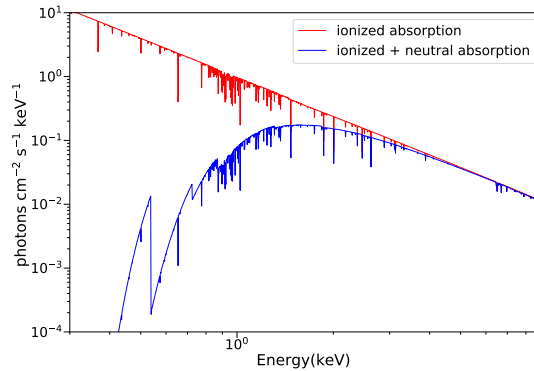


Figure 4.4: Example of the resulting X-ray spectrum of a absorbed power-law with photon index $\Gamma = 2$ by ionized (red), and neutral and ionized material (blue). Both spectra correspond to a column density of 10^{22}cm^{-2} , and covering fraction of 1. While the neutral absorption adds a curvature to the spectrum (also shown in Fig.X), the effect of the ionized absorber is to add absorption features on top of such continuum.

component. This scenario assumes that the absorber affects both the intrinsic and disk reflection at the same time because they arise in the same region of the AGN. The baseline model has the form:

$$M = Cte * Abs_{Gal}[cold\ partial\ covering * warm\ partial\ covering(intrinsic + reflection)] \quad (4.9)$$

All the tests mentioned above are made considering the effects of the absorption only on the intrinsic and disk reflection components. In order to test the effect of the warm absorption also on the black-body component, we perform different spectral fits for different combinations including these components. This can also provide information about the location of the absorbent material, which could be very close to the nucleus (possibly wind over the accretion disk) or further away (possibly BLR clouds). In this way, we have four different scenarios where the warm absorption affects: i) the intrinsic and reflected emission, but not on the black body; ii) the black body, but not on the intrinsic and reflected emission; iii) the black body and the reflected emission, but not on the intrinsic; and iv) the black body, the intrinsic, and the reflected emission. These four scenarios above described were tested for one black-body, for two black-body, and for APEC plus one black-body. We show in Figure 4.5 a sketch of the four scenarios tested, assuming the lamp-post

scenario for the corona (Fabian et al., 2017)¹. The reflection occurs in the inner part of the accretion disk, while the black-body emission arises in the outer parts, starting from a radius R_{cut} . In the first scenario the absorber exists up to R_{cut} , and is capable of absorbing both intrinsic and reflected emission. Because this material is not present beyond R_{cut} , the black-body emission does not suffer this absorption. The second scenario is similar, but the absorbing material appears from R_{cut} , so it only affects the black-body emission. In the third case, the material exists at all radius, but reaches only a small height respect to the accretion disk, so it only affects the reflected and the black-body emission. In the last scenario the material is also present at all radius, but reaches a sufficient height to affect all emission components. Due to the effect of the absorber on the different components, the first three scenarios are more probably associated to the wind over the accretion disk, while in the last scenario, the absorber material can be, in addition to the wind, BLR clouds, since being further away it is capable of intercepting the LOS and absorbing the nuclear emission. Note that these tests are an attempt to obtain clues about the location of the partially ionized partial covering material.

4.2.8 Simultaneous fit of the soft and hard spectra

Considering all the scenarios mentioned in the previous sections, we tested a total of 14 models on each sample object, and through AIC and F-test we obtained the preferred model/s for each source.

For the last test of our analysis, with the best model description of the soft excess among those proposed here, we allowed the parameters associated to the hard band components to vary in order to produce the final best fit, which includes simultaneously fitting the reflection model plus the soft excess model, in the range of 0.5 to 70 keV.

¹Note that our result is not depend on the geometry and location of the corona, although this is further discussed in Section 4.4

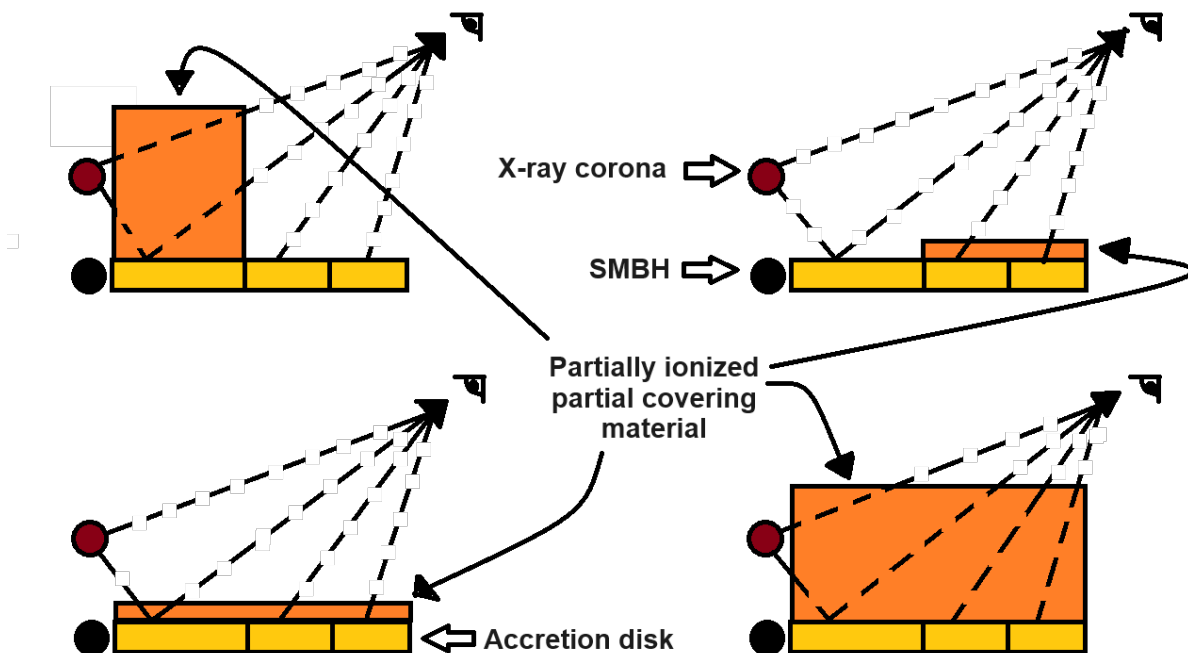


Figure 4.5: Sketch of the four tested scenarios for the localization of the partially ionized partial covering material. For simplicity we show only the right part of the accretion disk since the scenario is symmetrical on both sides. Orange region indicates the localization of the absorbing material. Note that the orientation of the accretion disk respect to the LOS not correspond to a type-1 AGN, however it is oriented this way for illustrative purposes.

4.3 Results

4.3.1 Initial extrapolation

The initial extrapolation of the preferred model by each source of the sample shows that all the objects require a soft excess component, however, such model is not capable of explaining the soft band below 3 keV for our objects. The χ_r^2 statistic obtained with this test is shown in Table 4.1 (column 2). The best result is obtained for Mrk 766^I when it is fitted with the ionized model, however note that, even in this case, we obtain a poor statistic of $\chi_r^2 = 6.69$ for this object. We show the histograms of the distribution of χ_r^2 for this test in Figure 4.6 (left).

Table 4.1: Statistical results obtained in the initial and cold partial covering (CPC) tests. Column (1) shows the name of the source (superscript indicates the hard model corresponding to the object: N for NEUTRAL and I for IONIZED models). Column (2) shows the results of the extrapolation from the hard model to the soft band. Results of the test on the cold partial covering component are shown in columns (3)-(5): allowing to vary the column density (nH), allowing to vary the column density and covering fraction (nH+Cfrac), and allowing to vary the column density and covering fraction of the intrinsic and reflection emission, respectively.

Source	Extrapolation	Intrinsic CPC		Intrinsic and reflection CPC
		nH	nH + Cfrac	
		$\chi^2/\text{d.o.f.}=\chi_r^2$	$\chi^2/\text{d.o.f.}=\chi_r^2$	
Mrk 335	33185/642=51.69	20742.1/641=32.36	20742.1/640=32.41	3538.2/640=5.53
Fairall 9	97954.1/960=102.04	97954.1/959=102.14	85694.3/958=89.45	85703/958=89.46
Mrk 1040	71669.4/1431=50.08	5044.7/1430=3.53	2584.4/1429=1.81	2606.7/1429=1.82
NGC 1365	1715681.2/1474=1163.96	1703372.8/1473=1156	1703372.8/1472=1157	6185.1/1472=4.2
Ark 120	45482.5/1443=31.52	45482.5/1442=31.54	18933.9/1441=13.14	20309.7/1441=14.09
NGC 3227	39256.3/1447=27.13	24164.7/1446=16.71	24164.7/1445=16.72	4618.9/1445=3.2
NGC 3783	12514.1/1034=12.10	5646.1/1033=5.47	2671.7/1032=2.59	4558.8/1032=4.42
NGC 4051	61458.8/1933=31.79	14050.8/1932=7.27	3573.9/1931=1.85	4457/1931=2.31
NGC 4151	1212669.7/2199=551.46	1212669.7/2198=551.71	1212669.7/2197=552	3424.6/2197=1.56
IRAS 13197-1627	23990.1/973=24.66	6053.9/972=6.23	6029.5/971=6.21	8779.3/971=9.04
NGC 5548	1092092.9/1442=757.35	1014892.2/1441=704	1014892.2/1440=704	5021.2/1440=3.49
NGC 7469	103208.4/923=111.82	9818.8/922=10.65	5893.7/921=6.4	5955.1/921=6.47
Mrk 915	20592.8/1035=19.90	10037.2/1034=9.71	1996.9/1033=1.93	-
NGC 4593 ^N	53269.8/1033=51.57	3179.5/1032=3.08	1950.2/1031=1.89	-
Mrk 766 ^N	55668.7/892=62.41	6733.3/891=7.56	2147.1/890=2.41	-
MCG -06-30-15 ^N	167672.3/968=173.22	4825.7/967=4.99	4825.7/966=4.99	-
Mrk 1044	220608.3/1168=188.88	38157.2/1167=32.7	32083.4/1166=27.52	32139.3/1166=27.56
IGRJ 19378-0617	189434.2/1174=161.36	20315.8/1173=17.32	14770.7/1172=12.6	14753.5/1172=12.59
NGC 4593 ^I	29967.5/1033=29.01	3434.4/1032=3.33	1817.4/1031=1.76	1815.8/1031=1.76
Mrk 766 ^I	5968.1/892=6.69	3301.6/891=3.71	2951.7/890=3.32	1995.8/890=2.24
MCG -06-30-15 ^I	41902.3/968=43.29	13567.2/967=14.03	13384.2/966=13.86	6341.8/966=6.57
Mrk 382	10644.3/598=17.80	5895.1/597=9.87	1825.2/596=3.06	-
IRAS 13224-3809	62608.4/702=89.19	62608.4/701=89.31	26794/700=38.28	-
Mrk 841	73740.8/857=86.05	9094.2/856=10.62	2598.2/855=3.04	-
MR 2251-178	150107.3/1209=124.16	44354.7/1208=36.72	3926.9/1207=3.25	-

4.3.2 Cold partial covering scenario

By allowing to vary the column density in the cold partial covering component we find that the fits improve for all the objects except in four of them (Fairall 9, Ark 120, NGC 4151, and IRAS 13224-3809). However the χ_r^2 is still over 3 in all objects. Furthermore, χ_r^2 is over 10 for 15 objects, and under five in only three objects (column 3 in Table 4.1).

We then allow to vary the covering fraction and column density at the same time. The fits significantly improved for all except eight objects, namely Mrk 335, NGC 1365, NGC 3227, NGC 4151, IRAS 13197-1627, NGC 5548, Mrk 766^I, and MCG -06-30-15^I (see column 4 in Table 4.1). This test allowed to achieve $\chi_r^2 < 3$ in 7 cases. Unfortunately, none of the objects presents good fits with $\chi_r^2 < 1.5$.

Finally, when we introduce the same absorber affecting both the intrinsic emission and disk reflection, we find that the largest improvement in the fits is for Mrk 335, NGC 1365, NGC 3227, NGC 4151, NGC 5548, and MCG -06-30-15^I, compared to previous test. Note

that, this last test was only applied to those objects that require the reflection component due to the accretion disk, i.e., for objects fitted with IONIZED and HYBRID models (column 5 in Table 4.1). With this test we achieve $\chi_r^2 < 3$ in two additional cases (NGC 4151 and Mrk 766) for a total of 8 objects with $\chi_r^2 < 3$. Yet none of the objects presents good fits with $\chi_r^2 < 1.5$.

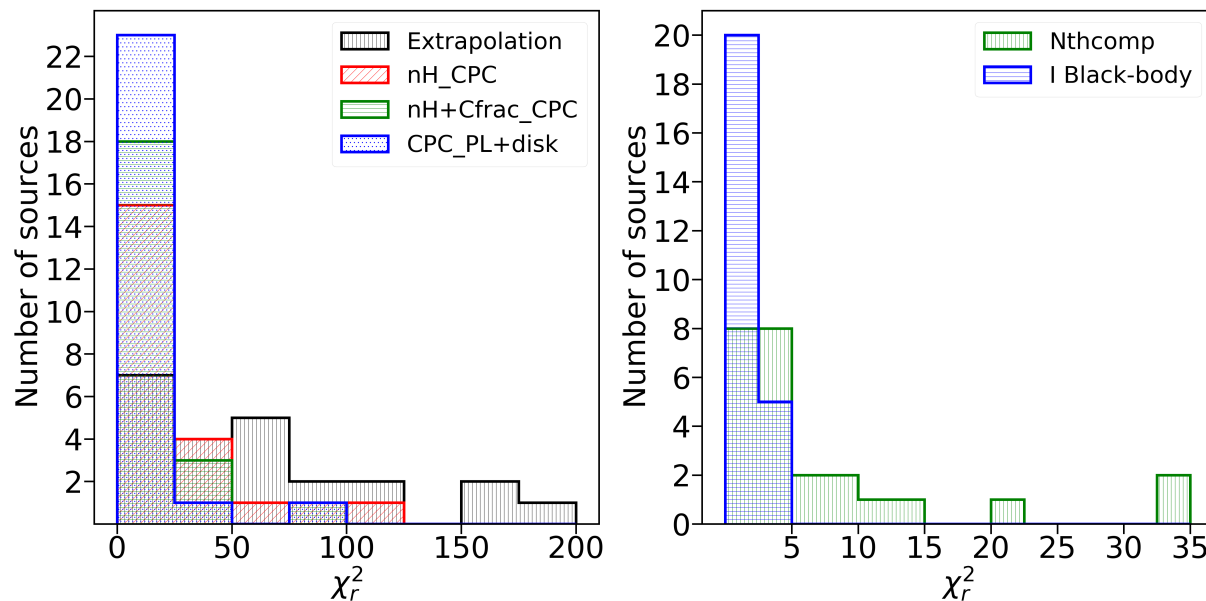


Figure 4.6: Histograms of χ_r^2 of the tests of the extrapolation and cold partial covering (left) and comptonization and black-body scenarios (right). nH_CPC and nH+Cfrac_CPC correspond to the tests when allow to vary only the column density, and the column density plus the covering fraction of the cold partial covering, respectively. CPC_PL+disk correspond to the test when we consider the same cold partial covering on the power-law and on the disk (see text).

We show in Figure 4.6 (left) the histograms of the distribution of the χ_r^2 for these three test. The largest χ_r^2 is obtained through the extrapolation test, while the χ_r^2 improves when we allow to vary the column density and covering fraction of the cold partial covering together. Note that, according to our criterion for determining when a fit is good ($\chi_r^2 < 1.5$), we have not yet found a good fit through the mentioned tests.

We keep this model for all the following tests because the absorber should affect both the intrinsic and disk reflection (see Section 4.2.7).

4.3.3 The soft excess as Comptonized material

Table 4.2: $\chi^2/\text{d.o.f.}=\chi_r^2$ statistics results obtained by testing different soft excess models. Column 2 NTHCOMP. Column 3 BBODY. Column 4 BBODY+BBODY. Column 5 BBODY+APEC. Second row in BBODY+BBODY column shows the F-test comparing the BBODY+BBODY and BBODY models.

Source	NTHCOMP	BBODY	kT	BBODY + BBODY	kT	APEC	kT BB, kT APEC, Z APEC
Mrk 335	$\frac{2645.3}{638}=4.15$	$\frac{1884.3}{638}=2.95$	$0.16\pm_{0.01}$	$\frac{1370.3}{636}=2.15$ 1×10^{-44}	$0.06\pm_{0.01}, 0.20\pm_{0.01}$	$\frac{1010.3}{635}=1.59$	$0.08\pm_{0.01}, 0.98\pm_{0.01}, 0.07\pm_{0.001}$
Fairall 9	$\frac{32969.8}{956}=34.49$	$\frac{4365.1}{956}=4.57$	$0.16\pm_{0.01}$	$\frac{1327.3}{954}=1.39$ 2.4×10^{-247}	$0.12\pm_{0.01}, 0.32\pm_{0.01}$	$\frac{1098.1}{953}=1.15$	$0.09\pm_{0.01}, 0.90\pm_{0.04}, 0.004\pm_{0.002}$
Mrk 1040	$\frac{2204}{1427}=1.54$	$\frac{2080}{1427}=1.46$	$0.40\pm_{0.01}$	$\frac{1693.5}{1425}=1.19$ 2.5×10^{-64}	$0.32\pm_{0.01}, 0.08\pm_{0.01}$	$\frac{1584.6}{1424}=1.11$	$0.33\pm_{0.02}, 0.17\pm_{0.01}, 0.01\pm_{0.002}$
NGC 1365	$\frac{5612.1}{1470}=3.82$	$\frac{2606.5}{1470}=1.77$	$0.28\pm_{0.01}$	$\frac{2566.8}{1468}=1.75$ 1.3×10^{-5}	$0.30\pm_{0.01}, *$	$\frac{2564.6}{1467}=1.75$	$0.29\pm_{0.01}, 23\pm_6, *$
Ark 120	$\frac{20309.7}{1439}=14.11$	$\frac{2536}{1439}=1.76$	$0.16\pm_{0.01}$	$\frac{1634.5}{1437}=1.14$ 8.6×10^{-138}	$0.12\pm_{0.01}, 0.29\pm_{0.01}$	$\frac{1791.7}{1436}=1.25$	$0.25\pm_{0.01}, 0.22\pm_{0.02}, 0.008\pm_{0.002}$
NGC 3227	$\frac{4619}{1443}=3.20$	$\frac{2491.2}{1443}=1.73$	$0.83\pm_{0.01}$	$\frac{1652.9}{1441}=1.15$ 4.3×10^{-129}	$0.33\pm_{0.01}, 0.08\pm_{0.01}$	$\frac{2444.6}{1440}=1.7$	$0.48\pm_{0.01}, *, *$
NGC 3783	$\frac{4558.8}{1030}=4.43$	$\frac{2099.8}{1030}=2.04$	$0.09\pm_{0.01}$	$\frac{1976.4}{1028}=1.92$ 3×10^{-14}	$0.09\pm_{0.01}, *$	$\frac{1954.2}{1027}=1.9$	$0.09\pm_{0.01}, 7\pm_1, *$
NGC 4051	$\frac{4457}{1929}=2.31$	$\frac{2080}{1929}=1.08$	$0.06\pm_{0.01}$	$\frac{1988.3}{1927}=1.03$ 1.4×10^{-19}	$0.09\pm_{0.01}, 0.24\pm_{0.01}$	$\frac{2004.1}{1926}=1.04$	$0.08\pm_{0.01}, 1.4\pm_{0.1}, *$
NGC 4151	$\frac{3424.6}{2195}=1.56$	$\frac{3262}{2195}=1.49$	$0.05\pm_{0.01}$	$\frac{2930.3}{2193}=1.34$ 8.6×10^{-52}	$0.10\pm_{0.01}, 0.69\pm_{0.02}$	$\frac{2947.5}{2192}=1.34$	$0.69\pm_{0.03}, 0.17\pm_{0.01}, 0.004\pm_{0.002}$
IRAS 13197-1627	$\frac{8516.8}{969}=8.79$	$\frac{2048.9}{969}=2.11$	$0.20\pm_{0.01}$	$\frac{1970.9}{967}=2.04$ 7.1×10^{-9}	$0.73\pm_{0.06}, 0\pm_{0.01}$	$\frac{1345.3}{966}=1.39$	$0.10\pm_{0.02}, 0.98\pm_{0.03}, 0.098\pm_{0.005}$
NGC 5548	$\frac{4431.2}{1438}=3.08$	$\frac{3498.9}{1438}=2.43$	$0.53\pm_{0.01}$	$\frac{3498.9}{1436}=2.44$ 1	$0.53\pm_{0.02}, 0.53\pm_{0.05}$	$\frac{2213.4}{1435}=1.54$	$0.56\pm_{0.01}, 0.14\pm_{0.01}, 0.42\pm_{0.34}$
NGC 7469	$\frac{5955.1}{919}=6.48$	$\frac{1075.7}{919}=1.17$	$0.11\pm_{0.01}$	$\frac{1027.8}{917}=1.12$ 8.5×10^{-10}	$0.12\pm_{0.01}, 0.29\pm_{0.01}$	$\frac{1028.4}{916}=1.12$	$0.10\pm_{0.01}, 0.56\pm_{0.03}, *$
Mrk 915	$\frac{1997}{1031}=1.94$	$\frac{1761.4}{1031}=1.71$	$0.39\pm_{0.01}$	$\frac{1504.2}{1029}=1.46$ 5.4×10^{-36}	$0.42\pm_{0.01}, 0.06\pm_{0.01}$	$\frac{1456.7}{1028}=1.42$	$0.41\pm_{0.02}, 0.07\pm_{0.02}, *$
NGC 4593 ^N	$\frac{1950.2}{1029}=1.90$	$\frac{1163.4}{1029}=1.13$	$0.09\pm_{0.01}$	$\frac{1061.5}{1027}=1.03$ 3.6×10^{-21}	$0.10\pm_{0.01}, 0.26\pm_{0.01}$	$\frac{1099.1}{1026}=1.07$	$0.06\pm_{0.01}, 0.42\pm_{0.02}, *$
Mrk 766 ^N	$\frac{2119.4}{888}=2.39$	$\frac{1132.6}{888}=1.28$	$0.08\pm_{0.01}$	$\frac{1132.6}{886}=1.28$ 1	$0.08\pm_{0.01}, *$	$\frac{994}{885}=1.12$	$0.09\pm_{0.01}, 1.46\pm_{0.06}, *$
MCG -06-30-15 ^N	$\frac{8559.7}{964}=8.88$	$\frac{2767.2}{964}=2.87$	$0.07\pm_{0.01}$	$\frac{1763.2}{962}=1.83$ 7.1×10^{-95}	$0.09\pm_{0.01}, *$	$\frac{2336.4}{961}=2.43$	$0.06\pm_{0.01}, 0.18\pm_{0.01}, *$
Mrk 1044	$\frac{24540}{1164}=21.08$	$\frac{3327.8}{1164}=2.86$	$0.14\pm_{0.01}$	$\frac{1794.4}{1162}=1.54$ 1.4×10^{-156}	$0.06\pm_{0.01}, 0.15\pm_{0.01}$	$\frac{1571.5}{1161}=1.35$	$0.11\pm_{0.01}, 1.05\pm_{0.01}, 0.01\pm_{0.001}$
IGRJ 19378-0617	$\frac{13238.5}{1170}=11.31$	$\frac{1577}{1170}=1.35$	$0.14\pm_{0.01}$	$\frac{1385}{1168}=1.19$ 1.2×10^{-33}	$0.15\pm_{0.01}, 0.39\pm_{0.01}$	$\frac{1439}{1167}=1.23$	$0.15\pm_{0.01}, 0.99\pm_{0.03}, 0.028\pm_{0.005}$
NGC 4593 ^I	$\frac{1815.8}{1029}=1.76$	$\frac{1207.7}{1029}=1.17$	$0.08\pm_{0.01}$	$\frac{1096.6}{1027}=1.07$ $\times 10$	$0.10\pm_{0.01}, 0.25\pm_{0.01}$	$\frac{1178.6}{1026}=1.15$	$0.08\pm_{0.01}, 1.93\pm_{0.12}, *$
Mrk 766 ^I	$\frac{1953.8}{888}=2.20$	$\frac{1509.5}{888}=1.7$	$0.06\pm_{0.01}$	$\frac{1244.7}{886}=1.4$ 7.8×10^{-38}	$0.08\pm_{0.01}, 0.21\pm_{0.01}$	$\frac{1022.3}{885}=1.16$	$0.06\pm_{0.01}, 1.62\pm_{0.03}, *$
MCG -06-30-15 ^I	$\frac{6341.9}{964}=6.58$	$\frac{4180.3}{964}=4.34$	$0.06\pm_{0.01}$	$\frac{1855.6}{962}=1.93$ 2.2×10^{-170}	$0.09\pm_{0.01}, 0.39\pm_{0.01}$	$\frac{3112.9}{961}=3.24$	$0.07\pm_{0.01}, 1.82\pm_{0.02}, *$
Mrk 382	$\frac{1726.9}{594}=2.91$	$\frac{718.3}{594}=1.21$	$0.08\pm_{0.01}$	$\frac{660.8}{592}=1.12$ 1.9×10^{-11}	$0.10\pm_{0.01}, 0.43\pm_{0.05}$	$\frac{697.7}{591}=1.18$	$0.07\pm_{0.01}, 0.21\pm_{0.01}, *$
IRAS 13224-3809	$\frac{23266.7}{698}=33.33$	$\frac{1346.9}{698}=1.93$	$0.12\pm_{0.01}$	$\frac{1223.9}{696}=1.76$ 3.4×10^{-15}	$0.12\pm_{0.01}, 0.52\pm_{0.02}$	$\frac{1104.7}{695}=1.59$	$0.11\pm_{0.01}, 0.74\pm_{0.01}, *$
Mrk 841	$\frac{2595.7}{853}=3.04$	$\frac{1153.4}{853}=1.35$	$0.07\pm_{0.01}$	$\frac{972.2}{851}=1.14$ 2.6×10^{-32}	$0.08\pm_{0.01}, *$	$\frac{973.2}{850}=1.14$	$0.09\pm_{0.01}, 5.8\pm_{1.9}, *$
MR 2251-178	$\frac{3927}{1205}=3.26$	$\frac{2415.6}{1205}=2.0$	$0.06\pm_{0.01}$	$\frac{1382.7}{1203}=1.15$ 1.8×10^{-146}	$0.10\pm_{0.01}, 0.40\pm_{0.02}$	$\frac{2415.6}{1202}=2.0$	$0.06\pm_{0.01}, *, *$

When we add NTHCOMP to the baseline model to fit the soft excess, we find that the fit improves for 10 objects (Mrk 335, Fairall 9, Mrk 1040, NGC 1365, IRAS 13197-1627, NGC 5548, Mrk 1044, IGRJ 19378-0617, Mrk 382, and IRAS 13224-3809), compared to the last test. We found that the object with the lowest fit statistic is Mrk 1040, with $\chi_r^2 = 1.54$ (see Table 4.2). According to our criteria ($\chi_r^2 < 1.5$), through this model, we do not obtain

a good fit for any object, while nine objects still show $\chi_r^2 > 3$. However, eight of them were already below $\chi_r^2 < 3$ from the previous test. Therefore, adding NTHCOMP makes a marginal improvement.

4.3.4 The soft excess as Black-body

We show in Table 4.2 the results when we add the black-body components to the baseline model. When we consider a single black-body we obtain $\chi_r^2 < 3$ for all sources, except for Fairall 9 and MCG-06-30-15^I (column 3 in Table 4.2). We find that the BBODY model give better fits than the NTHCOMP model for all objects. We show in Figure 4.7 (left) the χ_r^2 of the BBODY vs the $\Delta\chi^2$ of the BBODY and NTHCOMP models / d.o.f. We now obtain $\chi_r^2 < 1.5$ for ten sources (symbols to the left of the solid line in Figure 4.7, left), even more, the $\chi_r^2 < 1.2$ for four of them (symbols to the left of the dashed line in Figure 4.7 (left)).

Then, we add a second black-body component to the baseline model. In this test, we find that the fit improves for all objects compared to the model with a single black-body, except for NGC 5548 and Mrk 766^N. We also use the F-test in order to check if the two black-body model is required for the best fit. Indeed, we find that NGC 5548 and Mrk 766^N do not require the two black-body components. We show in Table 4.2 these results. We show in Figure 4.7 (right) the χ_r^2 of the BBODY+BBODY versus the $\Delta\chi^2$ of the BBODY and BBODY+BBODY models / d.o.f. we obtain $\chi_r^2 < 1.5$ for 16 cases (symbols to the left of the solid line in Figure 4.7(right)). Furthermore, we obtain $\chi_r^2 < 1.2$ for 11 cases (symbols to the left of the dashed line in Figure 4.7(right)).

4.3.5 Soft excess as host-galaxy circumnuclear contributors

When we add APEC to the baseline model, the statistics is worst for eight objects (Ark 120, NGC 3227, NGC 4051, NGC 4593^{N,I}, MCG-06-30-15^{N,I}, IGRJ 19378-0617, Mrk 382, and MR 2251-178), compared to the two black-body model, while this does not occur when we compare it with the only one black-body model. On the other hand, the baseline model with APEC give better results for Mrk 335, Fairall 9, IRAS 13197-1627, NGC 5548, MCG-06-30-15^N, Mrk 766^I, MCG-06-30-15^I, and IRAS 13224-3809, compared to such of

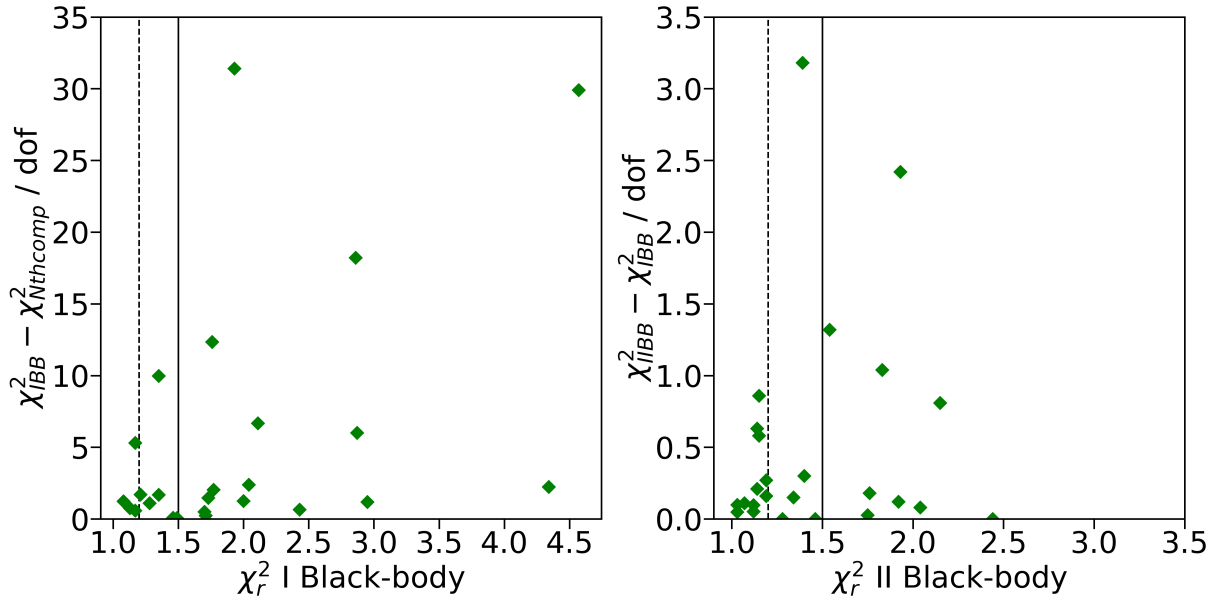


Figure 4.7: Left: χ_r^2 of the BBODY vs the $\Delta\chi^2$ of the BBODY and NTHCOMP / d.o.f. Right: χ_r^2 of the BBODY+BBODY versus the $\Delta\chi^2$ of the BBODY and BBODY+BBODY / d.o.f. We indicate with a vertical solid line at $\chi_r^2 = 1.5$ the value for which the fit is consider as a good fit. Also, we add a vertical dashed line at $\chi_r^2 = 1.2$ to indiate when the fit is better.

one or two black-bodies. We show in Table 4.2 the statistical results and the parameters obtained with this model. When we check the parameters obtained with the best fit, we find that the metal abundance is unrealistically low (< 0.01) for almost all objects, when the parameter is constrained. Also, we find plasma temperatures above 1 keV for eight sources, while $kT < 1$ keV is expected for the host galaxy (see Section 4.2.6). According to these results on the parameters of APEC, we decided to discard this model for the following tests.

4.3.6 Soft excess as partially ionized partial covering

We show en Table 4.3 the results obtained when we test the ionized absorber: (1) on the power-law and the disk but not on the black-body; (2) on the black-body but not on the power-law and disk; (3) on the black-body and the disk but no on the power-law and; (4) on the black-body, the power-law, and the disk. In order to determine when the two black-body is required compared to the one black-body model, we use the F-test statistics. We find that almost all spectra require two black-body components regardless of the absorption

model. In order to determine the best model for each one, we use the AIC. We find that for most spectra, more than one of the options are preferred: 10 spectra prefer a single model, and 15 spectra prefer more than one option. Among the eight tested scenarios (four for a single Black-body and four for two Black-body), six of them are chosen as the preferred option for at least one spectra. Among them, all the plausible combinations for the warm absorber for the two Black-body are included, plus two combinations when a single Black-body es included. We show in Figure 4.8 the histograms of the number of spectra preferring these six models. The most commonly preferred option is $(\text{xi}(\text{BB}+\text{BB})+\text{PL}+\text{D})$ for 10 spectra, while $(\text{xi}(\text{BB}+\text{BB}+\text{D})+\text{PL})$ and $\text{xi}(\text{BB}+\text{BB}+\text{PL}+\text{D})$ are preferred by four spectra, $(\text{BB}+\text{BB}+\text{xi}(\text{PL}+\text{D}))$ and $\text{xi}(\text{BB}+\text{PL}+\text{D})$ are preferred by three spectra, and $((\text{xi}*\text{BB})+\text{PL}+\text{D})$ is preferred by only one spectrum.

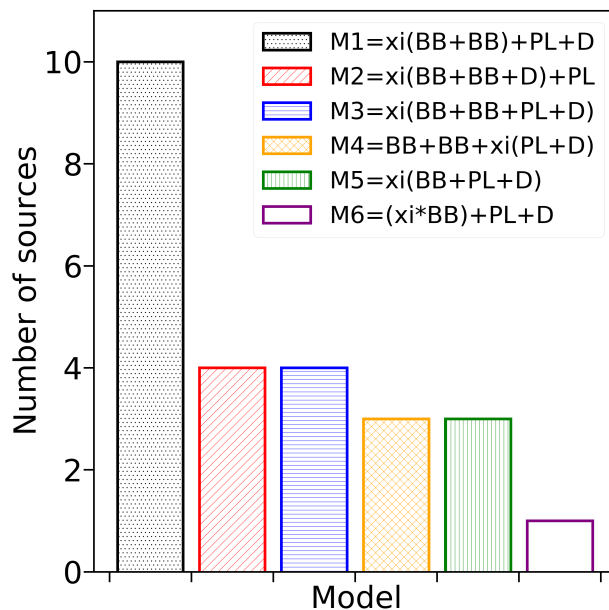


Figure 4.8: Histograms of the six models preferred by the sample.

Among the best fits obtained, there are five objects for which we obtain poor statistical results: Mrk 335 ($\chi_r^2 = 1.51$), NGC 1365 ($\chi_r^2 = 1.59$), NGC 3783 ($\chi_r^2 = 1.55$), IRAS 13197 ($\chi_r^2 = 1.62$), and IRAS 13224 ($\chi_r^2 = 1.75$). Interestingly, the first four objects are fitted with the HYBRID model in the hard band. Also, the two objects for which we obtain poor results in the hard band study, namely NGC 1365 ($\chi_r^2 = 1.58$) and NGC 3783 ($\chi_r^2 = 1.52$), still are bad in this soft band study.

Among the three objects equally fitted with the NEUTRAL and IONIZED models in the hard band (NGC 4593, Mrk 766, and MCG-06-30-15), we obtain a better fit in the soft band for NGC 4593 and MCG-06-30-15 when the hard NEUTRAL model is considered ($\chi_r^2 = 1.02$ vs $\chi_r^2 = 1.04$ and $\chi_r^2 = 1.07$ vs $\chi_r^2 = 1.10$, respectively). Therefore, the inclusion of the soft band might help to disentangle the best reflection model for some objects. However, this is not the case for Mrk 766 which is equally well fitted regardless of the hard-band model used. However, when the NEUTRAL model is considered, the object is fitted with the baseline model of a single black-body, while when the IONIZED model is considered, the object prefers the baseline model with two black-body components.

We also check the parameters obtained with the best model for each object. Note that, there are 15 spectra preferring more than one model. For these spectra, we compile the parameters of the best model according to AIC (those models for which $\text{AIC}=1$). We show in Table 4.4 the parameters of the best model among the preferred models by each spectrum. Figure 4.9 shows the distribution of kT of the two black-body components for the spectra fitted by these components. We find an average value of the effective temperature of 0.12 and 0.38 keV for the first and second black-body, respectively, with a relatively narrow distribution for the lower-temperature of the black-body.

Table 4.3: Statistical results obtained by testing the warm absorber on the Power-law and disk components. First and second rows of each object shows the $\chi^2/\text{d.o.f.}=\chi_r^2$ and the F-test, respectively. $\chi^2/\text{d.o.f.}=\chi_r^2$ in bold face indicates the preferred model/s by the source. Models are M_A: BB+xi(PL+D), M_B: BB+BB+xi(PL+D), M_C: (xi*BB)+PL+D, M_D: xi(BB+BB)+PL+D, M_E: xi(BB+D)+PL, M_F: xi(BB+BB+D)+PL, M_G: xi(BB+D+PL), and M_H: xi(BB+BB+D+PL)

Source	M _A	M _B	M _C	M _D	M _E	M _F	M _G	M _H
Mrk 335	$\frac{1518.7}{635}=2.39$	$\frac{1306}{633}=2.06$ 2×10^{-21}	$\frac{1098.8}{635}=1.73$	$\frac{956.7}{633}=\mathbf{1.51}$ 9×10^{-20}	$\frac{1103.7}{635}=1.74$	$\frac{970}{633}=1.53$ 2×10^{-18}	$\frac{1103.7}{635}=1.74$	$\frac{970}{633}=1.53$ 2×10^{-18}
Fairall 9	$\frac{4308.4}{953}=4.52$	$\frac{1143.3}{951}=1.2$ 1×10^{-274}	$\frac{1743.4}{953}=1.83$	$\frac{1081.3}{951}=\mathbf{1.14}$ 2×10^{-99}	$\frac{1836.6}{953}=1.93$	$\frac{1079.7}{951}=\mathbf{1.14}$ 2×10^{-110}	$\frac{4039.6}{953}=4.24$	$\frac{1078}{951}=\mathbf{1.13}$ 2×10^{-273}
Mrk 1040	$\frac{1599.7}{1424}=1.12$	$\frac{1554.5}{1422}=1.09$ 1×10^{-9}	$\frac{1608.2}{1424}=1.13$	$\frac{1504.7}{1422}=\mathbf{1.06}$ 3×10^{-21}	$\frac{1649.4}{1424}=1.16$	$\frac{1554.5}{1422}=1.09$ 5×10^{-19}	$\frac{1601.5}{1424}=1.12$	$\frac{1549.5}{1422}=1.09$ 6×10^{-11}
NGC 1365	$\frac{2397.4}{1467}=1.63$	$\frac{2383.3}{1465}=1.63$ 0.01	$\frac{2506.2}{1467}=1.71$	$\frac{2406.9}{1465}=1.64$ 1×10^{-13}	$\frac{2544.3}{1467}=1.73$	$\frac{2426.1}{1465}=1.66$ 7×10^{-16}	$\frac{2516.2}{1467}=1.72$	$\frac{2324.8}{1465}=\mathbf{1.59}$ 7×10^{-26}
Ark 120	$\frac{1936.7}{1436}=1.35$	$\frac{1611.5}{1434}=\mathbf{1.12}$ 6×10^{-58}	$\frac{1714.3}{1436}=1.19$	$\frac{1613.9}{1434}=\mathbf{1.13}$ 2×10^{-19}	$\frac{1925.1}{1436}=1.34$	$\frac{1611.3}{1434}=\mathbf{1.12}$ 4×10^{-56}	$\frac{1836.5}{1436}=1.28$	$\frac{1611.4}{1434}=\mathbf{1.12}$ 2×10^{-41}
NGC 3227	$\frac{1623}{1440}=1.13$	$\frac{1578.3}{1438}=\mathbf{1.1}$ 2×10^{-9}	$\frac{1665.5}{1440}=1.16$	$\frac{1588}{1438}=\mathbf{1.10}$ 1×10^{-15}	$\frac{1632.7}{1440}=1.13$	$\frac{1586}{1438}=\mathbf{1.10}$ 9×10^{-10}	$\frac{1606}{1440}=1.12$	$\frac{1593.9}{1438}=1.11$ 0.004
NGC 3783	$\frac{1876.7}{1027}=1.83$	$\frac{1770.3}{1025}=1.73$ 1×10^{-13}	$\frac{1735.3}{1027}=1.69$	$\frac{1649.1}{1025}=1.61$ 5×10^{-12}	$\frac{1772}{1027}=1.73$	$\frac{1714.5}{1025}=1.67$ 5×10^{-8}	$\frac{1709.2}{1027}=1.66$	$\frac{1592.1}{1025}=\mathbf{1.55}$ 2×10^{-16}
NGC 4051	$\frac{2073.9}{1926}=1.08$	$\frac{1959}{1924}=\mathbf{1.02}$ 2×10^{-24}	$\frac{2078.4}{1926}=1.08$	$\frac{1981.3}{1924}=1.03$ 1×10^{-20}	$\frac{1992.3}{1926}=1.03$	$\frac{1966.4}{1924}=1.02$ 3×10^{-6}	$\frac{2065}{1926}=1.07$	$\frac{1955.5}{1924}=\mathbf{1.02}$ 2×10^{-23}
NGC 4151	$\frac{2776}{2192}=1.27$	$\frac{2757.4}{2190}=1.26$ 6×10^{-4}	$\frac{3261.5}{2192}=1.49$	$\frac{2702.5}{2190}=\mathbf{1.23}$ 4×10^{-90}	$\frac{2816.4}{2192}=1.28$	$\frac{2747.6}{2190}=1.25$ 2×10^{-12}	$\frac{2763.7}{2192}=1.26$	$\frac{2757.4}{2190}=1.26$ 0.08
IRAS 13197	$\frac{1982.4}{966}=2.05$	$\frac{1857.9}{964}=1.93$ 3×10^{-14}	$\frac{1653.8}{966}=1.71$	$\frac{1562.7}{964}=\mathbf{1.62}$ 1×10^{-12}	$\frac{1649.9}{966}=1.71$	$\frac{1563}{964}=\mathbf{1.62}$ 5×10^{-12}	$\frac{1658.8}{966}=1.72$	$\frac{1564.6}{964}=\mathbf{1.62}$ 6×10^{-13}
NGC 5548	$\frac{1615.8}{1435}=1.13$	$\frac{1614.3}{1433}=1.13$ 0.51	$\frac{1856.4}{1435}=1.29$	$\frac{1591.1}{1433}=\mathbf{1.11}$ 1×10^{-48}	$\frac{1813.6}{1435}=1.26$	$\frac{1599.9}{1433}=\mathbf{1.12}$ 10×10^{-40}	$\frac{1603.9}{1435}=1.12$	$\frac{1589.8}{1433}=1.11$ 0.001
NGC 7469	$\frac{1030.6}{916}=1.13$	$\frac{1008.1}{914}=\mathbf{1.10}$ 4×10^{-5}	$\frac{1023.6}{916}=1.12$	$\frac{1011.9}{914}=1.11$ 0.005	$\frac{1030.2}{916}=1.12$	$\frac{1010.3}{914}=1.11$ 1×10^{-4}	$\frac{1031.3}{916}=1.13$	$\frac{1008.9}{914}=\mathbf{1.10}$ 4×10^{-5}
NGC 4593 ^N	$\frac{1060.9}{1026}=1.03$	$\frac{1044.4}{1024}=\mathbf{1.02}$ 3×10^{-4}	$\frac{1124.9}{1026}=1.1$	$\frac{1042.5}{1024}=\mathbf{1.02}$ 1×10^{-17}	-	-	$\frac{1060.6}{1026}=\mathbf{1.03}$	$\frac{1043.2}{1024}=\mathbf{1.02}$ 2×10^{-4}
Mrk 915	$\frac{1099.9}{1028}=1.07$	$\frac{1094.3}{1026}=1.07$ 0.07	$\frac{1097.7}{1028}=1.07$	$\frac{1079.5}{1026}=\mathbf{1.05}$ 2×10^{-4}	-	-	$\frac{1086.7}{1028}=\mathbf{1.06}$	$\frac{1079.1}{1026}=1.05$ 0.03
Mrk 766 ^N	$\frac{934.3}{885}=1.06$	$\frac{925.8}{883}=1.05$ 0.02	$\frac{919.3}{885}=\mathbf{1.04}$	$\frac{917.1}{883}=1.04$ 0.35	-	-	$\frac{928}{885}=\mathbf{1.05}$	$\frac{923.6}{883}=1.05$ 0.12
MCG ^N	$\frac{1559.2}{961}=1.62$	$\frac{1173}{959}=1.22$ 5×10^{-60}	$\frac{1222.1}{961}=1.27$	$\frac{1026.6}{959}=\mathbf{1.07}$ 5×10^{-37}	-	-	$\frac{1228.7}{961}=1.28$	$\frac{1059.8}{959}=1.11$ 2×10^{-31}
Mrk 1044	$\frac{3316}{1161}=2.86$	$\frac{1464.1}{1159}=1.26$ 2×10^{-206}	$\frac{1443.6}{1161}=1.24$	$\frac{1383.9}{1159}=\mathbf{1.19}$ 2×10^{-11}	$\frac{1438.1}{1161}=1.24$	$\frac{1378.4}{1159}=\mathbf{1.19}$ 2×10^{-11}	$\frac{1456.2}{1161}=1.25$	$\frac{1400.3}{1159}=1.21$ 1×10^{-10}
IGRJ 19378	$\frac{1494.9}{1167}=1.28$	$\frac{1321.8}{1165}=\mathbf{1.13}$ 7×10^{-32}	$\frac{1559.9}{1167}=1.34$	$\frac{1343.9}{1165}=1.15$ 2×10^{-38}	$\frac{1500}{1167}=1.29$	$\frac{1343.8}{1165}=1.15$ 2×10^{-11}	$\frac{1529.3}{1167}=1.31$	$\frac{1333.6}{1165}=1.14$ 7×10^{-30}
NGC 4593 ^I	$\frac{1086.3}{1026}=1.06$	$\frac{1066.5}{1024}=\mathbf{1.04}$ 8×10^{-5}	$\frac{1169}{1026}=1.14$	$\frac{1061.6}{1024}=\mathbf{1.04}$ 4×10^{-22}	$\frac{1097.7}{1026}=1.07$	$\frac{1096.4}{1024}=1.07$ 0.55	$\frac{1086.1}{1026}=1.06$	$\frac{1063}{1024}=\mathbf{1.04}$ 2×10^{-5}
Mrk 766 ^I	$\frac{1141.8}{885}=1.29$	$\frac{1064.9}{883}=1.21$ 4×10^{-14}	$\frac{1011.1}{885}=1.14$	$\frac{944.9}{883}=1.07$ 1×10^{-13}	$\frac{960.2}{885}=1.08$	$\frac{914.3}{883}=\mathbf{1.04}$ 4×10^{-10}	$\frac{1098.3}{885}=1.24$	$\frac{957.9}{883}=1.08$ 6×10^{-27}
MCG ^I	$\frac{732.8}{961}=1.8$	$\frac{1519.4}{959}=1.58$ 4×10^{-28}	$\frac{1239.8}{961}=1.29$	$\frac{1115.9}{959}=1.16$ 1×10^{-22}	$\frac{1145.7}{961}=1.19$	$\frac{1051.8}{959}=\mathbf{1.10}$ 2×10^{-18}	$\frac{1396.5}{961}=1.45$	$\frac{1146.2}{959}=1.20$ 7×10^{-42}
Mrk 382	$\frac{640.2}{591}=\mathbf{1.08}$	$\frac{637.4}{589}=1.08$ 0.28	$\frac{675.4}{591}=1.14$	$\frac{675.4}{589}=1.14$ 1	-	-	$\frac{639.5}{591}=\mathbf{1.08}$	$\frac{637}{589}=1.08$ 0.32
IRAS 13224	$\frac{1219.5}{695}=\mathbf{1.75}$	$\frac{1201.9}{693}=1.73$ 0.006	$\frac{1329.1}{695}=1.91$	$\frac{1324.8}{693}=1.91$ 0.33	-	-	$\frac{1219.5}{695}=\mathbf{1.75}$	$\frac{1205.6}{693}=1.74$ 0.02
Mrk 841	$\frac{937.7}{850}=\mathbf{1.1}$	$\frac{932.8}{848}=1.1$ 0.11	$\frac{1084.5}{852}=1.27$	$\frac{988.4}{850}=1.16$ 7×10^{-18}	-	-	$\frac{936}{850}=\mathbf{1.1}$	$\frac{932.2}{848}=1.1$ 1
MR 2251	$\frac{1315.7}{1202}=1.09$	$\frac{1273.1}{1200}=1.06$ 3×10^{-9}	$\frac{1375}{1202}=1.14$	$\frac{1237.4}{1200}=\mathbf{1.03}$ 3×10^{-28}	-	-	$\frac{1314.4}{1202}=1.09$	$\frac{1260.2}{1200}=1.05$ 1×10^{-11}

Table 4.4: Parameters of the best model preferred by the sources in the sample. Column density (nH) is in units of 10^{22}cm^{-2} . Ionization parameter (ξ) in $\log \text{erg cm s}^{-1}$. Effective temperature of the black-body (kT) in keV. CPC and WPC correspond to Cold or Warm Partial Covering, respectively. We indicate the model below the name of the source.

Source	CPC		WPC			BBODY 1	BBODY 2
	nH	Cfrac	nH	ξ	Cfrac	kT	kT
Mrk 335 ^H xi(BB+BB)+PL+D	*	$0.88 \pm_{0.01}^{0.01}$	$0.39 \pm_{0.01}^{0.03}$	$-0.24 \pm_{0.02}^{0.03}$	*	$0.13 \pm_{0.01}^{0.01}$	$0.48 \pm_{0.03}^{0.02}$
Fairall 9 ^H xi(BB+BB+D+PL)	*	*	$0.37 \pm_{0.08}^{0.03}$	$-0.48 \pm_{0.01}^{0.02}$	$0.6 \pm_{0.01}^{0.02}$	$0.13 \pm_{0.01}^{0.01}$	$0.36 \pm_{0.01}^{0.01}$
Mrk 1040 ^H xi(BB+BB)+PL+D	$0.63 \pm_{0.03}^{0.04}$	$0.71 \pm_{0.01}^{0.05}$	$0.9 \pm_{0.06}^{0.08}$	$0.27 \pm_{0.26}^{0.03}$	*	$0.18 \pm_{0.01}^{0.01}$	$0.55 \pm_{0.03}^{0.04}$
NGC 1365 ^H xi(BB+BB+D+PL)	$0.26 \pm_{0.04}^{0.04}$	*	$1.39 \pm_{0.07}^{0.09}$	$-1.18 \pm_{0.01}^{0.01}$	$0.96 \pm_{0.01}^{0.01}$	$0.22 \pm_{0.01}^{0.01}$	$0.78 \pm_{0.02}^{0.02}$
Ark 120 ^H xi(BB+BB+D)+PL	$2.85 \pm_{0.3}^{0.7}$	$0.52 \pm_{0.1}^{0.04}$	$0.87 \pm_{0.1}^{0.04}$	$0.27 \pm_{0.13}^{0.01}$	$0.39 \pm_{0.07}^{0.11}$	$0.13 \pm_{0.01}^{0.01}$	$0.28 \pm_{0.01}^{0.01}$
NGC 3227 ^H BB+BB+xi(PL+D)	$0.73 \pm_{0.16}^{0.11}$	*	$1.1 \pm_{0.19}^{0.12}$	*	$0.51 \pm_{0.07}^{0.07}$	$0.09 \pm_{0.01}^{0.01}$	$0.27 \pm_{0.02}^{0.01}$
NGC 3783 ^H xi(BB+BB+D+PL)	*	$0.66 \pm_{0.08}^{0.04}$	$2.11 \pm_{0.26}^{0.21}$	$0.5 \pm_{0.05}^{0.05}$	$0.94 \pm_{0.02}^{0.02}$	$0.13 \pm_{0.01}^{0.01}$	*
NGC 4051 ^H xi(BB+BB+D+PL)	$0.75 \pm_{0.09}^{0.16}$	*	$1.07 \pm_{0.62}^{0.25}$	$1.37 \pm_{0.15}^{0.17}$	$0.24 \pm_{0.02}^{0.03}$	$0.10 \pm_{0.01}^{0.01}$	$0.21 \pm_{0.01}^{0.01}$
NGC 4151 ^H xi(BB+BB)+PL+D	$10.49 \pm_{0.17}^{0.15}$	*	$2.36 \pm_{0.07}^{0.07}$	$0.27 \pm_{0.06}^{0.01}$	$0.99 \pm_{0.01}^{0.01}$	$0.11 \pm_{0.01}^{0.01}$	$0.53 \pm_{0.02}^{0.01}$
IRAS 13197-1627 ^H xi(BB+BB)+PL+D	$64.37 \pm_{0.62}^{0.63}$	*	$0.14 \pm_{0.01}^{0.01}$	$-1.27 \pm_{0.03}^{0.02}$	*	$0.14 \pm_{0.01}^{0.01}$	$0.52 \pm_{0.02}^{0.01}$
NGC 5548 ^H xi(BB+BB)+PL+D	$4.56 \pm_{0.06}^{0.07}$	$0.98 \pm_{0.01}^{0.02}$	$2.82 \pm_{0.15}^{0.08}$	$0.28 \pm_{0.01}^{0.01}$	*	$0.11 \pm_{0.01}^{0.01}$	$0.24 \pm_{0.01}^{0.01}$
NGC 7469 ^H BB+BB+xi(PL+D)	$0.56 \pm_{0.12}^{0.22}$	$0.46 \pm_{0.10}^{0.12}$	$1.76 \pm_{1.6}^{4.6}$	$2.74 \pm_{0.12}^{0.47}$	*	$0.12 \pm_{0.01}^{0.01}$	$0.32 \pm_{0.03}^{0.03}$
NGC 4593 ^N xi(BB+BB)+PL	$0.99 \pm_{0.36}^{0.43}$	$0.65 \pm_{0.16}^{0.25}$	$2.98 \pm_{2.53}^{3.55}$	$2.34 \pm_{0.16}^{0.16}$	*	$0.09 \pm_{0.01}^{0.01}$	$0.26 \pm_{0.02}^{0.02}$
Mrk 915 ^N xi(BB+BB)+PL	$3.1 \pm_{0.12}^{0.13}$	*	$1.68 \pm_{0.63}^{0.4}$	$0.32 \pm_{0.02}^{0.03}$	$0.94 \pm_{0.06}^{0.03}$	$0.11 \pm_{0.01}^{0.01}$	$0.3 \pm_{0.03}^{0.04}$
Mrk 766 ^N xi(BB)+PL	$0.31 \pm_{0.01}^{0.09}$	*	$0.77 \pm_{0.18}^{0.13}$	$0.53 \pm_{0.06}^{0.09}$	$0.83 \pm_{0.01}^{0.05}$	$0.13 \pm_{0.01}^{0.01}$	-
MCG -06-30-15 ^N xi(BB+BB)+PL	$3.45 \pm_{0.17}^{0.18}$	$0.66 \pm_{0.02}^{0.04}$	$2.95 \pm_{0.04}^{0.01}$	$0.31 \pm_{0.01}^{0.01}$	*	$0.11 \pm_{0.01}^{0.01}$	$0.27 \pm_{0.01}^{0.01}$
Mrk 1044 ^I xi(BB+BB+D)+PL	$2.72 \pm_{0.4}^{0.43}$	$0.24 \pm_{0.03}^{0.02}$	$0.27 \pm_{0.3}^{0.03}$	$-0.33 \pm_{0.03}^{0.01}$	$0.68 \pm_{0.02}^{0.29}$	$0.13 \pm_{0.01}^{0.01}$	$0.39 \pm_{0.01}^{0.02}$
IGRJ 19378-0617 ^I BB+BB+xi(PL+D)	$0.25 \pm_{0.08}^{0.08}$	$0.82 \pm_{0.07}^{0.07}$	$1.19 \pm_{0.17}^{0.18}$	$1.08 \pm_{0.04}^{0.02}$	$0.59 \pm_{0.06}^{0.06}$	$0.15 \pm_{0.01}^{0.01}$	$0.38 \pm_{0.01}^{0.01}$
NGC 4593 ^I xi(BB+BB)+PL+D	$0.49 \pm_{0.10}^{0.18}$	*	$0.6 \pm_{0.21}^{11.92}$	$2.42 \pm_{0.1}^{0.09}$	*	$0.09 \pm_{0.01}^{0.02}$	$0.21 \pm_{0.01}^{0.02}$
Mrk 766 ^I xi(BB+BB+D)+PL	$1.13 \pm_{0.11}^{0.12}$	$0.49 \pm_{0.01}^{0.03}$	$2.07 \pm_{0.31}^{0.39}$	$0.37 \pm_{0.02}^{0.02}$	*	$0.12 \pm_{0.01}^{0.01}$	$0.58 \pm_{0.05}^{0.08}$
MCG -06-30-15 ^I xi(BB+BB+D)+PL	$2.8 \pm_{0.12}^{0.13}$	$0.7 \pm_{0.01}^{0.03}$	$2.94 \pm_{0.04}^{0.01}$	$0.31 \pm_{0.01}^{0.01}$	*	$0.11 \pm_{0.01}^{0.01}$	$0.23 \pm_{0.01}^{0.02}$
Mrk 382 ^{NR} xi(BB+PL)	$11.86 \pm_{1.31}^{1.86}$	$0.48 \pm_{0.06}^{0.08}$	$6.9 \pm_{1.67}^{1.55}$	$2.01 \pm_{0.05}^{0.04}$	$0.68 \pm_{0.04}^{0.04}$	$0.11 \pm_{0.01}^{0.01}$	-
IRAS 13224-3809 ^{NR} xi(BB+PL)	$1.08 \pm_{0.03}^{0.03}$	*	$23.23 \pm_{0.11}^{0.39}$	$1.76 \pm_{0.09}^{0.08}$	$0.65 \pm_{0.02}^{0.01}$	$0.13 \pm_{0.01}^{0.01}$	-
Mrk 841 ^{NR} xi(BB+PL)	$0.36 \pm_{0.21}^{0.29}$	$0.22 \pm_{0.07}^{0.22}$	$82.76 \pm_{6.07}^{6.8}$	$2.3 \pm_{0.07}^{0.09}$	$0.4 \pm_{0.1}^{0.1}$	$0.09 \pm_{0.01}^{0.01}$	-
MR 2251 - 178 ^{NR} xi(BB+BB)+PL	$8.2 \pm_{0.38}^{0.41}$	$0.48 \pm_{0.01}^{0.01}$	$2.97 \pm_{0.01}^{0.01}$	$0.31 \pm_{0.01}^{0.01}$	$0.99 \pm_{0.01}^{0.01}$	$0.12 \pm_{0.01}^{0.01}$	$0.34 \pm_{0.01}^{0.01}$

Table 4.5: Statistical results obtained for each source of the sample fitting the best model only on the soft band and fitting the same model on the soft and hard band. We indicate with a superscript on the name of the source the hard model corresponding to the object: H for HYBRID, N for NEUTRAL, I for IONIZED, and NR for NON-REFL models. We indicate the soft model below to the name of the source.

Source	soft	soft + hard
Mrk 335 ^H	$\frac{956.7}{633} = \mathbf{1.51}$	$\frac{711.9}{617} = \mathbf{1.15}$
xi(BB+BB)+PL+D		
Fairall 9 ^H	$\frac{1078}{951} = \mathbf{1.13}$	$\frac{1053.5}{935} = \mathbf{1.13}$
xi(BB+BB+D+PL)		
Mrk 1040 ^H	$\frac{1504.7}{1422} = \mathbf{1.06}$	$\frac{1492.5}{1406} = \mathbf{1.06}$
xi(BB+BB)+PL+D		
NGC 1365 ^H	$\frac{2324.8}{1465} = \mathbf{1.59}$	$\frac{2308.7}{1449} = \mathbf{1.59}$
xi(BB+BB+D+PL)		
Ark 120 ^H	$\frac{1611.3}{1434} = \mathbf{1.12}$	$\frac{1604}{1418} = \mathbf{1.13}$
xi(BB+BB+D)+PL		
NGC 3227 ^H	$\frac{1578.3}{1438} = \mathbf{1.10}$	$\frac{1574.7}{1422} = \mathbf{1.11}$
BB+BB+xi(PL+D)		
NGC 3783 ^H	$\frac{1592.1}{1025} = \mathbf{1.55}$	$\frac{1476.3}{1009} = \mathbf{1.46}$
xi(BB+BB+D+PL)		
NGC 4051 ^H	$\frac{1955.5}{1924} = \mathbf{1.02}$	$\frac{1924.4}{1908} = \mathbf{1.01}$
xi(BB+BB+D+PL)		
NGC 4151 ^H	$\frac{2702.5}{2190} = \mathbf{1.23}$	$\frac{2695.8}{2174} = \mathbf{1.24}$
xi(BB+BB)+PL+D		
IRAS 13197-1627 ^H	$\frac{1562.7}{964} = \mathbf{1.62}$	$\frac{1375.7}{948} = \mathbf{1.45}$
xi(BB+BB)+PL+D		
NGC 5548 ^H	$\frac{1591.1}{1433} = \mathbf{1.11}$	$\frac{1578.6}{1417} = \mathbf{1.11}$
xi(BB+BB)+PL+D		
NGC 7469 ^H	$\frac{1008.1}{914} = \mathbf{1.10}$	$\frac{1003.7}{898} = \mathbf{1.12}$
BB+BB+xi(PL+D)		
NGC 4593 ^N	$\frac{1042.5}{1024} = \mathbf{1.02}$	$\frac{1042.1}{1014} = \mathbf{1.03}$
xi(BB+BB)+PL		
Mrk 915 ^N	$\frac{1079.5}{1026} = \mathbf{1.05}$	$\frac{1077.1}{1016} = \mathbf{1.06}$
xi(BB+BB)+PL		
Mrk 766 ^N	$\frac{919.3}{885} = \mathbf{1.04}$	$\frac{918.2}{875} = \mathbf{1.05}$
xi(BB)+PL		
MCG -06-30-15 ^N	$\frac{1026.6}{959} = \mathbf{1.07}$	$\frac{1024.9}{949} = \mathbf{1.08}$
xi(BB+BB)+PL		
Mrk 1044 ^I	$\frac{1378.4}{1159} = \mathbf{1.19}$	$\frac{1339.5}{1150} = \mathbf{1.16}$
xi(BB+BB+D)+PL		
IGRJ 19378-0617 ^I	$\frac{1321.8}{1165} = \mathbf{1.13}$	$\frac{1278.3}{1156} = \mathbf{1.11}$
BB+BB+xi(PL+D)		
NGC 4593 ^I	$\frac{1061.6}{1024} = \mathbf{1.04}$	$\frac{1060.1}{1015} = \mathbf{1.04}$
xi(BB+BB)+PL+D		
Mrk 766 ^I	$\frac{914.3}{883} = \mathbf{1.04}$	$\frac{896.4}{874} = \mathbf{1.03}$
xi(BB+BB+D)+PL		
MCG -06-30-15 ^I	$\frac{1051.8}{959} = \mathbf{1.10}$	$\frac{1021.3}{950} = \mathbf{1.08}$
xi(BB+BB+D)+PL		
Mrk 382 ^{NR}	$\frac{639.5}{591} = \mathbf{1.08}$	$\frac{638}{588} = \mathbf{1.09}$
xi(BB+PL)		
IRAS 13224-3809 ^{NR}	$\frac{1219.5}{695} = \mathbf{1.75}$	$\frac{1193.6}{692} = \mathbf{1.72}$
xi(BB+PL)		
Mrk 841 ^{NR}	$\frac{936}{850} = \mathbf{1.10}$	$\frac{935.9}{847} = \mathbf{1.10}$
xi(BB+PL)		
MR 2251 - 178 ^{NR}	$\frac{1237.4}{1200} = \mathbf{1.03}$	$\frac{1222}{1197} = \mathbf{1.02}$
xi(BB+BB)+PL		

4.3.7 Simultaneous fit of the soft and hard spectra

In our final test, we allow to vary the parameters of the soft and hard components of the baseline model. We show in Table 4.5 the statistical results obtained in each test. We find that the χ_r^2 significantly improves for three spectra: Mrk 335, NGC 3783, and IRAS 13197-1627. Through the final fit, we obtained $\chi_r^2 < 1.5$ for all spectra except two, even more, we obtained $\chi_r^2 < 1.2$ for all spectra except four of them. We obtain in Table 4.6 the parameters of the best soft+hard model of the sources. The main result is about the black-body components, which fit the soft excess. We find an average value of the effective temperature of 0.13 and 0.41 keV for the first and second black-body, respectively, with a relatively narrow distribution for the lower-temperature of the black-body (see Figure 4.9). Note that, the study of the rest of the parameters of the models is out of the scope of this thesis. However, we highlight that we find n_H of the cold partial covering $\leq 10^{22}$ in almost all objects for which we restrict the parameter, which is in agreement to the type-1 AGN view of our objects. The photon index, Γ , is also in agreement to the value expected for these objects ($\Gamma \sim 1.9$ Zdziarski et al., 1995). For the warm partial covering we find a wide range of values for the column density, ionization parameter, and covering fraction.

Finally, we show in Figure 4.11 the best fit obtained for each object of the sample. The objects that present ionized relativistic reflection show that this component also has contribution in the soft band, where, in combination with the black-body components, give the best fit for these objects. In the objects for which only the neutral/distant reflection is present, this component has not contribution in the soft band, and the soft excess is fitted through the black-body components. This is the same situation for the four objects fitted without reflection components, in which, the soft excess is fitted through the addition of one or two black-body components.

4.4 Summary and conclusions

We have studied the soft excess in the sample of 22 type-1 AGN (25 spectra in total) compiled in Victoria-Ceballos et al. (2023) with simultaneous observations of *XMM-Newton* and *NuSTAR*, in the range of 0.5 to 70 keV. For this, we test different physical and

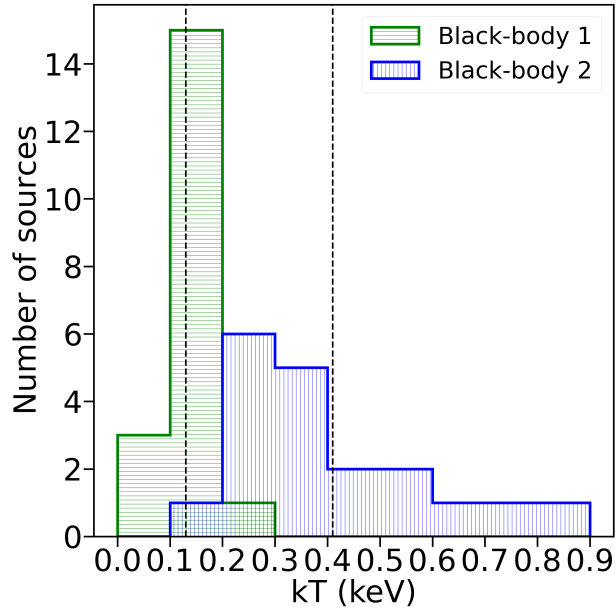


Figure 4.9: Effective temperature (kT) distribution of the two black-body components. Vertical dashed lines at 0.13 and 0.41 keV, indicate the mean value of kT of the first and second black-body components, respectively.

phenomenological models, performing a spectral fitting using the XSPEC spectral fitting package. The main results are as follows:

1. We find that all spectra in our sample have a soft excess.
2. We find that both, the cold and warm partial covering are need to fit the emission below 2 keV in the sample.
3. None of the spectra of the sample is well fitted using a comptonized component.
4. We find that the phenomenological model of black-body is necessary to obtain good fits for all spectra of the sample. Even more, 21 spectra require two black-body components, while only four are fitted with a single black-body.
5. 10 spectra are well fitted with a single model, while 15 spectra are statistically equally fitted with more than one model.
6. Considering the best model according to AIC, the preferred model by most spectra considers two black-body absorbed by warm partial covering, while the intrinsic

emission and the disk reflection are not affected by this absorption.

7. By allowing to vary all free parameters of the whole model (soft + hard band) we obtain $\chi_r^2 < 1.5$ for all spectra, except two of them.

Among the different scenarios tested to explain the soft excess in the AGN, we find that the Comptonization scenario (Magdziarz et al., 1998; Done et al., 2012; Gliozzi & Williams, 2020) is not capable of explaining this excess in the sample studied. This is clearly seen by the poor spectral fits obtained using the NTHCOMP model (see Section 4.3.3 and Table 4.2). We obtain only a marginal improvement when we add the NTHCOMP component to our baseline model. So, this scenario is ruled out.

On the other hand, we find that the scenarios of relativistically blurred reflection (Crummy et al., 2006; García et al., 2019; Waddell & Gallo, 2020) and/or relativistically smeared absorption (Gierliński & Done, 2004; Middleton et al., 2007; Done, 2007) in combination with one or two black-body components are necessary to explain the soft excess of the objects in the sample. Note that, while the hard reflection features are well associated to physical structures of the AGN, we require the use of the phenomenological model of black-body to fit the soft excess.

According to AIC, there is one model preferred by the majority of objects among the all tested models, which consists of two black-body components absorbed by warm partially ionized partial covering material for the soft band, disk plus torus reflection absorbed by cold partial covering material for the hard band, and the intrinsic emission absorbed by cold partial covering material.

Our results suggest that the soft excess has a possible origin in the accretion disk, due to a truncated disk with two different temperatures. Even more, according to the preferred model by the majority of the sample, there is a partially ionized partial covering material over the accretion disk, which absorbs the soft disk emission, but, this material does not affect the reflected emission by the disk. We speculate that this material is wind or clouds of ionized gas located on the accretion disk. We show in Figure 4.10 a sketch describing this scenario. The parameters of the models need to be further explored to understand if they support this proposed scenario.

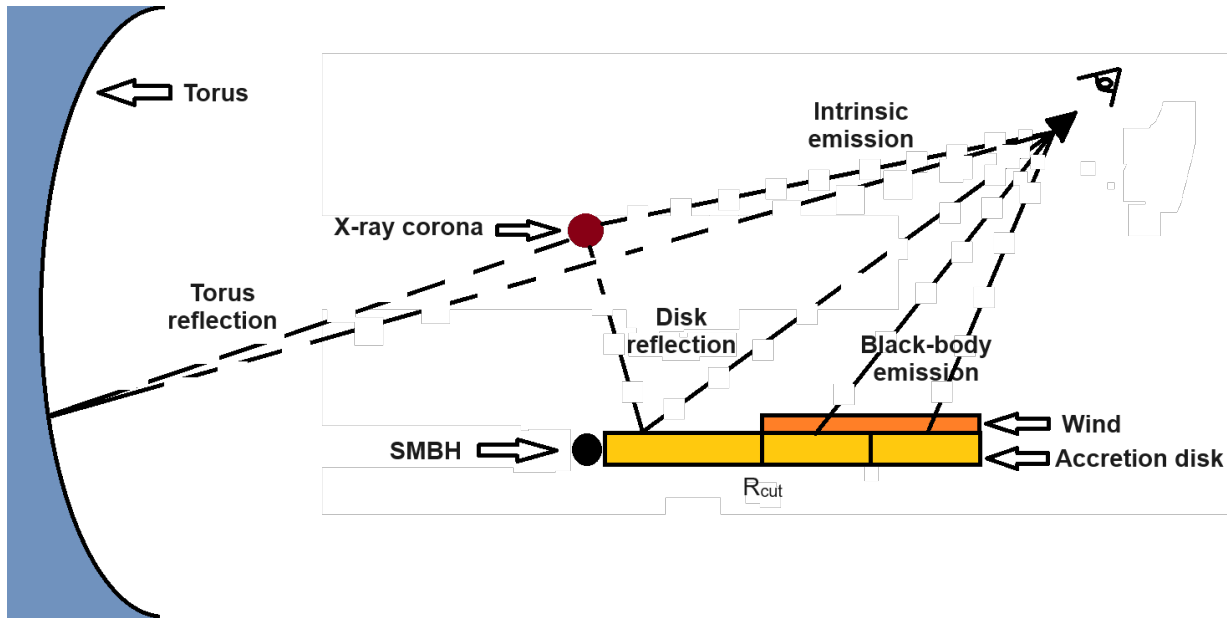


Figure 4.10: Sketch of the global physical scenario of the soft and hard emission according to our results about the preferred model by the sample. Note that some components disappear when the baseline model do not require disk or torus reflection, or neither of both.

Finally, recent works indicate that the geometry of the X-ray corona could be different from the lamp-post scenario generally assumed (Fabian et al., 2017) using X-ray polarization at least for IC 4329A (Pal et al., 2023). For this particular object they favor a conical geometry for the X-ray corona. Another possible geometry is the slab-like structure sandwiching the accretion disk (Haardt & Maraschi, 1993). We believe that the shape of the corona (and its location in the AGN) according to the lamp-post, slab, and conical scenarios, do not affect our analysis, which is done in the lamp-post framework. If the corona is a slab or conical instead, the need for black-bodies to explain the soft excess, its location and absorbers along the line-of-sight discussed in this chapter are still valid.

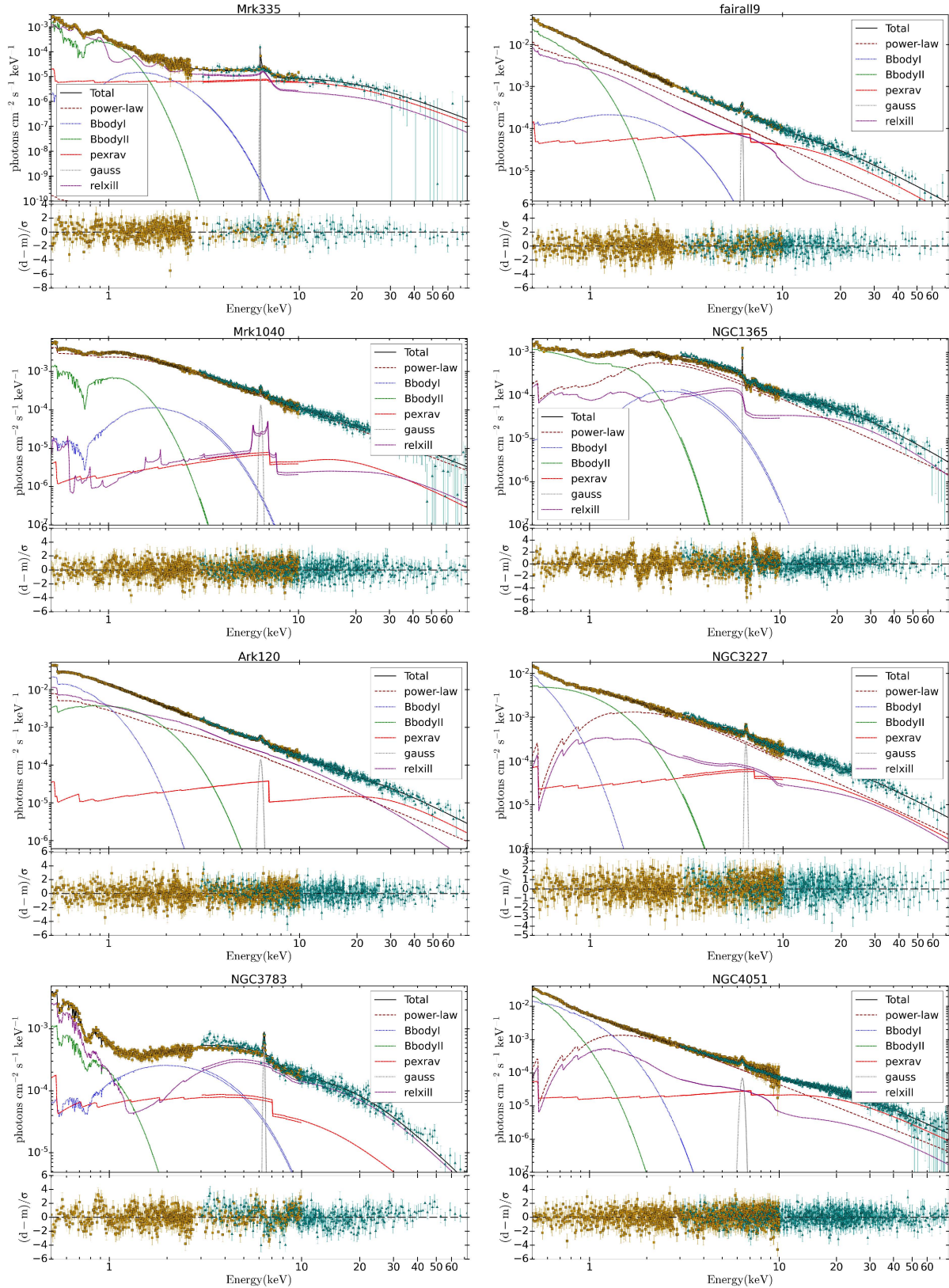


Figure 4.11: Best fit obtained for each object of the sample. We show the best fit (black solid line) to the data in the top panel and the ratio between model and data in the bottom panel. The gold dots and dark cyan diamonds show the data from *XMM-Newton* and *NuSTAR* respectively.

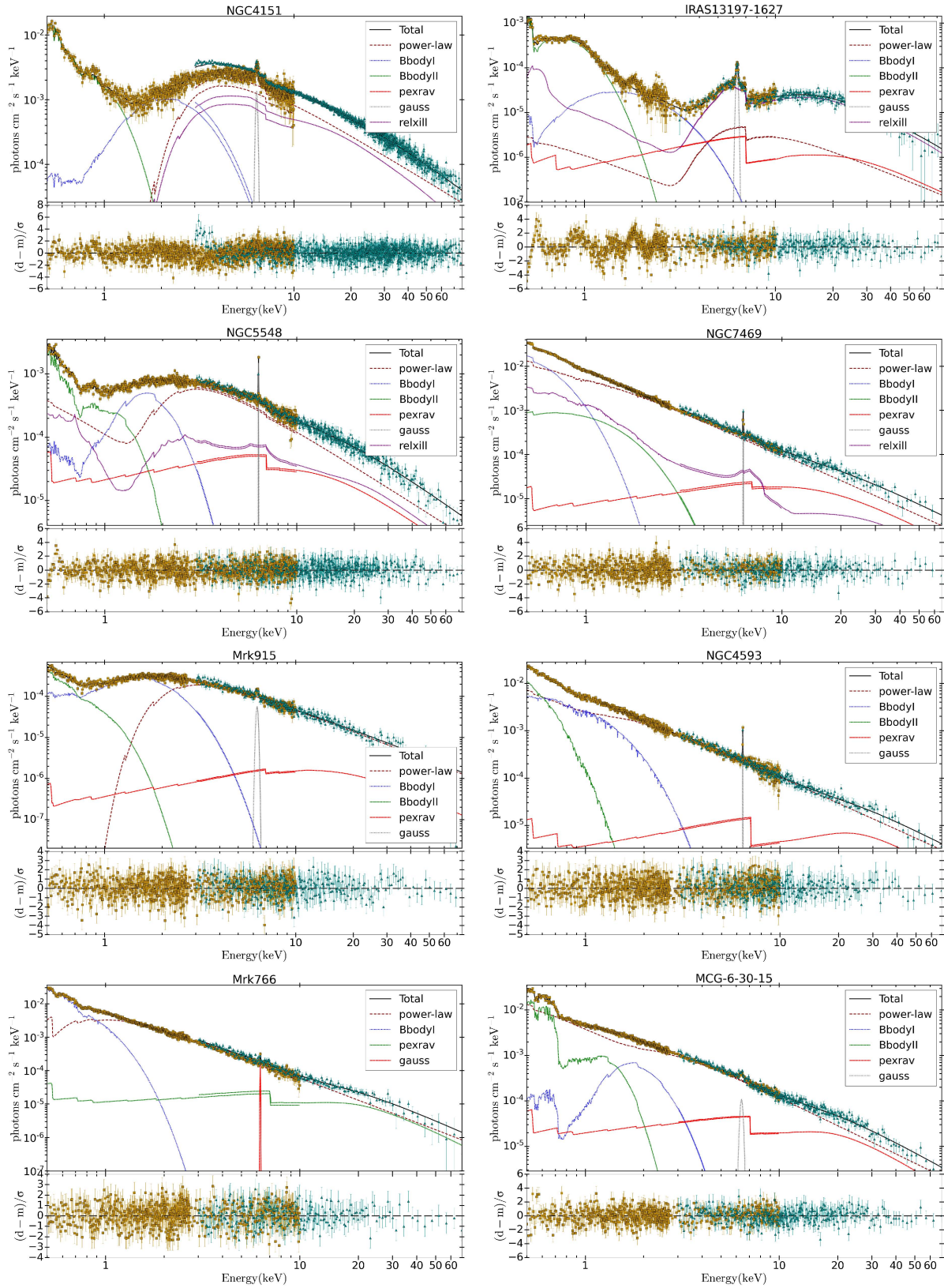


Figure 11 (Cont.)

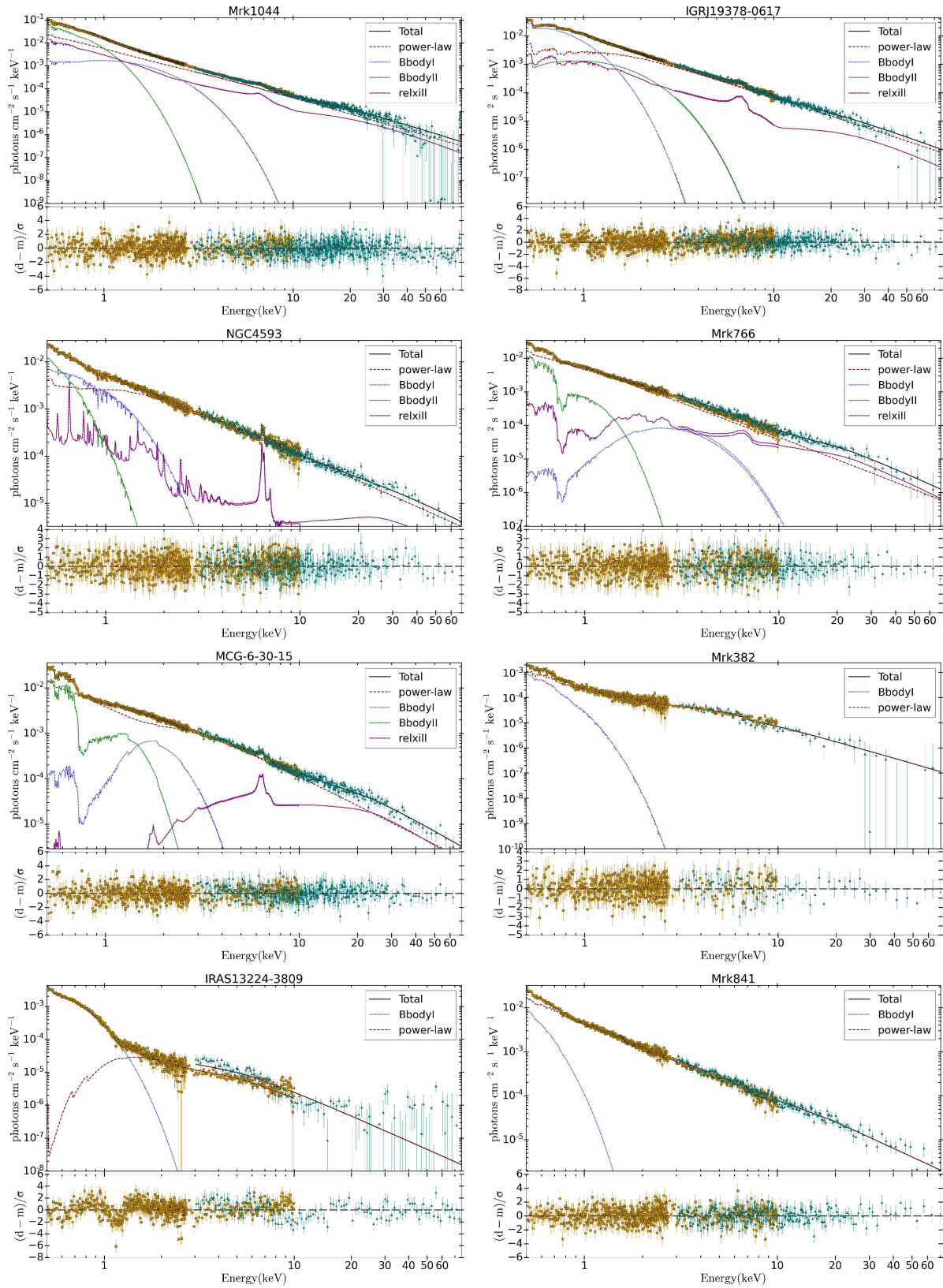


Figure 11 (Cont.)

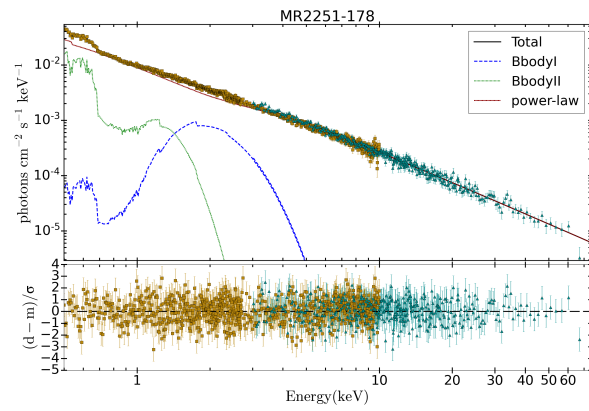


Figure 11 (Cont.)

CHAPTER 5

SUMMARY AND DISCUSSION

The physical details of the dusty torus in the AGN, such as the dust characteristics (both in terms of chemical composition and of grain size distribution) and its geometrical distribution, are still quite poorly understood (Ramos Almeida & Ricci, 2017). One way to study the dusty torus in AGN is throughout the fitting of the SED to dust models using different distributions and/or chemical compositions. The interpretation of high spatial resolution spectra, achieved by means of SED fitting techniques exploiting theoretical emission models, is the key to an unbiased study of the dust properties in AGN, limiting the effect of the host galaxy emission (Ramos Almeida et al., 2009, 2011; Alonso-Herrero et al., 2011; González-Martín et al., 2019).

In this thesis we have studied the dusty torus in the type-2 AGN NGC 1068 using N- and Q-band Michelle/Gemini spectra, performing our analysis through the spectral fitting of different available dust models, and also by creating our torus model for NGC 1068. Our main results were:

- Among the available models, the resulting best fit was obtained using the clumpy disk plus wind model by Hönic & Kishimoto (2017). However, the best fit was statistically unsatisfactory. We then explored the possibility of adding complexity to the models by untying one and then two parameters when doing the fits of the N and Q spectra separately. We found that the fit significantly improves using the smooth

torus model by Fritz et al. (2006) and four combinations of untied parameters. In this scenario, the emission in the two spectral ranges here considered is dominated by dust with different geometrical locations and distributions. These components are characterized by different values of the equatorial optical depth, the opening angle, and of the parameters regulating the dust density gradients. We interpret these results as a signal of the complexity of the dust in NGC 1068.

- For the 3D Monte Carlo radiative simulations, we created grids of SEDs testing the physical parameters of the torus and the shape and size of the dust grains. We used two concentric tori in all simulations. The final best fit consists of dust of 0.1-1 μm and inner radius of both tori of 0.2 pc. The parameters changing from both tori are: i) the exponent of the power-law describing the radial distribution $p_1=0.2$ and $p_2=1$, ii) the exponent of the polar distribution $q_1=3.2$, and $q_2=5.8$, iii) the half opening angle $\sigma_1=42$ and $\sigma_2=58$, iv) the outer radius $R_{\text{max},1}=1.8$ pc and $R_{\text{max},2}=28$ pc, and v) the equatorial optical depth to $\tau_{9.7\mu\text{m},1}=12$ and $\tau_{9.7\mu\text{m},2}=0.3$.

These results can be interpreted as a compelling evidence for a complex dusty torus for NGC 1068. We speculate that this can be understood as inner compact disk/torus plus an outer extended torus/wind, conforming either a flared disk or a dynamical fountain model for the dust. Furthermore, some mechanism for grain growth need to be claimed to explain the large grains required to fit the mid-infrared ground-based spectra of NGC 1068. Recently results of the dusty structure of NGC 1068 using VLTI/MATISSE observations presented by Gamez Rosas et al. (2022) identify dust emission surrounding the SMBH, in addition to emission due to a polar component, which is in agreement with the interpretation given in this work.

Meanwhile, there are different scenarios to explain the hard X-ray spectrum of the AGN, among which is relativistic reflection, and distant reflectors (Nardini et al., 2011; Patrick et al., 2011; Mehdipour et al., 2015). In the same way, there are different models, which are used throughout the fitting of the SED of the AGN. For instance, PEXRAV (Magdziarz & Zdziarski, 1995) assumes optically thick cold material distributed in a slab, RELXILL (Dauser et al., 2010; Garcıa et al., 2014) models irradiation of accretion by a

broken power law emissivity, REFLIONX (Ross et al., 1999; Ross & Fabian, 2005) assume an optically-thick atmosphere, and it adds fluorescence lines.

In this thesis we have studied the scattered medium in a sample of 22 Seyfert galaxies using simultaneous observations of *XMM-Newton* and *NuSTAR*. For this purpose we selected and tested a set of available reflection models using the *XSPEC* spectral fitting package.

In our sample, 18 sources show evidence of the reflection. Among them, 12 objects prefer a hybrid reflection model, which incorporates neutral and relativistic ionized medium; one object prefers a neutral reflection model; two objects prefer a relativistic ionized reflection model; and three objects equally prefer the neutral and relativistic ionized reflection models. Also, we find that four objects do not present the reflection component.

These results suggest that considering a hybrid scenario, in which the reflection from type-1 AGN has a contribution from at least two different media, can satisfactorily explain the observed spectra of most of these objects. In support of these results some authors have concluded that it is necessary to consider both neutral/distant and ionized/relativistic reflection components to satisfactorily fit the X-ray spectra above 3 keV of some AGN (Parker et al., 2019; Lohfink et al., 2016; Nardini et al., 2011; Walton et al., 2018). The strong intrinsic continuum phase of variable AGN is probably the explanation for the four objects for which we do not find reflection features.

Finally, we also studied the soft excess in the sample of 22 type-1 AGN compiled in Victoria-Ceballos et al. (2023) with simultaneous observations of *XMM-Newton* and *NuSTAR*, in the range of 0.5 to 70 keV. For this, we test different physical and phenomenological models, performing a spectral fitting using the *XSPEC* spectral fitting package. The main results were:

- All the objects in the sample show soft excess.
- None of the objects in the sample is well fitted using a comptonized component.
- The phenomenological model of black-body is necessary to obtain good fits for all the objects of our sample. Even more, 21 objects require two black-body components, while only four are fitted with a single black-body.

- Cold and warm partial covering are needed to fit the emission below 2 keV in the sample.

We speculate that our results are consistent with an origin of the soft excess in the accretion disk. Even more, according to the preferred model by the majority of the sample, there is a partially ionized partial covering material over the accretion disk, which absorbs the soft disk emission, that however, this material does not affect the reflected emission by the disk. We speculate that this material are clouds of ionized gas located on the accretion disk.

Through the work presented in this thesis we have addressed three questions that currently remain open and under debate in the field of the AGN: i) the geometry, chemical composition and distribution of the dusty torus; ii) the physical components in which X-ray reflection occurs; and iii) the origin of soft excess.

While these results do not end the discussion around these open questions, they do provide important clues in search of the final answer. Answering these questions concretely requires future plans. For the dusty torus, the creation of more complex models is required, which consider scenarios closer to the real physics and chemistry of the dust, for which the results of this work on the geometry, distribution and size of the dust can be the basis of new models to be developed. For the complete characterization of the X-ray emission of AGN, greater spectrum coverage and better resolution at high energies are required. With the availability of new broadband data, a more complete study can be carried out from different sources, based on the models obtained in this thesis. Finally, to explain the soft excess in the AGN through models, the creation of one that considers more than one scenario, as suggested by the results found in this thesis work, could give a more specific response to the observations in various samples of objects.

As a general highlight of this thesis work, we have demonstrated the need to consider more complete scenarios than those currently available, when attempting to explain the phenomenology around the AGN through models, particularly regarding the dusty torus and the X-ray spectrum of these objects.

The results obtained in this thesis, as well as the data and tools used, could contribute to the development of future research. In this chapter we will mention some of the future studies that can be developed from this work.

- **Incorporation of new sources to the sample**

Since our current results consider few objects preferring the reflection-in-accretion disk or reflection-in-torus models, it is difficult to determine if this depends on the AGN state. To obtain more robust results about the intrinsic properties of the AGN, specifically looking for a correlation among the accretion rate, the photon index and the reflecting medium, the number of objects in the sampled should be increased, either when they are released new data from simultaneous observations or even requesting observation time for candidate sources. The inclusion of new sources allows us to obtain a more clearer trend between the state of accretion and the X-ray reflection. The desired objects to be included in the sample must be selected according to their accretion rate, which must be in a range between -2.5 and 0. This would allow us to populate our accretion rate vs photon index plot, and check if there is a relationship between these parameters and the preferred model. Furthermore, it is desirable to have a minimum number of data per accretion rate bin. Considering a bin of 0.5 in the range of 0 to -2.5, we believe that having at least 10 objects

per bin would allow us to do a more robust analysis.

- **Study of the variability of the AGNs**

A natural extension of the work performed in our type-1 AGN sample is the study of the X-ray variability in the AGN. Since variability is an intrinsic characteristic of these objects, we have circumvented this by using simultaneous observations of the objects with *XMM-Newton* and *NuSTAR*. The results obtained about the reflection and soft excess models can be used and applied to the same objects using different available observations, to study the variability on such sources. It is expected that the time scales of the variability in the objects will provide clues about the location of each component. Currently, most of our objects present more than one simultaneous observation between *XMM-Newton* and *NuSTAR* (note that for this work we have taken only one observation according to our exposure time criterion), so it is feasible to carry out this work without requiring observation campaigns.

- **Study of the X-ray SED of NGC 1068 through SKIRT.**

Recent versions of SKIRT incorporate, in addition to dust, gas (Vander Meulen et al., 2023). Due to the fact that it is expected that dust and gas coexist on the internal walls of the torus, carrying out a simulation to obtain the SED in X-rays of NGC 1068 considering the same geometry obtained through the work in the infrared, allows us to know if this geometry is capable to explaining both bands at the same time. Note that, Bauer et al. (2015) fit the combined *NuSTAR*, *Chandra*, *XMM-Newton* and *Swift*-BAT spectra of NGC 1068, finding a complex reflector structure, consisting of multiple components: two nuclear and one extended.

7.1 Testing a complex model to fit the soft excess.

In Chapter 4 of this thesis we test different models to try to explain the soft excess considering the four scenarios proposed for its origin. In this section we show the results obtained by testing a more complex model, which aims to explain soft excess comprehensively: REXCOR.

REXCOR is a model that combines the effects of the ionized relativistic reflection and the emission from a warm corona to fit the 0.3-100 keV spectrum of the AGN (Xiang et al., 2022). This model considers a hot corona situated above of the SMBH illuminating the surface of a thin accretion disk, and a warm corona produced by accretion energy which is injected into the irradiated disc surface, altering the emission and reflection spectrum due to enhanced Comptonization and bremsstrahlung emission. Figure 7.1 shows an illustration of the components in the REXCOR model.

The model contains four parameters, in addition to the redshift and the normalization: the heating fraction, the photon index of the power-law, the warm corona heating fraction, and the warm corona Thomson depth. REXCOR also includes eight different grids, calculated for two different values of Eddington ratio, SMBH spin and height of the hot corona.

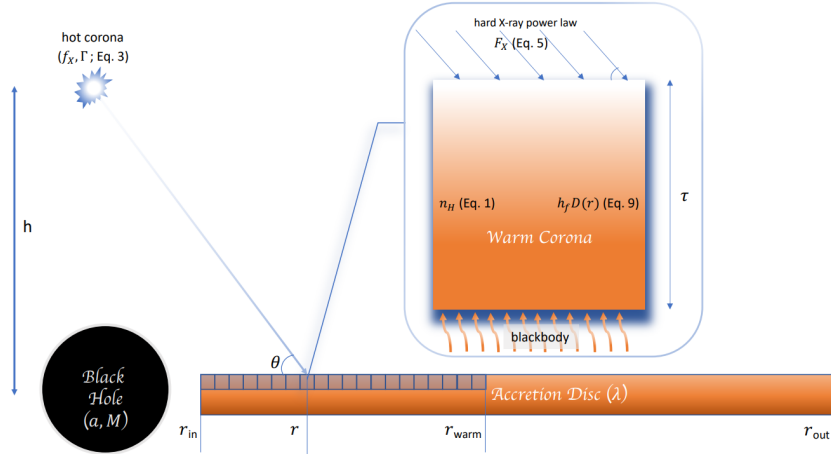


Figure 7.1: Illustration of the components of the REXCOR model. Figure from Xiang et al. (2022).

For test the model in our sample, we follow the same way of Xiang et al. (2022). For NGC 4593, (which is a source in our sample) their baseline model contemplate the galactic absorption, a component of warm absorption, two gaussian lines, the cut-off power-law, the REXCOR model, and ionized reflection; and has the form:

$$M = phabs * WA(zgauss1 + zgauss2 + zcutoffpl + rexcor + xillver) \quad (7.1)$$

Following this baseline model, we create a general model for all of our sources, which includes the same components, except for the Gaussian lines. We also replace the XILLVER model with REFLIONX, since they both model the same scenario:

$$M = Cte * phabs * zxipcf(zcutoffpl + rexcor + reflionx) \quad (7.2)$$

We test the eight grids included in REXCOR in our sample, i.e., we perform 176 spectral fits with this model in our sample of 22 sources. We show in Table 7.1 the statistical results obtained through the REXCOR model applied in each object of the sample. Note that we obtain satisfactory results only for two objects, namely Mrk 766 and Mrk 841.

Table 7.1: Statistical results obtained with the eight tables of the REXCOR model applied to the sample.

Source	0.01/0.99/20	0.01/0.99/5	0.01/0.9/20	0.01/0.9/5	0.1/0.99/20	0.1/0.99/5	0.1/0.9/20	0.1/0.9/5
Mrk 335	$\frac{1228.3}{631}=1.91$	$\frac{1363.4}{631}=2.16$	$\frac{3292.9}{631}=5.22$	$\frac{1403.3}{631}=2.22$	$\frac{1144.5}{631}=1.81$	$\frac{1217}{631}=1.93$	$\frac{1108.7}{631}=1.76$	$\frac{1191.6}{631}=1.89$
Fairall 9	$\frac{1358.4}{949}=1.43$	$\frac{1463.6}{949}=1.54$	$\frac{1504.7}{949}=1.59$	$\frac{1632.9}{949}=1.72$	$\frac{1303.7}{949}=1.37$	$\frac{1337.6}{949}=1.41$	$\frac{1297}{949}=1.37$	$\frac{1394.2}{949}=1.47$
Mrk 1040	$\frac{1792.3}{1420}=1.26$	$\frac{1749.4}{1420}=1.23$	$\frac{1838.9}{1420}=1.30$	$\frac{1847.7}{1420}=1.30$	$\frac{1759.7}{1420}=1.24$	$\frac{1818.1}{1420}=1.28$	$\frac{1766.6}{1420}=1.24$	$\frac{1808.8}{1420}=1.27$
NGC 1365	$\frac{15993.5}{1463}=10.93$	$\frac{7721.4}{1463}=5.28$	$\frac{6144.6}{1463}=4.2$	$\frac{9725.8}{1463}=6.65$	$\frac{7808.6}{1463}=5.34$	$\frac{5746.3}{1463}=3.93$	$\frac{8066.4}{1463}=5.51$	$\frac{5440.9}{1463}=3.72$
Ark 120	$\frac{2072.5}{1432}=1.45$	$\frac{2044.4}{1432}=1.43$	$\frac{2367}{1432}=1.65$	$\frac{2814}{1432}=1.97$	$\frac{1974}{1432}=1.38$	$\frac{2057.5}{1432}=1.44$	$\frac{1992.2}{1432}=1.39$	$\frac{1996.1}{1432}=1.39$
NGC 3227	$\frac{5427.9}{1436}=3.78$	$\frac{2639.8}{1436}=1.84$	$\frac{2977.6}{1436}=2.07$	$\frac{2595.5}{1436}=1.81$	$\frac{2092}{1436}=1.46$	$\frac{4658.5}{1436}=3.24$	$\frac{2090.9}{1436}=1.46$	$\frac{2314.4}{1436}=1.61$
NGC 3783	$\frac{4540.2}{1023}=4.44$	$\frac{4540.3}{1023}=4.44$	$\frac{4564.2}{1023}=4.46$	$\frac{4564.2}{1023}=4.46$	$\frac{4540.2}{1023}=4.44$	$\frac{4564.4}{1023}=4.46$	$\frac{4540.2}{1023}=4.44$	$\frac{4564.2}{1023}=4.46$
NGC 4051	$\frac{2171.7}{1922}=1.13$	$\frac{2157.5}{1922}=1.12$	$\frac{2191.5}{1922}=1.14$	$\frac{2291.5}{1922}=1.19$	$\frac{2139.1}{1922}=1.11$	$\frac{2239.3}{1922}=1.17$	$\frac{2093.1}{1922}=1.09$	$\frac{2181.7}{1922}=1.14$
NGC 4151	$\frac{5358.7}{2188}=2.45$	$\frac{5290.6}{2188}=2.42$	$\frac{5358.7}{2188}=2.45$	$\frac{5358.7}{2188}=2.45$	$\frac{5358.7}{2188}=2.45$	$\frac{5358.7}{2188}=2.45$	$\frac{5358.7}{2188}=2.45$	$\frac{5358.7}{2188}=2.45$
IRAS 13197-1627	$\frac{3152.6}{962}=3.28$	$\frac{3324.1}{962}=3.46$	$\frac{3523.9}{962}=3.66$	$\frac{6172.3}{962}=6.42$	$\frac{3152.4}{962}=3.28$	$\frac{3175}{962}=3.30$	$\frac{5788.5}{962}=6.02$	$\frac{3201.1}{962}=3.33$
NGC 5548	$\frac{5546}{1431}=3.88$	$\frac{5546}{1431}=3.88$	$\frac{5546}{1431}=3.88$	$\frac{5546}{1431}=3.88$	$\frac{5546}{1431}=3.88$	$\frac{5546}{1431}=3.88$	$\frac{5546}{1431}=3.88$	$\frac{5546}{1431}=3.88$
NGC 7469	$\frac{1194.7}{912}=1.31$	$\frac{1222.5}{912}=1.34$	$\frac{1189.3}{912}=1.3$	$\frac{1226.8}{912}=1.35$	$\frac{1194.6}{912}=1.31$	$\frac{1216.1}{912}=1.33$	$\frac{1327.3}{912}=1.46$	$\frac{1215.1}{912}=1.33$
Mrk 915	$\frac{1861.6}{1024}=1.82$	$\frac{1803.1}{1024}=1.76$	$\frac{1975}{1024}=1.93$	$\frac{2001.8}{1024}=1.95$	$\frac{1603.1}{1024}=1.57$	$\frac{1465.2}{1024}=1.43$	$\frac{1606.4}{1024}=1.57$	$\frac{1454.7}{1024}=1.42$
Mrk 1044	$\frac{4193.4}{1157}=3.62$	$\frac{2126.4}{1157}=1.84$	$\frac{9454.4}{1157}=8.17$	$\frac{3375.5}{1157}=2.92$	$\frac{1909.6}{1157}=1.65$	$\frac{1872}{1157}=1.62$	$\frac{2287.5}{1157}=1.98$	$\frac{1884}{1157}=1.63$
I GRJ 19378-0617	$\frac{2818.7}{1163}=2.42$	$\frac{2469.9}{1163}=2.12$	$\frac{2239.7}{1163}=1.93$	$\frac{2511.6}{1163}=2.16$	$\frac{1451}{1163}=1.25$	$\frac{1475.1}{1163}=1.27$	$\frac{1485.6}{1163}=1.28$	$\frac{1430.5}{1163}=1.23$
Mrk 766	$\frac{962.2}{881}=1.09$	$\frac{954.8}{881}=1.08$	$\frac{961.3}{881}=1.09$	$\frac{957.7}{881}=1.09$	$\frac{961.1}{881}=1.09$	$\frac{954.3}{881}=1.08$	$\frac{960.3}{881}=1.09$	$\frac{955}{881}=1.08$
NGC 4593	$\frac{1127.3}{1021}=1.10$	$\frac{1144.2}{1021}=1.12$	$\frac{1127.3}{1021}=1.10$	$\frac{1137.1}{1021}=1.11$	$\frac{1126.2}{1021}=1.1$	$\frac{1134.7}{1021}=1.11$	$\frac{1128.3}{1021}=1.11$	$\frac{1141.6}{1021}=1.12$
MCG -06-30-15	$\frac{1332.5}{957}=1.39$	$\frac{1348.3}{957}=1.41$	$\frac{1317}{957}=1.38$	$\frac{1325.8}{957}=1.39$	$\frac{1257.4}{957}=1.31$	$\frac{1169.1}{957}=1.22$	$\frac{1266.9}{957}=1.32$	$\frac{1197.2}{957}=1.25$
Mrk 382	$\frac{784.9}{587}=1.34$	$\frac{777.9}{587}=1.33$	$\frac{788.1}{587}=1.34$	$\frac{784.2}{587}=1.34$	$\frac{783.8}{587}=1.34$	$\frac{746.6}{587}=1.27$	$\frac{783.1}{587}=1.33$	$\frac{780.1}{587}=1.33$
IRAS 13224-3809	$\frac{2192.5}{691}=3.17$	$\frac{2086.5}{691}=3.02$	$\frac{1999.7}{691}=2.89$	$\frac{2169}{691}=3.14$	$\frac{2201.1}{691}=3.19$	$\frac{1594.7}{691}=2.31$	$\frac{1482.9}{691}=2.15$	$\frac{1580.8}{691}=2.29$
Mrk 841	$\frac{922.8}{846}=1.09$	$\frac{922.8}{846}=1.09$	$\frac{921.8}{846}=1.09$	$\frac{921.9}{846}=1.09$	$\frac{921.1}{846}=1.09$	$\frac{922.8}{846}=1.09$	$\frac{921.8}{846}=1.09$	$\frac{922.7}{846}=1.09$
MR 2251-178	$\frac{1838.5}{1198}=1.53$	$\frac{1452.6}{1198}=1.21$	$\frac{1680.2}{1198}=1.40$	$\frac{1460.4}{1198}=1.22$	$\frac{1455.3}{1198}=1.21$	$\frac{1412.8}{1198}=1.18$	$\frac{1447.9}{1198}=1.21$	$\frac{1411.4}{1198}=1.18$

BIBLIOGRAPHY

- Alonso-Herrero, A., Ramos Almeida, C., Mason, R., et al. 2011, , 736, 82
- Alston, W. N., Fabian, A. C., Kara, E., et al. 2020, *Nature Astronomy*, 4, 597.
doi:10.1038/s41550-019-1002-x
- Antonucci, R. 1993, , 31, 473
- Baes, M., Davies, J. I., Dejonghe, H., et al. 2003, , 343, 1081
- Baes, M., Verstappen, J., De Looze, I., et al. 2011, , 196, 22
- Baloković, M., Brightman, M., Harrison, F. A., et al. 2018, , 854, 42
- Barvainis, R. 1987, , 320, 537. doi:10.1086/165571
- Bauer, F. E., Arévalo, P., Walton, D. J., et al. 2015, , 812, 116. doi:10.1088/0004-637X/812/2/116
- Beckmann, V. & Shrader, C. R. 2012, *Active Galactic Nuclei*, ISBN-13: 978-3527410781.
350 pages. Wiley-VCH Verlag GmbH, 2012
- Bianchi, S., Chiaberge, M., Evans, D. A., et al. 2010, , 405, 553. doi:10.1111/j.1365-2966.2010.16475.x
- Bock, J. J., Neugebauer, G., Matthews, K., et al. 2000, , 120, 2904. doi:10.1086/316871

- Boissay, R., Ricci, C., & Paltani, S. 2016, , 588, A70. doi:10.1051/0004-6361/201526982
- Brightman, M. & Nandra, K. 2011, , 413, 1206. doi:10.1111/j.1365-2966.2011.18207.x
- Chelli, A., Perrier, C., Cruz-Gonzalez, I., et al. 1987, , 177, 51
- Crummy, J., Fabian, A. C., Gallo, L., et al. 2006, , 365, 1067. doi:10.1111/j.1365-2966.2005.09844.x
- Cameron, M., Storey, J. W. V., Rotaciuc, V., et al. 1993, , 419, 136. doi:10.1086/173467
- Dauser, T., Wilms, J., Reynolds, C. S., et al. 2010, , 409, 1534
- Diaz, Y., Arévalo, P., Hernández-García, L., et al. 2020, , 496, 5399. doi:10.1093/mnras/staa1762
- Ding, N., Gu, Q., Tang, Y., et al. 2022, , 659, A172. doi:10.1051/0004-6361/202142650
- Done, C. 2007, Progress of Theoretical Physics Supplement, 169, 248. doi:10.1143/PTPS.169.248
- Done, C. & Nayakshin, S. 2007, , 377, L59. doi:10.1111/j.1745-3933.2007.00303.x
- Done, C., Davis, S. W., Jin, C., et al. 2012, , 420, 1848. doi:10.1111/j.1365-2966.2011.19779.x
- Efstathiou, A., & Rowan-Robinson, M. 1995, , 273, 649
- Fabian, A. C., Rees, M. J., Stella, L., et al. 1989, , 238, 729
- Fabian, A. C., Zoghbi, A., Ross, R. R., et al. 2009, , 459, 540. doi:10.1038/nature08007
- Fabian, A. C., Lohfink, A., Belmont, R., et al. 2017, , 467, 2566. doi:10.1093/mnras/stx221
- Falocco, S., Carrera, F. J., Barcons, X., et al. 2014, , 568, A15. doi:10.1051/0004-6361/201322812
- Fanaroff, B. L. & Riley, J. M. 1974, , 167, 31P. doi:10.1093/mnras/167.1.31P

- Fritz, J., Franceschini, A., & Hatziminaoglou, E. 2006, , 366, 767
- Gómez Rosas, V., Isbell, J. W., Jaffe, W., et al. 2022, , 602, 403. doi:10.1038/s41586-021-04311-7
- García, J., Dauser, T., Lohfink, A., et al. 2014, , 782, 76
- García, J. A., Kara, E., Walton, D., et al. 2019, , 871, 88. doi:10.3847/1538-4357/aaf739
- George, I. M. & Fabian, A. C. 1991, , 249, 352. doi:10.1093/mnras/249.2.352
- Ghisellini, G., Haardt, F., & Matt, G. 1994, , 267, 743. doi:10.1093/mnras/267.3.743
- Gierliński, M. & Done, C. 2004, , 349, L7. doi:10.1111/j.1365-2966.2004.07687.x
- González-Martín, O., Masegosa, J., Márquez, I., et al. 2006, , 460, 45. doi:10.1051/0004-6361:20054756
- González-Martín, O., Masegosa, J., Márquez, I., et al. 2009, , 506, 1107. doi:10.1051/0004-6361/200912288
- González-Martín, O., Masegosa, J., García-Bernete, I., et al. 2019, , 884, 10. doi:10.3847/1538-4357/ab3e6b
- Giozzi, M. & Williams, J. K. 2020, , 491, 532. doi:10.1093/mnras/stz3005
- Gómez-Guijarro, C., González-Martín, O., Ramos Almeida, C., et al. 2017, , 469, 2720. doi:10.1093/mnras/stx1037
- Granato, G. L., & Danese, L. 1994, , 268, 235
- Guo, W.-J., Li, Y.-R., Zhang, Z.-X., et al. 2022, , 929, 19. doi:10.3847/1538-4357/ac4e84
- Haardt, F. & Maraschi, L. 1993, , 413, 507. doi:10.1086/173020
- Harrison, F. A., Craig, W. W., Christensen, F. E., et al. 2013, , 770, 103
- Heusler, M. 1996, *Helvetica Physica Acta*, 69, 501. doi:10.48550/arXiv.gr-qc/9610019

- Hickox, R. C. & Alexander, D. M. 2018, , 56, 625. doi:10.1146/annurev-astro-081817-051803
- Ho, L. C., Filippenko, A. V., Sargent, W. L. W., et al. 1997, , 112, 391. doi:10.1086/313042
- Hönig, S. F. & Kishimoto, M. 2010, , 523, A27. doi:10.1051/0004-6361/200912676
- Hönig, S. F., & Kishimoto, M. 2017, , 838, L20
- Jaffe, W., Meisenheimer, K., Röttgering, H. J. A., et al. 2004, , 429, 47
- Jansen, F., Lumb, D., Altieri, B., et al. 2001, , 365, L1
- Kaufmann, W. J. 1979, San Francisco : W. H. Freeman, c1979.
- Kellermann, K. I., Sramek, R. A., Schmidt, M., et al. 1994, , 108, 1163. doi:10.1086/117145
- Kormendy, J., & Ho, L. C. 2013, , 51, 511
- Koulouridis, E. 2014, , 570, A72
- Krongold, Y., Dultzin-Hacyan, D., & Marziani, P. 2003, Active Galactic Nuclei: From Central Engine to Host Galaxy, 523
- Laor, A. 1991, , 376, 90. doi:10.1086/170257
- Li, A. & Draine, B. T. 2001, , 554, 778. doi:10.1086/323147
- Liu, J. 2016, , 463, L108. doi:10.1093/mnras/164
- Liu, H., Wang, H., Abdikamalov, A. B., et al. 2020, , 896, 160. doi:10.3847/1538-4357/ab917a
- Lohfink, A. M., Reynolds, C. S., Pinto, C., et al. 2016, , 821, 11. doi:10.3847/0004-637X/821/1/11
- Magdziarz, P., & Zdziarski, A. A. 1995, , 273, 837
- Magdziarz, P., Blaes, O. M., Zdziarski, A. A., et al. 1998, , 301, 179. doi:10.1046/j.1365-8711.1998.02015.x

- Marchesi, S., Ajello, M., Marcotulli, L., et al. 2018, , 854, 49. doi:10.3847/1538-4357/aaa410
- Marchesi, S., Zhao, X., Torres-Albà, N., et al. 2022, , 935, 114. doi:10.3847/1538-4357/ac80be
- Mason, R. E., Geballe, T. R., Packham, C., et al. 2006, , 640, 612. doi:10.1086/500299
- Matsuoka, M., Piro, L., Yamauchi, M., et al. 1990, , 361, 440. doi:10.1086/169209
- Mehdipour, M., Kaastra, J. S., Kriss, G. A., et al. 2015, , 575, A22. doi:10.1051/0004-6361/201425373
- Middleton, M., Done, C., & Gierliński, M. 2007, , 381, 1426. doi:10.1111/j.1365-2966.2007.12341.x
- Min, M., Hovenier, J. W., & de Koter, A. 2003, , 404, 35. doi:10.1051/0004-6361:20030456
- Min, M., Waters, L. B. F. M., de Koter, A., et al. 2007, , 462, 667
- Miniutti, G., Ponti, G., Greene, J. E., et al. 2009, , 394, 443. doi:10.1111/j.1365-2966.2008.14334.x
- Moorwood, A. F. M. 1997, *Extragalactic Astronomy in the Infrared*, 301
- Nandi, P., Chatterjee, A., Chakrabarti, S. K., et al. 2021, , 506, 3111. doi:10.1093/mnras/stab1699
- Nandra, K., O'Neill, P. M., George, I. M., et al. 2007, , 382, 194
- Nardini, E., Fabian, A. C., Reis, R. C., et al. 2011, , 410, 1251. doi:10.1111/j.1365-2966.2010.17518.x
- Nenkova, M., Sirocky, M. M., Ivezić, Ž., & Elitzur, M. 2008, , 685, 147-159
- Nenkova, M., Sirocky, M. M., Nikutta, R., Ivezić, Ž., & Elitzur, M. 2008, , 685, 160-180
- Osterbrock, D. E. & Pogge, R. W. 1985, , 297, 166. doi:10.1086/163513

- Pal, I., Stalin, C. S., Chatterjee, R., et al. 2023, *Journal of Astrophysics and Astronomy*, 44, 87. doi:10.1007/s12036-023-09981-5
- Panagiotou, C. & Walter, R. 2019, , 626, A40. doi:10.1051/0004-6361/201935052
- Parker, M. L., Longinotti, A. L., Schartel, N., et al. 2019, , 490, 683. doi:10.1093/mnras/stz2566
- Pasetto, A., González-Martín, O., Esparza-Arredondo, D., et al. 2019, *The Astrophysical Journal*, 872, 69
- Patrick, A. R., Reeves, J. N., Porquet, D., et al. 2011, , 411, 2353. doi:10.1111/j.1365-2966.2010.17852.x
- Pier, E. A., & Krolik, J. H. 1992, , 401, 99
- Porquet, D., Reeves, J. N., Matt, G., et al. 2018, , 609, A42. doi:10.1051/0004-6361/201731290
- Pounds, K. A., Nandra, K., Stewart, G. C., et al. 1990, , 344, 132. doi:10.1038/344132a0
- Ramos Almeida, C., Levenson, N. A., Rodríguez Espinosa, J. M., et al. 2009, , 702, 1127. doi:10.1088/0004-637X/702/2/1127
- Ramos Almeida, C., Levenson, N. A., Alonso-Herrero, A., et al. 2011, , 731, 92
- Ramos Almeida, C. & Ricci, C. 2017, *Nature Astronomy*, 1, 679. doi:10.1038/s41550-017-0232-z
- Ricci, C. 2011, Ph.D. Thesis
- Ricci, C., Ueda, Y., Koss, M. J., et al. 2015, , 815, L13. doi:10.1088/2041-8205/815/1/L13
- Ross, R. R., Fabian, A. C., & Young, A. J. 1999, , 306, 461
- Ross, R. R., & Fabian, A. C. 2005, , 358, 211
- Schartmann, M., Meisenheimer, K., Camenzind, M., et al. 2005, , 437, 861

- Schurch, N. J. & Done, C. 2008, , 386, L1. doi:10.1111/j.1745-3933.2007.00395.x
- Shakura, N. I. & Sunyaev, R. A. 1973, , 24, 337
- Siebenmorgen, R., Heymann, F., & Efstathiou, A. 2015, , 583, A120
- Smith, R. K., Brickhouse, N. S., Liedahl, D. A., et al. 2001, , 556, L91. doi:10.1086/322992
- Sobolewska, M. A. & Done, C. 2007, , 374, 150. doi:10.1111/j.1365-2966.2006.11117.x
- Stalevski, M., Fritz, J., Baes, M., et al. 2012, , 420, 2756
- Stalevski, M., Ricci, C., Ueda, Y., et al. 2016, Monthly Notices of the Royal Astronomical Society, 458, 2288
- Teng, S. H., Wilson, A. S., Veilleux, S., et al. 2005, , 633, 664. doi:10.1086/491595
- Traina, A., Marchesi, S., Vignali, C., et al. 2021, , 922, 159. doi:10.3847/1538-4357/ac1fee
- Turner, T. J. & Pounds, K. A. 1989, , 240, 833. doi:10.1093/mnras/240.4.833
- Urry, C. M. & Padovani, P. 1995, , 107, 803. doi:10.1086/133630
- van Bemmell, I. M., & Dullemond, C. P. 2003, , 404, 1
- Vander Meulen, B., Camps, P., Stalevski, M., et al. 2023, , 674, A123. doi:10.1051/0004-6361/202245783
- Vasudevan, R. V., Mushotzky, R. F., Reynolds, C. S., et al. 2014, , 785, 30. doi:10.1088/0004-637X/785/1/30
- Victoria-Ceballos, C. I., González-Martín, O., Masegosa, J., et al. 2023, arXiv:2308.01992. doi:10.48550/arXiv.2308.01992
- Waddell, S. G. H. & Gallo, L. C. 2020, , 498, 5207. doi:10.1093/mnras/staa2783
- Walton, D. J., Brightman, M., Risaliti, G., et al. 2018, , 473, 4377. doi:10.1093/mnras/stx2659

Wittkowski, M., Kervella, P., Arsenault, R., et al. 2004, , 418, L39. doi:10.1051/0004-6361:20040118

Xiang, X., Ballantyne, D. R., Bianchi, S., et al. 2022, , 515, 353. doi:10.1093/mnras/stac1646

Zdziarski, A. A., Johnson, W. N., Done, C., et al. 1995, , 438, L63. doi:10.1086/187716